

# **NONLINEAR DYNAMIC ANALYSIS OF HIGH SPEED ROLLING ELEMENT BEARINGS**

**THESIS**

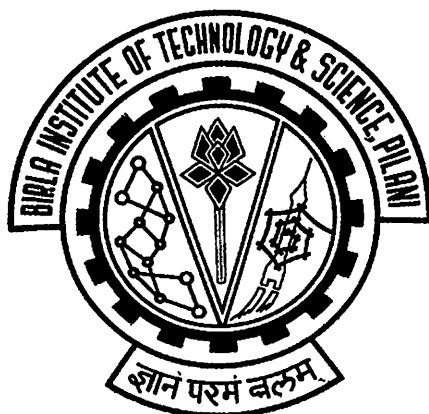
Submitted in partial fulfillment  
of the requirements for the degree of  
**DOCTOR OF PHILOSOPHY**

By

**Suraj Prakash Harsha**

Under the Supervision of

**Prof. Ravi Prakash**



**BIRLA INSTITUTE OF TECHNOLOGY & SCIENCE  
PILANI (RAJASTHAN) INDIA**

**2004**

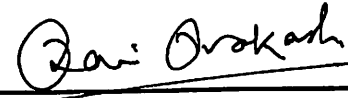
***DEDICATED TO MY PARENTS***

**BIRLA INSTITUTE OF TECHNOLOGY & SCIENCE  
PILANI (RAJASTHAN)**

**CERTIFICATE**

This is to certify that the thesis entitled “**Nonlinear Dynamic Analysis of High Speed Rolling Element Bearings**” and submitted by **Suraj Prakash Harsha** ID.No. **2000PHXF018** for award of Ph.D. Degree of the Institute, embodies original work done by him under my supervision.

Signature in full of the Supervisor



Name in capital block letters:

**RAVI PRAKASH**

Designation:

**Professor of Mechanical Engineering Group &  
Dean, Research & Consultancy Division**

Date: 29/9/04

## ACKNOWLEDGEMENTS

I wish to express deep sense of gratitude and sincere thanks to my thesis supervisor Prof. Ravi Prakash, Dean, Research and Consultancy Division for his able guidance, encouragement and suggestions throughout the period of this research work. It has been a privilege for me to work under his guidance.

Gratitude is also accorded to B.I.T.S., Pilani for providing all the necessary facilities to complete the research work. My special thanks go to Prof. S. Venkateswaran, Vice-Chancellor, B.I.T.S., Pilani for giving me an opportunity to do research at the Institute. I also thank Prof. L. K. Maheshwari, Director, B.I.T.S.-Pilani, Pilani Campus, Prof. K. E. Raman Deputy Director (Administration), Prof. V. S. Rao, Deputy Director (Off-Campus) and Prof. A. K. Sarkar, Dean Instruction Division and Faculty Division-I of the institute for providing the necessary infrastructure and other facilities.

Much appreciation is expressed to Prof. Sandeep Kumar, Sungai Petani, Malaysia and Prof. R. R. Mishra for their valuable suggestions, moral support and assistance.

Special thanks to Prof. B. R. Natarajan, Dean Distance Learning Programmes Division for his guidance and invaluable assistance throughout my research work.

I also express my gratitude for the kind and affectionate enquiries about the work and the encouragement given by Research and Consultancy Division staff and my colleagues.

Finally a very special expression of appreciation is extended to my parents Shri J. P. Harsha and Smt. Vimla Harsha and to younger brother Mahendra Harsha. Without their encouragement, patience, and understanding this endeavor would not have been possible. I would like to record my special affection and thanks to my wife Sangeeta, whose constant persuasion and moral support has been a source of inspiration to me. I also thank my daughter Kirti and son Aditya for having cheerfully sacrificing the time that rightfully belonged to them.

## ABSTRACT

Analysis of the vibrations of the rotor supported by rolling element bearings is becoming important with the increasing demands on running accuracy. Recently, a lot of research is being directed towards rolling element bearings, which act not only as structural elements but also as source of vibrations. This work attempts to study the vibration response of high-speed rotor supported by rolling element bearings and both the balanced and unbalanced rotor conditions have been selected for the present study. A mathematical model has been proposed which takes into account the sources of non-linearity such as Hertzian contact, radial internal clearance, distributed defects and sources of parametric excitation, which are the varying compliance of rolling element bearings.

The analytical formulation accounts for tangential and radial motions of rolling elements, as well as for the rotor, the inner and the outer races. The contacts between the rolling elements and races are treated as nonlinear springs whose stiffnesses are obtained on the basis of the Hertzian elastic contact deformation theory. The application of Lagrange equation leads to a system of nonlinear ordinary differential equations governing the motion of the rotor bearing system. The system equations of motion have non-analytic stiffness terms, which are found to be numerically stiff. The implicit type numerical integration technique Newmark-  $\beta$  with Newton-Raphson method has been used for the solution of these equations. Various techniques like higher order Poincarè maps, phase trajectories, non-autonomous shooting technique and Fast Fourier Transformations are used for studying the nature of the response. Theoretical analysis for the balanced and the unbalanced rotor over a wide range of rotor speed has revealed several regions of instability and deterministic chaotic response. An important finding from the present analysis is the existence of unstable and chaotic response region at very high speeds, primarily due to the bearing clearance.

The model also predicts discrete spectrum with specific frequency components for each order of waviness. For outer race waviness, the spectrum has components at outer race defect frequency ( $f_{bp}$ ) and its harmonics. In case of inner race waviness, the waviness order to number of rolling elements and its multiples give rise to spectral components at the inner race defect frequency ( $f_{vp}$ ) and its multiples. Other orders of waviness generate side band at multiples of rotor frequency about these peaks. In the case of off-size rolling element, the model predicts

discrete spectra having significant components at multiples of cage frequency. The effects of the parameters like the rotor speed, the radial internal clearance, the unbalanced rotor force and the surface imperfections on dynamic response are analyzed theoretically and these results are found to match fairly well with the published results.

# TABLE OF CONTENTS

ACKNOWLEDGEMENT	i
ABSTRACT	ii
TABLE OF CONTENTS	iv
LIST OF TABLES	vii
LIST OF FIGURES	viii
LIST OF SYMBOLS	xiii
<b>CHAPTER 1: INTRODUCTION</b>	<b>1</b>
1.1 BACKGROUND	1
1.2 OBJECTIVE OF THE STUDY	3
1.3 ORGANIZATION OF THE THESIS	3
<b>CHAPTER 2: LITERATURE REVIEW</b>	<b>5</b>
2.1 CLEARANCE NON-LINEARITY	5
2.2 DISTRIBUTED DEFECTS NON-LINEARITY	8
2.3 MODELING OF ROLLING ELEMENT BEARINGS	12
<b>CHAPTER 3: SOURCES OF VIBRATIONS GENERATION</b>	<b>16</b>
3.1 INTRODUCTION	16
3.2 VIBRATION SOURCES	17
3.2.1 Parametric Excitations	17
3.2.2 Distributed Defects	19
3.2.2.1 Description of Waviness	19
3.2.2.2 Excitation Frequencies	19
3.3 SUMMARY OF EXCITATION FREQUENCIES	26

**CHAPTER 4: DYNAMIC ANALYSIS OF ROLLING ELEMENT BEARING DUE  
TO PARAMETRIC EFFECTS**

		28
4.1	INTRODUCTION	28
4.2	PROBLEM FORMULATION	30
4.3	METHODS OF SOLUTION	40
4.4	METHODS OF ANALYSIS	41
	4.4.1 Poincarè Maps	43
	4.4.2 The Non-autonomous Shooting Method	45
4.5	RESULTS & DISCUSSIONS	47
	4.5.1 Static Bearing Stiffness	47
	4.5.2 Results of Theoretical Simulation	47
	4.5.2.1 Response for point contact at $\gamma_0 = 20 \mu\text{m}$ , $W = 6 \text{ N}$ and $F_u = 0$	48
	4.5.2.2 Response for point contact at $\gamma_0 = 12 \mu\text{m}$ , $W = 6 \text{ N}$ and $F_u = 0$	60
	4.5.2.3 Response for point contact at $\gamma_0 = 20 \mu\text{m}$ , $W = 6 \text{ N}$ and $F_u = 15\%W$	73
	4.5.2.4 Response for line contact at $\gamma_0 = 1 \mu\text{m}$ , $W = 6 \text{ N}$ and $F_u = 0$	84
	4.5.2.5 Response for line contact at $\gamma_0 = 0.5 \mu\text{m}$ , $W = 6 \text{ N}$ and $F_u = 0$	111
	4.5.2.6 Response for line contact at $\gamma_0 = 1 \mu\text{m}$ , $W = 6 \text{ N}$ and $F_u = 15\%W$	127
4.6	CONCLUSIONS	136



<b>CHAPTER 5: DYNAMIC ANALYSIS OF ROLLING ELEMENT BEARINGS WITH DISTRIBUTED DEFECTS</b>	147
5.1 INTRODUCTION	148
5.2 PROBLEM FORMULATION	149
5.3 RESULTS & DISCUSSIONS	151
5.3.1 Results of Theoretical Simulation	151
5.3.1.1 Outer Race Waviness	151
5.3.1.2 Inner Race Waviness	161
5.3.1.3 Ball Waviness	176
5.3.1.4 Ball Size Variation	186
5.4 CONCLUSIONS	205
<b>CHAPTER 6: CONCLUSIONS AND SCOPE FOR FUTURE WORK</b>	207
<b>REFERENCES</b>	210
<b>Appendix A PROPERTIES OF ROLLING ELEMENT BEARINGS</b>	218
<b>Appendix B ROLLING ELEMENT BEARING STIFFNESS</b>	220
<b>Appendix C THE VARIATIONAL EQUATIONS</b>	224
<b>Appendix D MODIFIED NEWMARK - <math>\beta</math> METHOD</b>	226
<b>LIST OF PUBLICATIONS</b>	228

## LIST OF TABLES

Table No.	Title	Page No.
3.1	The excitation frequencies of different sources in rolling bearing	26
4.1	Nature of solutions for $\gamma_0 = 20\mu\text{m}$ , $W = 6\text{ N}$	63
4.2	Nature of solutions for $\gamma_0 = 12\mu\text{m}$ , $W = 6\text{ N}$	78
4.3	Nature of solutions for $\gamma_0 = 20\mu\text{m}$ , $W = 6\text{ N}$ and $F_u = 15\%W$	89
4.4	Nature of solutions for $\gamma_0 = 1\mu\text{m}$ , $W = 6\text{ N}$	110
4.5	Nature of solutions for $\gamma_0 = 0.5\mu\text{m}$ , $W = 6\text{ N}$	133
4.6	Nature of solutions for $\gamma_0 = 1\mu\text{m}$ , $W = 6\text{ N}$ and $F_u = 15\%W$	145
5.1	Summary of outer race waviness	160
5.2	Summary of inner race waviness	180
5.3	Summary of ball waviness	190
5.4	Summary of ball size variation	204
A.1	Geometric and physical properties used for the ball and roller bearings	218

## LIST OF FIGURES

Figure No.	Title	Page No.
1.1	Input-output possibilities for linear and nonlinear system	2
3.1	The flexibility of the rolling contacts in a rolling element bearing is represented by nonlinear springs	18
3.2	In the presence of a radial load the rolling elements can lose contact with the races leading to severe parametric excitations	18
3.3	Waviness at the inner and outer races	20
3.4	Race waviness model	21
3.5	Wave of the race	21
3.6	Ball waviness with inner race	27
3.7	Presence of an off-sized ball in a ball set	27
4.1	A schematic diagram of a rolling element bearing	31
4.2	Mass-spring model of the rolling element bearing	31
4.3	Rigid body structure of inner race	34
4.4	Rolling elements with its degree of freedom	34
4.5	Effect of step size on stability of system	42
4.6	Poincarè maps	42
4.7	Vertical and horizontal critical frequency	46
4.8	Response plot for $\gamma_0 = 20\mu\text{m}$ , $W = 6\text{ N}$	49
4.9	Response at 1500 rpm for $\gamma_0 = 20\mu\text{m}$ , $W = 6\text{ N}$	50
4.10	Response at 1950 rpm for $\gamma_0 = 20\mu\text{m}$ , $W = 6\text{ N}$	51
4.11	Response at 2100 rpm for $\gamma_0 = 20\mu\text{m}$ , $W = 6\text{ N}$	52
4.12	Response at 2400 rpm for $\gamma_0 = 20\mu\text{m}$ , $W = 6\text{ N}$	53
4.13	Response at 2700 rpm for $\gamma_0 = 20\mu\text{m}$ , $W = 6\text{ N}$	55
4.14	Response at 4000 rpm for $\gamma_0 = 20\mu\text{m}$ , $W = 6\text{ N}$	56
4.15	Response at 6000 rpm for $\gamma_0 = 20\mu\text{m}$ , $W = 6\text{ N}$	57
4.16	Response at 7250 rpm for $\gamma_0 = 20\mu\text{m}$ , $W = 6\text{ N}$	58

4.17	Response at 7600 rpm for $\gamma_0 = 20\mu\text{m}$ , $W = 6\text{ N}$	59
4.18	Response at 8900 rpm for $\gamma_0 = 20\mu\text{m}$ , $W = 6\text{ N}$	61
4.19	Response at 9900 rpm for $\gamma_0 = 20\mu\text{m}$ , $W = 6\text{ N}$	62
4.20	Response plot for $\gamma_0 = 12\mu\text{m}$ , $W = 6\text{ N}$	64
4.21	Response at 2400 rpm for $\gamma_0 = 12\mu\text{m}$ , $W = 6\text{ N}$	66
4.22	Response at 2500 rpm for $\gamma_0 = 12\mu\text{m}$ , $W = 6\text{ N}$	67
4.23	Response at 2800 rpm for $\gamma_0 = 12\mu\text{m}$ , $W = 6\text{ N}$	68
4.24	Response at 2900 rpm for $\gamma_0 = 12\mu\text{m}$ , $W = 6\text{ N}$	69
4.25	Response at 3100 rpm for $\gamma_0 = 12\mu\text{m}$ , $W = 6\text{ N}$	70
4.26	Response at 8900 rpm for $\gamma_0 = 12\mu\text{m}$ , $W = 6\text{ N}$	71
4.27	Response at 8950 rpm for $\gamma_0 = 12\mu\text{m}$ , $W = 6\text{ N}$	72
4.28	Response at 9200 rpm for $\gamma_0 = 12\mu\text{m}$ , $W = 6\text{ N}$	74
4.29	Response at 10000 rpm for $\gamma_0 = 12\mu\text{m}$ , $W = 6\text{ N}$	75
4.30	Response at 10900 rpm for $\gamma_0 = 12\mu\text{m}$ , $W = 6\text{ N}$	76
4.31	Response at 10950 rpm for $\gamma_0 = 12\mu\text{m}$ , $W = 6\text{ N}$	77
4.32	Unbalance force ( $F_u$ ) acting on rolling element bearing	79
4.33	Response plot, $\gamma_0 = 20\mu\text{m}$ , $W = 6\text{ N}$ and $F_u = 15\%W$	79
4.34	Response at 2000 rpm for $\gamma_0 = 20\mu\text{m}$ , $W = 6\text{ N}$ , $F_u = 15\%W$	81
4.35	Response at 3500 rpm for $\gamma_0 = 20\mu\text{m}$ , $W = 6\text{ N}$ , $F_u = 15\%W$	82
4.36	Response at 4000 rpm for $\gamma_0 = 20\mu\text{m}$ , $W = 6\text{ N}$ , $F_u = 15\%W$	83
4.37	Response at 7000 rpm for $\gamma_0 = 20\mu\text{m}$ , $W = 6\text{ N}$ , $F_u = 15\%W$	85
4.38	Response at 8700 rpm for $\gamma_0 = 20\mu\text{m}$ , $W = 6\text{ N}$ , $F_u = 15\%W$	86
4.39	Response at 9000 rpm for $\gamma_0 = 20\mu\text{m}$ , $W = 6\text{ N}$ , $F_u = 15\%W$	87
4.40	Response at 10000 rpm for $\gamma_0 = 20\mu\text{m}$ , $W = 6\text{ N}$ , $F_u = 15\%W$	88
4.41	Response plot for $\gamma_0 = 1\mu\text{m}$ and $W = 6\text{ N}$	90
4.42	Response at 1500 rpm for $\gamma_0 = 1\mu\text{m}$ , $W = 6\text{ N}$	92
4.43	Response at 2200 rpm for $\gamma_0 = 1\mu\text{m}$ , $W = 6\text{ N}$	93
4.44	Response at 2500 rpm for $\gamma_0 = 1\mu\text{m}$ , $W = 6\text{ N}$	94

4.45	Response at 3800 rpm for $\gamma_0 = 1\mu\text{m}$ , $W = 6\text{N}$	95
4.46	Response at 4000 rpm for $\gamma_0 = 1\mu\text{m}$ , $W = 6\text{N}$	96
4.47	Response at 4050 rpm for $\gamma_0 = 1\mu\text{m}$ , $W = 6\text{N}$	97
4.48	Response at 5100 rpm for $\gamma_0 = 1\mu\text{m}$ , $W = 6\text{N}$	98
4.49	Response at 5200 rpm for $\gamma_0 = 1\mu\text{m}$ , $W = 6\text{N}$	99
4.50	Response at 5500 rpm for $\gamma_0 = 1\mu\text{m}$ , $W = 6\text{N}$	100
4.51	Response at 7000 rpm for $\gamma_0 = 1\mu\text{m}$ , $W = 6\text{N}$	101
4.52	Response at 7100 rpm for $\gamma_0 = 1\mu\text{m}$ , $W = 6\text{N}$	103
4.53	Response at 7500 rpm for $\gamma_0 = 1\mu\text{m}$ , $W = 6\text{N}$	104
4.54	Response at 8000 rpm for $\gamma_0 = 1\mu\text{m}$ , $W = 6\text{N}$	105
4.55	Response at 8200 rpm for $\gamma_0 = 1\mu\text{m}$ , $W = 6\text{N}$	106
4.56	Response at 8500 rpm for $\gamma_0 = 1\mu\text{m}$ , $W = 6\text{N}$	107
4.57	Response at 10000 rpm for $\gamma_0 = 1\mu\text{m}$ , $W = 6\text{N}$	108
4.58	Response at 10200 rpm for $\gamma_0 = 1\mu\text{m}$ , $W = 6\text{N}$	109
4.59	Response plot for $\gamma_0 = 0.5\mu\text{m}$ and $W = 6\text{N}$	112
4.60	Response at 1800 rpm for $\gamma_0 = 0.5\mu\text{m}$ , $W = 6\text{N}$	113
4.61	Response at 2800 rpm for $\gamma_0 = 0.5\mu\text{m}$ , $W = 6\text{N}$	114
4.62	Response at 3500 rpm for $\gamma_0 = 0.5\mu\text{m}$ , $W = 6\text{N}$	115
4.63	Response at 3800 rpm for $\gamma_0 = 0.5\mu\text{m}$ , $W = 6\text{N}$	117
4.64	Response at 4000 rpm for $\gamma_0 = 0.5\mu\text{m}$ , $W = 6\text{N}$	118
4.65	Response at 4900 rpm for $\gamma_0 = 0.5\mu\text{m}$ , $W = 6\text{N}$	119
4.66	Response at 5000 rpm for $\gamma_0 = 0.5\mu\text{m}$ , $W = 6\text{N}$	120
4.67	Response at 5100 rpm for $\gamma_0 = 0.5\mu\text{m}$ , $W = 6\text{N}$	121
4.68	Response at 7000 rpm for $\gamma_0 = 0.5\mu\text{m}$ , $W = 6\text{N}$	122
4.69	Response at 7100 rpm for $\gamma_0 = 0.5\mu\text{m}$ , $W = 6\text{N}$	123
4.70	Response at 7300 rpm for $\gamma_0 = 0.5\mu\text{m}$ , $W = 6\text{N}$	124
4.71	Response at 7600 rpm for $\gamma_0 = 0.5\mu\text{m}$ , $W = 6\text{N}$	125
4.72	Response at 8500 rpm for $\gamma_0 = 0.5\mu\text{m}$ , $W = 6\text{N}$	126

4.73	Response at 8700 rpm for $\gamma_0 = 0.5 \mu\text{m}$ , $W = 6\text{N}$	128
4.74	Response at 9300 rpm for $\gamma_0 = 0.5 \mu\text{m}$ , $W = 6\text{N}$	129
4.75	Response at 10500 rpm for $\gamma_0 = 0.5 \mu\text{m}$ , $W = 6\text{N}$	130
4.76	Response at 10800 rpm for $\gamma_0 = 0.5 \mu\text{m}$ , $W = 6\text{N}$	131
4.77	Response at 11000 rpm for $\gamma_0 = 0.5 \mu\text{m}$ , $W = 6\text{N}$	132
4.78	Response plot for $\gamma_0 = 1 \mu\text{m}$ , $W = 6 \text{ N}$ and $F_u = 15\%W$	134
4.79	Response at 1200 rpm for $\gamma_0 = 1 \mu\text{m}$ , $W = 6 \text{ N}$ and $F_u = 15\%W$	137
4.80	Response at 3500 rpm for $\gamma_0 = 1 \mu\text{m}$ , $W = 6 \text{ N}$ and $F_u = 15\%W$	138
4.81	Response at 3700 rpm for $\gamma_0 = 1 \mu\text{m}$ , $W = 6 \text{ N}$ and $F_u = 15\%W$	139
4.82	Response at 4500 rpm for $\gamma_0 = 1 \mu\text{m}$ , $W = 6 \text{ N}$ and $F_u = 15\%W$	140
4.83	Response at 5500 rpm for $\gamma_0 = 1 \mu\text{m}$ , $W = 6 \text{ N}$ and $F_u = 15\%W$	141
4.84	Response at 8000 rpm for $\gamma_0 = 1 \mu\text{m}$ , $W = 6 \text{ N}$ and $F_u = 15\%W$	142
4.85	Response at 9000 rpm for $\gamma_0 = 1 \mu\text{m}$ , $W = 6 \text{ N}$ and $F_u = 15\%W$	143
4.86	Response at 10700 rpm for $\gamma_0 = 1 \mu\text{m}$ , $W = 6 \text{ N}$ and $F_u = 15\%W$	144
5.1	Response plot for outer race waviness at $N_w = 7$	153
5.2	Response plot for outer race waviness at $N_w = 8$	154
5.3	Response plot for outer race waviness at $N_w = 12$	155
5.4	Response plot for outer race waviness at $N_w = 16$	157
5.5	Response plot for outer race waviness at $N_w = 17$	158
5.6	Response plot for outer race waviness at $N_w = 21$	159
5.7	Response plot for outer race waviness at $N_w = 31$	160
5.8	Response plot for inner race waviness at $N_w = 2$	163
5.9	Response plot for inner race waviness at $N_w = 3$	164
5.10	Response plot for inner race waviness at $N_w = 4$	165
5.11	Response plot for inner race waviness at $N_w = 6$	166
5.12	Response plot for inner race waviness at $N_w = 7$	168
5.13	Response plot for inner race waviness at $N_w = 8$	169
5.14	Response plot for inner race waviness at $N_w = 9$	170
5.15	Response plot for inner race waviness at $N_w = 10$	171

5.16	Response plot for inner race waviness at $N_w = 11$	172
5.17	Response plot for inner race waviness at $N_w = 12$	173
5.18	Response plot for inner race waviness at $N_w = 13$	174
5.19	Response plot for inner race waviness at $N_w = 14$	175
5.20	Response plot for inner race waviness at $N_w = 15$	177
5.21	Response plot for inner race waviness at $N_w = 16$	178
5.22	Response plot for inner race waviness at $N_w = 17$	179
5.23	Response plot for ball waviness at $N_w = 2$	182
5.24	Response plot for ball waviness at $N_w = 4$	183
5.25	Response plot for ball waviness at $N_w = 6$	184
5.26	Response plot for ball waviness at $N_w = 8$	185
5.27	Response plot for ball waviness at $N_w = 10$	187
5.28	Response plot for ball waviness at $N_w = 12$	188
5.29	Response plot for ball waviness at $N_w = 14$	189
5.30	Response plot for ball size variation at $N_b = 3$	192
5.31	Response plot for ball size variation at $N_b = 4$	193
5.32	Response plot for ball size variation at $N_b = 5$	194
5.33	Response plot for ball size variation at $N_b = 6$	195
5.34	Response plot for ball size variation at $N_b = 7$	196
5.35	Response plot for ball size variation at $N_b = 8$	197
5.36	Response plot for ball size variation at $N_b = 9$	199
5.37	Response plot for ball size variation at $N_b = 10$	200
5.38	Response plot for ball size variation at $N_b = 11$	201
5.39	Response plot for ball size variation at $N_b = 13$	202
5.40	Response plot for ball size variation at $N_b = 16$	203
A.1	Dimensions of rolling element bearing	218
B.1	Geometry of contacting bodies	223
D.1	Newmark constant-average acceleration scheme	226

## LIST OF SYMBOLS

$I$  = moment of inertia of each rolling element  
 $I_{\text{rotor}}$  = moment of inertia of the rotor  
 $I_{\text{in}}$  = moment of inertia of the inner race  
 $I_{\text{out}}$  = moment of inertia of the outer race  
 $K$  = periodic order  
 $L$  = arc length, mm  
 $m_{\text{in}}$  = mass of the inner race, kg  
 $m_j$  = mass of the rolling elements, kg  
 $m_{\text{out}}$  = mass of the outer race, kg  
 $m_{\text{rotor}}$  = mass of the rotor, kg  
 $n$  = waviness order  
 $N$  = number of wave lobes  
 $N_b$  = number of balls  
 $N_w$  = number of waves per circumference  
 $p$  = excitation order  
 $q$  = constant associated with waviness order  
 $R$  = radius of outer race  
 $r$  = radius of inner race  
 $r_{\text{in}}$  = position of mass center of inner race  
 $r_{\text{out}}$  = position of mass center of outer race  
 $T$  = kinetic energy of the bearing system  
 $T_{\text{rotor}}$  = kinetic energy of the cage  
 $T_{\text{i_race}}$  = kinetic energy of the inner race  
 $T_{\text{o_race}}$  = kinetic energy of the outer race  
 $T_{\text{r.e.}}$  = kinetic energy of the rolling elements  
 $V$  = potential energy of the bearing system  
 $V_{\text{rotor}}$  = potential energy of the cage  
 $V_{\text{i_race}}$  = potential energy of the inner race  
 $V_{\text{o_race}}$  = potential energy of the outer race  
 $V_{\text{r.e.}}$  = potential energy of the rolling elements  
 $V_{\text{springs}}$  = potential energy of the springs  
 $x, y$  = state space variables  
 $x_{\text{in}}, y_{\text{in}}$  = center of inner race  
 $x_{\text{out}}, y_{\text{out}}$  = center of outer race  
 $\{x_k\}$  = the sequence of  $x_k$   
 $\delta$  = deformation at the point of contact at inner and outer race  
 $(\dot{\phi})_{\text{in}}$  = angular velocity of inner race  
 $(\dot{\phi})_{\text{out}}$  = angular velocity of outer race  
 $\gamma$  = internal radial clearance  
 $\lambda$  = wave length, mm  
 $\omega_{\text{cage}}$  = angular velocity of cage  
 $\omega_{\text{rotor}}$  = angular velocity of rotor  
 $\omega_{\text{inner}}$  = angular velocity of inner race



$(\Pi)_{in}$  = amplitude of the wave at inner race

$(\Pi)_{out}$  = amplitude of the wave at outer race

$\rho_j$  = radial position of the rolling element

$\rho_r$  = radius of each rolling element

$\phi_t$  = a flow

$\phi_t(x_0)$  = the point at time  $t$  on the trajectory emanating from  $x_0$  at time  $t=0$ , used with autonomous systems

$\phi_t(x_0, t_0)$  = the point at time  $t$  on the trajectory emanating from  $x_0$

$\phi_t(x^*, t_0)$  = the periodic solution to the variational equation non-autonomous case

$\mathbf{IR}$  = the real numbers

$\Sigma$  = a hyperplane

$S^1 \times S^1$  = the two - torus

$\theta_j$  = angular position of rolling element

$\chi_j$  = position of  $j^{\text{th}}$  rolling element from the center of inner race

**VC** = Varying compliance frequency

**BPV** = Ball Passage Vibration

**WPF** = Wave Passage Frequency

### 1.1 BACKGROUND

Rolling element bearing is one of the essential elements of rotating machinery ranging from conventional power driven machines to the present sophisticated information storage devices. One of the important issues in rolling element-bearing application is the reduction of noise and vibrations originating from these bearings. These bearings generate vibrations during operation even if they are geometrically and elastically perfect. This is an inherent feature of the type of bearing and is due to the use of a finite number of rolling elements to carry the external loads. The other possible sources of rolling element-bearing vibrations are the unbalanced rotor force and the distributed defects of the rolling elements. The importance of a clear understanding of vibrations associated with rolling element bearings is therefore obvious.

Recent advances in materials and production techniques have enabled the development of bearings for very high speeds. One such application is the gas turbine, which operates at very high speeds resulting in considerable increase in stress levels in bearings. The dynamics of bearing for such an application becomes difficult because of centrifugal forces acting on the rolling elements and the slipping of the rolling elements as they roll on the race. Despite such difficulty, it is very important to model the dynamic behavior of the bearing for high-speed and high performance applications. The dynamic modeling of the bearing for such high performance applications enters the domain of nonlinear systems. This is not surprising, since the nonlinear modeling of the system has proved to be more realistic under stringent conditions. During the last 30 years researchers have documented irregular and unpredictable dynamic behavior of rigid rotor supported by rolling element bearings under external excitation. Nonlinear phenomena occurring in these systems are responsible for these irregular and unpredictable effects that lead to chaos. The possible output of linear and nonlinear system is shown in Fig. 1.1 (Thomson and Stewart, 1986).

Rolling element bearings can be used for diverse applications compared to various kinds of bearings such as film bearings, foil bearings and magnetic bearings that are suitable for specialized applications.

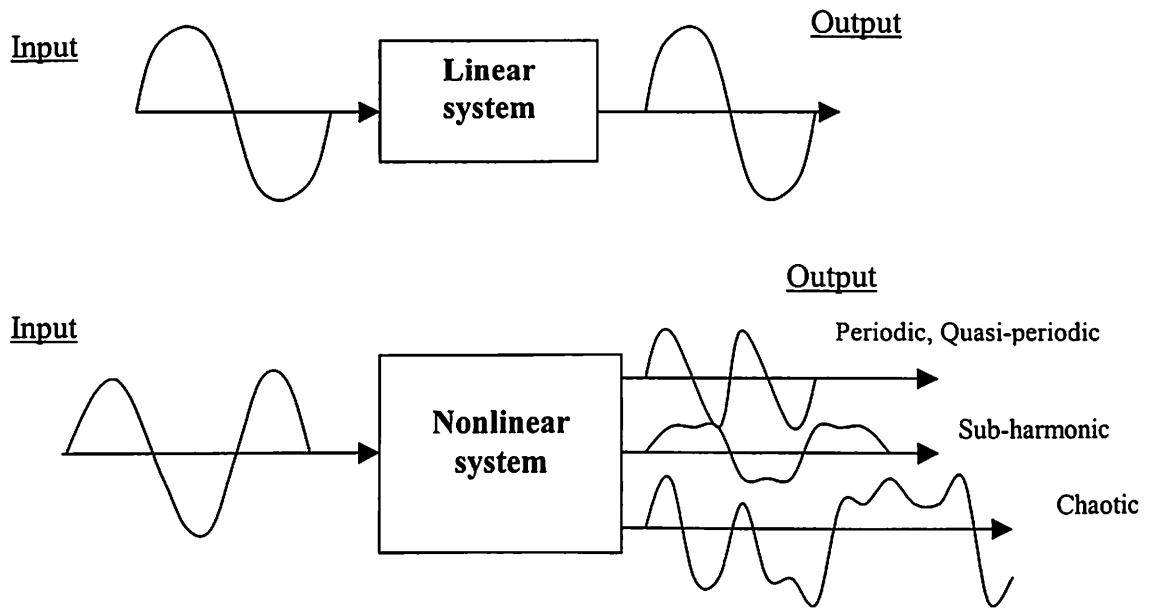


**Fig. 1.1** Input-output possibilities for linear and nonlinear system (Thomson and Stewart, 1986)

For example, rolling element bearings can be used as miniature ball bearings for sensitive and precise components such as inertial guidance gyroscope as well as for very large bearings (about 1.5 m diameter) used for rolling mills. Several advantages make the rolling element bearings desirable where noise is not the consideration. The frictional loss is considerably reduced, which in turn results in less heat generation. The stiffness of the rolling element bearing is very high as compared to the conventional hydrodynamic bearing and therefore bearing deflection is less sensitive to load fluctuation. One major advantage is that very simple lubrication system is needed which is generally a self-supply system requiring negligible maintenance. The other advantage is less requirement of space for rolling element bearing. Moreover the rolling element bearing can take up both radial and axial loads for most of the applications. The disadvantage of the rolling element bearing is generation of noise and their failure due to fatigue of races / rolling elements.

## **1.2 OBJECTIVE OF THE STUDY**

The objective of this study is to analyze the nonlinear effects introduced by rolling element bearings in a rigid horizontal rotor. The sources of non-linearity are due to Hertzian contact, radial internal clearance and source of parametric excitation, which is the varying compliance of a rolling element bearing. Radial internal clearance, which is provided in the design of bearing to compensate for the thermal expansion, introduces the non-linearity in dynamic behavior. Finite number of rolling elements rotating with different velocities with respect to the inner race generate a time varying stiffness component. These rolling element effects introduce a high degree of non-linearity in the bearings, which results in a nonlinear dynamic behavior of the system.

The work reported in the literature till now on this particular problem has taken only self excited vibrations into account i. e. parametric effect. There is very little work reported in the literature on the effect of nonlinear and parametric stiffness variation on the dynamic response of rolling element bearing except some experimental work done by Sunnersjo (1985). Hence, in this investigation, a theoretical analysis could be performed to study the dynamic response of a rigid rotor supported by rolling bearing. However, the analysis will be carried out within certain constraints for simplifying the analysis i.e. the deformation will be assumed elastic, sinusoidal surface waviness and constant damping. In the present research work an attempt could be made also to study the effects of inclusion of unbalanced rotor force and distributed defects on dynamic response.

### 1.3 ORGANIZATION OF THE THESIS

Chapter 1 gives an introduction to sources of non-linear vibrations in rotor bearing system.

Chapter 2 deals with a critical review of the published literature on clearance non-linearity, surface imperfections non-linearity, modeling of bearings and solution techniques for nonlinear system dynamic analysis with theoretical and experimental studies on nonlinear rotor dynamics including chaotic response.

Chapter 3 focuses especially on the sources of vibration generation and their physical descriptions. The important sources of vibration generation considered are the nonlinear stiffnesses, the unbalanced rotor force and the surface imperfections of the contacting surfaces.

Chapter 4 covers the dynamic analysis of rolling element bearing due to parametric and unbalanced rotor effects. The analytical formulation accounts for the tangential and the radial motions of the rolling elements, the rotor, the inner and the outer races. Application of Lagrange equation leads to a system of nonlinear ordinary differential equations governing the motion of the bearing system. The numerical integration technique Newmark-  $\beta$  with Newton-Raphson method has been used for solution of the system equations. The various parameters of study for point and line contact are rotor speed, radial internal clearance and unbalanced rotor force. Techniques for studying nonlinear systems such as FFT, phase plots, Poincarè maps and non-autonomous shooting method are used to study the nature of dynamic response. An analysis of the regions of periodic, sub-harmonic, quasi-periodic and chaotic response of an existing rotor bearing system is also included in this chapter.

The dynamic analysis of rolling element bearing due to surface imperfections has been presented in Chapter 5. The surface imperfections considered are: the waviness of outer race, inner race and rolling elements and off-size rolling element. Surface imperfections existing in the rolling elements of a rolling element bearing have been regarded as excitation sources in the form of bearing frequencies, i.e. principal frequencies, their harmonics and side band frequencies. In addition, the regions of instability and stability are found out and a detailed study on the nature of response is also included. The predicted resonance and vibrations generated by the rotor bearing system are compared with the experimental and theoretical results of the various authors available in the literature.

Chapter 6 presents a comprehensive discussion and conclusions arising out of the present work. The scope for future work is also incorporated in this Chapter.

The vibration analysis of rotor bearing system is becoming more important as demand on running accuracy is increasing. Increasing interest is being devoted to rolling element bearings, not only as structural elements but also as sources of vibration. Development in rotor dynamics has been driven by the objective of high speed and low weight of rotors (Lalanne, 1990 and Rao, 1996). The combination of high speed and low weight has made higher order effects such as non-linearity significant. It is essential that these effects be taken into account at design stage, as at high speed the failure can be very dangerous. The study of nonlinear rotor dynamics and phenomena of chaos in rotor dynamics has been reviewed extensively by Ishida (1994). As Ishida has traced, research in nonlinear rotor dynamics started in 1950's. A rotor system with a circular shaft cross-section and with a circular disc, which is also called a symmetrical rotor, was first system to be studied experimentally by Yamamoto (1957) and theoretically by Mitropolskii' (1960) using asymptotic method.

### 2.1 CLEARANCE NON-LINEARITY

Clearance in mechanical components introduces very strong non-linearity. Clearance, provided in the design of bearing to compensate for the thermal expansion, is also a source of vibration and introduces the non-linearity in the dynamic behaviour. The study of the effect of clearance non-linearity on the response of rotors has attracted a lot of attention lately because of the development of high-speed rotors such as space shuttle main engine turbo-pump rotor. Clearance non-linearity is different from most of the other non-linearities because it cannot be approximated by a mathematical series. Yamamoto (1955) has analytically investigated the vibratory behavior of a vertical rotor supported on ball bearings with radial clearance. He has concluded that the maximum amplitude of vibration at critical speed decreases with increasing radial clearance.

The dynamic response of rotors in bearing clearance has been studied by Ehrich (1966, 1967, 1988, 1991). These studies have shown the appearance of subharmonic and

chaotic response in rotors. Ehrich (1972) has attempted to explain theoretically the appearance of linear combination of two frequencies during a test run of gas turbine. These frequencies are first the rotational frequency and second the asynchronous frequency because of possible trapping of fluid in the rotor. He has attributed the appearance of these frequencies to the truncation of basic "beat frequency" waveform occurring due to clearance in the rotor bearing system. Bentley (1974) and Muszynska (1984) studied the effect of bearing clearances at sub-critical speed. They reported the presence of 2<sup>nd</sup> and 3<sup>rd</sup> order sub-harmonic vibration based on their experiments. Computer simulations of varying compliance vibrations in rolling bearings were first presented by Sunnersjo (1978). Hertzian theory gives a quasi-linear relation of force to local displacement but, as he noticed, another cause of non-linearity is the varying number of rolling elements in the load zone. Childs (1982) has presented an explanation for the subharmonic response of rotors in presence of bearing clearances using perturbation techniques assuming small non-linearity. Dynamic effects of varying compliance have been studied for the special case of plane motion of a rigid rotor under pure radial load by Gad et al. (1984a). They showed that resonance occurs when varying compliance frequency coincides with frequency of the system. They also pointed out that for certain speeds, varying compliance could exhibit its sub and super-harmonic vibrations for rotor bearing systems.

Saito (1985) has reported the study of nonlinear unbalance response of horizontal Jeffcott rotor supported on ball bearings with radial clearance. He observed that the amplitude of vibration suddenly becomes large on exceeding the critical unbalance. The study of excessive vibrations of the liquid oxygen pumps in the space shuttle main engine pump by Childs and Moyer (1985) and Beatty and Hine (1989) during hot firing ground testing has shown that the clearance non-linearity by itself generates frequency component incommensurate with rotational frequency. Day (1987) carried out an analytical study of a rotor supported on bearings with clearance. A special frequency named nonlinear natural frequency is defined by Day (1987) and is used to develop the solution of the non-linear Jeffcott rotor as singular asymptotic expansions. This nonlinear frequency, which is the ratio of cross stiffness and damping, is incommensurate with respect to the rotational frequency. Choi and Noah (1987) have studied the nonlinear

steady state response of a rotor support system using harmonic balance method with FFT. Kim and Noah (1990) have studied a horizontal Jeffcott rotor supported on bearing with clearance. Stability analysis of the steady state motion was performed by Kim and Noah (1990) and their work also deals with characterization of bifurcations. Quasi-periodic motion is shown to occur as a result of secondary Hopf bifurcation owing to increase of destabilizing cross coupling stiffness coefficient in their model.

Ehrich (1992) has theoretically analyzed the model of a Jeffcott rotor system operating eccentrically with a clearance and in local contact with stator possessing the characteristics of a bilinear oscillator. Sub-critical super-harmonic and super-critical sub-harmonic responses have been reported, which are shown to be the mirror images of each other. The response of the theoretical model compares well with the test data of an Aero-engine Gas Turbine. Goldman and Muszynska (1994) have studied the orderly and chaotic dynamic responses of simple mechanical structures with clearance and impact. In the first part of their work experimental results from a simulator of a rotating machine with one loose pedestal are presented with a summary of analytical results. The second part discusses the existence of main and higher order resonance in structures with clearances and impact, which are excited by external periodic forces. The dynamic behavior of externally excited rotor / stator systems with occasional, partly rubbing conditions has been studied by Goldman and Muszynska (1994 (a)). The only source of non-linearity was found due to impacting. The results of this model compare well with the experimental results obtained previously by other researchers. The results of numerical simulation are presented in form of bifurcation diagrams, rotor lateral vibration, time-base waves and orbits.

The dynamics of a shaft disc arrangement with a bearing clearance non-linearity has been analyzed by Flowers and Wu (1996). Numerical simulation and limit cycle analysis have been performed by Flowers and Wu (1996). The authors have shown the generation of super-harmonic response, multi-valued response and periodic behavior. They have also conducted experiments to study the effect of bearing clearance on shaft disc lateral vibration response and observed the presence of super-harmonics. The appearance of super harmonics is attributed to bearing clearance and non-symmetrical stiffness. Kim and Noah (1996) have studied the theoretical model of Jeffcott rotor with bearing



clearance. They have used a modified HBM/AFT method to obtain quasi-periodic response.

In the present work, the radial internal clearance has been taken as an important parameter for theoretical study of rolling element bearing. This study has been carried out for both balanced and unbalanced rotor conditions having point and line contact of rolling element bearing. The case of a balanced rotor has been studied by Choi and Noah (1987) and Kim and Noah (1996). However, they have not analyzed the case of an unbalanced rotor for point and line contact with nonlinear contact stiffness. Therefore, an effort has been made to analyze this in the present study.

## **2.2 DISTRIBUTED DEFECTS NON-LINEARITY**

It is generally known that a rolling element bearing may generate vibrations due to varying compliance (Sunnensjo, 1978), or time varying contact forces, which exist between the various components of the bearing (Meyer et al., 1980). The nature of response to vibration, changes with the presence of defect in bearing components. One large class of bearing defects may be categorized as point or local defects. This includes cracks, pits and spalls in the running surface, as well as particle contamination of the bearing lubricant. Defects of this kind manifest themselves in the bearing's vibration signal as vibratory transients, which result from discontinuities in the contact forces as the defect undergoes rolling contact.

The other important class of bearing defects can be characterized as distributed defects, which involve the entire structure of the bearing. Distributed defects include misaligned races, surface waviness of the bearing components and off-size rolling element (Meyer et al., 1980). These defects give rise to excessive contact forces, which in turn result in premature surface fatigue and ultimate failure. These defects may result either from manufacturing error or from abrasive wear. Hence, study of vibrations generated by these defects is important for quality inspection as well as for condition monitoring. Several researchers have investigated the correlation between the bearing vibration and the surface quality with an aim to evolve a vibration test procedure and quality limits for use within the bearing industry.

It is generally accepted that it is not possible to produce a perfect surface or contour even with the best machine tools and this applies to ball bearing manufacturing as well. Surface waviness is a manufacturing imperfection. An imperfection is called waviness if wavelength of the waviness profile is much longer than the Hertzian contact width (Wardle and Poon, 1983). It may be caused by different manufacturing malfunctions such as uneven wear of the grinding wheel, variable interactions between the tool and work piece, vibrations of machine elements or movements of the work piece in the fixture. The importance of running surface waviness from the point of view of vibration has been known for a long time but no study has been conducted due to the difficulty in measurement of surface waviness. Research on the contribution of waviness to the rotor-bearing vibrations received a thrust in 1960s, with the availability of vibration testing machines, which could measure the surface waviness too (SKF, 1961). Systematic studies, both analytical as well as experimental, of vibrations caused by geometrical imperfections were first made by Tallian and Gustafsson (1963, 1965). They investigated the vibrations of the stationary outer race of a bearing under axial load. They also studied the effect of waviness and pointed out that lower order race waviness affects the amplitude of the vibrations at the Ball Passage Frequency (BPF).

Yhland (1967) examined the relationship between waviness and the resulting vibration spectrum. According to Yhland (1967) for a bearing with  $N_b$  rolling elements, if  $p$  and  $q$  are integers equal to or greater than 1 and 0 respectively, vibration in the radial direction measured at a point on the outer diameter of outer race. The bearing outer race moves as a rigid body when  $p = 1$ . For  $p > 1$ , vibrations are of the flexural type where  $p$  is the number of lobes per circumference of the outer race deflection curve. Cena and Hobbs (1972) concluded that the effect of ball waviness on the vibration of ball bearing systems is more significant than the effect of race waviness.

The distributed defects are likely to increase the repetitive surface and subsurface stresses to which the bearing races are subjected, causing eventually their fatigue failure. Therefore, a study of the vibratory response of bearing races due to distributed defects assumes importance. Meyer et al. (1980) proposed a model to predict the vibratory displacement of races due to distributed defects on the moving races or on the rolling elements under axial load. Mayer et al. (1980) derived expressions for radial

displacement of the stationary bearing race. They studied the race waviness, theoretically and concluded that the vibration spectrum of a ball bearing with wavy surface would have peaks at (i)  $N_b \omega_{inner}$ , (ii)  $\omega_{cage}$ , (iii) ball passage frequency (BPF) and its super-harmonics and (iv) around the wave passage frequency (WPF) and its super-harmonics at  $\pm N_w \omega_{inner}$ , where  $N_w$  is the number of waves. Thomas (1982) pointed out that waviness contributes to low frequency noise, so at relatively low speeds, it causes few problems with precision bearings. It becomes a serious problem only when components possess relatively large amplitude of waviness or at high speeds.

Wardle and Poon (1983) and Sayles and Poon (1981) found that the problem of the severe vibrations and noise problem in bearings can be attributed to the waviness. They reported that the waviness produces vibrations at frequencies up to approximately 300 times the rotational speed but the phenomenon is more predominant at frequencies below about 60 times the rotational speeds. Wardle and Poon (1983) also found the relation between the number of balls and number of waves for severe vibrations to occur. When the number of balls and waves are equal, severe vibrations occur because in such case there is symmetry of loading and all balls vibrate in same phase. Sunnersjo (1985) studied the vibration of a radially loaded bearing due to inner race waviness and varying roller diameter. However, he did not consider the elastic deformation of bearing elements in his study. Rahnejat and Gohar (1985) studied squeeze film damping for the rolling motion of a rigid rotor supported by two identical bearings. They showed that even in the presence of an elastohydrodynamic lubricating film between the balls and the races, a peak at the BPF appears in the spectrum. As expected, resonance occurs when the BPF coincides with a natural frequency.

Wardle (1988a, 1988b) showed theoretically as well as experimentally that outer race waviness produces vibrations at the harmonics of outer race ball passage frequency. Similar observations have also been reported by Gustafsson et al. (1963). Rahnejat and Gohar (1985) and Franco et al. (1992) indicated that inner race waviness is somewhat more complicated than what Gustafsson et al. (1963) and Meyer et al. (1980) have predicted. Wardle (1988a) showed that in case of inner race waviness, the axial vibrations take place at frequencies harmonic with the ball to inner race passage rate  $N_b (\omega_{cage} - \omega_{inner})$ , whereas radial vibrations occur at frequencies  $N_b (\omega_{cage} - \omega_{inner}) \pm \omega_{inner}$ .

displacement of the stationary bearing race. They studied the race waviness, theoretically and concluded that the vibration spectrum of a ball bearing with wavy surface would have peaks at (i)  $N_b\omega_{inner}$ , (ii)  $\omega_{cage}$ , (iii) ball passage frequency (BPF) and its super-harmonics and (iv) around the wave passage frequency (WPF) and its super-harmonics at  $\pm N_w\omega_{inner}$ , where  $N_w$  is the number of waves. Thomas (1982) pointed out that waviness contributes to low frequency noise, so at relatively low speeds, it causes few problems with precision bearings. It becomes a serious problem only when components possess relatively large amplitude of waviness or at high speeds.

Wardle and Poon (1983) and Sayles and Poon (1981) found that the problem of the severe vibrations and noise problem in bearings can be attributed to the waviness. They reported that the waviness produces vibrations at frequencies up to approximately 300 times the rotational speed but the phenomenon is more predominant at frequencies below about 60 times the rotational speeds. Wardle and Poon (1983) also found the relation between the number of balls and number of waves for severe vibrations to occur. When the number of balls and waves are equal, severe vibrations occur because in such case there is symmetry of loading and all balls vibrate in same phase. Sunnersjo (1985) studied the vibration of a radially loaded bearing due to inner race waviness and varying roller diameter. However, he did not consider the elastic deformation of bearing elements in his study. Rahnejat and Gohar (1985) studied squeeze film damping for the rolling motion of a rigid rotor supported by two identical bearings. They showed that even in the presence of an elastohydrodynamic lubricating film between the balls and the races, a peak at the BPF appears in the spectrum. As expected, resonance occurs when the BPF coincides with a natural frequency.

Wardle (1988a, 1988b) showed theoretically as well as experimentally that outer race waviness produces vibrations at the harmonics of outer race ball passage frequency. Similar observations have also been reported by Gustafsson et al. (1963). Rahnejat and Gohar (1985) and Franco et al. (1992) indicated that inner race waviness is somewhat more complicated than what Gustafsson et al. (1963) and Meyer et al. (1980) have predicted. Wardle (1988a) showed that in case of inner race waviness, the axial vibrations take place at frequencies harmonic with the ball to inner race passage rate  $N_b (\omega_{cage} - \omega_{inner})$ , whereas radial vibrations occur at frequencies  $N_b (\omega_{cage} - \omega_{inner}) \pm \omega_{inner}$ .

Wardle (1998a) also argued that only specific orders of waviness generate vibrations. Axial vibrations are produced when the number of waves per circumference is an integral multiple of the number of balls, whereas radial vibrations are produced by waviness of the order of  $N_w = iN_b \pm 1$ . Some of Wardle's arguments were later proved by Franco et al. (1992). Wardle (1988a) also pointed out that ball waviness produces vibrations in the axial direction at frequencies given by  $2i\omega_{ball}$ , while radial vibrations occur at frequencies given by  $2i\omega_{ball} \pm \omega_{cage}$ . He also indicated that only even orders of ball waviness produce vibrations. This was also pointed out by Yhland (1967). Su et al. (1992, 1993) investigated the effect of surface irregularities on the demodulated spectra of a bearing.

Choudhury and Tandon (1998) proposed a theoretical model to predict the vibration response of rolling bearing due to distributed defects under radial load. They discussed about race mode or flexural vibration of races due to various types of distributed defects in rolling bearings. Aktürk (1999) investigated the effect of bearing surface waviness on the rotor vibrations. He predicted the discrete spectrum with specific frequency components for each order of waviness for outer race, inner race and ball waviness. A nonlinear model to analyze the ball bearing vibration due to the waviness in a rigid rotor supported by two or more ball bearings has also been proposed by Jang and Jeong (2002). They investigated the vibration frequencies and their harmonics resulting from the various kinds of waviness in rolling elements.

It is not possible to produce a set of identical balls even with the best machine tools. There is always some difference between ball diameters (less than the machine tolerance). This is known as off-sized ball effect. The presence of off-sized balls in a bearing introduces further untoward vibrations in the rotor bearing system. As a result of experiments, a specific relationship has been found to exist between the internal dimensions of bearings and the vibration factors for the different components. The rolling elements being more important than the outer and inner race (SKF, 1961). Tamura (1968) showed experimentally that the axial stiffness of ball bearing varies with the cage position, since the number of loaded balls at any instant gets changed by the balls' diameter difference. The appearance of rotor axial resonance was also reported by Tamura (1968) as a multiple of angular velocity of the cage, when it was operating close to the natural frequency of the system. Barish (1969) studied the effect of an off-sized

ball on the ball speed variation. He reported that if one ball is bigger than the rest of balls in a bearing, it would lag continuously since it will have a smaller contact angle and lower speed, resulting in particular vibrations. Meyer et al. (1980) investigated the off-sized ball problem analytically and came to the same conclusion as Tamura (1968). Yamamoto et al. (1981) also observed experimentally a peak at the cage rotational speed and another one at twice the cage speed due to off-sized ball.

Gupta (1988) showed that an increase in the size of an off-sized ball results in some performance deterioration. He reported that the shape of the cage whirl orbit changes from circular to somewhat polygonal with increasing difference in ball size. Similar findings have also been reported by Barish (1969). The problem of an off-sized ball using angular contact ball bearings was studied by Aktürk et al. (1992). They reported that vibrations occur due to off-sized balls at the cage speed only. Franco et al. (1992) observed vibrations due to off-sized balls at the cage speed with the random distribution of off-sized balls within the bearing. They showed that when there is one oversized ball in a bearing the most dominant vibration occurs at the cage speed. Aktürk and Gohar (1998) studied the effect of ball size variation in the bearings on the rotor vibrations. They showed that off-sized balls in the bearing cause vibration at a particular cage speed and its harmonics, depending on the arrangement within the bearing.

In the present work, a theoretical model is proposed to predict the vibration response of rolling element bearings due to distributed defects under radial load. The distributed defects considered are the surface waviness of inner race, outer race and rolling element and off-sized rolling element.

## **2.3 MODELING OF THE ROLLING ELEMENT BEARING**

The modeling and study of rolling element bearings considering the radial internal clearance, finite number of rolling elements and Hertzian contact has been done theoretically by Perret (1950) and Meldau (1951). Tamura and Taniguchi (1960) have experimentally studied the motion of a horizontal shaft supported on a ball bearing. The balls were moved in small steps for one ball passage. The results of their study matched with the findings of Perret (1950) and Meldau (1951).

Sunnersjo (1978) reported theoretical and experimental work on a non-linear model of rolling element bearings supporting a horizontally balanced rotor with a constant vertical radial load. The non-linearity introduced was due to Hertzian contact, radial internal clearance and parametric effect owing to varying compliance. This work was an improvement on previous work by Perret (1950) and Meldau (1951) based on their experimental investigation and also due to inclusion of inertia and damping force. White (1979) has derived an expression relating non-linear stiffness and frequency response functions for the bearings commonly used in machines. The stiffness of a rolling element bearing was derived considering the restoring force provided by the individual elements arising out of the radial force acting on the bearing.

Tamura and Tsuda (1980) theoretically studied the radial stiffness characteristics of a ball bearing including the effect of fluctuations in stiffness due to ball revolutions. The Newton Raphson method applied to solve the static running accuracy problem (first examined by Perret, 1950 and Meldau, 1951). The fluctuations of the linearized stiffness and the motion of inner race have been analyzed in detail by Tamura and Tsuda (1980). Gargiulo (1980) has developed a new set of equations for providing an initial estimate of the stiffness of rolling element bearings.

Igarashi and Hamada (1982) published their experimental study on the vibrations produced by rolling bearings with only one defect. They derived theoretical expressions for the recurrence frequency and main frequency of the vibration pulses. The pulse intervals were found to be fixed regardless of the dent size and the pulse recurrence frequency was in agreement with the derived equations. In yet another paper, Igarashi and Yabe (1983) deals with the sound characteristics of a rolling bearing with one defect in either race or ball. They observed that the vibration and sound had the same recurrence frequency although former had sharper waveform. Igarashi and Kato (1985) further analyzed the characteristics of vibrations produced by bearings having multiple defects. The characteristics established help in detecting the defects in ball bearings and find their location, number and size. Sunnersjo (1985) has investigated the character of defect generated frequencies and varying compliance frequencies in rolling element bearings.

Lim and Singh (1990) have developed a mathematical model for a rolling element bearing. A comprehensive bearing stiffness matrix has been proposed by them and it

demonstrates a coupling between the shaft bending motion and the flexural motion on the casing plate. Rahnejat and Gohar (1990) have investigated theoretically, the vibration response of a rotating shaft supported by two radial deep groove ball bearings. The model includes the effects of elasto-hydrodynamic lubrication, waviness on bearing race surface and a constant radial vertical load. The equations of motion are solved by constant average acceleration method using the principle of trapezoidal rule. Frequency spectra and phase plane plots have been presented which help in understanding the non-linear dynamics of the system.

Mevel and Guyader (1993) have developed a theoretical model of ball bearing supporting a balanced horizontal rigid rotor with a constant vertical radial force. This is similar to the work done by Fukata et al. (1985) but more results have been reported for parametric studies undertaken and routes to chaos traced out. Chaos in this model of bearing has been reported to result from sub-harmonic route and quasi-periodic period route. The paper reported the appearance of period doubling and tripling, alternately. Mode locking appears intermittently when quasi-periodic nature results in the two frequencies becoming commensurate. Mevel and Guyader (1993) have reported that reduction of load on ball bearings is such that it leads to the loss of contact between the ball and the race and that seems to be the source of chaotic behavior.

Sankarvelu et al. (1994) have used arc length continuation technique for obtaining dynamic characteristics of ball bearing. The ball bearings selected for study support a constant vertical load on a horizontal rotor. They reported that the arc length continuation method takes less computation time as compared to the direct integration method. The steady state response and stability analysis simultaneously can be obtained using this method. The eigen values of the Floquet matrix are obtained with shooting technique, which give the bifurcation points. Sankarvelu et al. (1994) have taken similar system for their study as used by Fukata et al. (1985). This work reports the appearance of chaotic response due to intermittency. Padmanabhan and Singh (1995) have investigated the multiplicative effect in non-linear time varying systems. This work has shown that multiplicative effect causes sub-harmonic response as well as extended non-linear regimes when compared to the additive case.



Tiwari and Vyas (1995) have estimated the non-linear stiffness parameter of rolling element bearings in rotor systems. The theoretical results are compared with experimental findings. The rotor bearing system is modeled by Fokker Plank equations and the resulting vibrations are due to the random imperfections of the bearing surfaces and assembly. Tiwari and Vyas (1997) have further extended their earlier work on a balanced rotor to estimate bearing parameters in a non-linear rotor bearing system experiencing small residual imbalance forces along with random forces. Various examples are modeled as an approximate Markovian process and a Fokker Plank equation is derived to describe it. Marsh and Yantek (1997) have attempted to overcome the problem of stiffness measurement of rolling element bearing under static conditions, which arises primarily because of the stiffness of the bearing pedestal and test fixtures. They measured the frequency response functions by carrying out dynamic tests on a test fixture. Chu and Holmes (1998) have investigated theoretically and experimentally the dynamic response of a flexible rotor supported by a squeeze film damper. A fast numerical integration technique has been used to speed up the computation time when investigating non-linear behavior of the system. Datta and Farhang (1997) have developed a theoretical model to investigate the structural vibrations of a rolling element bearing. They investigated the effect of stiffness nonlinearity for ball and roller bearing in their study.

A detailed study of rolling element bearing considering the parametric effects because of varying compliance, non-linear effects and distributed defects has been carried out in the present work. Theoretical expressions have been formulated for a balanced as well as unbalanced rotor. The case of a balanced rotor has been studied in the works by Fukata (1985), Mevel and Guyader (1987), Sankaravelu et al. (1994) and Datta and Farhang (1999). None of the above works has taken the case of an unbalanced rotor for point and line contact, which has been analyzed in the present investigation. The effects of distributed defects are also analyzed and discussed in the present study.

## Chapter 3

# GENERATION OF VIBRATIONS IN ROLLING ELEMENT BEARINGS

### 3.1 INTRODUCTION

Even if the geometry of a rolling element bearing is perfect, it will still produce vibrations. The vibrations are caused by the rotation of a finite number of loaded rolling contacts between the rollers and the guiding races. Since these contacts are elastic, the bearing stiffness becomes explicitly dependent on time. In general, a time varying stiffness causes vibrations, even in absence of external loads. Since the stiffness can be regarded as a system parameter, the variable stiffness is known as *parametric excitation*. It is one of the major sources of vibration in rolling element bearings. The first systematic research on this topic was conducted by Perret (1950) and Meldau (1951).

In general, it is not possible to produce a perfect surface or contour even with best machine tools, which is also applicable to bearing manufacturing. Due to irregularities in grinding and honing processes, the contacting surfaces of the rollers and the guiding races always deviate from their perfect shape. The surface features are considered in terms of wavelength of the order of Hertzian contact width. The surface features are termed as “roughness” if their wavelength is less than the contact width, whereas longer wavelength features are termed as waviness (Sunnarsjo, 1985). Waviness may be caused by different manufacturing malfunctions such as uneven wear of the wheel in various operations, variable interactions between the tool and work piece and vibrations of machine elements or movements of the work in the fixture. Waviness consists of sinusoidal shaped defects on the outer surface of the components. The number of waves per unit circumference is called the wave number. Waviness defects cause variations in the contact loads when the bearing is running. The magnitude of variation depends on the amplitude of the defect and the nonlinear stiffness. Due to the variations in contact loads, vibrations are generated in the bearing. Defects with different wave numbers cause vibrations at distinct frequencies, each with a characteristic vibration mode. The importance of running surface

waviness from the point of view of vibration has been known for a long time. One of the first investigations in this field was made by Tallian and Gustafsson (1965).

## 3.2 SOURCES OF VIBRATIONS

The sources of vibrations in a rolling element bearing are described with their physical descriptions. The sources considered are nonlinear spring stiffness and the distributed defects of the contacting surfaces.

### 3.2.1 Parametric Excitation

The flexibility of the rolling contact in a rolling element bearing can be represented by nonlinear springs (Hertz, 1881). When the mass of the rolling elements is neglected, the contacts at inner and outer races may be assumed to act like springs as shown in Fig. 3.1. Often, rolling element bearings are subjected to an externally applied load to preload the Hertzian contacts. When the rolling element set and the cage rotates with a constant angular velocity ( $\omega_{cage}$ ), a parametrically excited vibration is generated and transmitted through the outer race. The characteristic frequency of this vibration equals  $N_b \times \omega_{cage} / 2\pi$  and is called the *varying compliance frequency* (VC). This is the frequency at which the rolling elements pass an observation point fixed on the outer race. In case of rotation, peak amplitude of vibrations is generated at the varying compliance frequency and its harmonics. Since the contact behaviour is nonlinear, the effect of an asymmetric stiffness distribution in the application is enhanced by the introduction of a radial or misaligned external load. In the extreme case, the rolling elements lose contact with the races and the system becomes strongly nonlinear.

The area where the rolling elements are still in contact with the races is generally referred to as the loaded zone as shown in Fig. 3.2. A phenomenon closely related to parametric excitations is parametric resonance. These excitations are unstable or large amplitude solutions that are not directly related to the natural frequencies of the system (Nayfeh and Mook, 1979). In a nonlinear system, parametric resonance can change the system response dramatically. Under extreme loading conditions, it might even lead to a chaotic behavior (Mevel and Guyader, 1993).

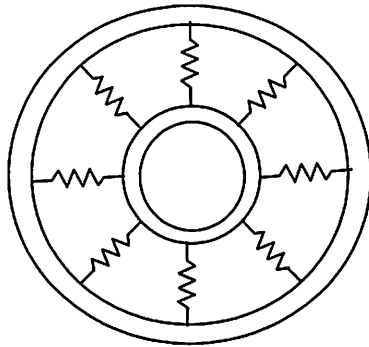


**Fig. 3.1** The flexibility of the rolling contacts in a rolling element bearing is represented by nonlinear springs

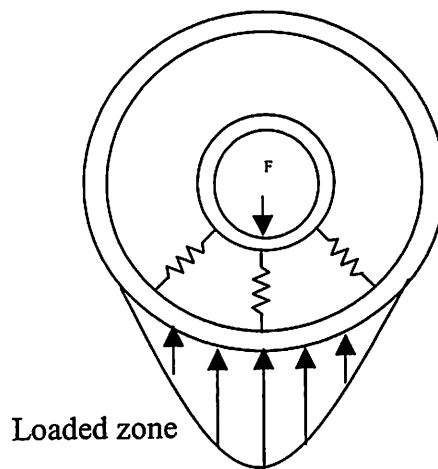


**Fig. 3.2** In the presence of a radial load, some of the rolling elements can lose contact with the races leading to severe parametric excitations

### 3.2.1 Distributed Defects

#### 3.2.1.1 Description of Waviness

An important source of vibration in rolling element bearings is waviness. Waviness is normally realized in the form of peaks and valleys of varying height and width. This causes problem in mathematical modeling of waviness effect. A statistical approach is needed in order to formulate a mathematical model. If the races are assumed to bend due to roller loads then the flexural vibrations of the races as well as of the rigid body motion have to be considered. To avoid these problems, the inner and outer races are assumed to have negligible bending under the roller loads. A sinusoidal wavy surface on bearing components is assumed as shown in Fig. 3.3. Moreover, the wavelength is assumed to be much longer than the roller to race footprint width. The wave geometry is assumed to be unaffected by contact distortion. Waviness causes variation in the contact loads when the bearing is running (Aktürk, 1999). The magnitude of variation depends on the amplitude of the waviness and the stiffness in the contact. Due to variation in the contact loads, vibrations are generated in the bearing. The resulting vibration modes of the races can either be of extensional, flexural or rigid body, depending on the number of rolling elements and the wavenumber of the defect. Waves are described in terms of two important parameters: the wave length ( $\lambda$ ), which is the distance taken up by a single cycle of a wave and its amplitude ( $I$ ). For an imperfect surface the wavelength ( $\lambda$ ) is inversely proportional to the number of waves ( $N_w$ ). Waviness exists on the both races of a bearing as shown in Fig. 3.4.

#### 3.2.1.2 Excitation Frequencies

The rotational speeds of the inner and outer races, the cage and the rolling elements are different. As a result the inner race, outer race and rolling element waviness generate vibrations of distinct frequencies. The excitation frequencies are proportional to the rotational speed of the rotor. The ratio between the excitation frequency and the rotor frequency is referred to as excitation order. The excitation orders generated by the bearing are rational numbers so that they can easily be detected in the vibration spectrum. A comprehensive overview of the vibrations generated in rolling element bearings has been provided by Wardle (1988) and Yhland (1992).

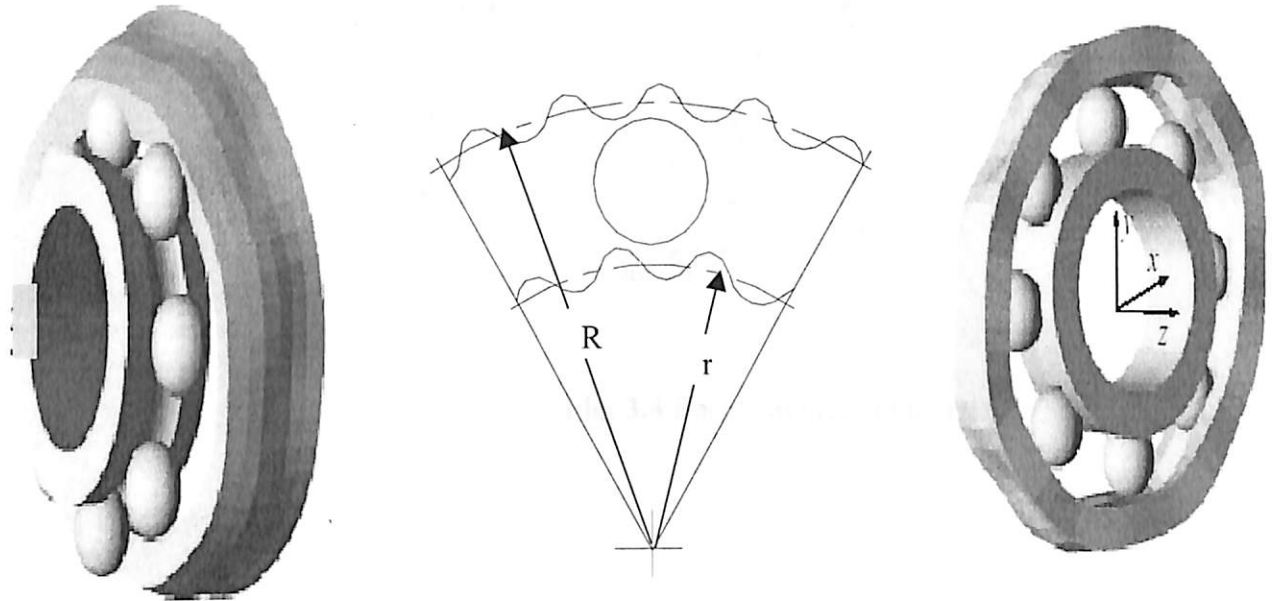


**Fig. 3.3** Waviness at inner and outer race

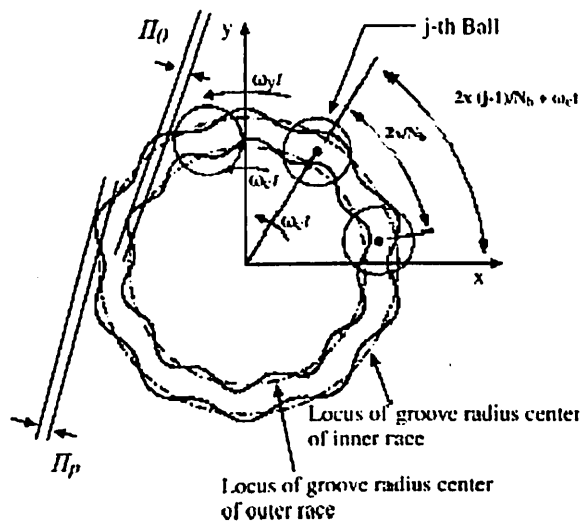


Fig. 3.4 Race waviness model

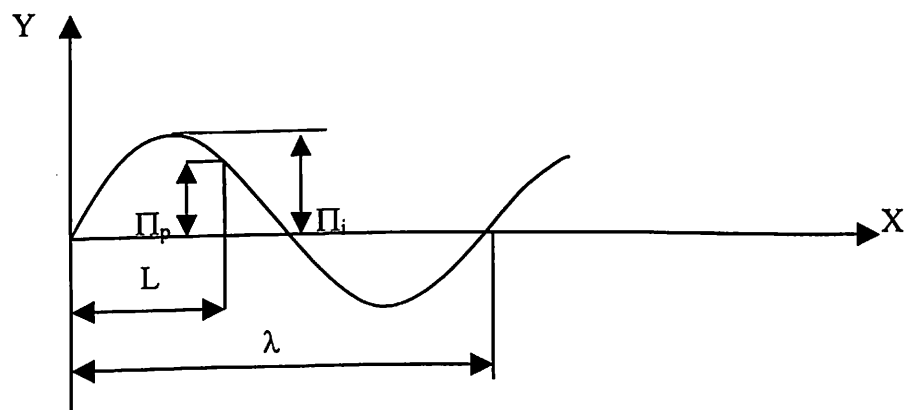


Fig. 3.5 Description of the race wave

In the present work, symbols  $\omega_{inner}$ ,  $\omega_{cage}$  and  $\omega_{roll}$  have been used to denote the angular speeds of the inner race, the cage and the rolling elements respectively. An integer  $q \geq 0$  is introduced to indicate the harmonics of the varying compliance frequency. Another integer  $k \geq 0$  is also introduced, which is associated with the vibration mode of inner and outer races of bearing.

#### A. Inner Race Waviness

When the rolling element is moving round the inner race, it follows the rolling surface contour continuously. It is assumed that there exists no slip condition i.e. rolling element is always in contact with inner race and also it is assumed that the inner race surface has a circumferential sinusoidal wavy feature. The amplitude of wavy surface is often measured with respect to the central point at a certain angle from the reference axis. Hence the amplitude of sinusoidal wave is given by,

$$\Pi = \Pi_p \sin\left(2\pi \frac{L}{\lambda}\right) \quad (3.1)$$

The inner race has circumference sinusoidal wavy surface and therefore the radial clearance consist of a constant part and a variable part. Hence, the amplitude of the wave of inner race may be written as,

$$(\Pi)_{in} = (\Pi_o) + (\Pi_p) \sin\left(2\pi \frac{L}{\lambda}\right) \quad (3.2)$$

Where  $\Pi_p$  is the maximum amplitude of wave and  $\Pi_o$  is original wave amplitude (or constant clearance) as shown in Fig. 3.5.

The arc length ( $L$ ) of the wave of inner race at the contact angle is,

$$L = r\theta_j \quad (3.3)$$

For an imperfect surface with  $N_w$  waves, the wavelength ( $\lambda$ ) is inversely proportional to the number of waves  $N_w$  i.e.,

$$\lambda \propto \frac{1}{N_w} \quad (3.4)$$



For the inner race the wavelength ( $\lambda$ ) is ratio of length of the inner race circumference to the number of waves on circumference, which is given by,

$$\lambda = \frac{2r\pi}{N_w} \quad (3.5)$$

Where  $r$  is radius of inner race.

The amplitude of the waves of inner race at the contact angle is given by following equation:

$$(\Pi)_{in} = (\Pi_o) + (\Pi_p) \sin(N_w \theta_j) \quad (3.6)$$

Where  $\theta_j$  is the contact angle of  $j^{th}$  rolling element. As the inner race is moving at the speed of rotor and roller center is moving at the speed of the cage, the contact angle may be written as:

$$\theta_j = \frac{2\pi}{N_b} (j-1) + (\omega_{cage} - \omega_{inner}) \times t \quad (3.7)$$

$$\text{where } \omega_{cage} = \frac{1}{2} \omega_{inner} \left[ 1 - \frac{\rho_j}{R_p} \right] + \frac{1}{2} \omega_{outer} \left[ 1 + \frac{\rho_j}{R_p} \right] \quad (3.8)$$

where  $R_p$  is the pitch radius.

At the initial time and initial position, point  $a$  and point  $b$  are assumed at the circumference of the inner race and at the roller center respectively from a reference axis as shown in Fig. 3.4. After ' $t$ ' time taken, the cage will lag the rotor and a result of this, the  $j^{th}$  roller will be at the angle of  $-(\omega_{inner} \times t - \omega_{cage} \times t)$ , so ball centre will lag the inner race. Hence the instantaneous amplitude of waviness at the contact angle may be given by:

$$(\Pi)_{in} = (\Pi_o) + (\Pi_p) \sin \left[ N_w \left( \frac{2\pi}{N_b} (j-1) + (\omega_{cage} - \omega_{inner}) \times t \right) \right], \quad j = 1, 2, 3, \dots, N_b \quad (3.9)$$

Where  $N_b$  is the number of rolling element,  $t$  is the time coordinate.

For an observer at a fixed location on the outer race, the vibrations generated by the inner race waviness are modulated at the varying compliance frequency, resulting in combination harmonics. The frequency of the vibrations due to inner race waviness depends on the waviness order ( $n$ ) and is given as (Yhland, 1992):

$$n = qN_b \pm k \quad (3.10)$$

The angular excitation frequencies caused by inner race waviness are given as (Yhland, 1992):

$$\omega = qN_b(\omega_{inner} - \omega_{cage}) \pm k\omega_{inner} \quad (3.11)$$

### B. Outer Race Waviness

The outer race waviness is usually of the same order of magnitude as inner race waviness. The outer race surface also has circumferential sinusoidal wavy surface. If one assumes the outer race to be stationary and the rolling element to be rotating at the speed of cage, the amplitude of sinusoidal wave of outer race may be written as,

$$\Pi = \Pi_o \sin\left(2\pi \frac{L'}{\lambda'}\right) \quad (3.12)$$

The arc length (L') of the wave of outer race at the contact angle is,

$$L' = R\theta_j \quad (3.13)$$

For the outer race, the wavelength is ratio of length of the outer race circumference to the number of waves on circumference and is given by,

$$\lambda' = \frac{2R\pi}{N_w} \quad (3.14)$$

Where R is radius of outer race.

Hence, the amplitude of the wave of outer race may be written as,

$$(\Pi)_{out} = (\Pi_o) + (\Pi_p) \sin(N_w \theta_j) \quad (3.15)$$

The contact angle ( $\theta_j$ ) is given by,

$$\theta_j = \frac{2\pi}{N_b}(j-1) + \omega_{cage} \times t \quad (3.16)$$

From Equations (3.15) and (3.16) one may write,

$$(\Pi)_{out} = (\Pi_o) + (\Pi_p) \sin\left[N_w \left(\frac{2\pi}{N_b}(j-1) + \omega_{cage} \times t\right)\right] \quad (3.17)$$

For a rolling element at an angular position  $\theta_j$ , the inner race contact point will be at  $[r + (\Pi)_{in}]$  and for this rolling element the outer race contact point will be at  $[R - (\Pi)_{out}]$ .

From bearing geometry one may write,

$$[R - (\Pi)_{out}] - [r + (\Pi)_{in}] = 2(\rho_r) \quad (3.18)$$

Where  $\rho_r$  is the radius of rolling element.

For an observer fixed on the outer race, the vibrations generated by outer race waviness are not modulated. As a consequence, the individual wavenumbers do not generate vibrations with unique frequencies, which make the detection of outer race waviness more difficult than that of inner race. With outer race waviness, the effect of several wavenumbers can be observed at the varying compliance frequency and its harmonics. The frequency of the vibrations due to outer race waviness depends on the waviness order ( $n$ ) and is given as (Yhland, 1992):

$$n = qN_b \pm k \quad (3.19)$$

The angular excitation frequencies are given as (Yhland, 1992):

$$\omega = qN_b \omega_{cage} \quad (3.20)$$

In terms of the response, outer race waviness behaves in a similar manner as parametric excitations.

### C. Ball Waviness

The waviness on the rolling elements is usually several times less than the waviness on the inner and outer race. For low rotational speeds, the defects with only even wavenumbers generate vibrations (Aktürk, 1999). Balls are free to spin about any axis and the axis may even change during the rotation. In order to calculate the waviness of balls, a simple case is considered where a ball with a perfectly sinusoidal wavy surface rotates about an axis as shown in Fig. 3.6. The amplitude of the ball waviness is,

$$a_j = a_p \sin(N_w \theta_j) \quad (3.21)$$

This will cause a change in the ball diameter ( $\Delta d_b$ ) through inner and outer contacts, which is given by,

$$\Delta d_b = 2(\Pi_p) \sin(N_w \theta_j) \quad (3.22)$$

where  $N_w = 2, 4, 6, \dots$

The effect of ball waviness on the general clearance can be expressed as,

$$(\Pi)_b = 2(\Pi_p) \sin(N_w \omega_{roll} t) \quad (3.23)$$

The vibrations generated by ball waviness are always the cumulative effect of all the rolling elements. The vibrations are modulated with the cage frequency. Hence, for each wavenumber of the rolling element, vibrations are generated at multiple frequencies (Aktürk, 1999).

For an observer fixed on the outer race, the vibrations generated by outer race waviness are not modulated. As a consequence, the individual wavenumbers do not generate vibrations with unique frequencies, which make the detection of outer race waviness more difficult than that of inner race. With outer race waviness, the effect of several wavenumbers can be observed at the varying compliance frequency and its harmonics. The frequency of the vibrations due to outer race waviness depends on the waviness order ( $n$ ) and is given as (Yhland, 1992):

$$n = qN_b \pm k \quad (3.19)$$

The angular excitation frequencies are given as (Yhland, 1992):

$$\omega = qN_b \omega_{cage} \quad (3.20)$$

In terms of the response, outer race waviness behaves in a similar manner as parametric excitations.

### C. Ball Waviness

The waviness on the rolling elements is usually several times less than the waviness on the inner and outer race. For low rotational speeds, the defects with only even wavenumbers generate vibrations (Aktürk, 1999). Balls are free to spin about any axis and the axis may even change during the rotation. In order to calculate the waviness of balls, a simple case is considered where a ball with a perfectly sinusoidal wavy surface rotates about an axis as shown in Fig. 3.6. The amplitude of the ball waviness is,

$$a_j = a_p \sin(N_w \theta_j) \quad (3.21)$$

This will cause a change in the ball diameter ( $\Delta d_b$ ) through inner and outer contacts, which is given by,

$$\Delta d_b = 2(\Pi_p) \sin(N_w \theta_j) \quad (3.22)$$

where  $N_w = 2, 4, 6, \dots$

The effect of ball waviness on the general clearance can be expressed as,

$$(\Pi)_b = 2(\Pi_p) \sin(N_w \omega_{roll} t) \quad (3.23)$$

The vibrations generated by ball waviness are always the cumulative effect of all the rolling elements. The vibrations are modulated with the cage frequency. Hence, for each wavenumber of the rolling element, vibrations are generated at multiple frequencies (Aktürk, 1999).

For wavenumber  $n=2q$ , the angular excitation frequencies due to ball waviness are given as (Yhland, 1992):

$$\omega = 2q\omega_{roll} \pm k\omega_{cage} \quad (3.24)$$

#### D. Ball Size Variations

Ball size variations can be regarded as a special case of ball waviness by making  $q=0$  in Eq. (3.24). Hence, the angular frequency of the vibration generated by ball size variations may be given as (Yhland, 1992):

$$\omega = \pm k\omega_{cage} \quad (3.25)$$

Due to the different ball sizes, which move with the rotational speed of the cage, the race is deformed into a complex shape as shown in Fig. 3.7.

### 3.4 SUMMARY OF EXCITATION FREQUENCIES

The main excitation frequencies in a rolling element bearing together with the corresponding angular frequencies are summarized in Table 3.1. Also, the corresponding vibration modes of the inner and outer races are listed. The integer  $q$  refers to harmonics of the varying compliance frequency,  $N_b$  denotes the number of rolling elements and  $\omega_{inner}$ ,  $\omega_{cage}$  and  $\omega_{roll}$  denote, the angular frequency of the inner race, the cage and the rolling elements respectively.

**Table 3.1** The Excitation Frequencies of Different Sources in Rolling Bearing

Vibration source	Wavenumber	$\omega$ (rad / sec)
Parametric excitations	<i>N. A.</i>	$qN_b\omega_{cage}$
Inner race waviness	$n = qN_b \pm k$	$qN_b(\omega_{inner} - \omega_{cage}) \pm k\omega_{inner}$
Outer race waviness	$n = qN_b \pm k$	$qN_b\omega_{cage}$
Ball waviness	$n = 2q$	$2qN_b\omega_{roll} \pm k\omega_{cage}$ , $n \neq qN_b \pm 1$
Ball size variations	<i>N. A.</i>	$k\omega_{cage}$

(*N. A.*: Not Applicable)

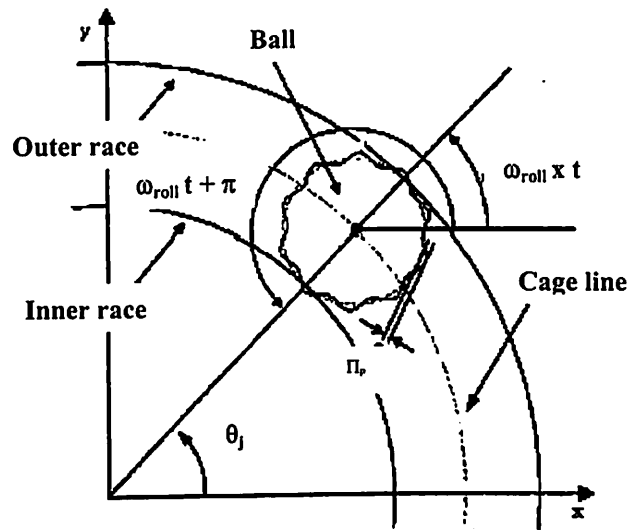


Fig. 3.6 Ball waviness with races

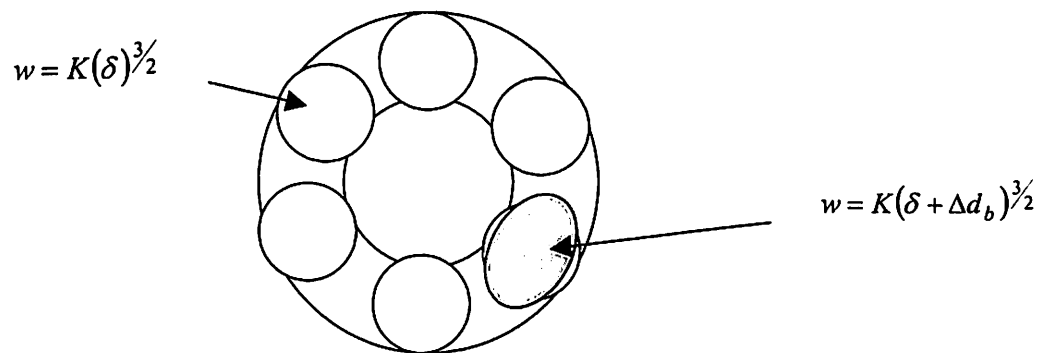


Fig. 3.7 Presence of an off-sized ball in a set of balls

# ***DYNAMIC ANALYSIS OF ROLLING ELEMENT BEARINGS WITH PARAMETRIC EFFECTS***

In this chapter the vibration response of a rotor bearing system due to parametric excitations is dealt. The self-excited vibrations in perfectly balanced rotor are due to varying compliance of the bearing, which arises because of the geometric and the elastic characteristics of the bearing assembly varying according to the cage position. Unbalanced forces in a rotor are unavoidable. However good the balancing may be for a rotor, the unbalanced forces cannot be completely neglected (Rao, 1996). The inclusion of the unbalanced forces make the system bi-periodically excited. The two exciting frequencies are the rotational frequency of the rotor and the varying compliance frequency. The studies undertaken by Day (1987), Kim and Noah (1990, 1996) have taken the effect of unbalanced force without considering the varying compliance effect. Also in their work, the bearing is considered to have only the clearance non-linearity. Hence, effectively their work is about single frequency excited systems. In the present investigation, the effects like radial internal clearance, varying compliance and unbalanced rotor have been considered and analyzed in detail for a rotor bearing system.

### **4.1 INTRODUCTION**

Parametrically excited vibrations, which occur in a bearing irrespective of its quality and accuracy, are called varying compliance vibrations. The varying compliance effect was theoretically studied by Perret (1950) for a deep groove ball bearing having ten balls subjected to a constant external load. Perret has calculated the elastic deformation between the race and balls on the basis of the Hertzian contact theory, which gives a nonlinear force-deformation relationship. Other causes of stiffness variation are the positive radial internal clearance and the finite number of balls, the positions of which change periodically. These cause periodic changes in the stiffness of bearing assembly. Taking into account these sources of stiffness variation, the stiffness of the complete ball

bearing system becomes a function of the ball race contact stiffness, the radial internal clearance, the external load and the angular position of the cage.

Sunnersjo (1978) studied the varying compliance vibration theoretically and experimentally, taking inertia and damping forces into account. His analysis was part of a study of vibrations due to form errors of bearings and was performed for roller bearings. Gad et al. (1984b) derived the spring properties of ball bearings in order to solve the vibration problem by computer simulation. The radial and axial forces versus displacement plots showed the spring property of the ball bearing in the radial and axial directions respectively. Fukata et al. (1985) were the first to take up the study of varying compliance vibrations and the nonlinear dynamic response for the ball bearings supporting a horizontal rotor. Rahnejat and Gohar (1985) analyzed the vibrations of radial ball bearings. The bearings and the oil films were considered as nonlinear springs and dampers rotating round the spindle. Structural vibrations of ball bearings, according to Balmount' et al. (1987) are governed by two factors. One of these is the contact load from which the ball deforms into a polyhedral shape, rotation of which transmits the deformation to other parts of the machine. The other factor is the motion of balls relative to the line of action of the radial load, which causes fluctuations in the rigidity of the bearing. Mevel and Guyader (1994) have further studied the bearing model used by Fukata et al. (1985) through an improved nonlinear analysis of the ball bearing model. Datta and Farhang (1997) presented a nonlinear model for structural vibrations in rolling element bearings, considering the stiffness as nonlinear spring. They observed the vibration response due to stiffness variations. Zheng and Hasebe (2000) analyzed the non-linear dynamic behavior of a complex rotor bearing system with multi degrees of freedom and non-closed form of bearing forces. They showed that the Newmark time integration technique produces accurate results for the nonlinear systems.

This chapter deals with the structural dynamic response of a rotor supported by rolling element bearings. The mathematical model takes into account the sources of non-linearity such as Hertzian contact force, varying compliance and radial internal clearance resulting in transition from no-contact to contact state between rolling elements and races. The parameters of study are rotational speed of rotor, radial internal clearance and unbalanced rotor force for point and line contact.



## 4.2 PROBLEM FORMULATION

In this section, a mathematical model for analyzing the structural vibrations in rolling element bearings has been developed. Initially the expressions for kinetic and potential energies are formulated for all the components of rolling element bearing. The equations of motion that have been derived by using these energy expressions and the Lagrange equation, describe the dynamic behavior of complex model. A schematic diagram of rolling element bearing is shown in Fig. 4.1. For investigating the characteristics of structural vibrations of a rolling element bearing, the bearing assembly is modelled as a spring mass system, in which the outer race of the bearing is fixed in a rigid support and the inner race is fixed rigidly with the rotor. A constant radial force assumed to be acting on the system.

In the mathematical modeling, the rolling element bearing is considered as a spring mass system in which the rolling elements are assumed to act as nonlinear contact springs as shown in Fig. 4.2. Since the Hertzian forces arise only when there is contact deformation, the springs are required to act only during compression. In other words, the respective spring forces come into play when the instantaneous spring length is shorter than its unstressed length. Otherwise a separation between rolling element and the races takes place and the resultant force becomes zero. A real rotor-bearing system is generally very complicated and difficult to model. So for simplifying the mathematical model, the following assumptions have been made:

1. Deformations occur according to the Hertzian theory of elastic contact. Small elastic deformations of the rolling elements and the races have been taken into account, but plastic deformations have been neglected.
2. The rolling elements, the inner and outer races and the rotor have motions in the plane of bearing only.
3. The angular velocity of the cage remains constant.
4. The rollers in a rolling element bearing have no angular rotation about their axes, i.e., there is no skewing. Hence, there is no interaction of the corners of the rollers with the cage and the flanges of the races.
5. All the bearing components and the rotor are rigid, i.e. there is no bending.

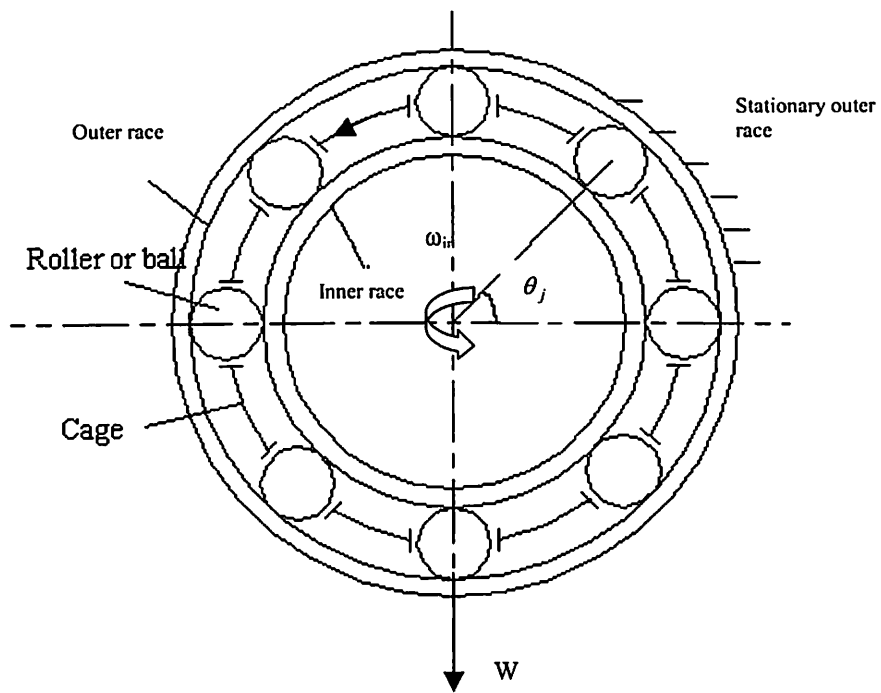


**Fig. 4.1** Schematic diagram of a rolling element bearing

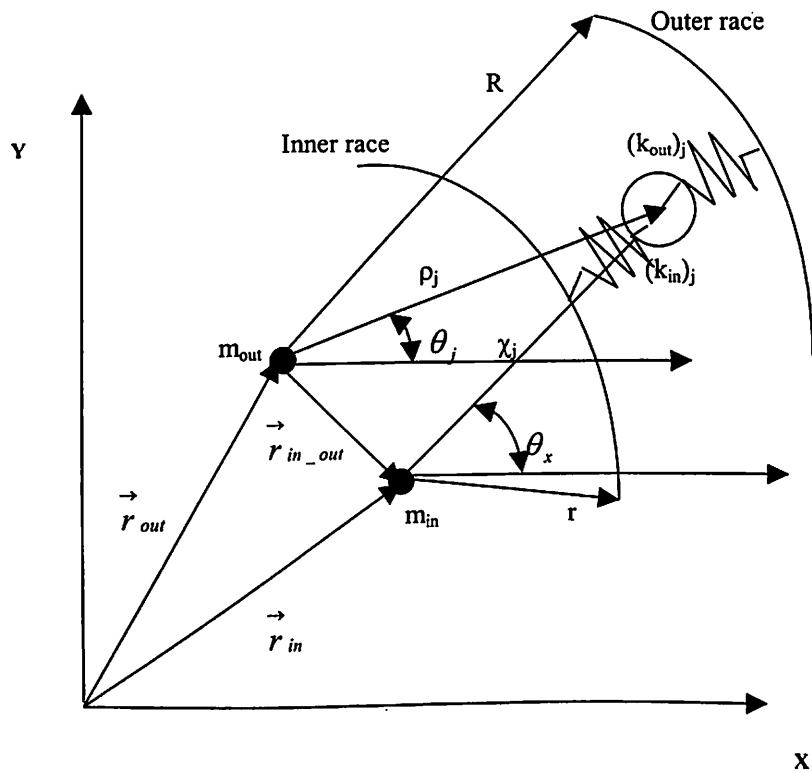


**Fig. 4.2** Mass-spring model of the rolling element bearing

6. The bearings operate under isothermal conditions. Hence, all thermal effects that may arise due to the rise in temperature, such as change of lubricant viscosity, expansion of the rolling elements and the races and reduction of endurance limit of the material, are absent.
7. There is no slipping of balls as they roll on the surface of the races. Since there is perfect rolling of the balls on the surface of the races and the two points of a ball touching the races have different linear velocities, the centre of the ball has a resultant translational velocity.
8. The damping of a ball bearing is very small. This damping is present because of friction and small amount of lubrication. The estimation of damping of ball bearing is very difficult because of the dominant extraneous damping which swamps the damping of the bearing.
9. The cage ensures the constant angular separation ( $\beta$ ) between rolling elements. Hence, there is no interaction between rolling elements. In addition, at any given instant, some of the rolling elements will be in contact with both races. Therefore,

$$\beta = \frac{2\pi}{N_b} \quad (4.1)$$

As pointed out above, the presence of the cage ensures constant angular separation between the adjacent rolling elements. Therefore, the azimuth angles of rolling elements  $i$  ( $i = 2, 3, \dots, N$ ) are related to that of the first rolling element by the following relations.

$$\begin{aligned} \theta_2 &= \theta_1 + \beta \\ \theta_3 &= \theta_1 + 2\beta \quad \dots\dots\dots \\ \dots\dots\dots \theta_N &= \theta_1 + (N-1)\beta \end{aligned} \quad (4.2)$$

Therefore,

$$\dot{\theta}_1 = \dot{\theta}_2 = \dot{\theta}_3 = \dots\dots\dots = \dot{\theta}_N = \dot{\theta} \quad (4.2a)$$

The equations of motion that describe the dynamic behavior of the complete model can be derived by using Lagrange equation for a set of independent generalized coordinates, as:

$$\frac{d}{dt} \frac{\partial T}{\partial \dot{p}} - \frac{\partial T}{\partial p} + \frac{\partial V}{\partial p} = \{f\} \quad (4.3)$$

where  $T$ ,  $V$ ,  $p$  and  $f$  are the kinetic energy, the potential energy, the vector with generalized degree-of-freedom (DOF) coordinate and the vector with generalized contact forces respectively.

The kinetic and potential energies can be subdivided into contributions from the various components i.e. from the rolling elements, the inner race, the outer race and the rotor.

The total kinetic energy ( $T$ ) of the rotor-bearing system is the sum of the rolling elements, inner and outer races and the rotor. That is,

$$T = T_{r.e.} + T_{i\_race} + T_{o\_race} + T_{rotor} \quad (4.4)$$

The subscripts  $i\_race$ ,  $o\_race$  and  $rotor$  refer to the inner race, the outer race and the rotor respectively. The subscript  $r. e.$  indicates the rolling elements.

The potential energy is provided by deformations of the balls within the races and deformations occur according to Hertzian contact theory of elasticity. Potential energy formulation is done taking the horizontal plane as datum through the global origin. The total potential energy ( $V$ ) of the bearing system is the sum of the potential energies of the balls, inner and outer races, springs and the rotor. That is,

$$V = V_{r.e.} + V_{i\_race} + V_{o\_race} + V_{springs} + V_{rotor} \quad (4.5)$$

where  $V_{r.e.}$ ,  $V_{i\_race}$ ,  $V_{o\_race}$  and  $V_{rotor}$  are the potential energies due to elevation of the rolling element, inner and outer races and the rotor, respectively.  $V_{springs}$  is potential energy due to nonlinear spring contacts between rollers and the races.

#### A. Contribution of the inner race

Apart from local deformations in the contacts, the inner race is considered as a rigid body as shown in Fig. 4.3. The kinetic energy of the inner race about its center of mass is evaluated in the  $x$ ,  $y$ -frame. The position of the origin of the moving frame relative to the reference frame is represented by transitional DOF  $\dot{x}_{in}$  and  $\dot{y}_{in}$ .

The expression for the kinetic energy of the inner race is written as,

$$T_{i\_race} = \frac{1}{2} m_{in} \left( \dot{r}_{in} \bullet \dot{r}_{in} \right) + \frac{1}{2} I_{in} \dot{\phi}_{in}^2 \quad (4.6)$$

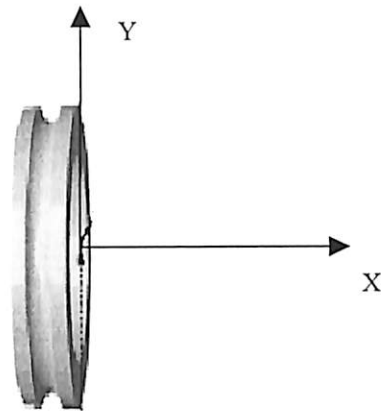


**Fig. 4.3** Rigid body structure of inner race

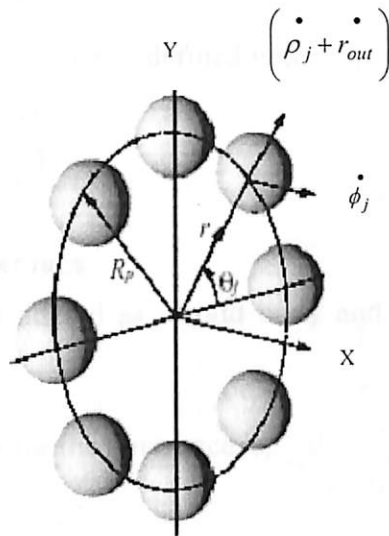


**Fig. 4.4** Rolling elements with its degree of freedom

The position of the inner race centre  $(x_{in}, y_{in})$  is defined with respect to the fixed outer race center.

The displacement vector showing the location of inner race center with respect to that of outer race center is given by,

$$\vec{r}_{in} = \vec{r}_{out} + \vec{r}_{in\_out} \quad (4.7)$$

$$\text{or, } \vec{r}_{in} = \left( \vec{x}_{in} + \vec{x}_{out} \right) \hat{i} + \left( \vec{y}_{in} + \vec{y}_{out} \right) \hat{j} \quad (4.8)$$

Differentiation of  $r_{in}$  with respect to time (t) gives,

$$\dot{\vec{r}}_{in} = \left( \dot{x}_{in} \hat{i} + \dot{y}_{in} \hat{j} \right) \quad (4.9)$$

where  $\dot{x}_{out}$  and  $\dot{y}_{out}$  have been set to zero, because the outer race is assumed to be stationary.

$$\text{Hence, } T_{i\_race} = \frac{1}{2} m_{in} \left( \dot{x}_{in}^2 + \dot{y}_{in}^2 \right) + \frac{1}{2} I_{in} \dot{\phi}_{in}^2 \quad (4.10)$$

Since the position of the inner race is defined with respect to the outer race centre, the potential energy for the inner race is,

$$V_{i\_race} = m_{in} g (y_{in\_out} + y_{out}) \quad (4.11)$$

### B. Contribution of the outer race

The outer race is also considered as a rigid body and is assumed to be stationary.

Hence,  $\dot{r}_{out} = 0$  and  $\dot{\phi}_{out} = 0$ .

The kinetic energy expression for the outer race is,

$$T_{o\_race} = \frac{1}{2} m_{out} \left( \dot{r}_{out} \cdot \dot{r}_{out} \right) + \frac{1}{2} I_{out} \dot{\phi}_{out}^2 = 0 \quad (4.12)$$

The potential energy of the outer race is,

$$V_{o\_race} = m_{out} g y_{out} \quad (4.13)$$

### C. Contribution of the rolling elements

The rolling elements are also considered as rigid bodies. For the determination of their contribution to the kinetic energy, the position of the  $j^{\text{th}}$ -rolling element is described by two translational degree of freedom as shown in Fig. 4.4 on page number 34.

The kinetic energy due to the rolling elements may be estimated by summing up the energy due to individual elements as,

$$T_{r.e.} = \sum_{j=1}^{N_b} T_j \quad (4.14)$$

The position of the centre of the roller is defined with respect to the outer race centre. Hence, the kinetic energy of the  $j^{\text{th}}$ -rolling element may be written as,

$$T_j = \frac{1}{2} m_j \left( \dot{\rho}_j + r_{out} \right) \cdot \left( \dot{\rho}_j + r_{out} \right) + \frac{1}{2} I_j \dot{\phi}_j^2 \quad (4.15)$$

The displacement vector showing the location of  $j^{\text{th}}$ -rolling elements is:

$$\vec{\rho}_j = (\rho_j \cos \theta_j) \hat{i} + (\rho_j \sin \theta_j) \hat{j} \quad (4.16)$$

and for the outer race centre, it is:

$$\vec{r}_{out} = x_{out} \hat{i} + y_{out} \hat{j} \quad (4.17)$$

The summation of equations (4.16) and (4.17) after differentiation with respect to time ( $t$ ) leads to the following expression:

$$\begin{aligned} \left( \dot{\rho}_j + r_{out} \right) \cdot \left( \dot{\rho}_j + r_{out} \right) &= \dot{\rho}_j^2 \cos^2 \theta_j + \dot{\rho}_j^2 \sin^2 \theta_j \cdot \dot{\theta}_j^2 - 2 \dot{\rho}_j \cdot \rho_j \cdot \dot{\theta}_j \cos \theta_j \sin \theta_j \\ &+ \dot{x}_{out}^2 + 2 \dot{x}_{out} \left( \dot{\rho}_j \cos \theta_j - \rho_j \sin \theta_j \cdot \dot{\theta}_j \right) + \dot{\rho}_j^2 \sin^2 \theta_j + \dot{\rho}_j^2 \cos^2 \theta_j \cdot \dot{\theta}_j^2 + 2 \dot{\rho}_j \cdot \rho_j \cdot \dot{\theta}_j \cos \theta_j \sin \theta_j \\ &+ \dot{y}_{out}^2 + 2 \dot{y}_{out} \left( \dot{\rho}_j \sin \theta_j + \rho_j \cos \theta_j \cdot \dot{\theta}_j \right) \end{aligned} \quad (4.18)$$

The outer race is assumed to be stationary, hence  $\dot{x}_{out} = 0$  and  $\dot{y}_{out} = 0$ . Therefore Eq.

(4.18) becomes,

$$\left( \dot{\rho}_j + r_{out} \right) \cdot \left( \dot{\rho}_j + r_{out} \right) = \dot{\rho}_j^2 \cos^2 \theta_j + \dot{\rho}_j^2 \sin^2 \theta_j \cdot \dot{\theta}_j^2 + \dot{\rho}_j^2 \sin^2 \theta_j + \dot{\rho}_j^2 \cos^2 \theta_j \cdot \dot{\theta}_j^2 \quad (4.19)$$

$$\text{or, } \begin{pmatrix} \dot{\rho}_j + r_{out} \\ \dot{\theta}_j \end{pmatrix} \bullet \begin{pmatrix} \dot{\rho}_j + r_{out} \\ \dot{\theta}_j \end{pmatrix} = \left( \dot{\rho}_j^2 + \rho_j^2 \cdot \dot{\theta}_j^2 \right) \quad (4.20)$$

From the equation (4.15), one may get,

$$T_j = \frac{1}{2} m_j \left( \dot{\rho}_j^2 + \rho_j^2 \cdot \dot{\theta}_j^2 \right) + \frac{1}{2} I_j \dot{\phi}_j^2 \quad (4.21)$$

It is assumed that there is no slip, hence the relative transitional velocity of outer race and rolling element must be equal and opposite in direction. Therefore, the contact equation for  $j^{\text{th}}$  –rolling element and the outer race may be written as,

$$R(\dot{\phi}_{out} - \dot{\theta}_j) = -\rho_r(\dot{\phi}_j - \dot{\theta}_j) \quad (4.22)$$

Since the outer race is stationary, hence

$$\dot{\phi}_{out} = 0 \quad (4.23)$$

The rotation of  $j^{\text{th}}$  rolling element about its centre of mass is,

$$\dot{\phi}_j = \dot{\theta}_j \left( 1 + \frac{R}{\rho_r} \right) \quad (4.24)$$

Now the kinetic energy of the rolling elements can be written as,

$$T_{r.e.} = \sum_{j=1}^{N_b} \frac{1}{2} m_j \left( \dot{\rho}_j^2 + \rho_j^2 \cdot \dot{\theta}_j^2 \right) + \frac{1}{2} I_j \dot{\theta}_j^2 \left( 1 + \frac{R}{\rho_r} \right)^2 \quad (4.25)$$

For the rolling elements, the potential energy due to elevation is,

$$V_{r.e.} = \sum_{j=1}^{N_b} m_j g (\rho_j \sin \theta_j + y_{out}) \quad (4.26)$$

$$\text{or, } V_{r.e.} = m g N_b y_{out} + \sum_{j=1}^{N_b} (m_j g \rho_j \sin \theta_j) \quad (4.27)$$

#### D. Contribution of the rotor

The kinetic energy of the rotor is estimated by assuming that its centre remains coincident with the inner race. Hence, the kinetic energy of the rotor is:

$$T_{rotor} = \frac{1}{2} m_{rotor} (\dot{x}_{in}^2 + \dot{y}_{in}^2) + \frac{1}{2} I_{rotor} \dot{\theta}_{rotor}^2 \quad (4.28)$$



Since the rotor centre coincides with the inner race center and position of the inner race centre is defined with respect to outer race center. Hence, the potential energy of the rotor may be expressed as,

$$V_{rotor} = m_{rotor} g (y_{in\_out} + y_{out}) \quad (4.29)$$

#### E. Contribution of the contact deformation

The contacts between rolling elements and races are treated as nonlinear springs, whose stiffnesses are obtained by Hertzian theory of elasticity. The expression of potential energy due to the contact deformation of the springs is written as,

$$V_{springs} = \sum_{j=1}^{N_b} \frac{1}{2} k_{in} \delta_{in}^2 + \sum_{j=1}^{N_b} \frac{1}{2} k_{out} \delta_{out}^2 \quad (4.30)$$

Where  $k_{in}$  and  $k_{out}$  are the nonlinear stiffnesses due to Hertzian contact effects (please see Appendix C).

The deformation at contact points between the  $j^{th}$ -rolling element and inner race is,

$$\delta_{in} = \{r + \rho_r\} - \chi_j \quad (4.31)$$

In this expression, if  $\{r + \rho_r\} > \chi_j$ , compression takes place and restoring force acts.

If  $\{r + \rho_r\} < \chi_j$ , there is no compression and restoring force is equal to zero.

Similarly, at the outer race the deformation at the contact points is,

$$\delta_{out} = [R - \{\rho_j + \rho_r\}] \quad (4.32)$$

In this expression, if  $R < \{\rho_j + \rho_r\}$ , compression takes place and restoring force acts.

If  $R > \{\rho_j + \rho_r\}$ , there is no compression and restoring force is equal to zero.

The bearing is assumed to be free from local and distributed defects. The distributed defects are surface waviness of the components, misaligned races and off sized rolling elements. Local defects are because of cracks, pits and spalls on the rolling surfaces. Some of the frequency components generated because of these defects are same as varying compliance frequency as reported by Sunnersjo (1985), Tandon and Nakra (1993) and Aktürk (1999).

We have considered the bearing as a whole. For that the rolling elements are arranged equi-spaced around the bearing. They also move around the races with equal velocity, which is physically possible because of the cage. The radial internal clearance ( $\gamma_0$ ) is the

clearance between the imaginary circles, which circumscribe the rolling elements and the outer race. For a horizontal rotor the radial internal clearance reduces as the rotor settles down due to the radial constant force. Hence, with the consideration of radial internal clearance ( $\gamma_0$ ), the contact deformations at the inner and outer races are,

$$\delta_{in} = \{r + \rho_r + \gamma_0\} - \chi_j \quad (4.33)$$

$$\delta_{out} = \{R - \{\rho_j + \rho_r + \gamma_0\}\} \quad (4.34)$$

#### F. Equations of motion

The kinetic energy and potential energy contributed by the inner race, outer race, balls, rotor and springs, can be differentiated with respect to the generalized coordinates  $\rho_j$  ( $j = 1, 2, \dots, N_b$ ),  $x_{in}$ , and  $y_{in}$  to obtain the equations of motion. For the generalized coordinates  $\rho_j$ , where  $j = 1, 2, \dots, N_b$ , the equations are:

$$\begin{aligned} m_j \ddot{\rho}_j + m_j g \sin \theta_j + m_j \rho_j \dot{\theta}^2 - (k_{in})[\delta_{in}]_+ \frac{\partial \chi_j}{\partial \rho_j} + (k_{out})[\delta_{out}]_+ + \frac{1}{2} \frac{\partial k_{in}}{\partial \rho_j} [\delta_{in}]_+^2 \\ + \frac{1}{2} \frac{\partial k_{out}}{\partial \rho_j} [\delta_{out}]_+^2 = 0; \quad j = 1, 2, \dots, N_b \end{aligned} \quad (4.35)$$

For the generalized coordinate  $x_{in}$  the equation is:

$$(m_{in} + m_{rotor}) \ddot{x}_{in} - \sum_{j=1}^{N_b} k_{in} [\delta_{in}]_+ \frac{\partial \chi_j}{\partial x_{in}} = F_u \sin(\omega t) \quad (4.36)$$

For the generalized coordinate  $y_{in}$  the equation is:

$$(m_{in} + m_{rotor}) \ddot{y}_{in} + (m_{in} + m_{rotor}) g - \sum_{j=1}^{N_b} k_{in} [\delta_{out}]_+ \frac{\partial \chi_j}{\partial y_{in}} = W + F_u \cos(\omega t) \quad (4.37)$$

This is a system of  $(N_b + 2)$  second order, non-linear differential equations. No external radial force is allowed to act on the bearing system and no external mass is attached to the outer race. The "+" sign as subscript in these equations indicates that if the expression inside the bracket is greater than zero, then the rolling element at angular location  $\theta_j$  is loaded giving rise to restoring force. If the expression inside the bracket is negative or zero, then the rolling element is not in the load zone and restoring force is set to zero. For the balanced rotor condition, the unbalance rotor force ( $F_u$ ) is set to be zero.

The deformation of spring at inner race  $\chi_j$  (Fig. 4.2), can be obtained as,

$$x_{in} + \chi_j \cos \theta_x = x_{out} + \rho_j \cos \theta_j \quad (4.38)$$

$$y_{in} + \chi_j \sin \theta_x = y_{out} + \rho_j \sin \theta_j \quad (4.39)$$

From these two equations, the expression for  $\chi_j$  is,

$$\chi_j = \left[ (x_{out} - x_{in})^2 + \rho_j^2 + 2\rho_j(x_{out} - x_{in})\cos\theta_j + 2\rho_j(y_{out} - y_{in})\sin\theta_j + (y_{out} - y_{in})^2 \right]^{1/2} \quad (4.40)$$

Now the partial derivatives of  $\chi_j$  with respect to  $\rho_j$ ,  $x_{in}$  and  $y_{in}$  are:

$$\frac{\partial \chi_j}{\partial \rho_j} = \frac{\rho_j + (x_{out} - x_{in})\cos\theta_j + (y_{out} - y_{in})\sin\theta_j}{\chi_j} \quad (4.41)$$

$$\frac{\partial \chi_j}{\partial x_{in}} = \frac{(x_{out} - x_{in}) - \rho_j \cos \theta_j}{\chi_j} \quad (4.42)$$

$$\frac{\partial \chi_j}{\partial y_{in}} = \frac{(y_{out} - y_{in}) - \rho_j \sin \theta_j}{\chi_j} \quad (4.43)$$

### 4.3 METHODS OF SOLUTION

The two coupled non-linear second order differential equations (4.35 – 4.37) are solved by numerical integration technique (please see Appendix D) to obtain the radial displacement and velocity of the rolling elements. This integration technique is a time domain approach. The non-analytic nature of the stiffness term renders the system equations difficult for analytical solution. A numerical integration algorithm models the real system, which is continuous time, by a discrete time system. Numerical integration is the solution of difference equations rather than the continuous time differential equations. The state of the system at an initial time is known from the assumed initial conditions. The state variables are calculated from the difference equations at an increment of  $\Delta t$  time and the procedure is continued for the desired length of time. As the time step  $\Delta t$  for the numerical integration is made smaller, the model comes closer to a realistic stream. The size of time step  $\Delta t$  is determined very easily for a linear system so as to accurately track the highest frequency. For nonlinear systems, the size of time step is determined by taking into account the error introduced and also to avoid generation of “spurious” results, all of which can lead to unstable solutions (Tongue, 1984). The longer the time to

reach steady state vibrations, the longer computational time needed and hence the more expensive will be the computation.

#### 4.3.1 Choice of step size and initial condition

For the numerical technique used, the initial conditions and step size are very important for good and computationally inexpensive solution. Particularly for nonlinear systems, different initial conditions mean a totally different system and hence different solutions. The larger the time step,  $\Delta t$ , the faster is the computation. On the other hand the time step should be small enough to achieve accuracy. However, very small time steps can increase the truncation errors. The Newmark- $\beta$  method has a provision for estimating local truncation error. For various speeds and  $W = 6$  N, the system is numerically integrated on a Silicon Graphics workstation for a number of time step sizes. The local truncation error and CPU time are plotted against the time step as shown in Fig. 4.5. One can see that region A-A' gives the best results. Therefore an optimization should be made between them. The time step for the investigation taken to be  $\Delta t = 10^{-5}$  sec. At time  $t = 0$  the following assumptions are made:

- i. The rotor is held at the center of the bearing and all balls are assumed to have equal axial preload.
- ii. The rotor is given initial displacements and velocities. For fast convergence the initial displacements are set to the following values:  
 $x_0 = 10^{-6}$  m and  $y_0 = 10^{-4}$  m. The initial velocities are assumed to be zero:  
 $\dot{x}_0 = 0$  and  $\dot{y}_0 = 0$ .
- iii. When  $t > \Delta t$  the initial conditions have already passed and the normal procedure commences.

Rolling elements are radially preloaded in order to ensure the continuous contact of all the rolling elements and the raceways, otherwise a chaotic behavior might be observed.

#### 4.4 METHODS OF ANALYSIS

Several methods used to analyze the results obtained by numerical integration are described below.

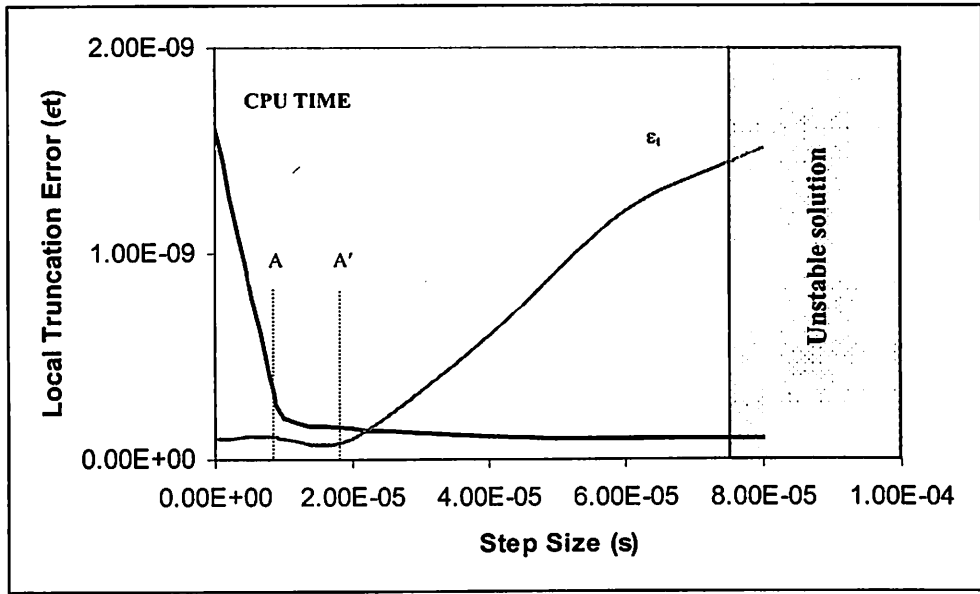


Fig. 4.5 Effect of step size on stability of system

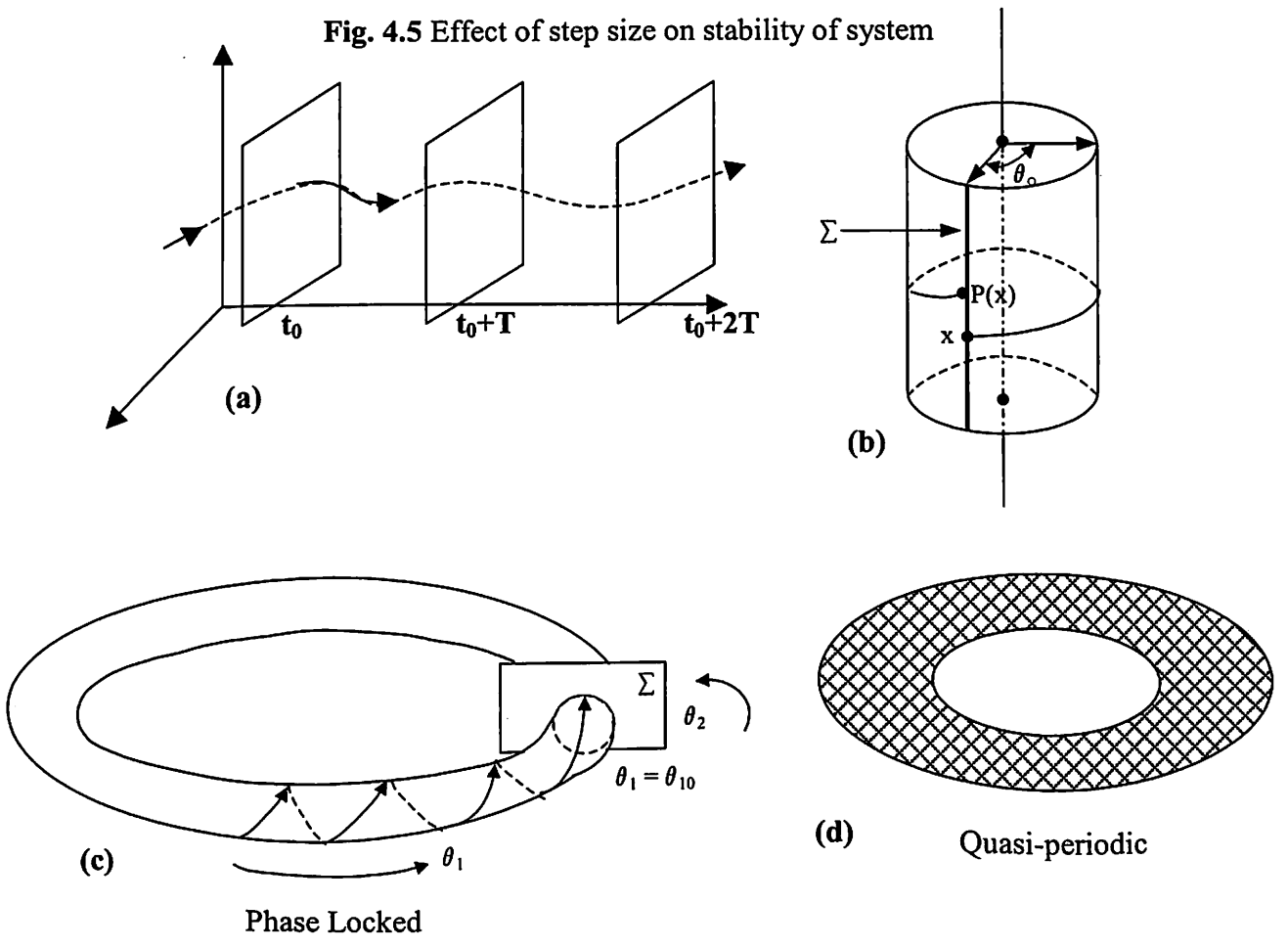


Fig. 4.6 Poincaré maps

#### 4.4.1 Poincarè Map

Poincarè map is a classical technique for analyzing dynamical systems (Nayfeh and Balachandran, 1994). It replaces the flow of an  $n^{\text{th}}$  order continuous time system with a  $(n-1)^{\text{th}}$  order discrete time system called the Poincarè map.

The usefulness of Poincarè maps lies in the reduction of order and the fact that it bridges the gap between continuous and discrete time systems. A periodic  $n^{\text{th}}$  order non-autonomous system with minimum period  $T$  can be transformed into an  $(n+1)^{\text{th}}$  order autonomous system in the cylindrical state space  $IR \times S^1$ , (Fig. 4.6 (a, b)). Considering the

$n$ -dimensional hyper plane  $\Sigma = IR \times S^1$  defined by,

$$\Sigma = \{(x, \theta) \in IR^n \times S^1 : \theta = \theta_0\} \quad (4.44)$$

Every  $T$  seconds, the trajectory or the solution of (Eq. 4.35-4.37) intersects  $\Sigma$ . The resulting map  $P_N : \Sigma \rightarrow \Sigma (IR^n \rightarrow IR^n)$  defined by  $P_N$  is called the Poincarè map for the non-autonomous system.

$$P_N^K(x) = \Phi_{t_0+KT}(x, t_0), K = 0, 1, \dots \quad (4.45)$$

This is similar to the action of flashing a stroboscope with period  $T$ .  $\Phi_x(x^*, t_0)$  is a periodic solution of a non-autonomous system if for all  $t$ ,

$$\Phi_t(x^*, t_0) = \Phi_{t+T}(x^*, t_0) \quad (4.46)$$

For minimum period  $T > 0$ , if  $T$  is some integer multiple  $K$  of the forcing period  $T_f$ , the solution  $\Phi_t(x^*, t_0)$  is called a period- $K$  solution. Period-one solution is called a fundamental solution and if  $K > 1$ , a period- $K$  solution is referred to as a  $K^{\text{th}}$  subharmonic.

A period-one solution of a continuous-time system corresponds to a fixed point  $x^*$  of the Poincarè map  $P_N$ . A  $K^{\text{th}}$  order subharmonic corresponds to a period- $K$  closed orbit  $\{x_1^*, \dots, x_K^*\}$  of the Poincarè map  $P_N$ . The Poincarè map freezes any periodic component of the solution that is commensurate with the forcing frequency. The spectrum consists of a spike at frequency zero and spikes at integer multiples of  $1/T_f$ . The spectrum of a  $K^{\text{th}}$  order subharmonic contains spike of frequency zero and spike at integer multiples of  $1/KT_f$ . The Poincarè map of a period-one (or period- $K$ ) solution is a single point (or  $K$  points).

### A. Quasi-periodic solution

A quasi-periodic solution is a sum of periodic waveforms each of whose frequency is one of the various sums and differences of a finite set of base frequencies. If there are  $p$  base frequencies then it is a  $p$ -periodic solution (different from a period- $p$  periodic solution).

The spectrum of a quasi-periodic waveform consists of spikes at frequencies  $f_i$ , (which are the frequencies of waveforms adding to give the solution) and  $Kf_i$  ( $K=1,2,\dots$ ). Some of these components may have zero amplitude. The time response of the quasi-periodic solution shows amplitude modulation where there is a carrier frequency ( $f_c$ ) and a modulation frequency ( $f_m$ ). In the spectrum, the spikes are at frequencies  $[f_c \pm K f_m]$ . If the base frequency lock onto some common time period solution, it is called phase locked or mode locked or frequency locked solution (Nayfeh and Balanchandran, 1994) as shown in Fig. 4.6 (c). The Poincarè map of a quasi-periodic solution is either a dense collection of points on a closed curve or a finite number of points when there is phase locking (Fig. 4.6 (c, d)). In general, Poincarè limit is a set of  $K$ -periodic trajectory having one or more embedded ( $K-1$ ) tori.

### B. Chaotic solution

A solution, which is a bounded and steady state solution, but neither an equilibrium point (not periodic) nor quasi-periodic, is a chaotic solution (Parker and Chua, 1989). The frequency spectra are broadband which may have spikes at identifiable frequencies. The Poincarè map of a chaotic solution has a fractal structure, which repeats itself as the map is magnified.

### C. High order Poincarè maps

For a dynamical system where the solution trajectory flows in a  $n$ -dimensional hyper space, the behavior of the system can be understood by generating higher order Poincarè maps. The sampling action of the Poincarè map reduces the dimensions of a limit set by one i. e., a limit cycle becomes a point, a torus becomes a circle and a  $K$ -torus becomes a ( $K-1$ )-torus. Another sampling may further reduce the dimensions of the limit set. This idea leads to higher order Poincarè maps.

#### 4.4.2 The Non-autonomous Shooting Method

The non-autonomous shooting method is used for finding out the fixed point of the steady state solution. The fixed point used as the initial condition for numerical integration results in a steady state solution with no transient. When some arbitrary initial conditions are taken, transients are formed, which take some time to die down. For non-linear system the transients may lead to instability. On taking fixed point as initial conditions, the transients are not formed resulting in saving of a considerable computational time.

Let  $P_N$  be the Poincarè map associated with a non-autonomous system with minimum period  $T$  where,

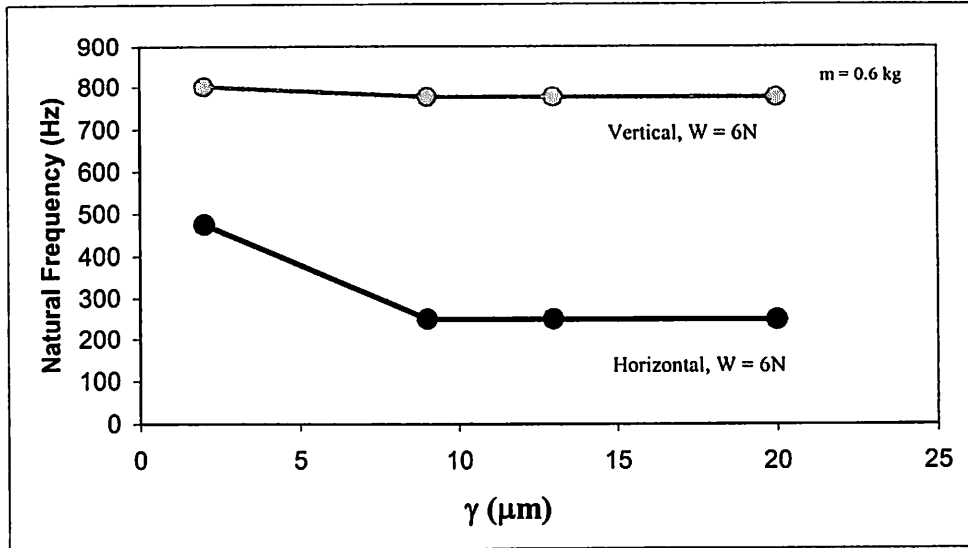
$$P_N(x) = \phi_{t_0+T}(x, t_0) \quad (4.47)$$

Here  $\phi_t$  is the solution of the variational equation and is integrated simultaneously with  $\phi_t$  (please see Appendix C). The Newton Raphson algorithm is applied to Eq. 4.47 and this is called non-autonomous shooting method. The characteristic multipliers are the eigen values of  $\phi_{t_0+T}(x, t_0)$  and can be found using the QR algorithm (Press et. al. 1992).

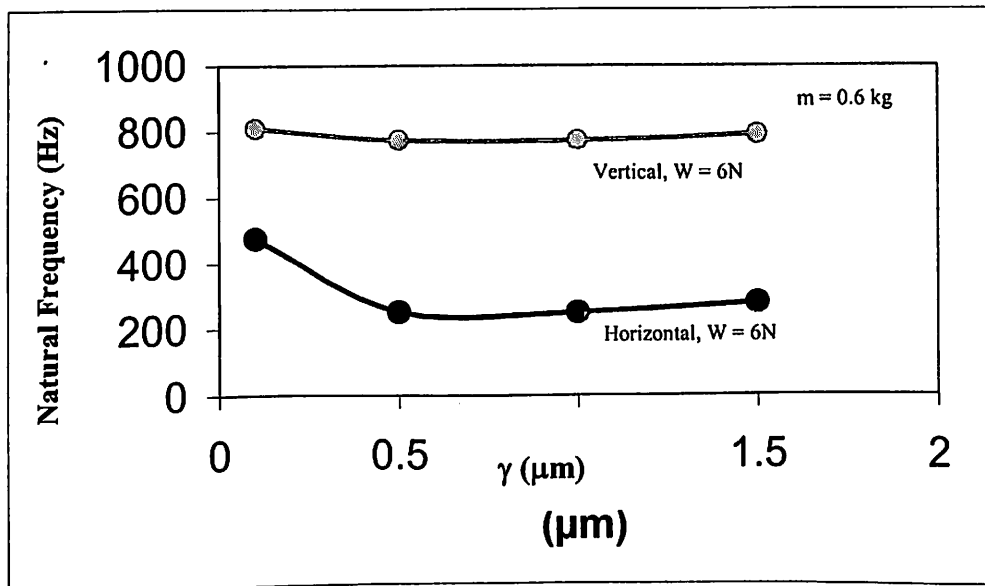
The eigen values of the monodromy matrix, called Floquet or characteristic multipliers, provide a measure of local orbital divergence or convergence along a particular direction over one period of the closed orbit. Particularly, the following informations about the stability of the system and the nature of bifurcation can be derived.

- a. If all the multipliers are located within the unit circle, the system is stable.
- b. If one of the multipliers leaves the unit circle through  $-1$ , this indicates period multiplying bifurcation.
- c. If one of multipliers leaves the circle through  $+1$ , this would indicate bifurcation possibly including a saddle point.
- d. If a pair of complex conjugate multipliers leaves the unit circle, a Hopf, or a secondary Hopf bifurcation could occur.





(a) Point contact



(b) Line contact

Fig. 4.7 Vertical and horizontal critical frequency

## 4.5 RESULTS AND DISCUSSION

Theoretical results are obtained for a rotor supported by rolling element bearing using the techniques discussed in sections 4.3 and 4.4. The results are discussed below.

### 4.5.1 Static Bearing Stiffness

The dimensions of the rolling element bearing considered in the present study are given in Appendix A. The stiffness of the rolling element bearing has been estimated for **point/line** contact with the vertical force of 6N by using Hertzian contact theory (please see Appendix B). From Fig.4.7, it can be seen that the stiffness remains practically constant till a radial clearance of 9  $\mu\text{m}$  for ball bearing (point contact) while for rolling bearing (line contact) stiffness remains practically constant till a radial clearance of 0.5  $\mu\text{m}$ . For theoretical simulation the values of radial internal clearance are taken to be 20  $\mu\text{m}$  and 12  $\mu\text{m}$  (for point contact) and 1  $\mu\text{m}$  and 0.5  $\mu\text{m}$  (for line contact).

### 4.5.2 Results of Theoretical Simulation

The system equations (4.35-4.37) have been solved for different combinations of parameters for the rolling element bearing. The parameters of study are:

- i. Speed of rotor
- ii. Radial internal clearance ( $\gamma_0$ )
- iii. Unbalanced rotor force ( $F_u$ )

Fukata et al. (1985), Mevel and Guyader (1993), Sankarvelu et al. (1994) have all taken the same bearing, which is used in the present study. These studies have focused more on parametric effect involving change in speed and constant vertical force for ball bearings. Radial internal clearance as a parameter has not been considered for study. In the present report, besides speed as a parameter of study, effect of radial internal clearance has also been considered. Radial internal clearance is an important parameter of study because even if the clearance is inevitable, it can be controlled to some extent.

Time response plots are obtained for the combination of above parameters under this study. These plots are generated by numerical integration to reach steady state when peak-to-peak value of x and y displacements are obtained. For reaching steady state for the first speed, the initial conditions are taken as the fixed-point solution. For successive

speeds, the initial conditions are taken as the steady state solution obtained for the preceding speed. For a non-linear system the response plots have regions of multi-valued solution, which are generally the high amplitude regions (Thompson and Stewart, 1986). The generation of the response curve such that the  $i^{\text{th}}$  steady state speed solution is near the  $(i-1)^{\text{th}}$  steady state speed solution and it is ensured that the entire response curve is plotted throughout otherwise there is a danger of the solution jumping from one response curve to another.

#### 4.5.2.1 Response for point contact at $\gamma_0 = 20 \mu\text{m}$ , $W = 6 \text{ N}$ and $F_u = 0$

The overall response plot of rolling element bearing for *point* contact with radial internal clearance of  $20 \mu\text{m}$  and radial load of  $6\text{N}$  is shown in Fig. 4.8. The peak-to-peak (pp) vertical response is less than the peak-to-peak horizontal response in regions of high amplitude. The overall response plot has a very rough appearance. Three regions can be identified which have high pp response. These regions are shown in Fig. 4.8 bounded by lines A-A', B-B' and C-C'.

Three regions of period-one unstable response are shown on Fig. 4.8. The first region from 955 to 5950 rpm has period doubling bifurcations. This is also a region of multi-valued region. The eigen values of the monodromy matrix go out through  $-1$ . Figure 4.9 shows the nature of the solution at 1500 rpm. The VC and its harmonic (super-harmonic) character of the frequency spectra is also brought-out by the Poincaré map with the closed orbit. One region of chaotic behavior is seen in this region. For the first chaotic region, 1920 to 2640 rpm, the loss of stability is seen to be due to the eigen values crossing  $+1$ . In this region, the period doubling bifurcations give way to chaos at about 1920 rpm and this chaotic region extends up to 2650 rpm. The chaotic solutions at 1950, 2100 and 2400 rpm are shown in Fig. 4.10 to 4.12, respectively. The frequency spectrum has a band structure as seen in-between spikes of varying compliance (VC) and its multiples. The Poincaré maps of chaotic solutions have fractal structures that repeat as the map is magnified. The time responses also show beat and chaos like behavior. It is clear that loss of periodicity is one characteristic of chaotic solution.

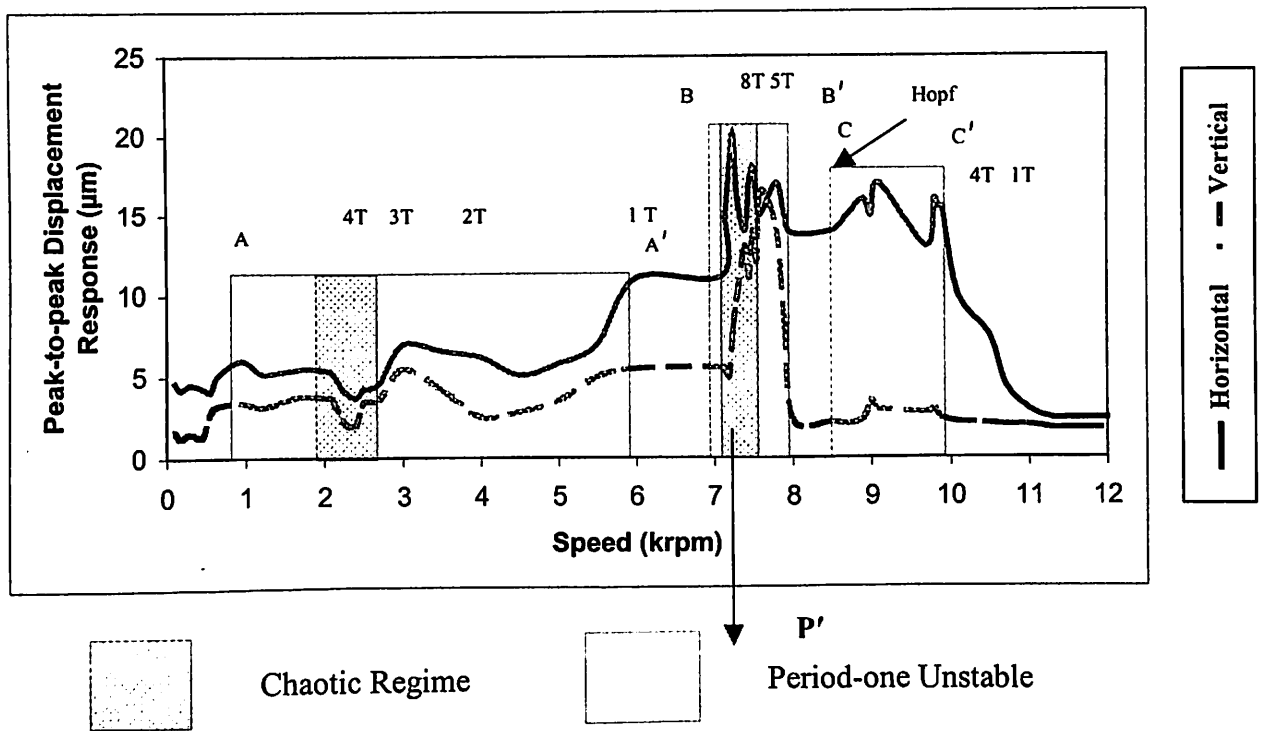
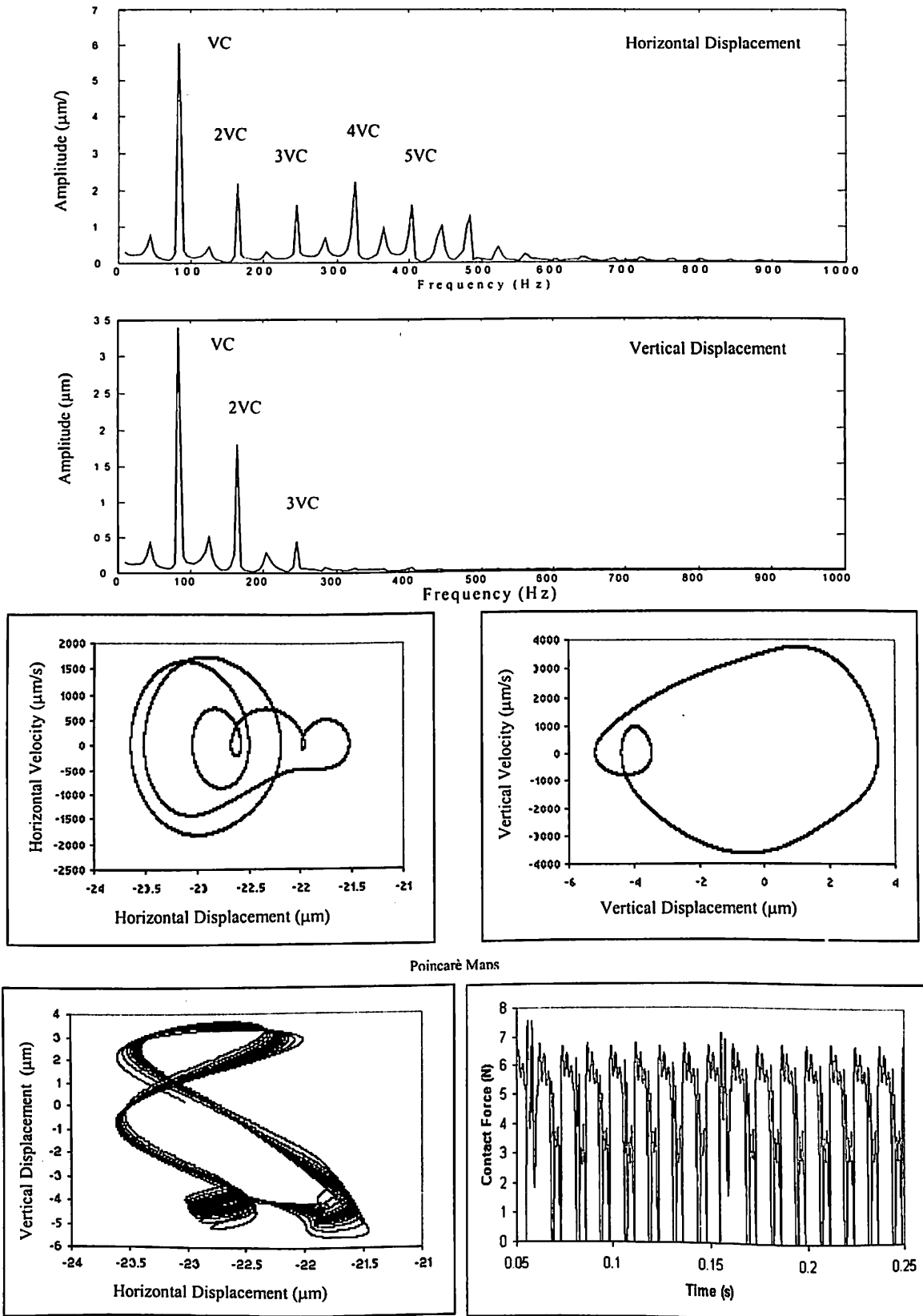
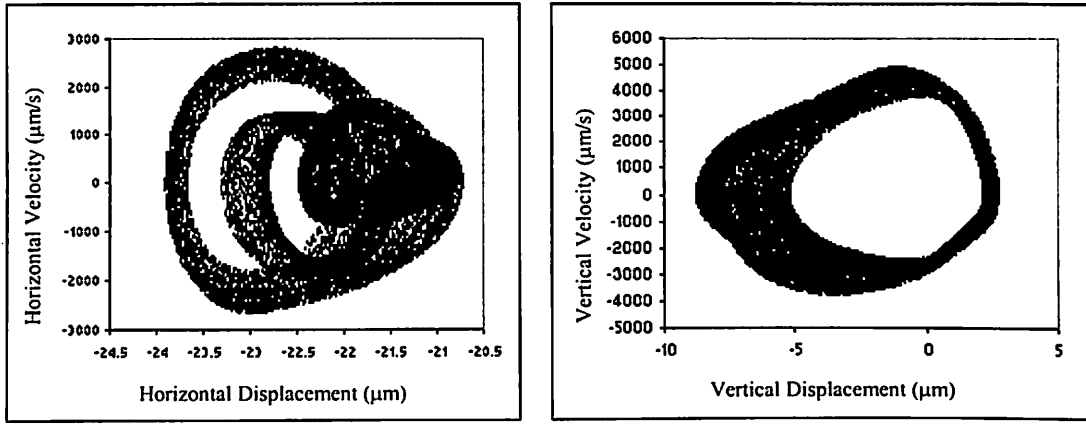


Fig. 4.8 Response plot for  $\gamma_0 = 20\mu\text{m}$ ,  $W = 6 \text{ N}$



**Fig. 4.9** Response at 1500 rpm for  $\gamma_0 = 20\mu\text{m}$ ,  $W = 6\text{ N}$



Poincaré Maps

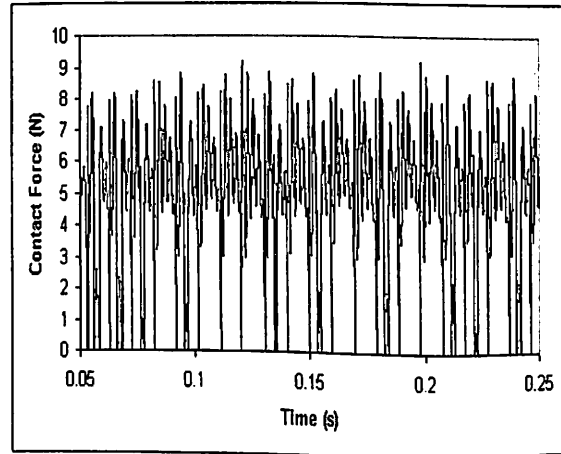
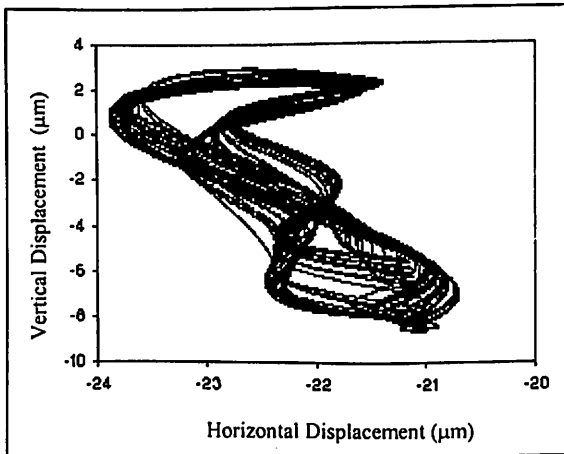
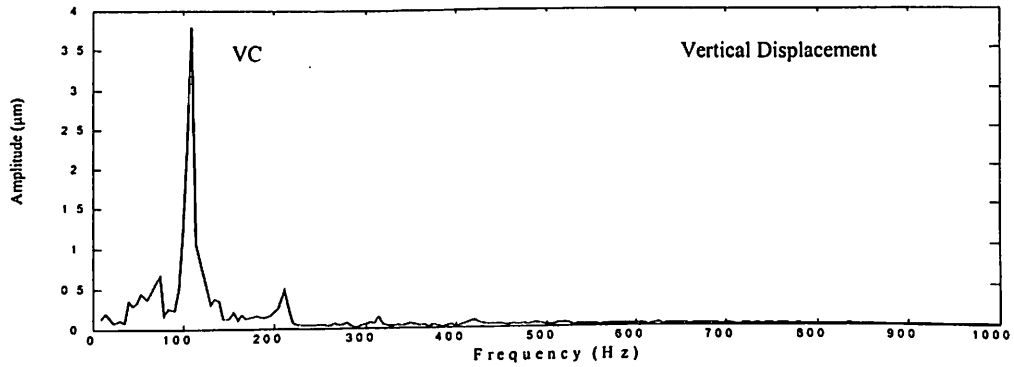
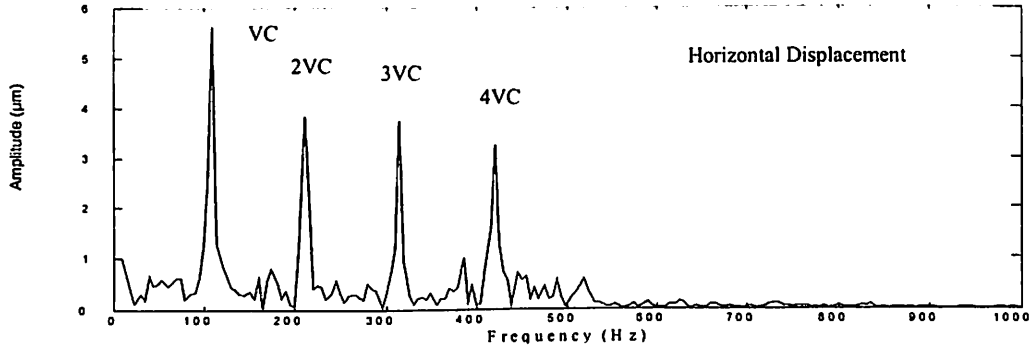
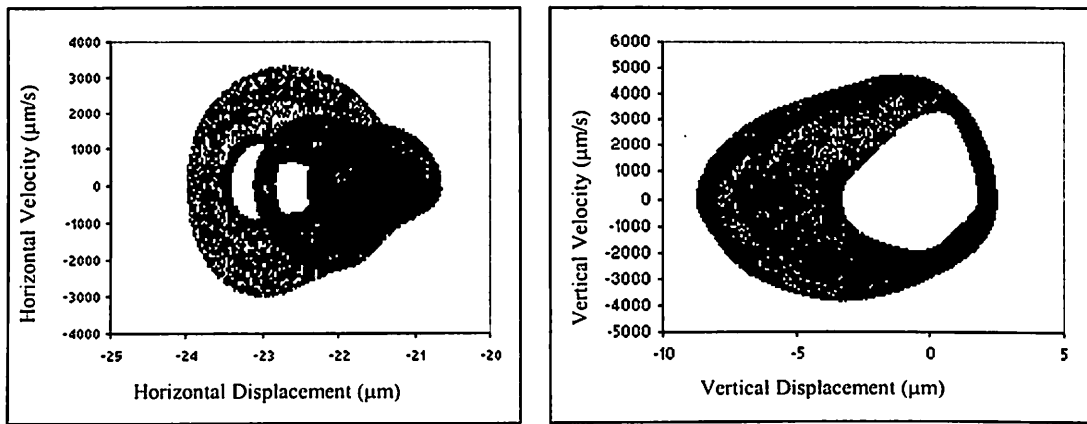


Fig. 4.10 Response at 1950 rpm for  $\gamma_0 = 20\mu\text{m}$ ,  $W = 6\text{ N}$



Poincaré Maps

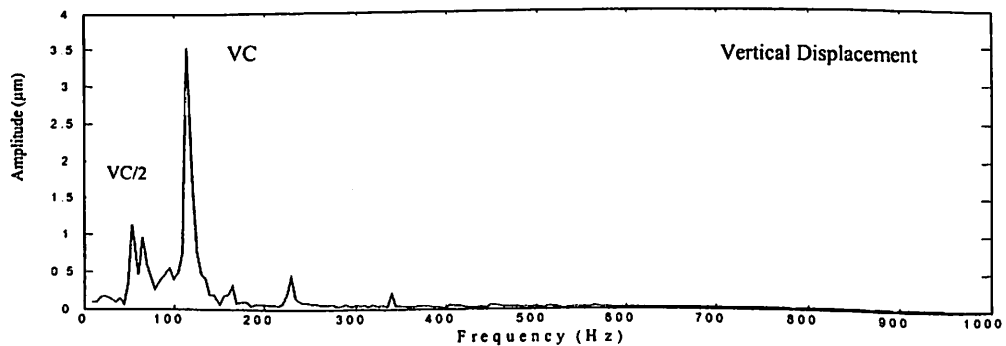
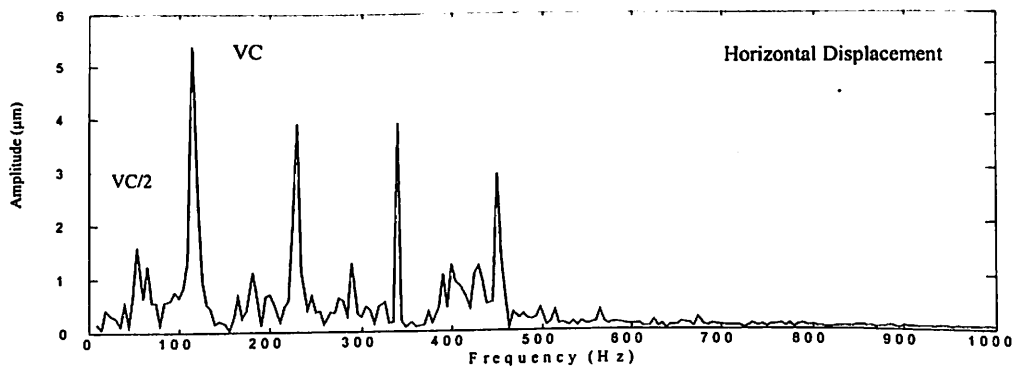
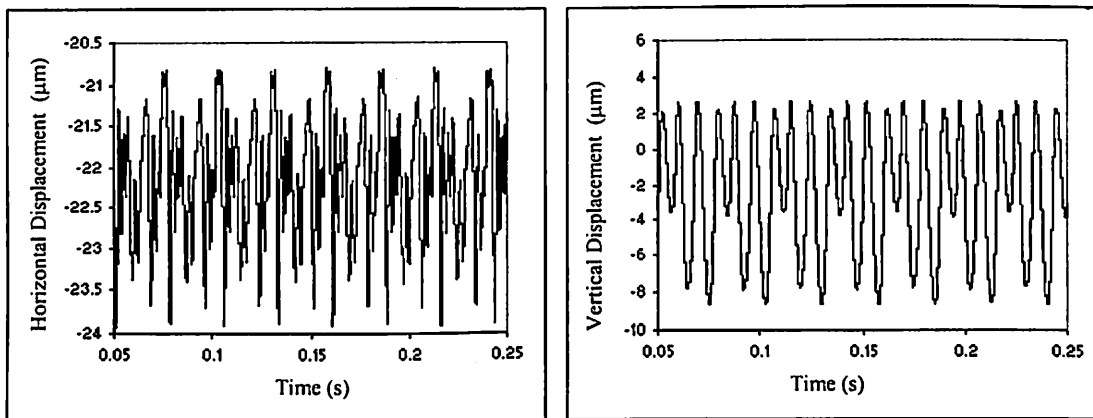


Fig. 4.11 Response at 2100 rpm for  $\gamma_0 = 20\mu\text{m}$ ,  $W = 6\text{ N}$

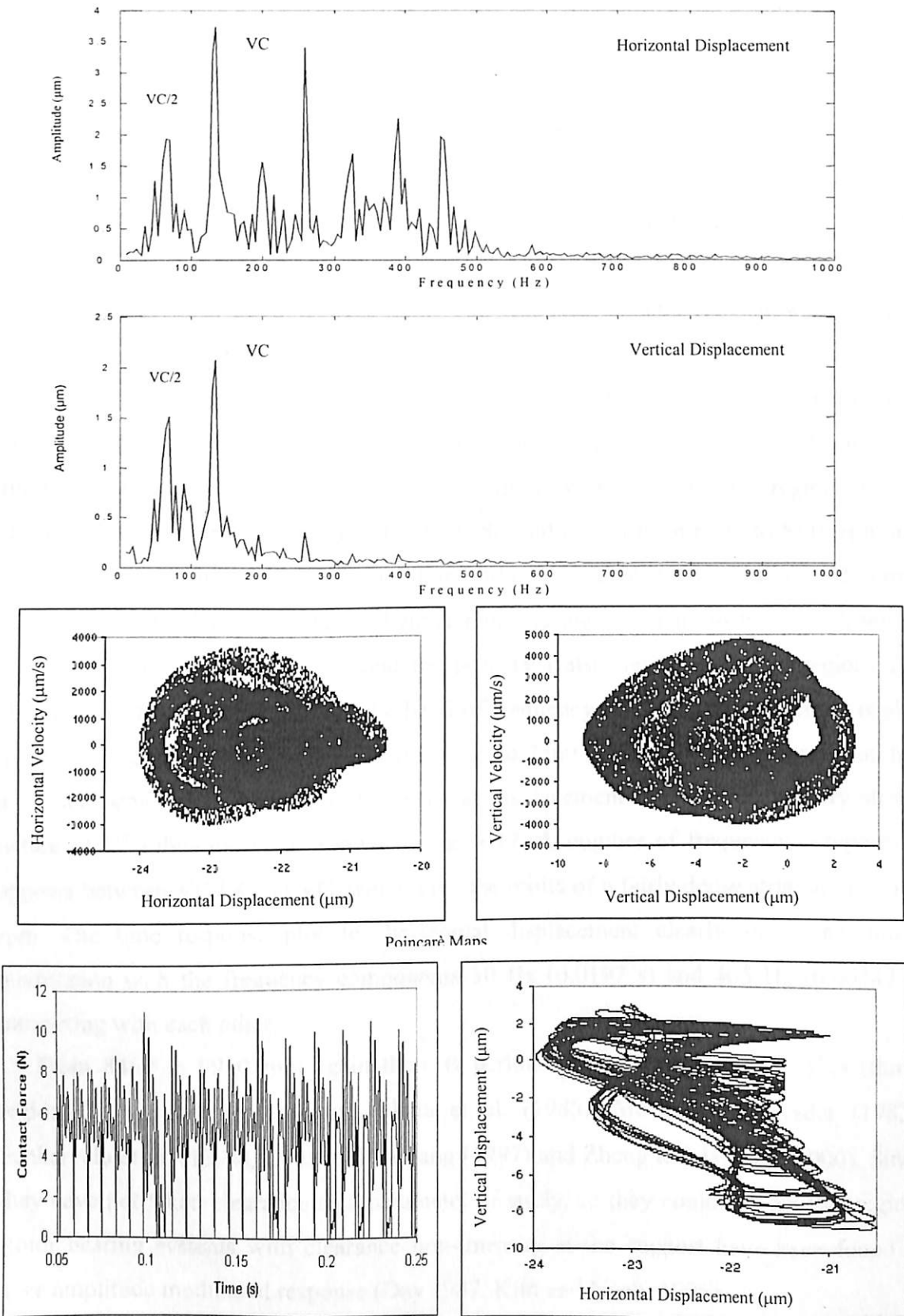


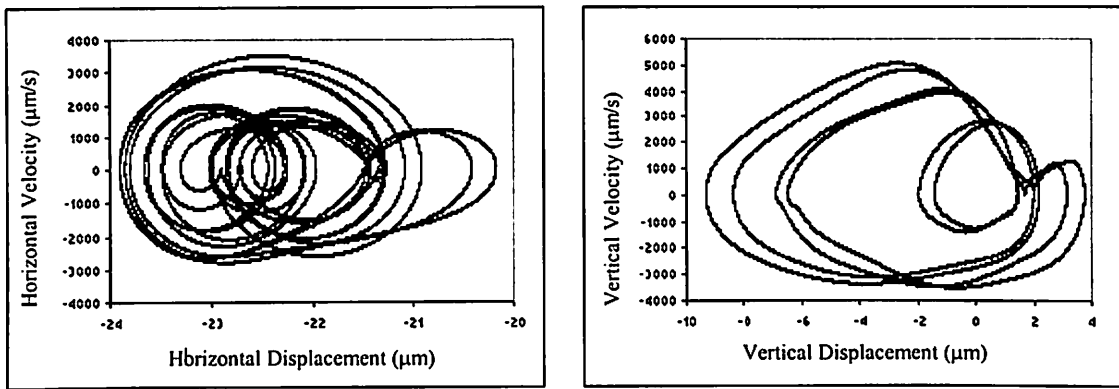
Fig. 4.12 Response at 2400 rpm for  $\gamma_0 = 20\mu\text{m}$ ,  $W = 6\text{ N}$



The route to chaos by sudden loss of stability through a limit point has been shown by Sankarvelu et al. (1994). From speeds of 2680 rpm onwards, stability returns and there are period doubling bifurcations. At 2700 rpm, the 4<sup>th</sup> subharmonic appears as shown in Fig. 4.13. As speed further increases, stability returns by a torus solution between 2900 to 4120 rpm. Figure 4.14 shows the response at 4000 rpm and it is clear from the response that the 2-T (2<sup>nd</sup> sub-harmonic) nature of solution is obtained. Below 5940 rpm the response is “period-one” unstable. Further increase in speed returns the stability in the speed range between 5955 to 6985 rpm. The response at 6000 rpm shows 1T stable behavior as shown in Fig. 4.15.

Fukata et al. (1985) and Mevel and Guyader (1993) have reported period-one unstable behavior or chaos around the vertical and horizontal critical speeds. In their study one observes that the large clearance results in very wide unstable regions, which are not necessarily around the critical speeds. Second region from 6995 to 8110 rpm has period doubling bifurcations. Period doubling bifurcation gives way to chaos at 7250 rpm as shown in Fig. 4.16. The chaotic behavior in this region seems to be very strong as compared to the previous region and the peak (P') also develops in this region. The chaotic attractor is spread out and the band of frequency in the spectrum formed is also quite prominent. The chaotic region extends up to 7560 rpm after which the solution has a 8<sup>th</sup> subharmonic at 7600 rpm. The vertical displacement response has a very strong nature of 8<sup>th</sup> subharmonic as shown in Fig. 4.17. A number of frequency components appears between  $VC / 8$  and  $VC$ , which give the orbits of a fairly dense structure at 7600 rpm. The time response plot for horizontal displacement clearly shows amplitude modulation with the frequency components 50 Hz (0.0197 s) and 405 Hz (0.00247 s) interacting with each other.

From 8460 to 9910 rpm again there is period-one unstable behavior. This (third) region C-C' is not reported by Fukata et al. (1985), Mevel and Guyader (1983), Sankarvelu et al. (1994), Datta and Farhang (1997) and Zheng and Hasebe (2000). Since they have not taken clearance as a parameter of study, so they could not get this region. Rotor bearing systems with clearance non-linearity at the support have been found to have amplitude modulated response (Day 1987, Kim and Noah, 1996).



Poincaré Maps

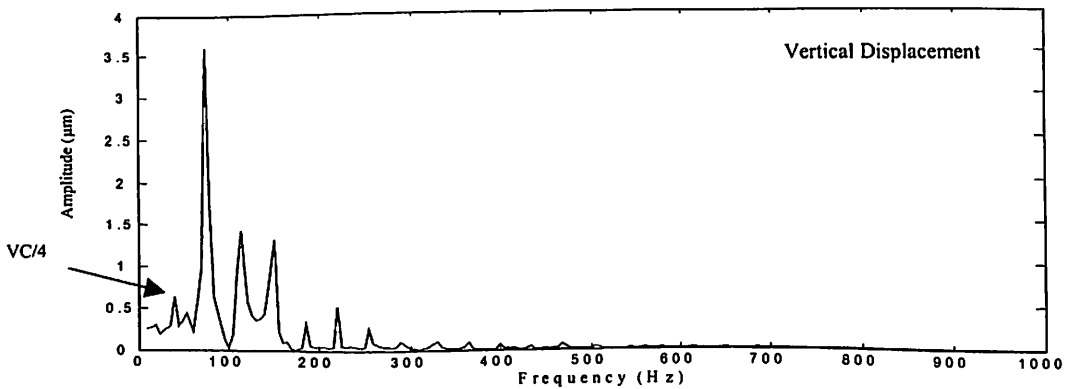
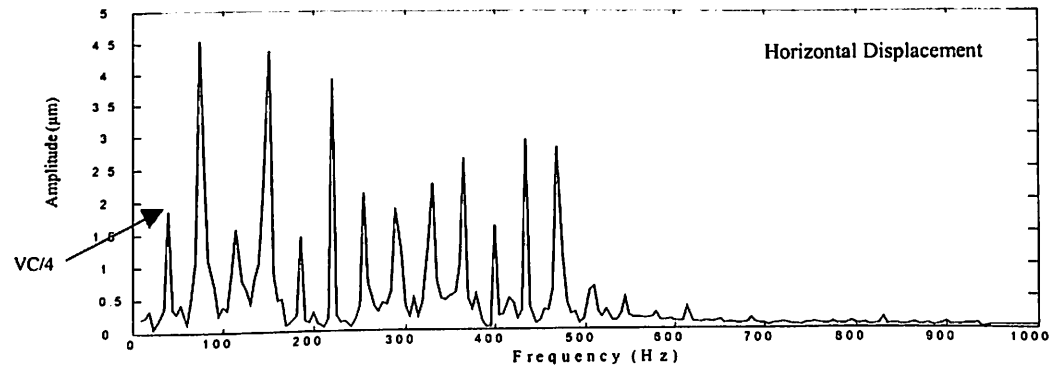
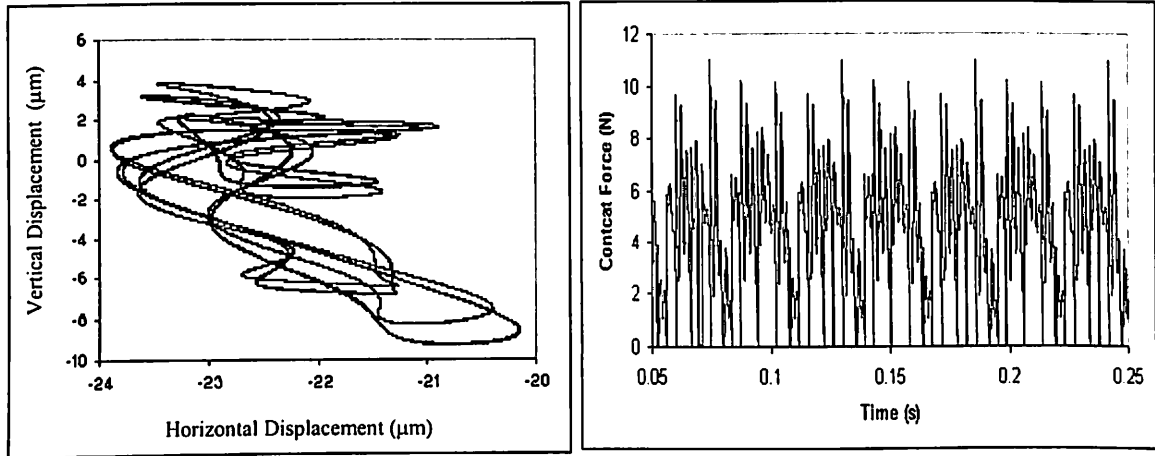
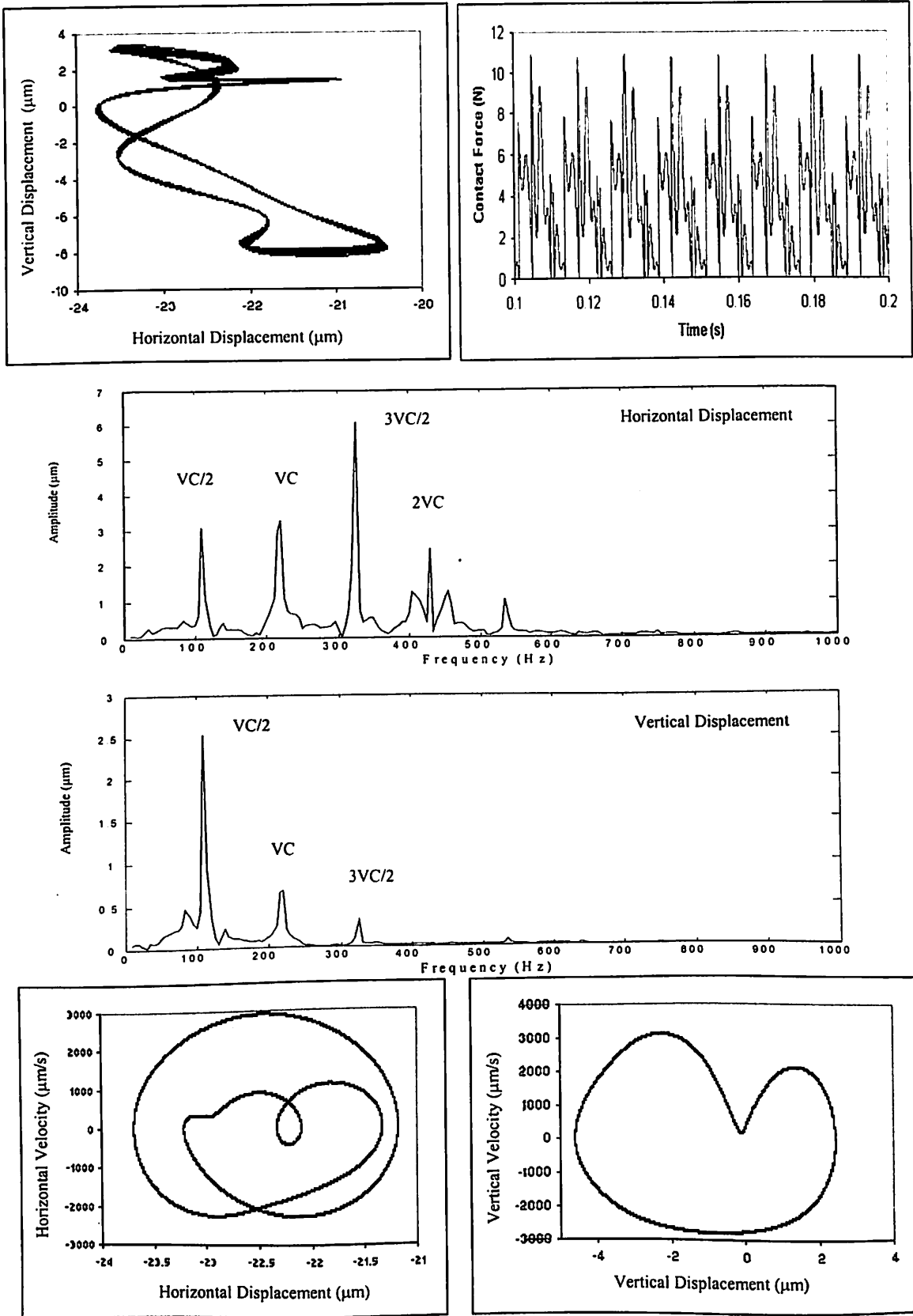
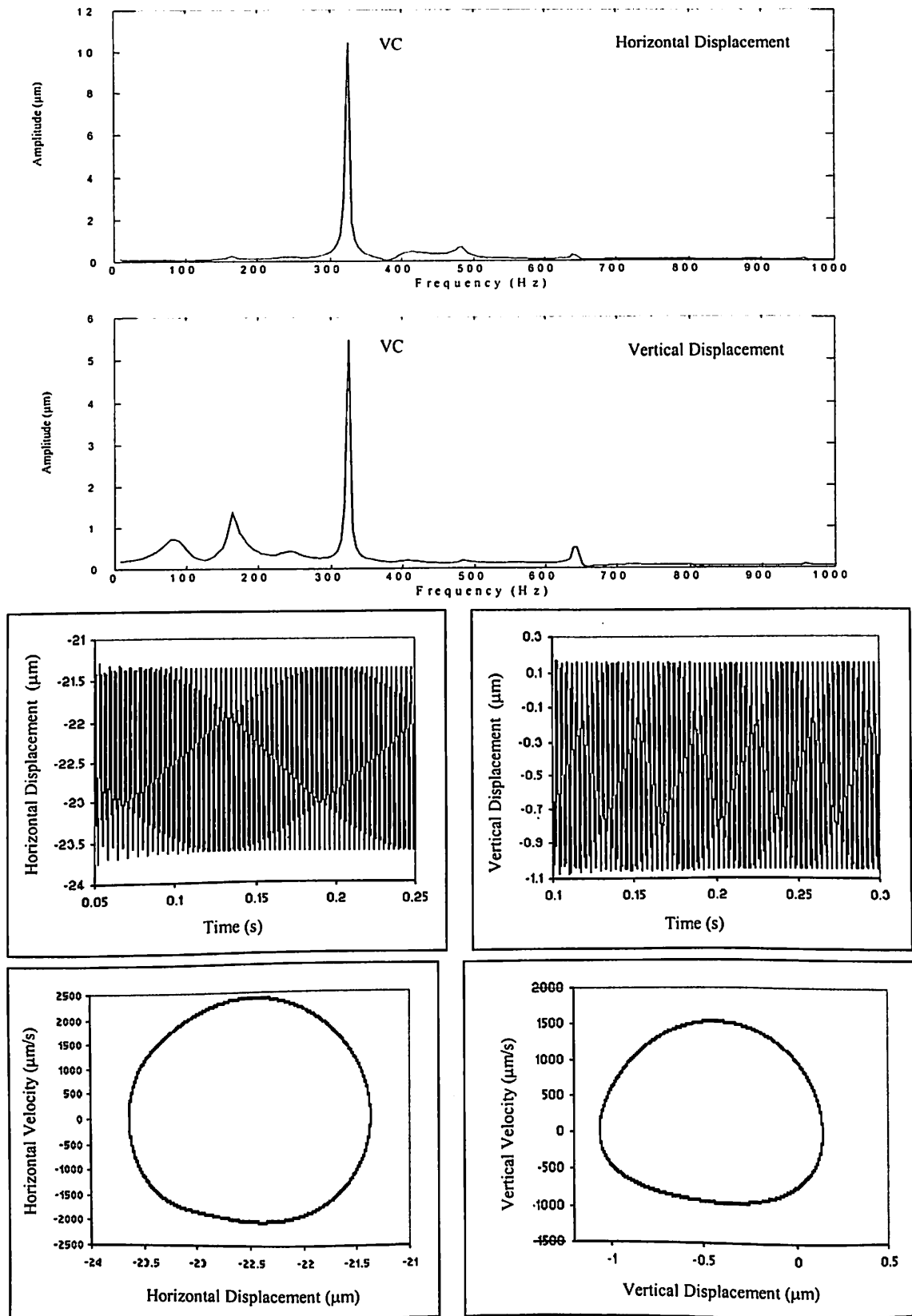


Fig. 4.13 Response at 2700 rpm for  $\gamma_0 = 20\mu\text{m}$ ,  $W = 6\text{ N}$



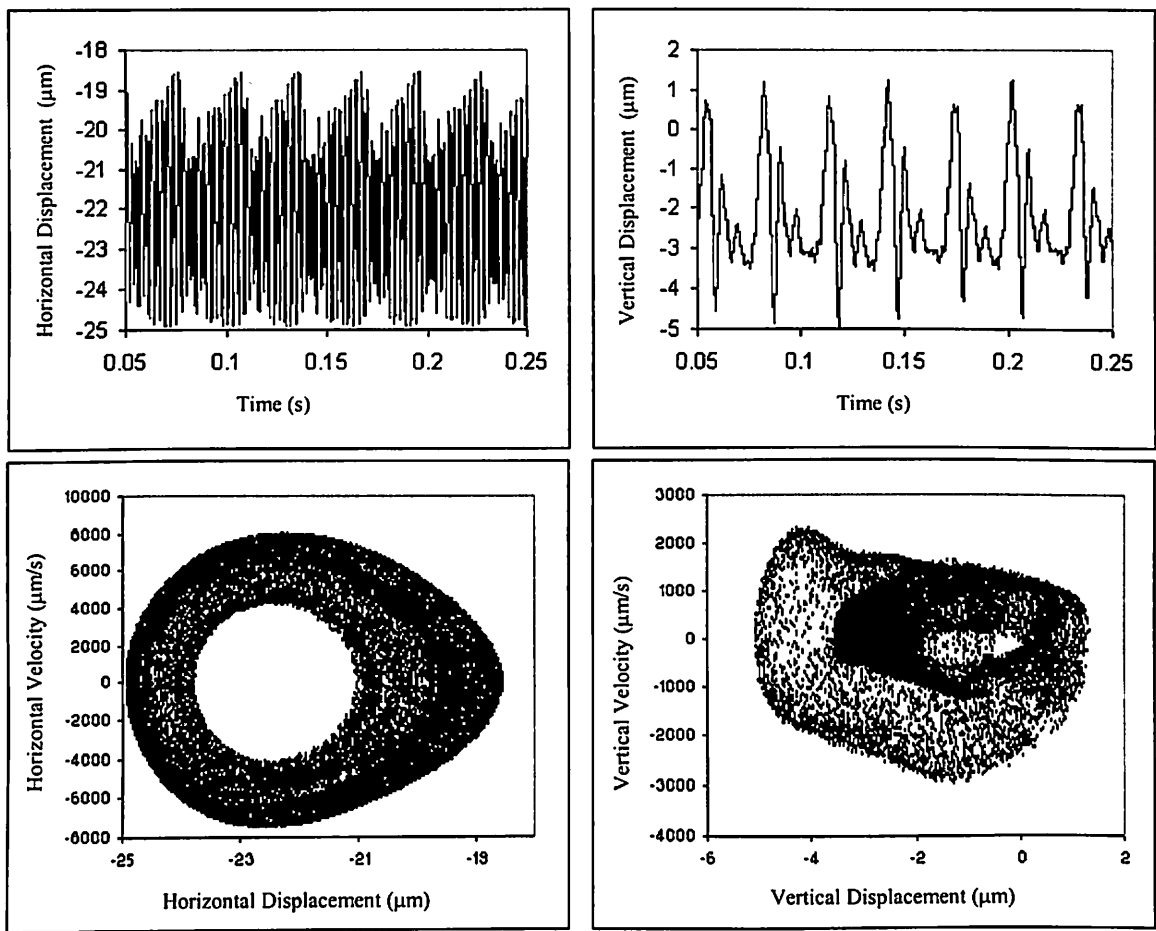
Poincaré Maps

Fig. 4.14 Response at 4000 rpm for  $\gamma_0 = 20\mu\text{m}$ ,  $W = 6\text{ N}$



Poincaré Maps

Fig. 4.15 Response at 6000 rpm for  $\gamma_0 = 20\mu\text{m}$ ,  $W = 6\text{ N}$



Poincaré Maps

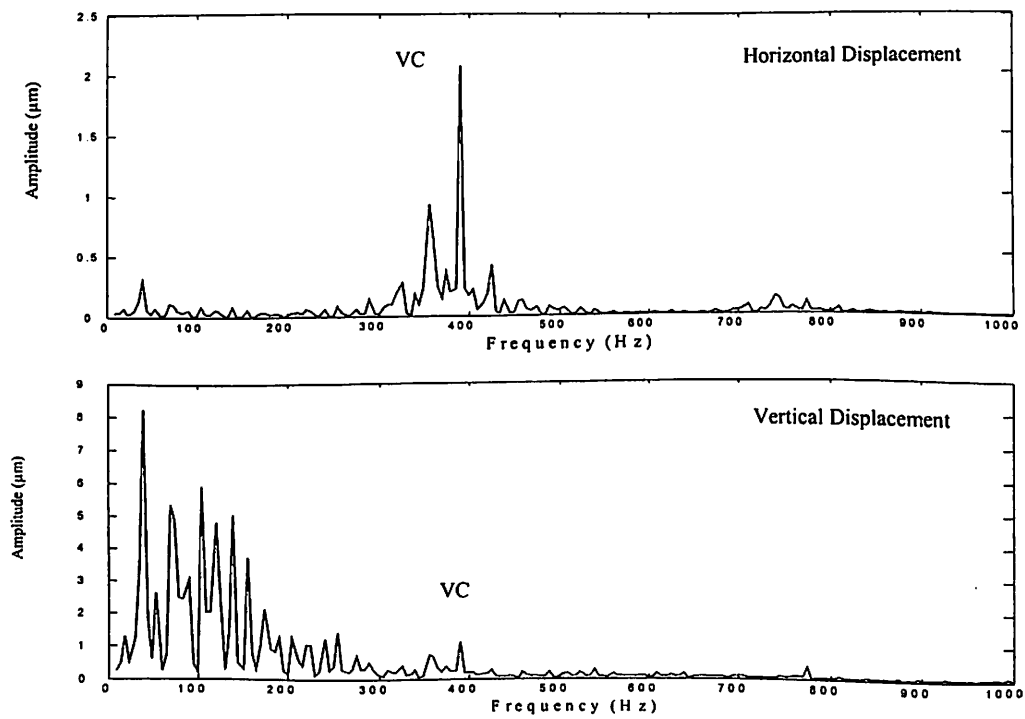


Fig. 4.16 Response at 7250 rpm for  $\gamma_0 = 20\mu\text{m}$ ,  $W = 6\text{ N}$

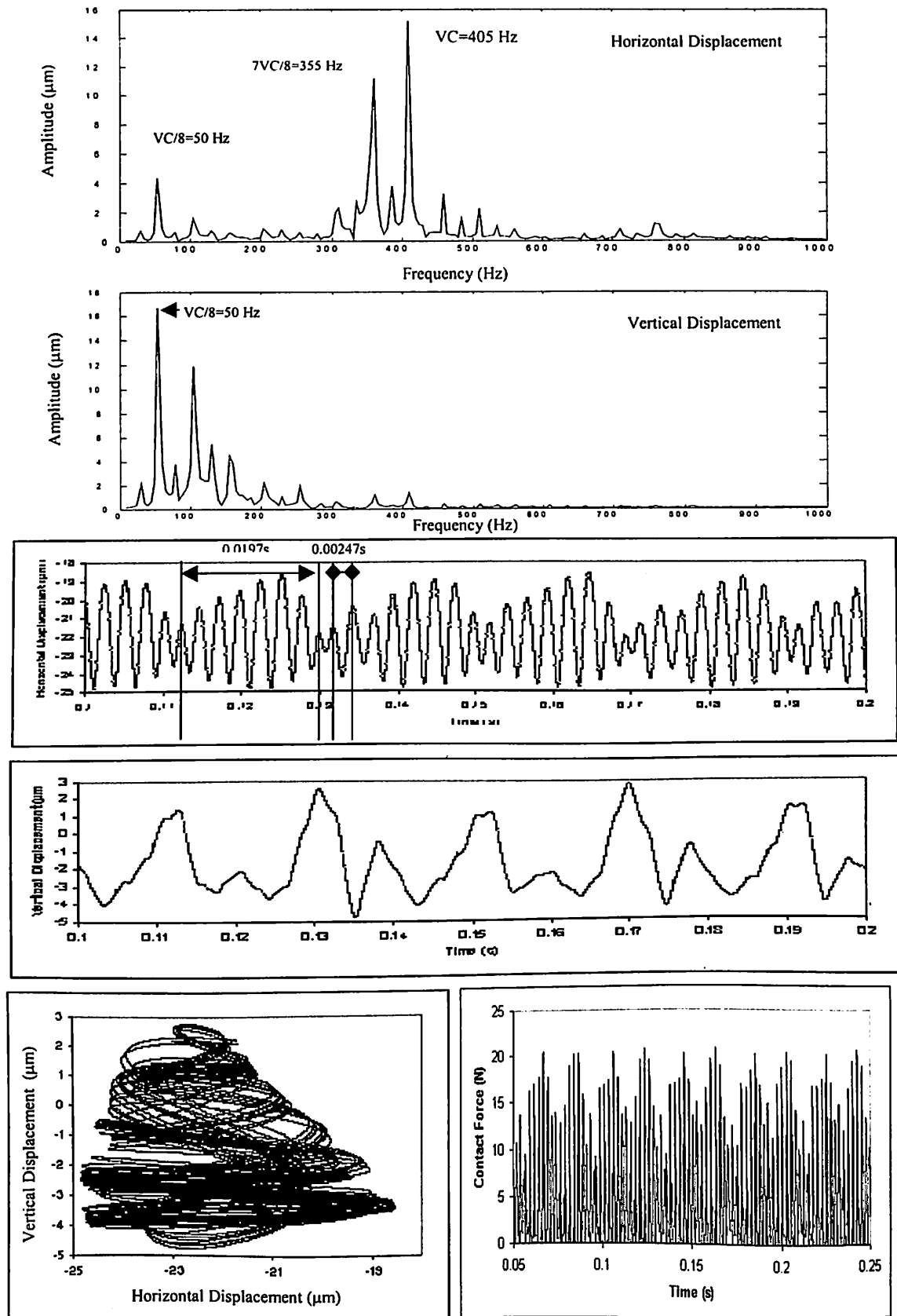


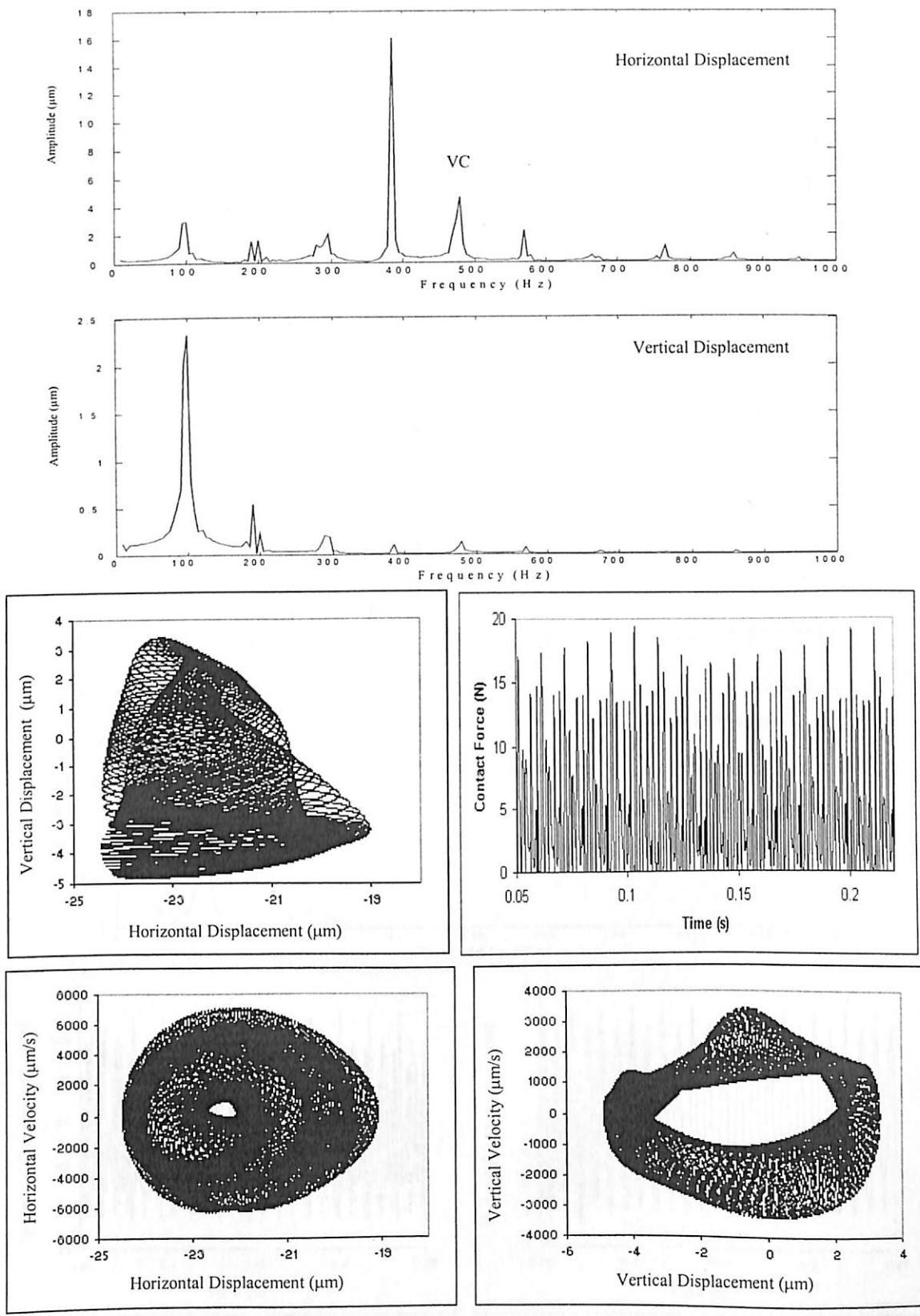
Fig. 4.17 Response at 7600 rpm for  $\gamma_0 = 20\mu\text{m}$ ,  $W = 6$  N

It is seen from the solutions of the rotor bearing system by numerical integration that under certain conditions, the response has amplitude modulation. This amplitude modulation is the result of the presence of a frequency, which is incommensurate with respect to the basic input excitation frequency. This is a result of the system undergoing Hopf bifurcation. At 8900 rpm, by way of Hopf bifurcation, the solution becomes unstable. It is seen that the frequency generated due to Hopf bifurcation changes with speed. The phase plot and Poincarè map shown in Fig. 4.18 give an indication of a quasi-periodic response because of 'net' structure. The time response of the horizontal displacement has more amplitude modulations because of the Hopf bifurcation. As speed is increased to 9900 rpm 4<sup>th</sup> subharmonic behavior predominates as shown in Fig. 4.19, which gives way to 1T stable behavior upto 10895 rpm and onwards. No indication of chaos is observed here. The nature of response for various speeds is given in Table 4.1.

#### 4.5.2.2 Response for point contact at $\gamma_0 = 12 \mu\text{m}$ , $W = 6 \text{ N}$ and $F_u = 0$

The overall response plot of a rolling element bearing for point contact with radial internal clearance of  $12 \mu\text{m}$  and radial load of 6N is shown in Fig. 4.20. The overall response plot has a low rough appearance. Two regions can be identified which have high pp response. Two regions are shown in Fig. 4.20 bounded by lines A-A' and B-B'.

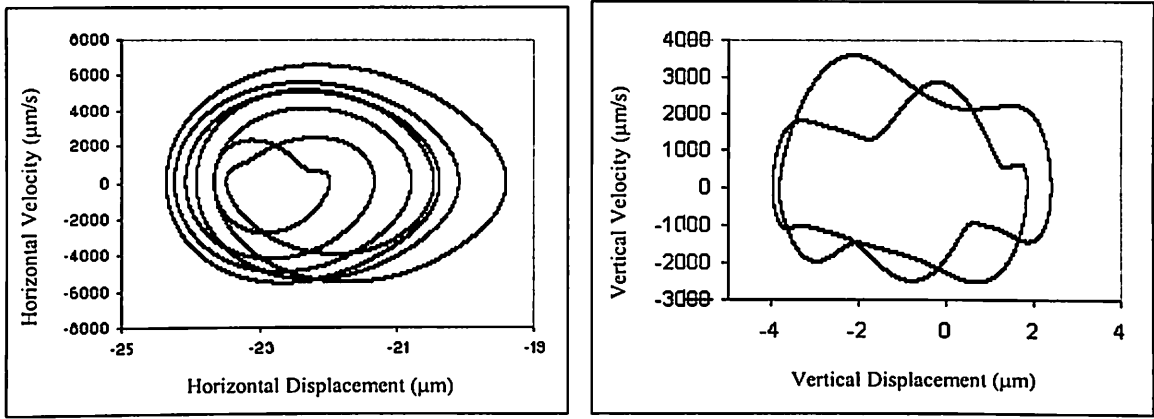
From Fig. 4.6 (a) of stiffness estimation in vertical and horizontal directions, it is seen that for radial internal clearance ( $\gamma_0$ ) of  $12 \mu\text{m}$  and  $20 \mu\text{m}$ , the stiffness value practically remains same. On analyzing the response plot for peak-to-peak amplitude against speed for the cases of radial internal clearance ( $\gamma_0$ ) of  $12 \mu\text{m}$  and  $20 \mu\text{m}$  (Fig. 4.8 and Fig. 4.20), it is observed that the peak (shown by P' in the Fig. 4.8) develops at a lower speed at higher radial clearance. For  $12 \mu\text{m}$  radial clearance (in Fig. 4.20), the peak (P') is at 9000 rpm and for  $20 \mu\text{m}$  radial clearance, it occurs at 7150 rpm. This shift in peak indicates an increase in the value of stiffness as clearance decreases. On comparing Fig. 4.8 with Fig. 4.20, it can be seen that the period-one unstable regions shift towards lower speed as clearance is increased.



Poincaré Maps

**Fig. 4.18** Response at 8900 rpm for  $\gamma_0 = 20\mu\text{m}$ ,  $W = 6\text{ N}$





Poincaré Map

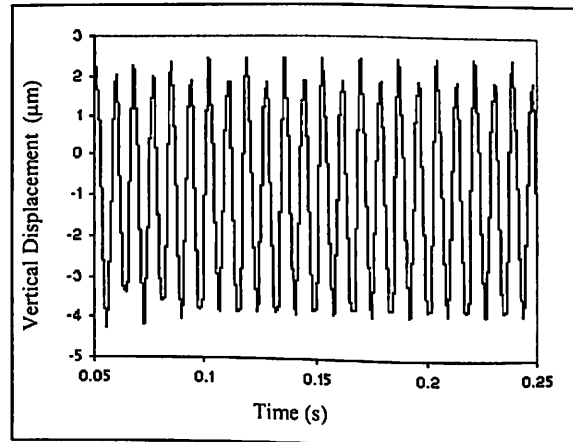
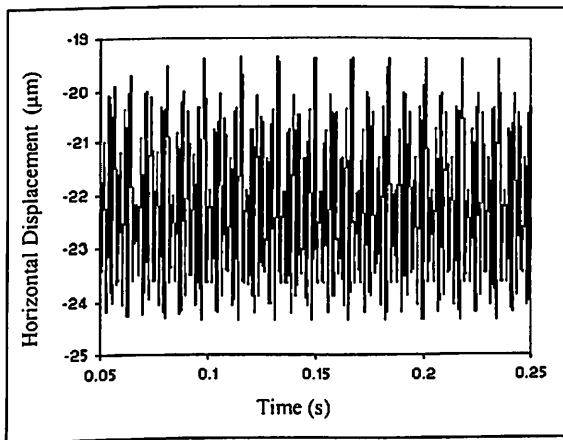
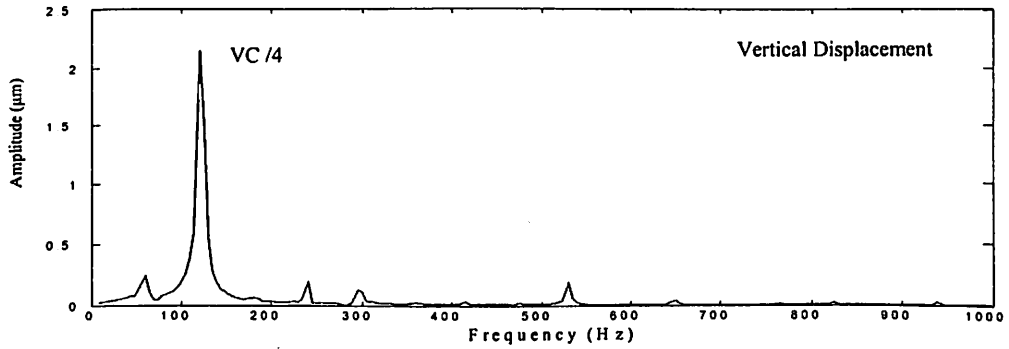
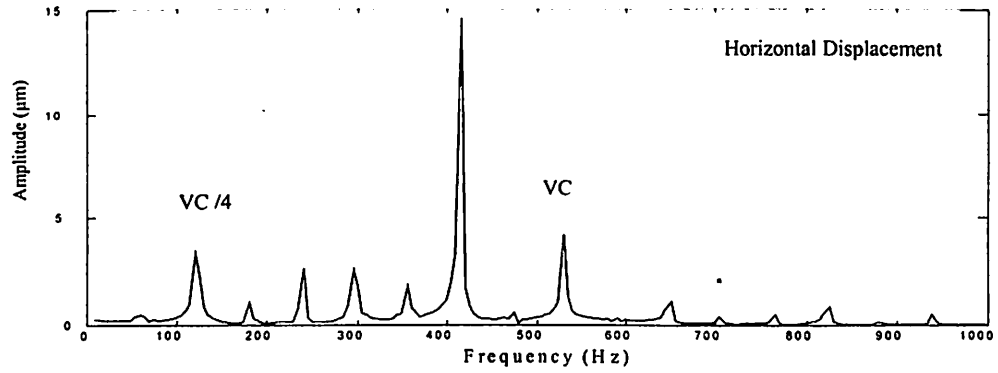


Fig. 4.19 Response at 9900 rpm for  $\gamma_0 = 20\mu\text{m}$ ,  $W = 6\text{ N}$

**Table 4.1** Nature of solutions for  $\gamma_0 = 20\mu\text{m}$ ,  $W = 6 \text{ N}$ 

<b>Speed (RPM)</b>	<b>Nature of Response</b>
Upto 915	1T stable low amplitude
955 – 1800	Period-one unstable (at VC and harmonics)
1920 – 2640	Chaotic
2700	4T
2900 – 5940	2T
5955 – 6985	1T
7195 – 7560	Chaotic
7600	8T
7715 – 8400	5T
8460 – 9100	Hopf (Quasi-periodic)
9900	4T
10895	1T

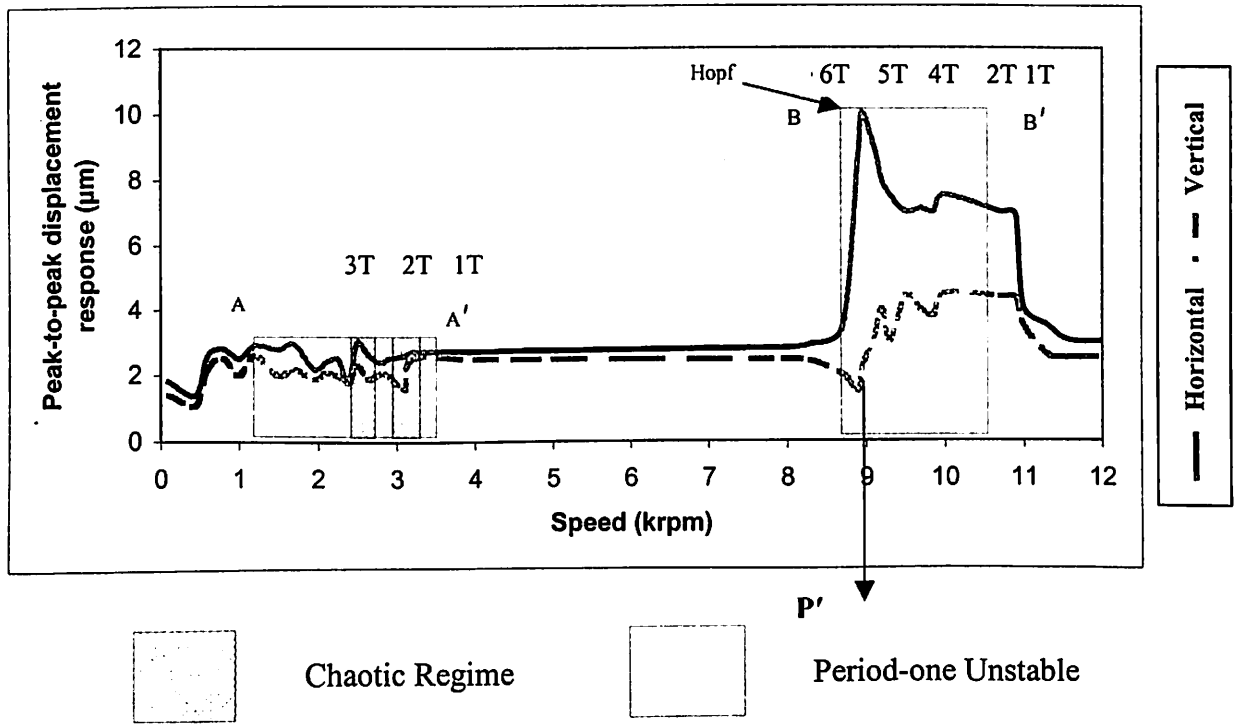


Fig. 4.20 Response plot for  $\gamma_0 = 12\mu\text{m}$ ,  $W = 6\text{ N}$

Two regions of period-one unstable response are shown in Fig. 4.20. Period-one solution becomes unstable from 1245 to 3580 rpm, because of period doubling bifurcations. The solution undergoes pitchfork bifurcations till 2400 rpm after which at 2470 rpm the chaotic solution is obtained. Figure 4.21 shows the nature of solution at 2400 rpm. The VC and its harmonics (super-harmonic) character of the frequency spectra is also brought-out by the Poincarè map with the closed orbit. The first chaotic region is observed in speed range 2470-2730 rpm. The chaotic solution at 2500 rpm is shown in Fig. 4.22. The frequency spectrum has a band structure as seen in-between spikes of VC and its multiples. The fine-layered structure of the strange attractor is also clear from the Poincarè map. From 2755 to 2820 rpm, the period-one solution is again unstable. Fig. 4.23 shows the 3<sup>rd</sup> subharmonic nature of solution at 2800 rpm.

As speed increases, the second chaotic region appears between 2880 to 3425 rpm, the loss of stability is seen to be by the eigen values crossing +1. In this region, the period doubling bifurcations give way to chaos at about 2880 rpm and this region extends up to 3425 rpm. The chaotic solutions at 2900 rpm and at 3100 rpm are shown in Figs. 4.24 and 4.25 respectively. The chaotic attractor is spread out and the band of frequency in the spectrum formed is also quite prominent. As speed increases, the period-one solution becomes unstable in the speed range from 3580 to 8925 rpm as shown in Fig. 4.20. Also the peak-to-peak response goes down (Fig. 4.20), which is an indication of the end of multi-valued region of response. The response in Fig. 4.26 at 8900 rpm shows 1T stable behavior.

At the end of 8950 rpm a Hopf bifurcation occurs and again the peak-to-peak response goes up. At 8950 rpm (Fig. 4.27), the response is mode locked with the ratio between the varying compliance frequency (477 Hz) and the newly generated frequency (79.5) becomes 6 (i.e.  $p = 6$ ). It is seen that the frequency generated due to Hopf bifurcation changes with speed. As speed increases, the value of  $p$  decreases acquiring values 5 and 4 at 9200 rpm (Fig. 4.28) and 10,000 rpm (Fig. 4.29) respectively. From Figures 4.28 to 4.30, the quasi-periodic nature of response can be seen from the frequency spectrum and the phase plots.

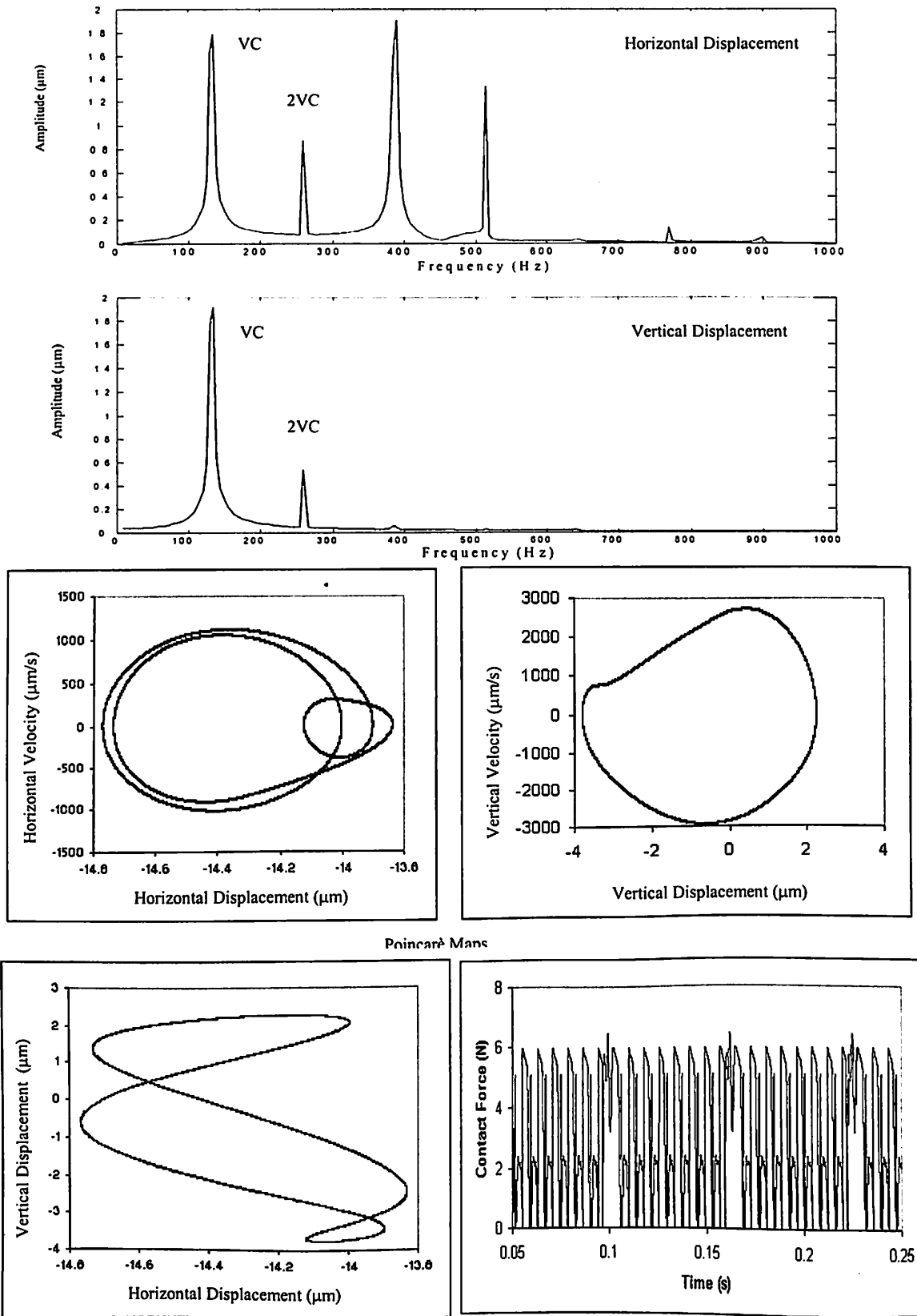


Fig. 4.21 Response at 2400 rpm for  $\gamma_0 = 12\mu\text{m}$ ,  $W = 6\text{ N}$

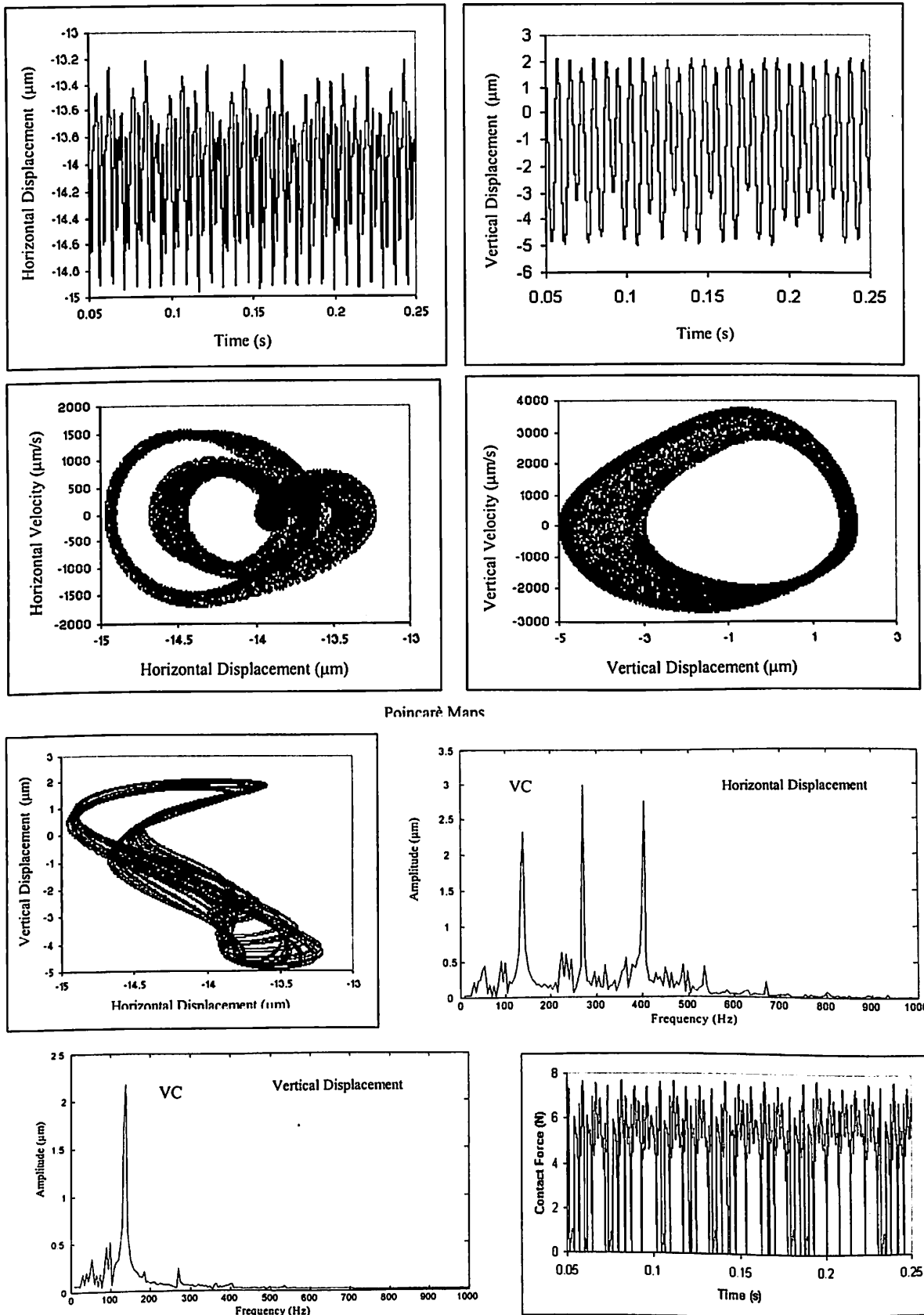


Fig. 4.22 Response at 2500 rpm for  $\gamma_0 = 12\mu\text{m}$ ,  $W = 6\text{ N}$

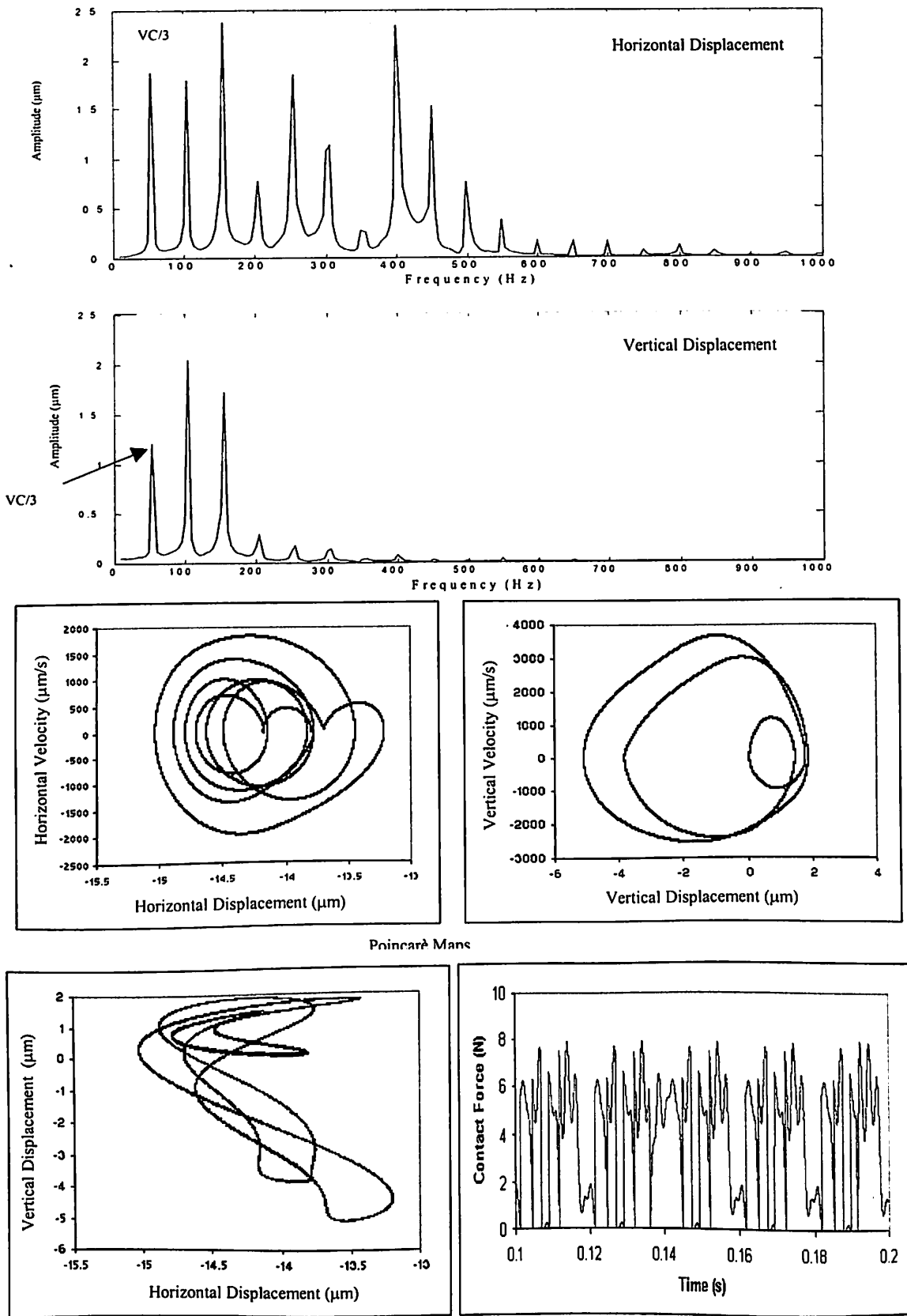
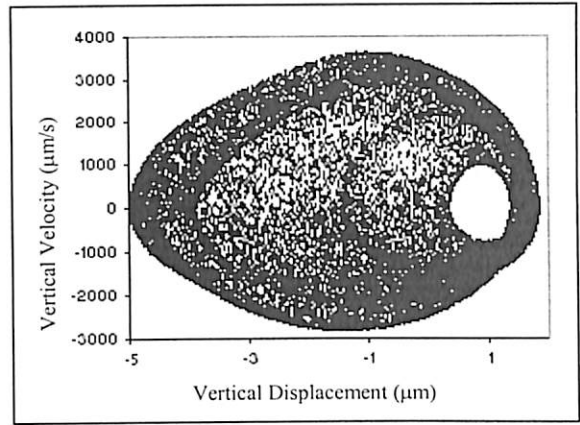
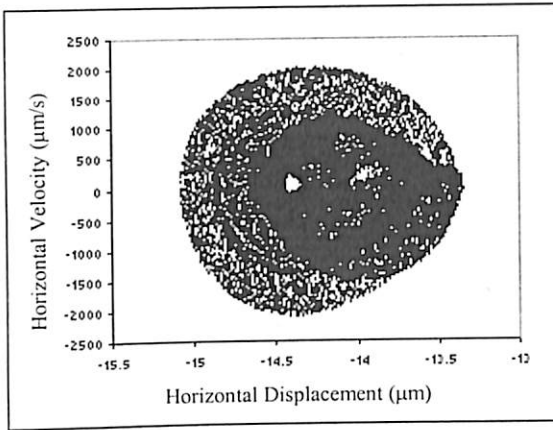


Fig. 4.23 Response at 2800 rpm for  $\gamma_0 = 12\mu\text{m}$ ,  $W = 6\text{ N}$



Poincaré Maps

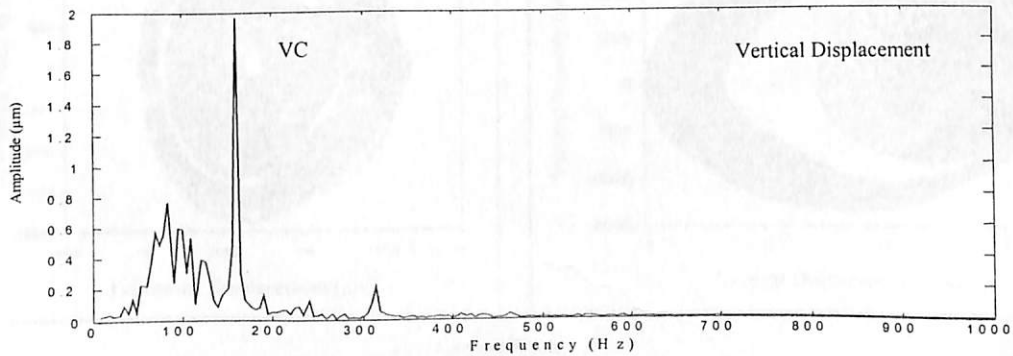
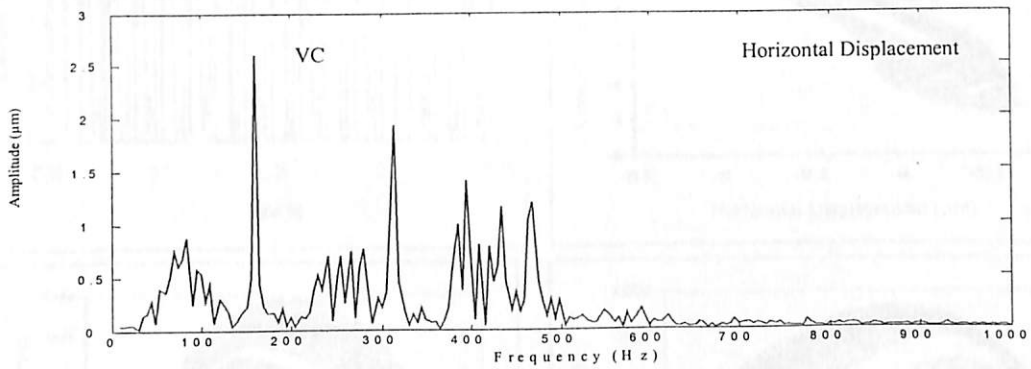
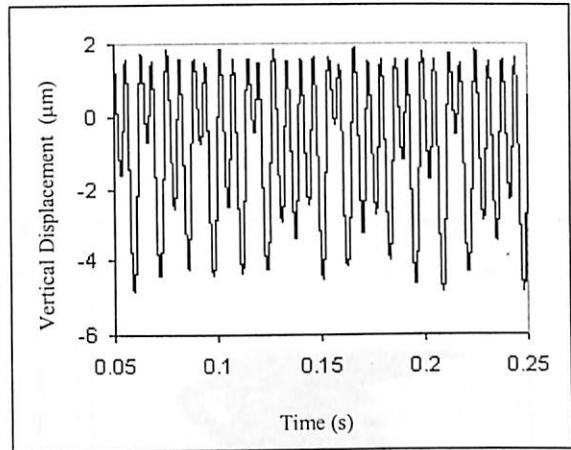
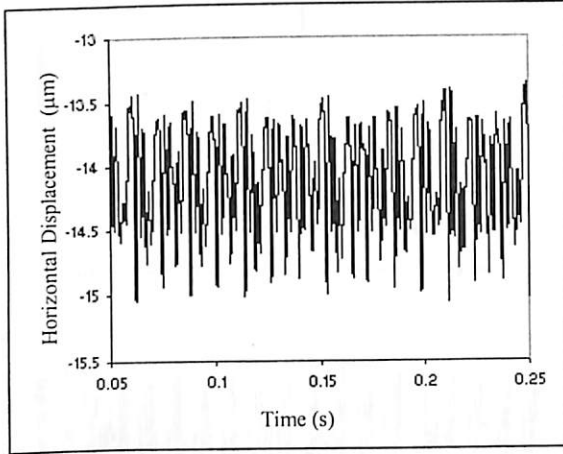
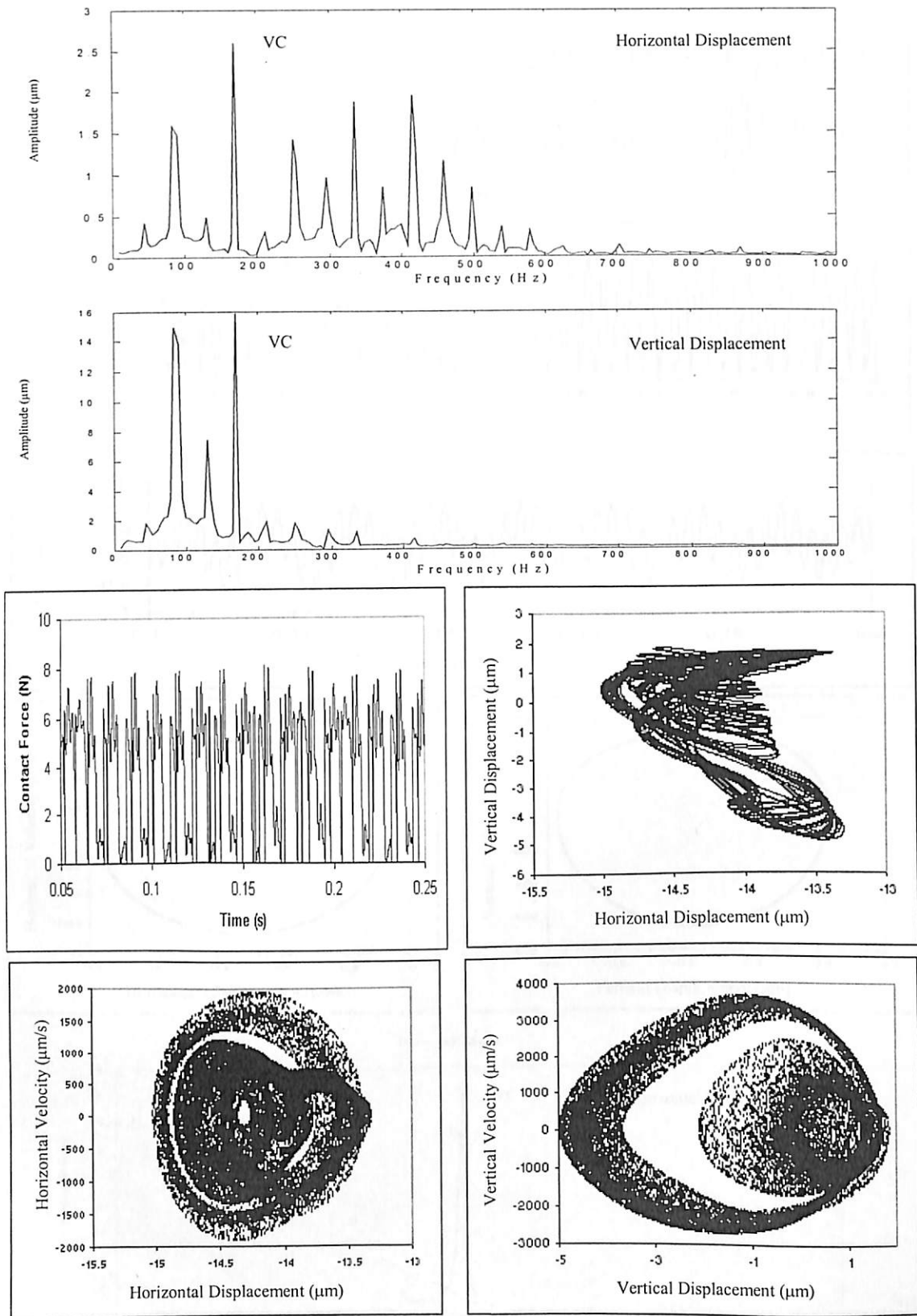


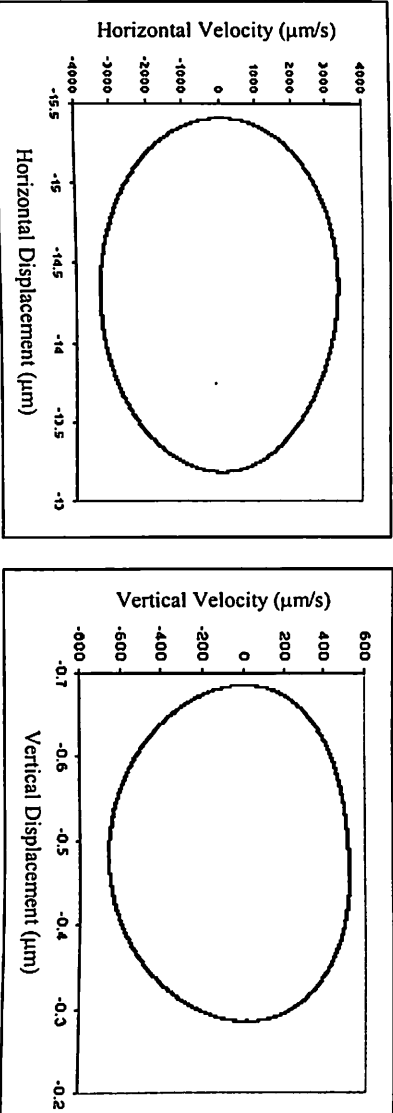
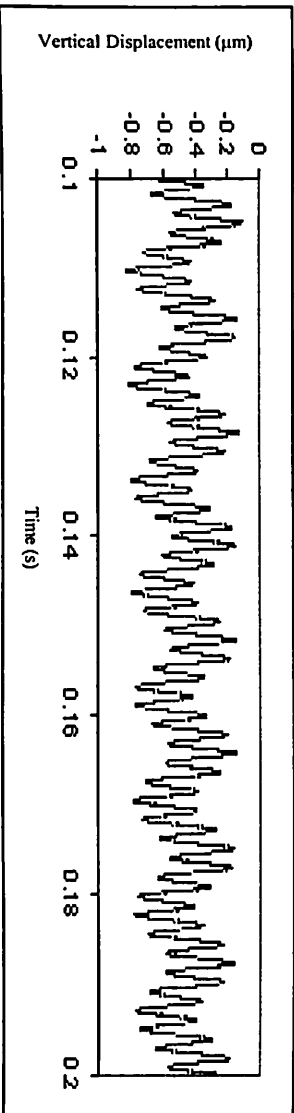
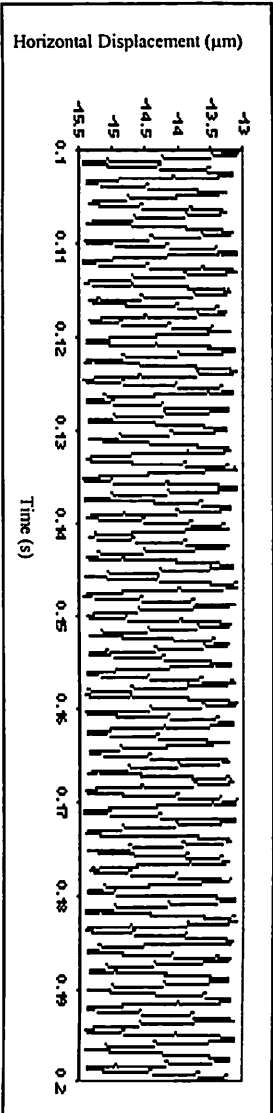
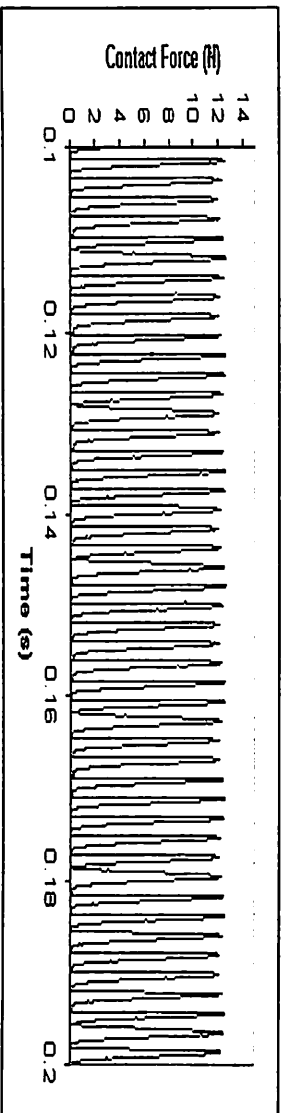
Fig. 4.24 Response at 2900 rpm for  $\gamma_0 = 12\mu\text{m}$ ,  $W = 6\text{ N}$





Poincaré Maps

Fig. 4.25 Response at 3100 rpm for  $\gamma_0 = 12\mu\text{m}$ ,  $W = 6\text{ N}$



Poincaré Maps

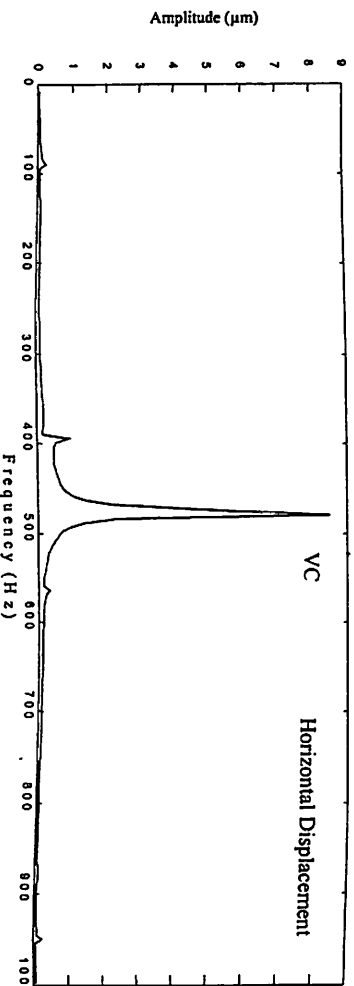


Fig. 4.26 Response at 8900 rpm for  $y_0 = 12\mu\text{m}$ ,  $W = 6\text{ N}$

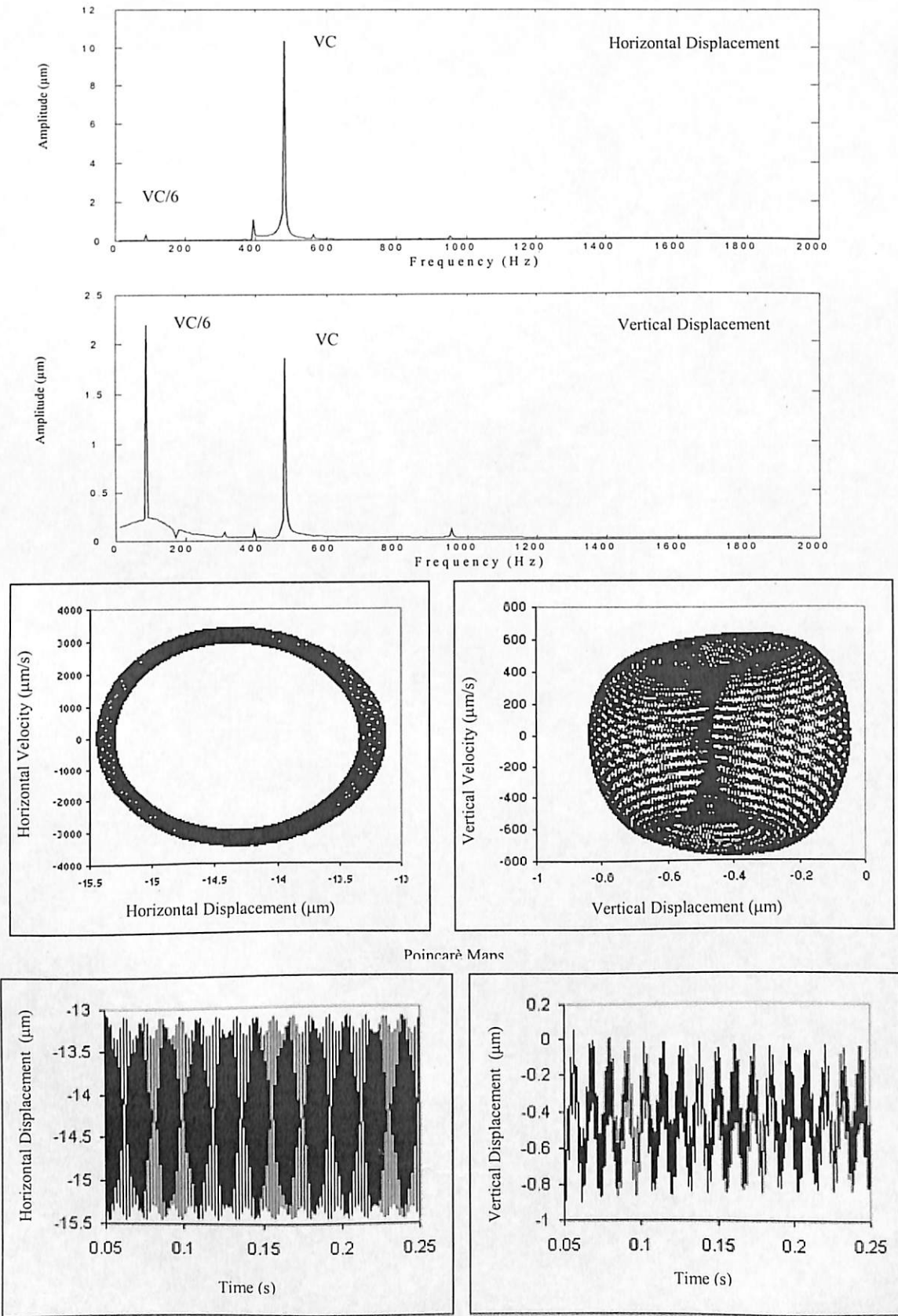


Fig. 4.27 Response at 8950 rpm for  $\gamma_0 = 12\mu\text{m}$ ,  $W = 6\text{ N}$

The structure of orbit plots from Figs. 4.28 to 4.30 shows relatively short time period at 9200 rpm, which goes up at 10,000 rpm and again goes down at 10900 rpm. This region of bifurcation extends upto 10925 rpm. No chaos is found in this region because of lower radial clearance (12  $\mu\text{m}$ ). The torus solution becomes 1T stable solution at 10950 rpm (Fig. 4.31). The nature of response for various speeds is given in Table 4.2.

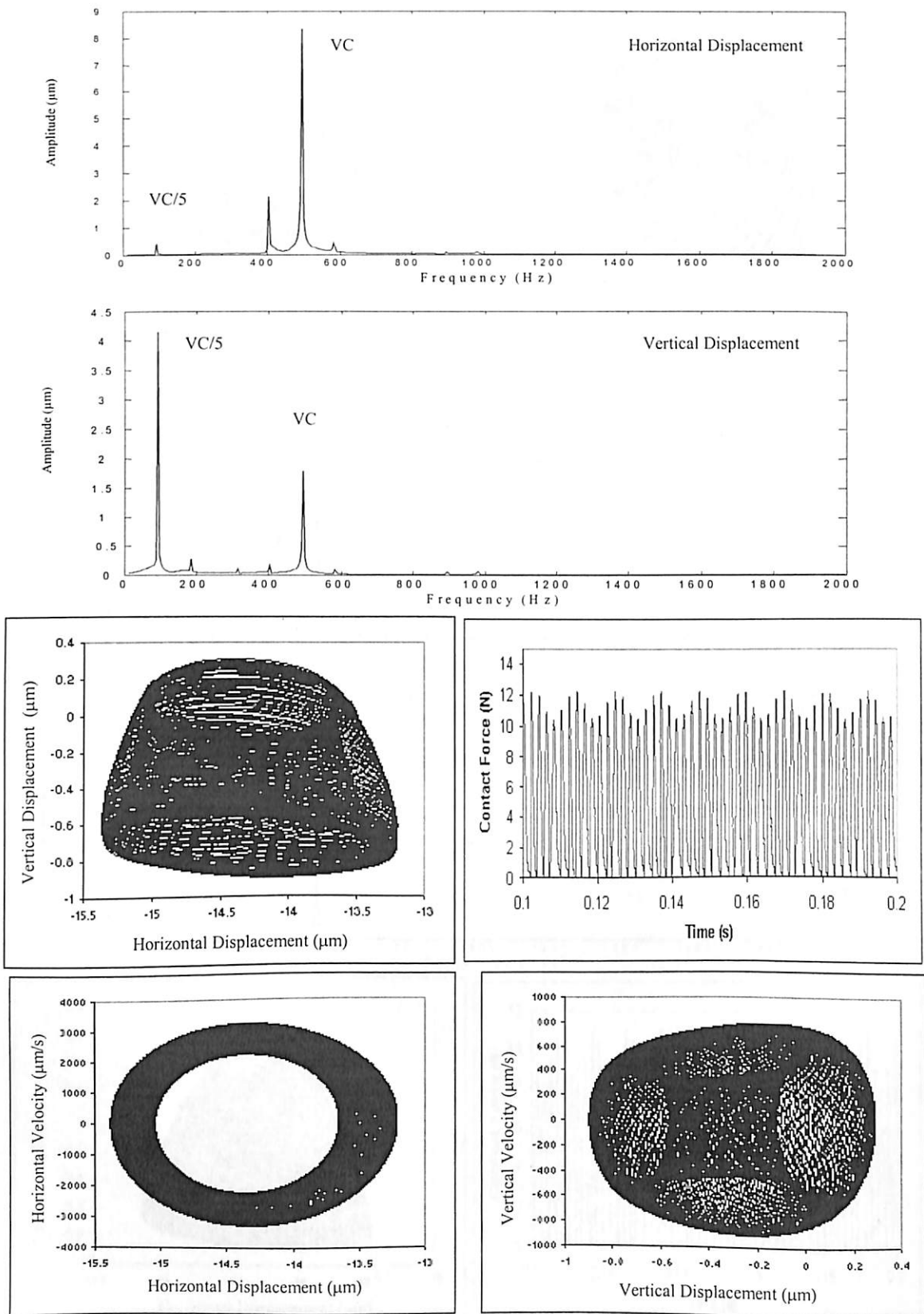
#### 4.5.2.3 Response for point contact at $\gamma_0 = 20 \mu\text{m}$ , $W = 6 \text{ N}$ and $F_u = 15\%W$

A rolling element bearing with *point contact* supporting a rigid horizontal rotor with an unbalanced force ( $F_u$ ) is taken for theoretical simulation as shown in Fig. 4.32.

Speed response plots have been generated for combination of radial internal clearance and unbalanced force. The frequency components corresponding to  $\frac{1}{2} X$ ,  $X$  (rotational frequency),  $2X$ ,  $3X$ ,  $4X$  have also been filtered from the overall response plot and plotted against speed. Even the most precise rotor balancing exercises are not able to eliminate the unbalance in rotors. Therefore, any study of rotors supported on rolling element bearing without consideration of unbalance force is rather incomplete and unrealistic. To simplify the study, constant unbalanced force is assumed in the entire speed range. The unbalance force and radial internal clearance value have been taken as 15% of  $W$  and  $20\mu\text{m}$  respectively.

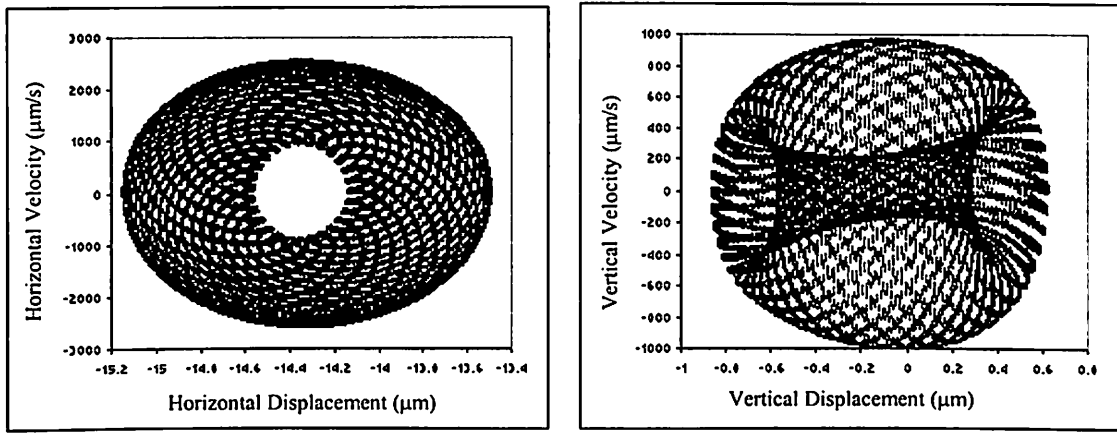
The overall response plot of rolling element bearing for point contact with radial internal clearance of  $20 \mu\text{m}$ , unbalanced force ( $F_u$ ) = 15% of  $W$  and radial load ( $W$ ) of  $6\text{N}$  is shown in Fig. 4.33. The overall response plot has a highly rough appearance. Two regions are shown in Fig. 4.33 bounded by lines A-A' and B-B'.

From Fig. 4.33, it is observed that the value of vertical displacement is less than the value of horizontal displacement in entire speed range. The response plot (Fig. 4.33) is a combination of responses that are due to varying compliance and other peaks as a result of unbalanced force. The high amplitude region starting from 525 rpm has stable periodic orbit unlike the balanced case (Fig. 4.8).



Poincaré Maps

**Fig. 4.28** Response at 9200 rpm for  $\gamma_0 = 12\mu\text{m}$ ,  $W = 6\text{ N}$



Poincaré Maps

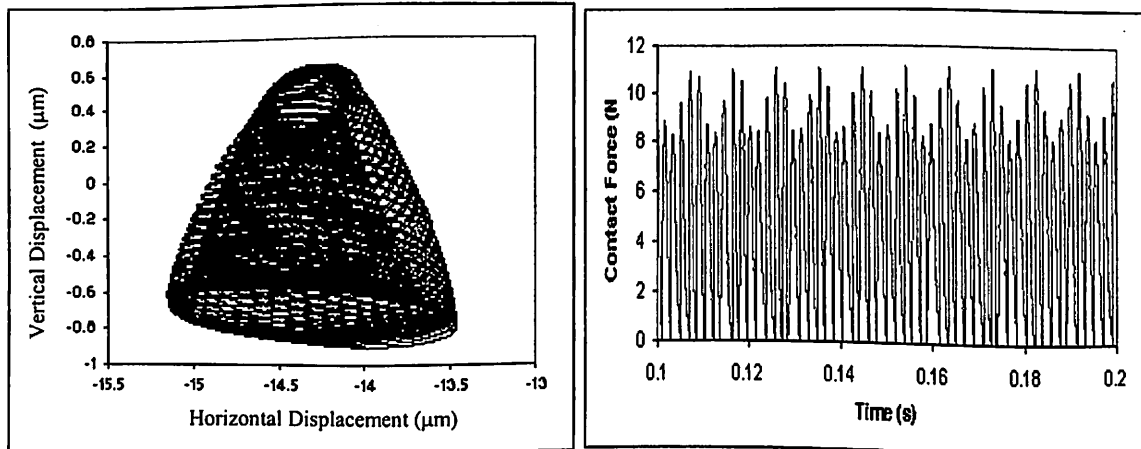
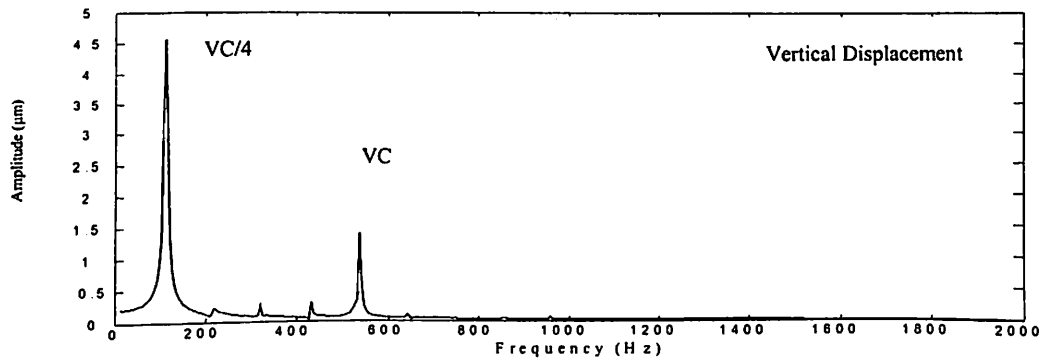
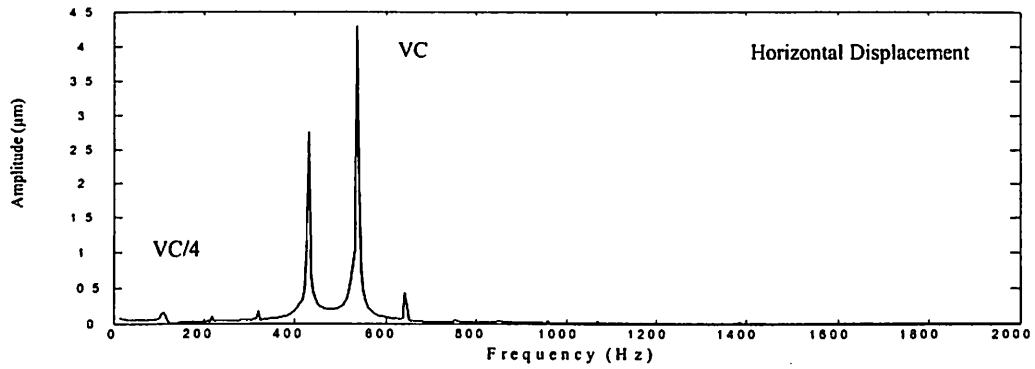
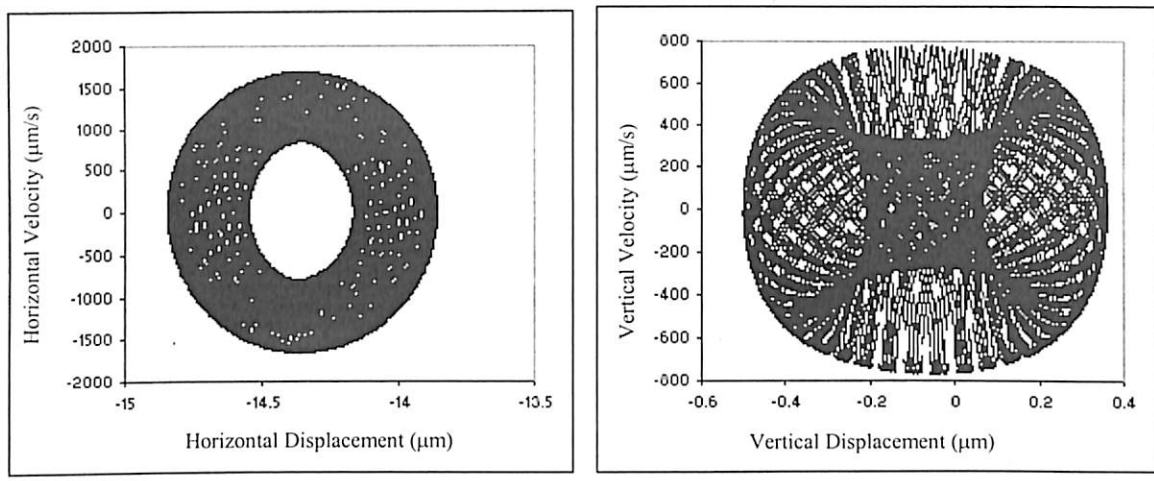


Fig. 4.29 Response at 10000 rpm for  $\gamma_0 = 12\mu\text{m}$ ,  $W = 6\text{ N}$



Poincaré Maps

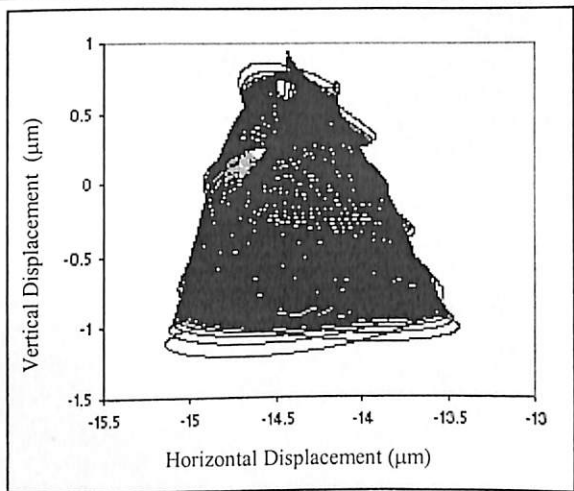
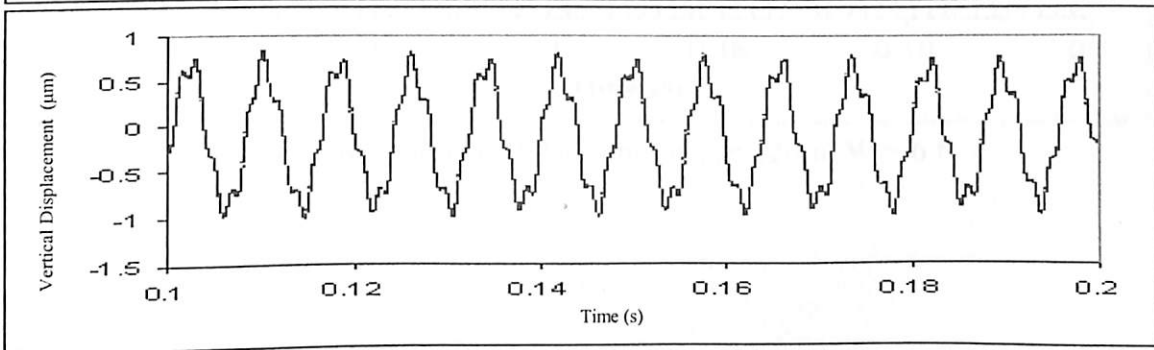
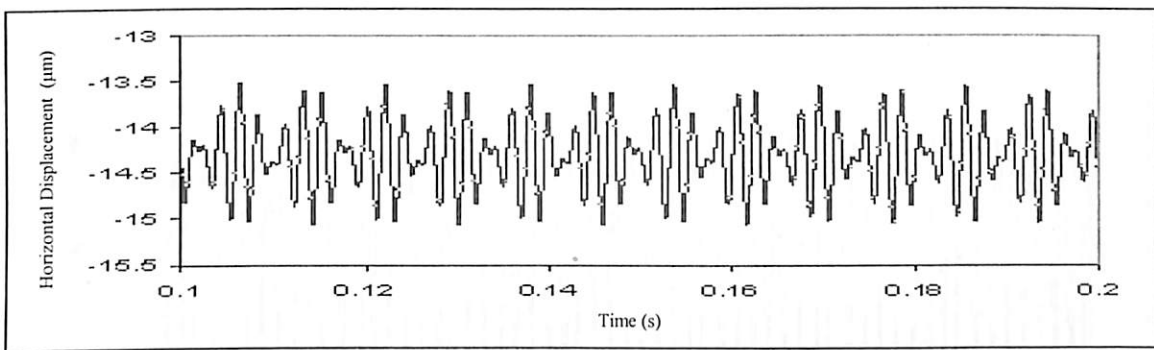
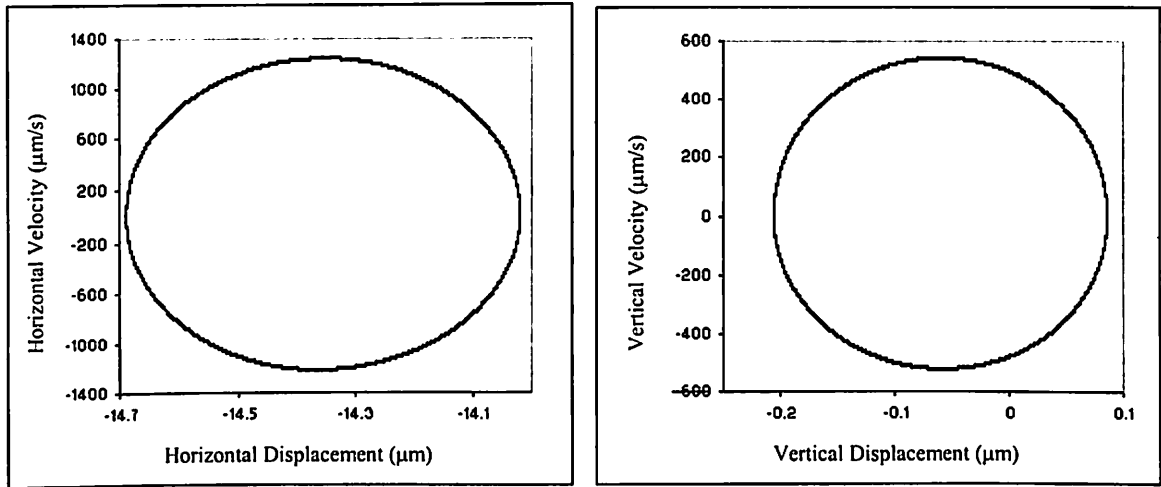


Fig. 4.30 Response at 10900 rpm for  $\gamma_0 = 12\mu\text{m}$ ,  $W = 6 \text{ N}$



Poincaré Maps

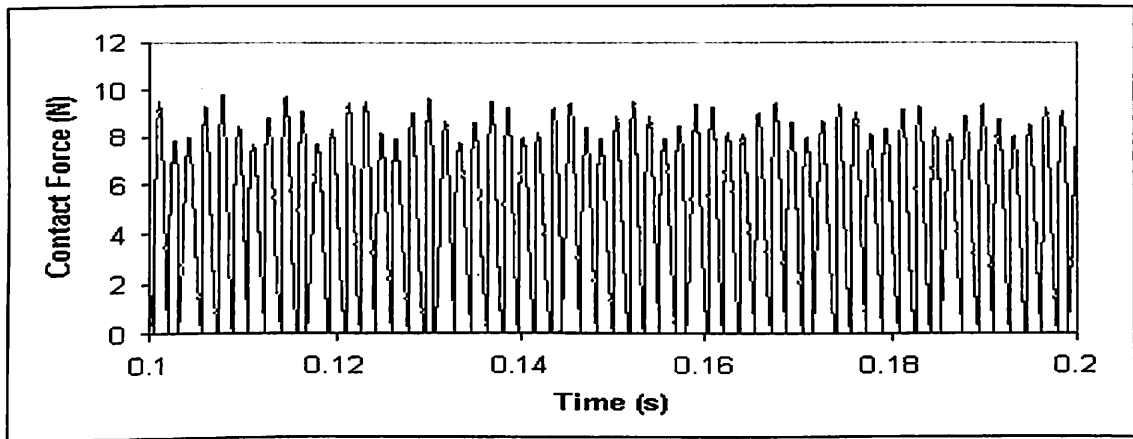


Fig. 4.31 Response at 10950 rpm for  $\gamma_0 = 12\mu\text{m}$ ,  $W = 6\text{ N}$



**Table 4.2** Nature of solutions for  $\gamma_0 = 12\mu\text{m}$ ,  $W = 6 \text{ N}$ 

Speed (RPM)	Nature of Response
upto 1215	1T stable low amplitude
1245 – 2400	Period-one unstable (at VC and harmonics)
2470 – 2730	Chaotic
2755 - 2820	3T
2880 – 3425	Chaotic
3450 - 3575	2T
3580 - 8925	1T
8950	Hopf (VC=477.3 Hz, FH=79.5 Hz)
9200	Hopf (VC=490.6 Hz, FH=98.2 Hz)
10000	Hopf (VC=533.3 Hz, FH=133.3 Hz)
10900	Hopf (VC=581.3 Hz, FH=290.6 Hz)
10950 and onwards	1T

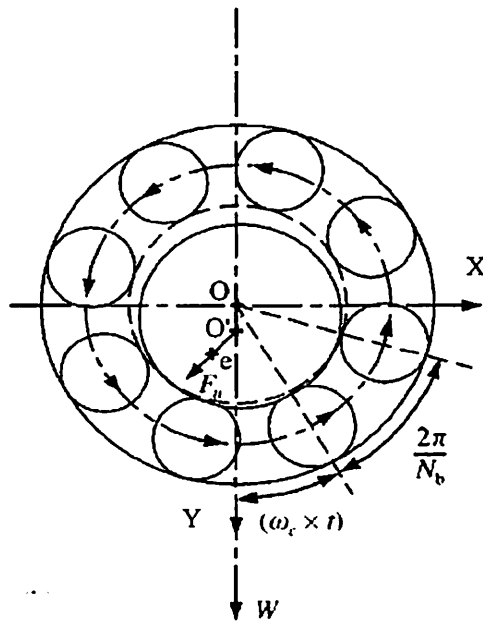


Fig. 4.32 Unbalance force ( $F_u$ ) acting on rolling element bearing

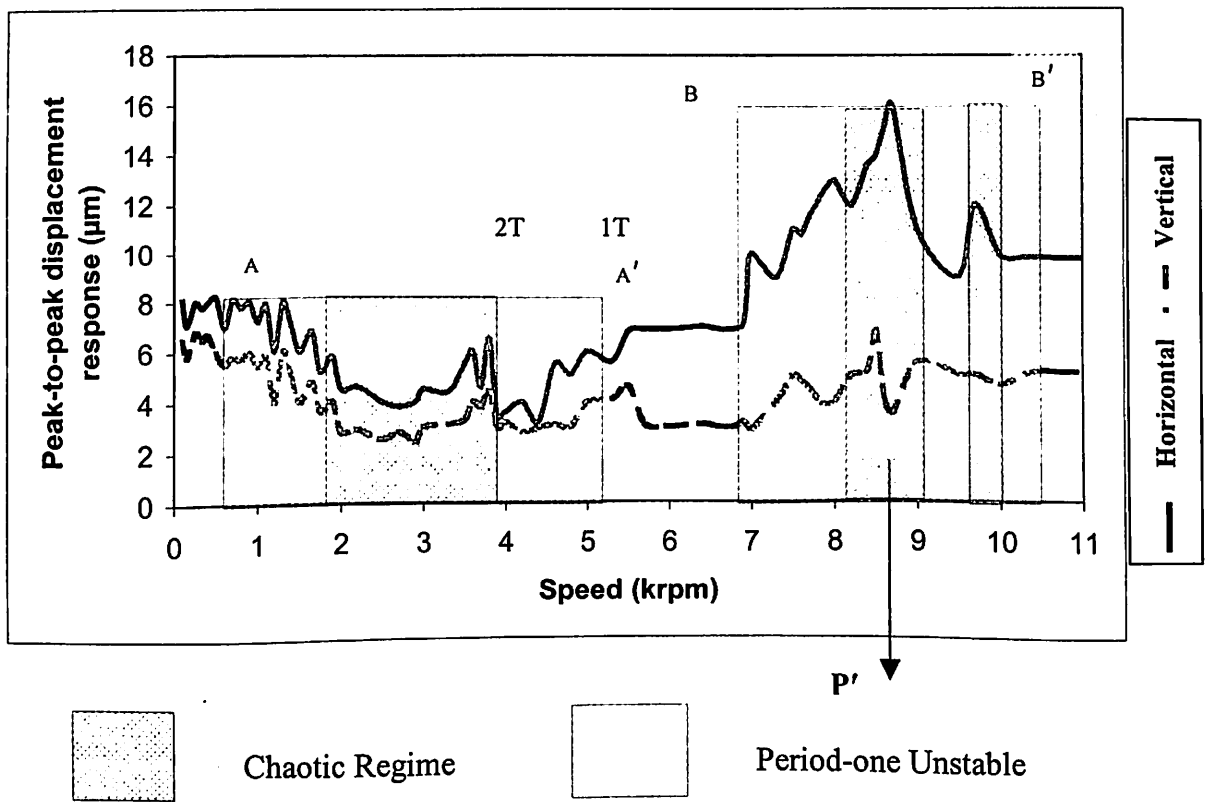
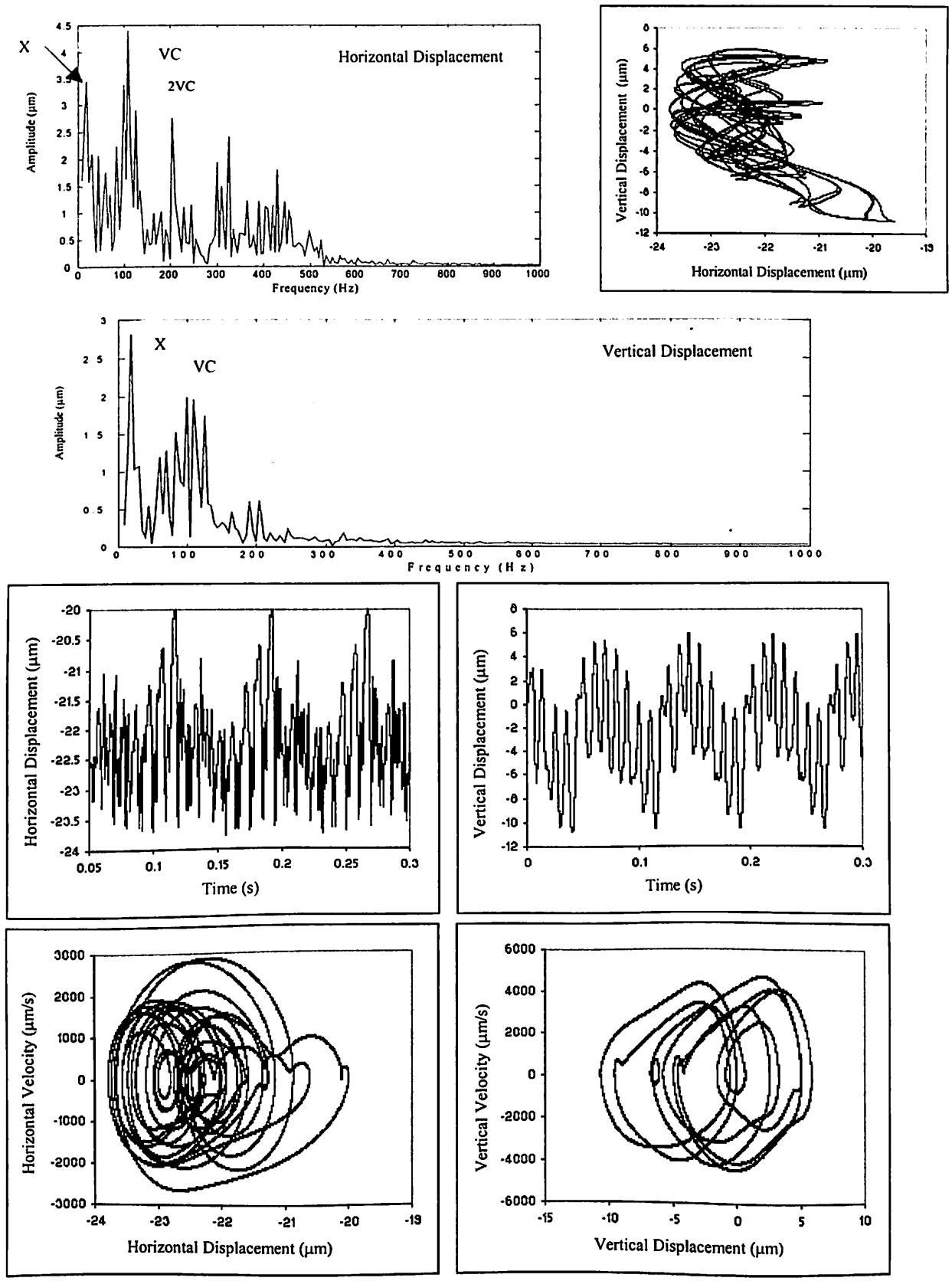


Fig. 4.33 Response plot for  $\gamma_0 = 20 \mu\text{m}$ ,  $W = 6 \text{ N}$  and  $F_u = 15\%W$

Period-one solution becomes unstable from 740 to 5300 rpm because of period doubling bifurcations. The solution undergoes pitchfork bifurcations till 1900 rpm after which chaotic solution is obtained at 1970 rpm. At this speed chaos just begins to develop. Figure 4.34 shows the nature of solution at 2000 rpm. The dense band of frequency spectrum shows the presence of both the rotational frequency ( $X$ ) and the varying compliance ( $VC$ ) frequency. The presence of dense regions in the orbit is indicative of the onset of chaos. It cannot be considered perfectly periodic, since the two spectra are not exactly line spectra. The orbit is complicated because of the mixed nature of the response as shown in Fig. 4.34. For the first chaotic region occurring between 1970-3940 rpm, the loss of stability is seen to be due to the eigen values crossing  $+1$ . The chaotic solution at 3500 rpm is shown in Fig. 4.35. The frequency spectrum has a band structure as seen in-between spikes of  $VC$ ,  $X$  and their multiples. Also, both the frequency components interact to produce sum and difference combination frequencies. The fine-layered structure of the strange attractor is also clear from Poincarè maps. The orbit at this speed does not repeat itself. The Poincarè maps of chaotic solutions have fractal structures that repeat as the map is magnified. The time responses also show beat and chaos like behavior. It is clear that loss of periodicity is one characteristic of chaotic solution.

At 4000 rpm, the response shown in Fig. 4.36 can be considered neither perfectly chaotic nor perfectly periodic. It is not perfectly or predominantly chaotic because the two spectra for horizontal and vertical displacements have only a slightly banded structure in comparison to spectra at 3500 rpm (Fig. 4.35). It cannot be considered perfectly periodic, since the two are not exactly line spectra. The orbit is complicated because of the mixed nature of the response. The presence of sub-synchronous frequency of  $X/3$  (22.3 Hz) along with the weak varying compliance component in the vertical displacement spectrum and that of sub-synchronous at  $X/3$  (22.3 Hz) with strong varying compliance components in the horizontal displacement spectrum is intersecting. The system again goes into period doubling bifurcations as speed increases upto 5300 rpm. Further increase in speed, returns stability in the speed range from 5345 to 6780 rpm.



Poincaré Maps

Fig. 4.34 Response at 2000 rpm for  $\gamma_0 = 20\mu\text{m}$ ,  $W = 6\text{N}$ ,  $F_u = 15\%W$

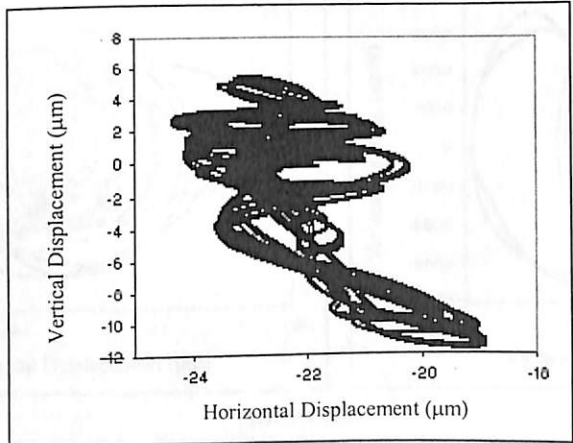
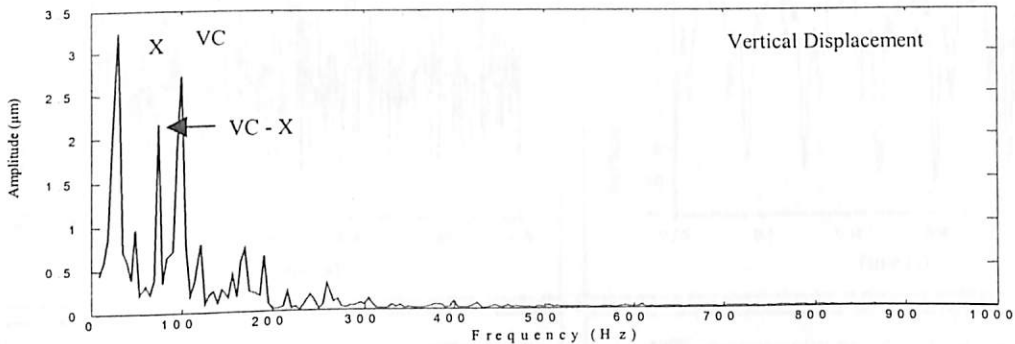
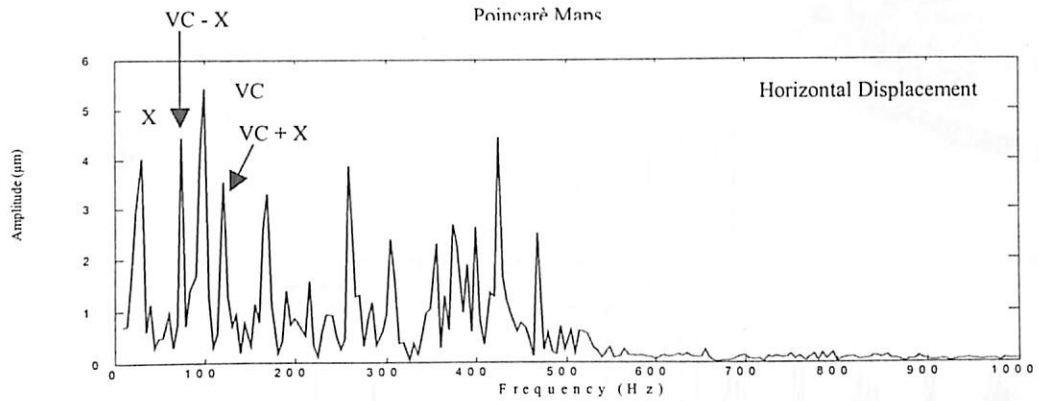
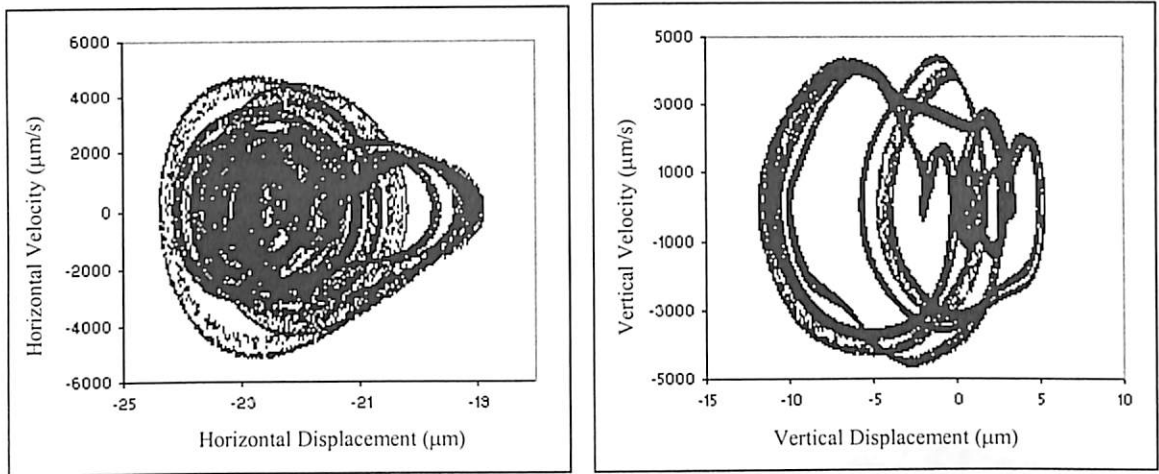
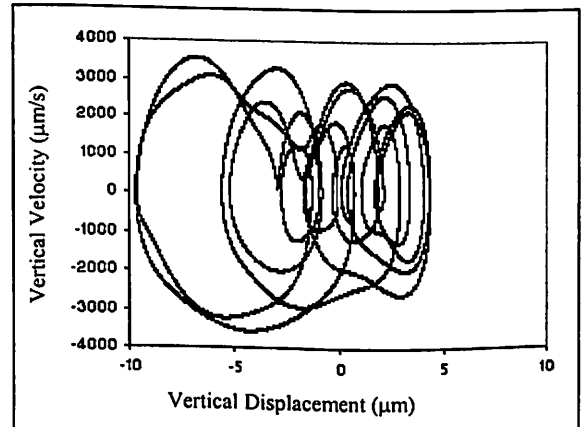
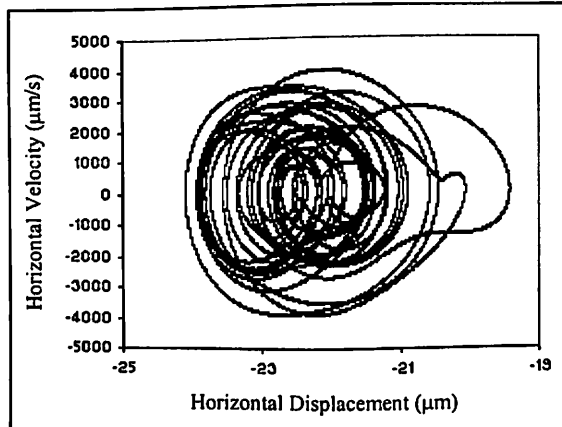
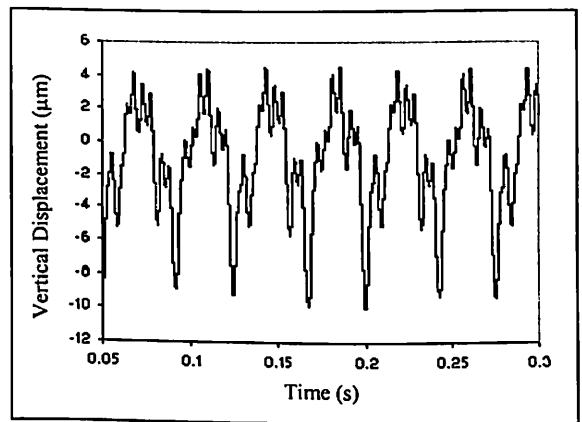
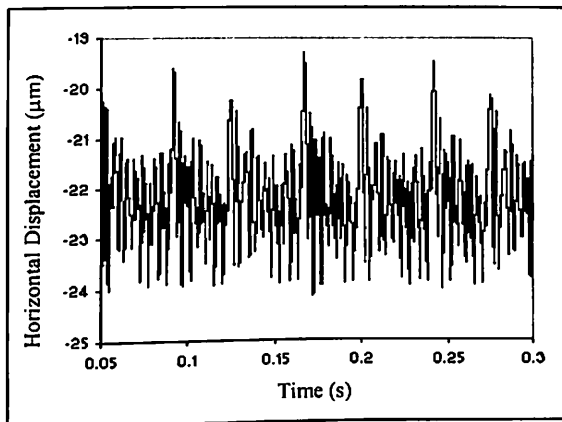
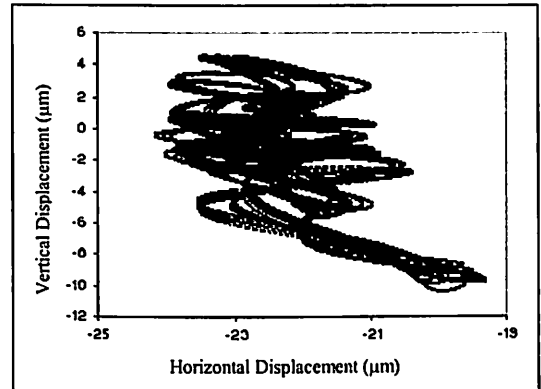
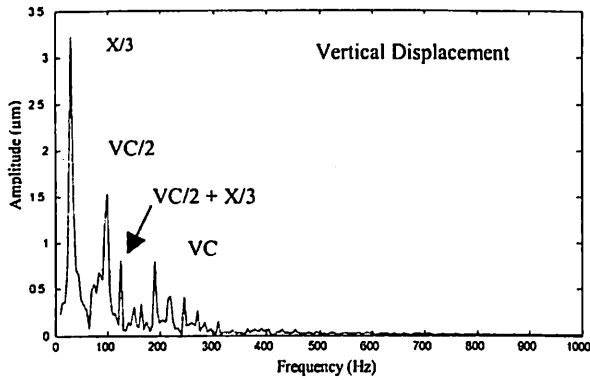
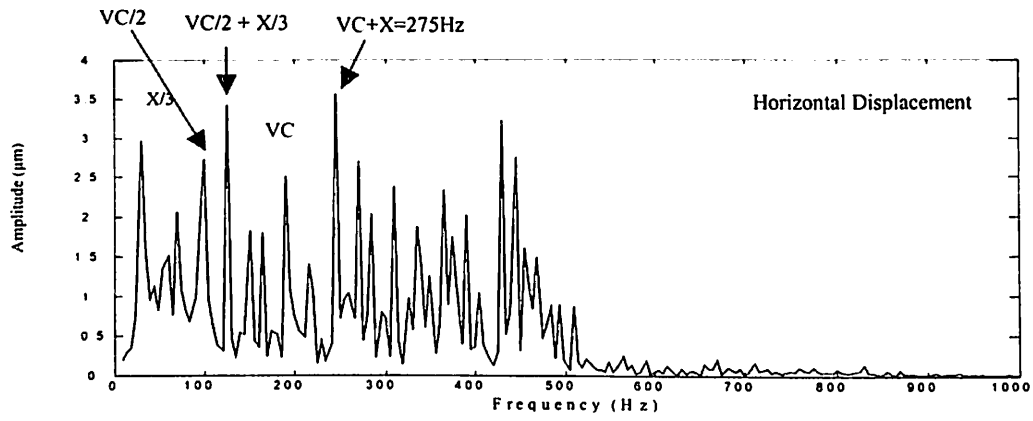


Fig. 4.35 Response at 3500 rpm for  $\gamma_0 = 20\mu\text{m}$ ,  $W = 6\text{N}$ ,  $F_u = 15\%W$



Poincaré Map

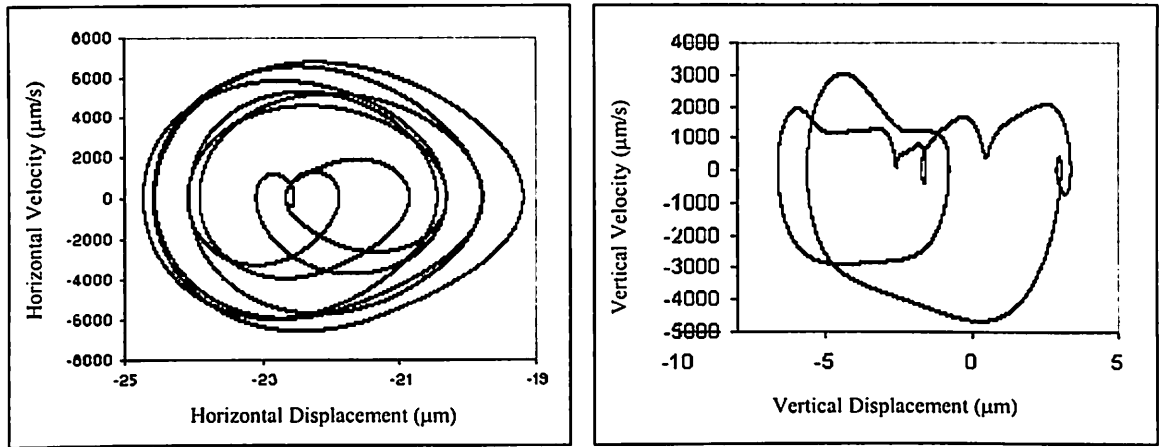
Fig. 4.36 Response at 4000 rpm for  $\gamma_0 = 20\mu\text{m}$ ,  $W = 6\text{N}$ ,  $F_u = 15\%W$

The high amplitude region of unstable period solution starts from 6890 rpm and extends upto 10200 rpm. At 7000 rpm, the response becomes periodic as shown in Fig. 4.37. The peaks appear in the frequency spectra at  $X/3$  (39 Hz),  $VC$  (374 Hz),  $VC + X/2$  (431 Hz) and at  $VC - X/2$  (314.5 Hz). The multi-loop orbit also shows periodic nature. Two regions of chaotic behavior are seen in this region. For the first chaotic region 8100 to 9050 rpm, the loss of stability is seen to be due to eigen values crossing +1. In Figures 4.38 and 4.39, the chaotic response at 8700 rpm and 9000 rpm is shown by band structure of frequency spectra. This band structure develops around  $X/2$  in the vertical displacement response and in the entire speed range for the horizontal displacement response. The fine-layered structure of the strange attractor is also clear from Poincaré maps. The presence of dense regions in the orbit is indicative of chaos.

Period-one solution becomes unstable from 9080 to 9750 rpm, because of period doubling bifurcations. As speed increases, the second chaotic region appears between 9750 to 10040 rpm, the loss of stability is seen to be due to the eigen values crossing +1. In this region, the period doubling bifurcations give way to chaos at about 9750 rpm and this region extends upto 10100 rpm. The chaotic solution at 10000 rpm is shown in Fig. 4.40. The peaks appear in frequency spectrum at  $X/2$  (81 Hz) and  $VC - 3X/4$  (396 Hz). The chaotic attractor is spread out and the band of frequency in the spectrum formed is also quite prominent. Further increase in speed, brings the system to perfect stability at 10180 rpm. The peak-to-peak response at this speed also goes down (Fig. 4.33), which is an indication of the end of multi-valued region of response. The nature of response for various speeds is given in Table 4.3.

#### 4.5.2.4 Response for line contact at $\gamma_0 = 1 \mu\text{m}$ , $W = 6 \text{ N}$ and $F_u = 0$

The overall response plot of rolling element bearing for *line* contact with radial clearance  $1 \mu\text{m}$  and radial load of 6N is shown in Fig. 4.41. The peak-to-peak vertical response is less than the peak-to-peak horizontal response in regions of high amplitude as shown in Fig. 4.41. The overall response plot has a very rough appearance. Two regions can be identified which have high pp response. These regions are shown to be bounded by lines A-A' and B-B' in Fig. 4.41.



Poincaré Maps

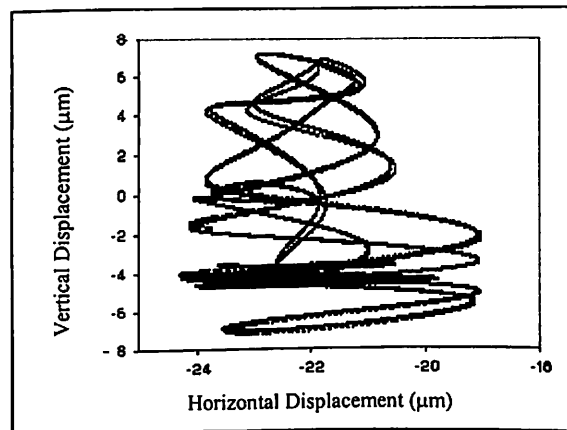
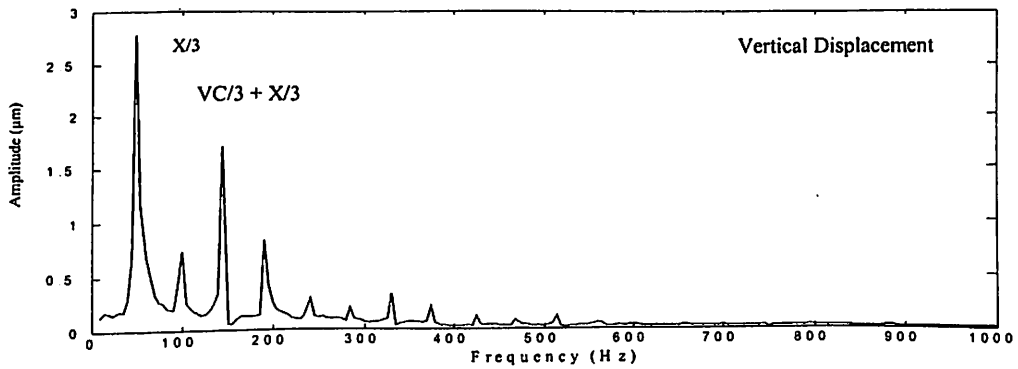
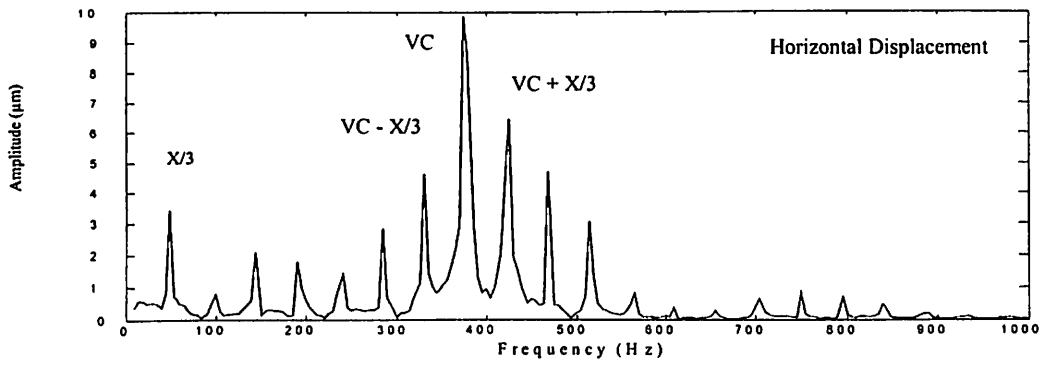
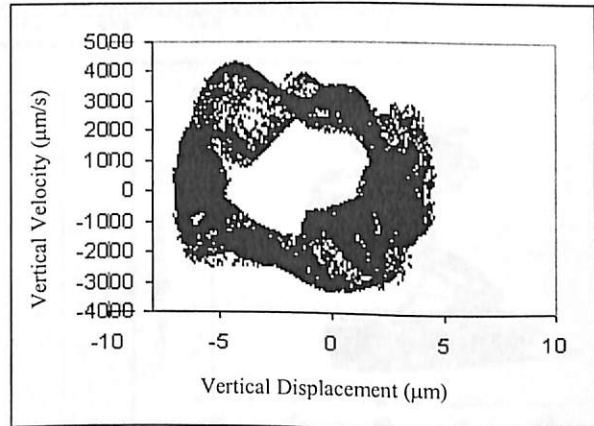
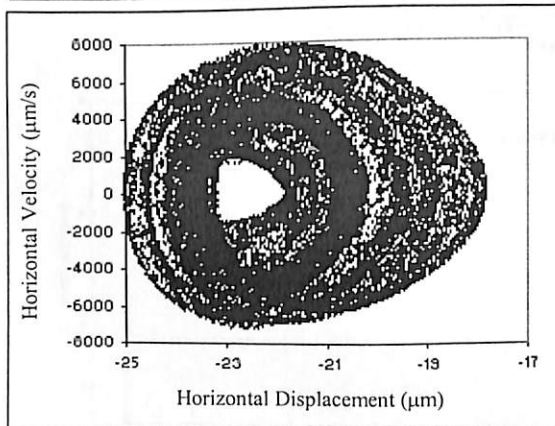
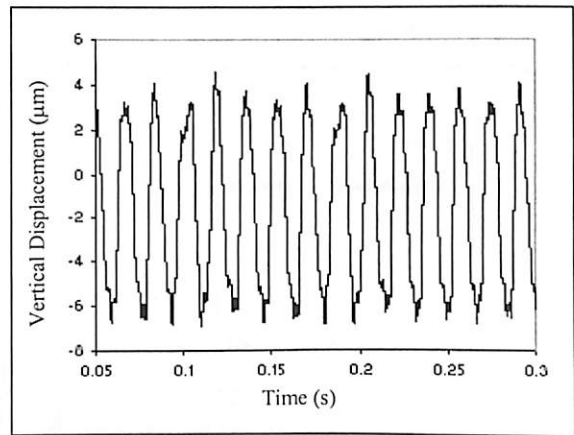
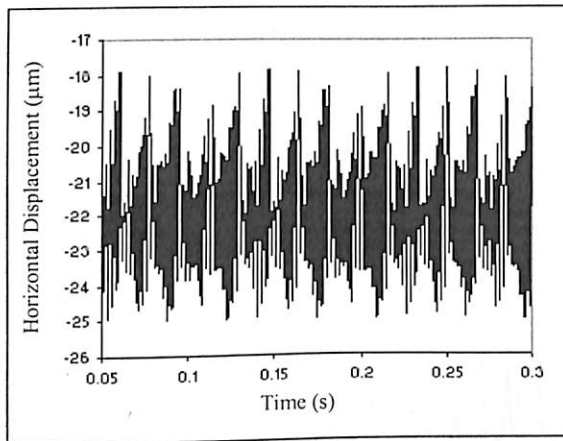
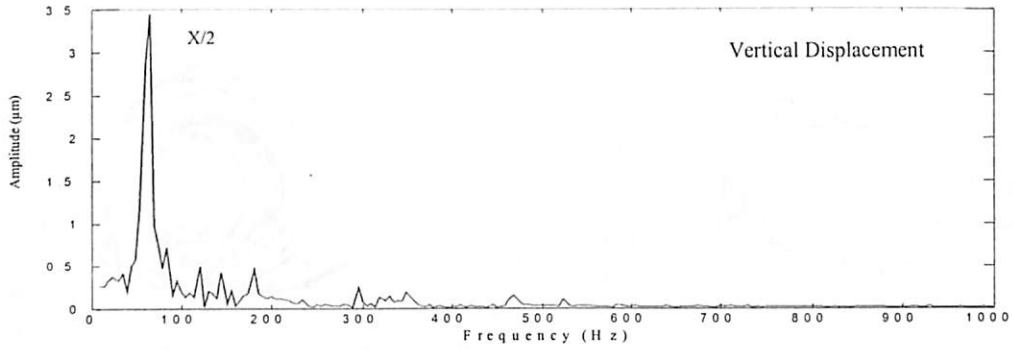
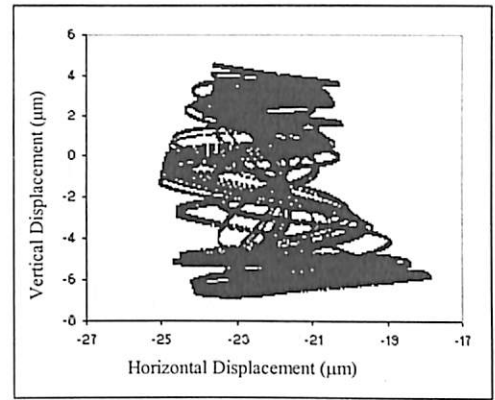
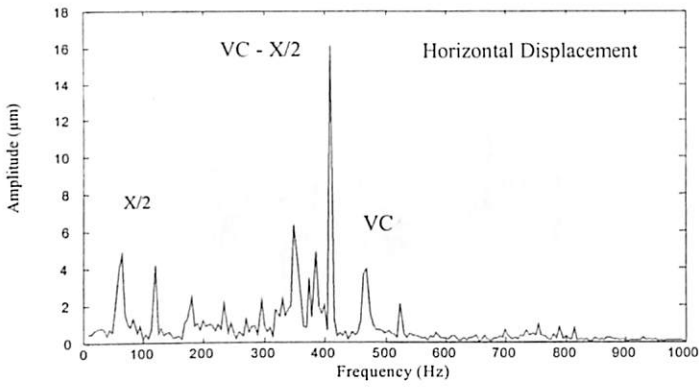


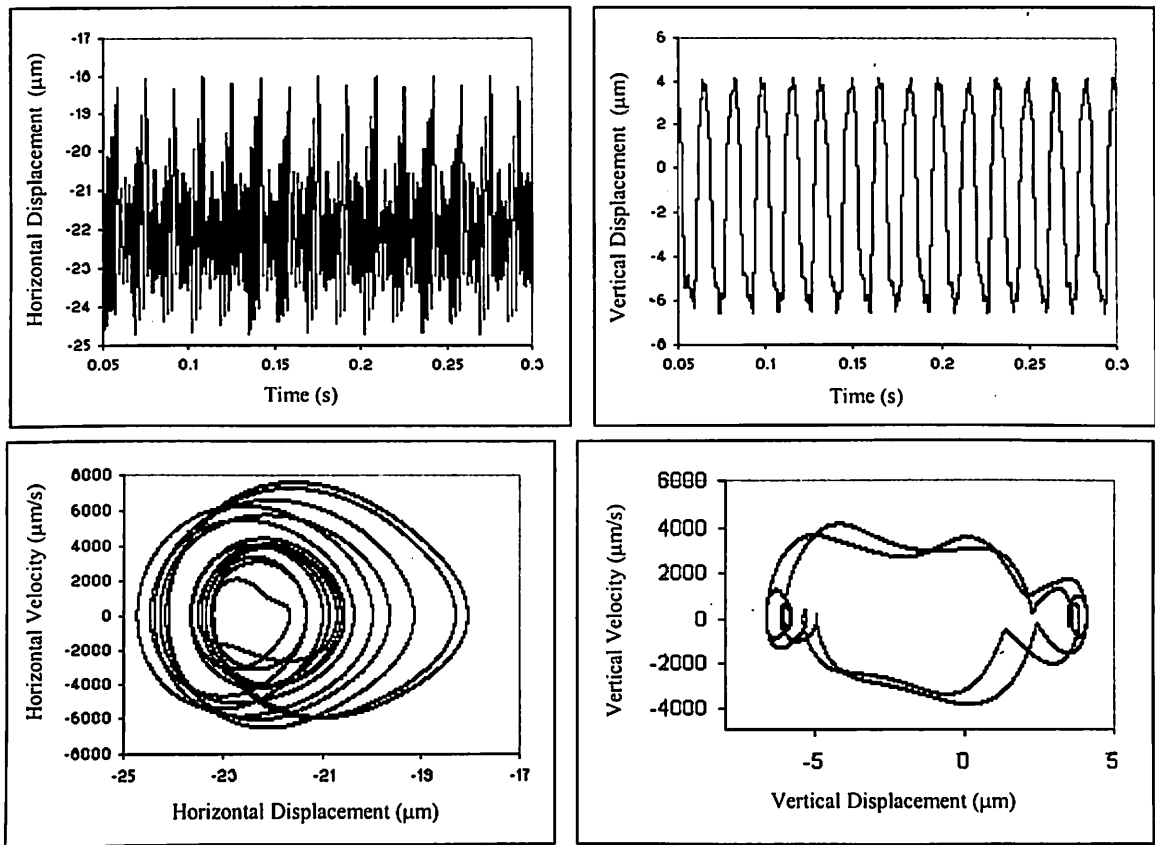
Fig. 4.37 Response at 7000 rpm for  $\gamma_0 = 20\mu\text{m}$ ,  $W = 6\text{N}$ ,  $F_u = 15\%W$





Poincaré Maps

Fig. 4.38 Response at 8700 rpm for  $\gamma_0 = 20\mu\text{m}$ ,  $W = 6\text{N}$ ,  $F_u = 15\%W$



Poincaré Map

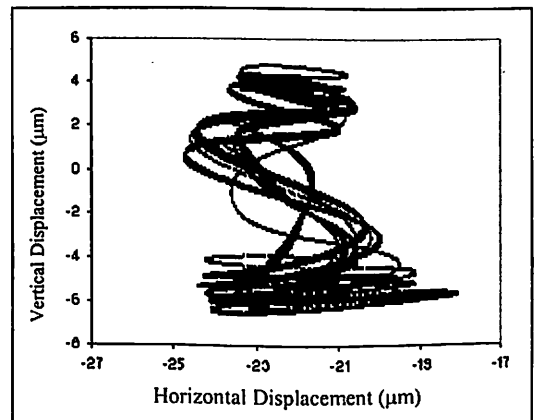
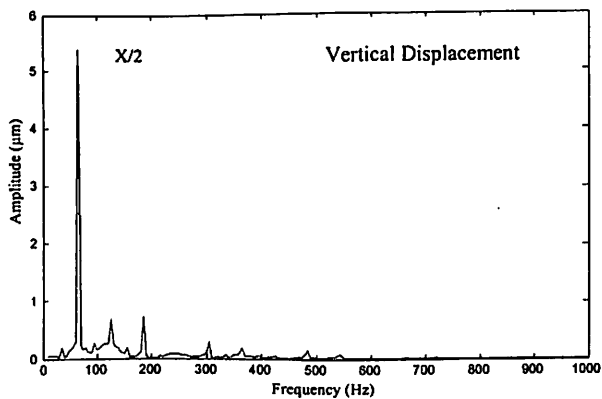
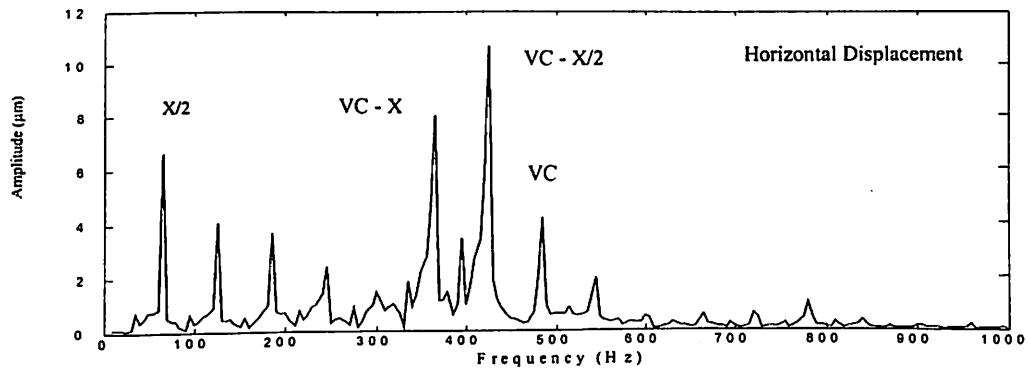
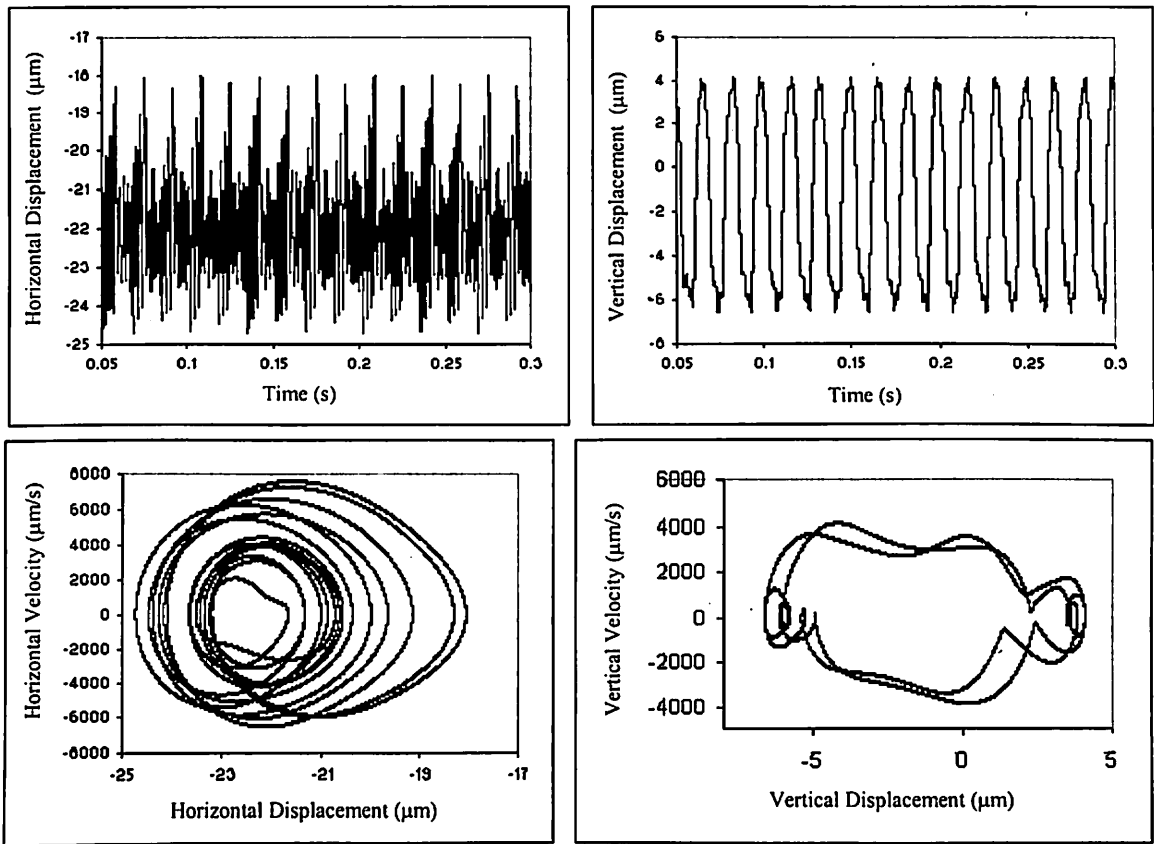


Fig. 4.39 Response at 9000 rpm for  $\gamma_0 = 20\mu\text{m}$ ,  $W = 6\text{N}$ ,  $F_u = 15\%W$



Poincaré Maps

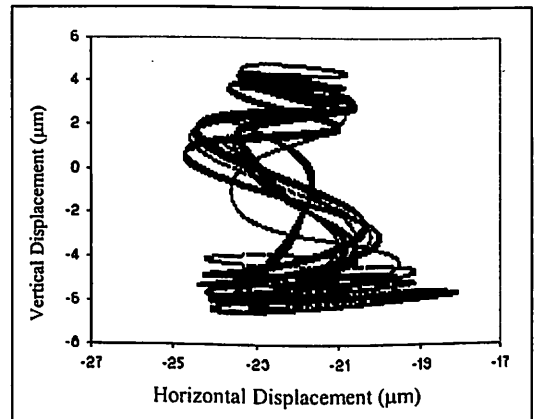
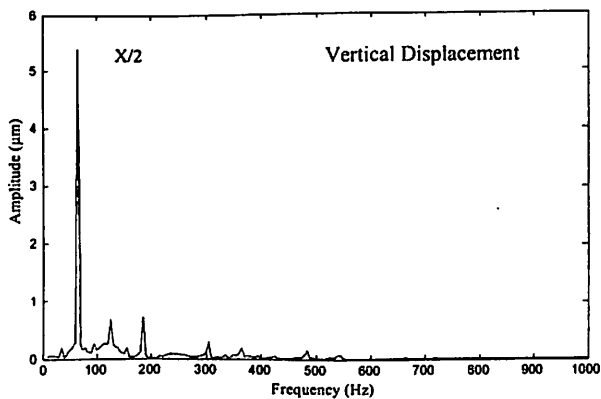
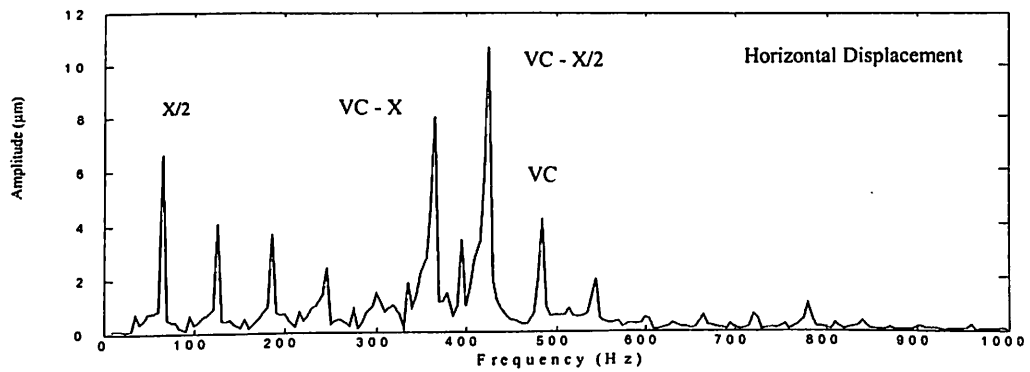
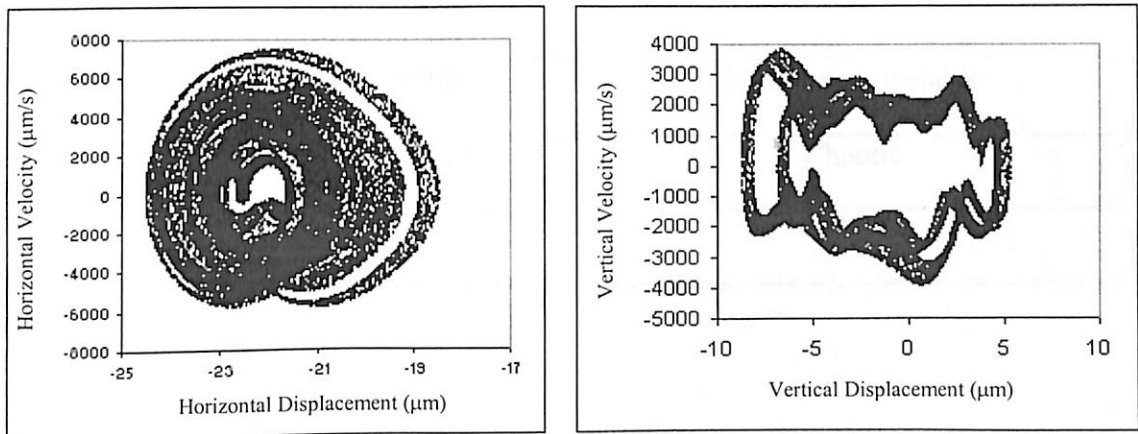
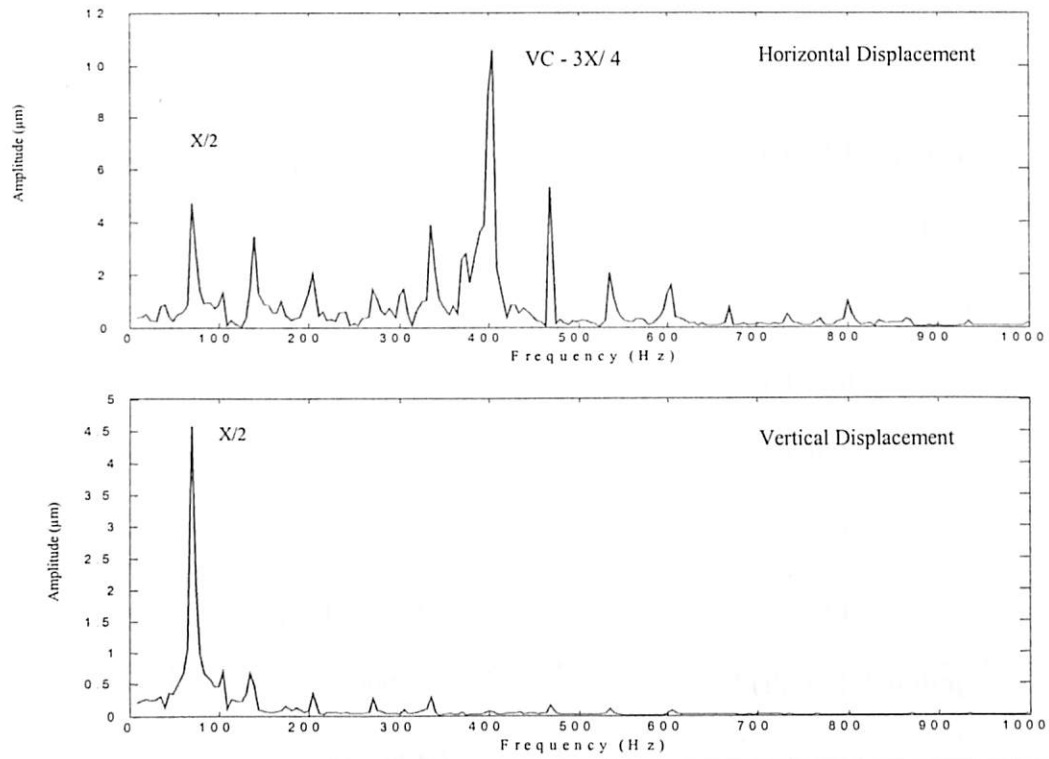


Fig. 4.39 Response at 9000 rpm for  $\gamma_0 = 20\mu\text{m}$ ,  $W = 6\text{N}$ ,  $F_u = 15\%W$



Poincaré Maps

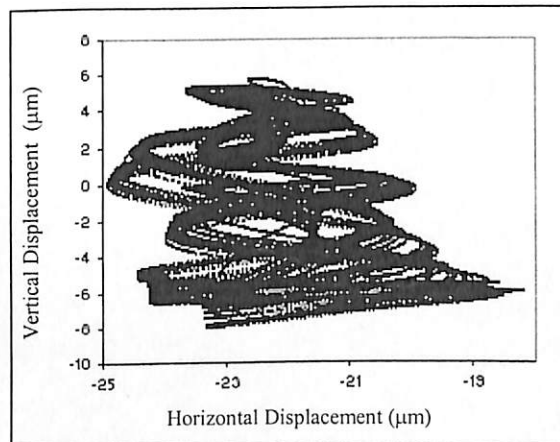


Fig. 4.40 Response at 10000 rpm for  $\gamma_0 = 20\mu\text{m}$ ,  $W = 6\text{N}$ ,  $F_u = 15\%W$

**Table 4.3** Nature of solutions for  $\gamma_0 = 20\mu\text{m}$ ,  $W = 6\text{N}$  and  $F_u = 15\%W$

<b>Speed (RPM)</b>	<b>Nature of Response</b>
Upto 710	1T stable low amplitude
740 – 1900	Period-one unstable (at VC and harmonics)
1970 – 3940	Chaotic
4000 – 5300	2T
5345 – 6780	1T
7000	X/3 (Period doubling)
8100 – 9050	Chaotic
9080 – 9700	Period-one unstable
9750 – 10040	Chaotic
10180	1T

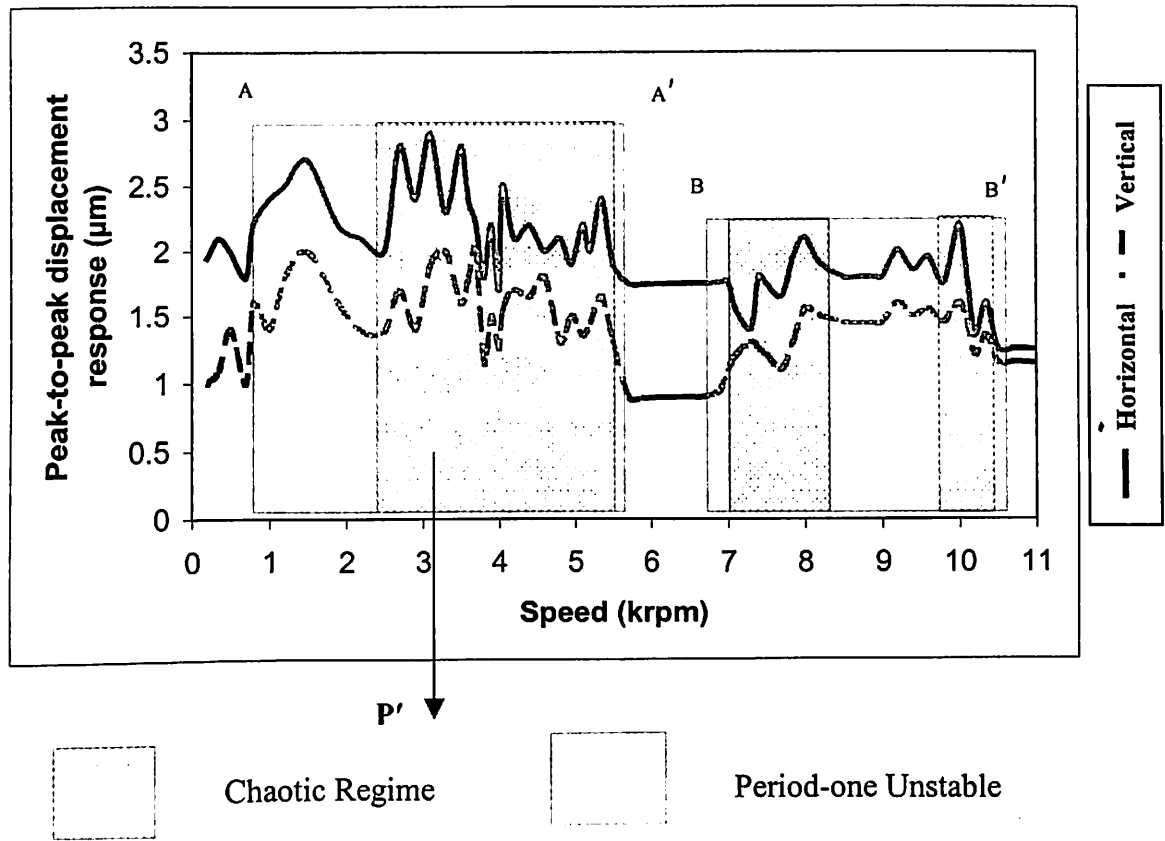


Fig. 4.41 Response plot for  $\gamma_0 = 1 \mu\text{m}$  and  $W = 6 \text{ N}$

Two regions of period-one unstable response are shown in Fig. 4.41. The first region from 780 to 5615 rpm has period doubling bifurcations. This is also a multi-valued region. The eigen values of the monodromy matrix go out through  $-1$ . Fig. 4.42 shows the nature of solution at 1500 rpm. The VC and its harmonics (super-harmonic) character of the frequency spectra is also brought-out by the Poincarè map.

The chaos is at the developing stage from 1950 rpm. Fig. 4.43 shows the nature of solution at 2200 rpm. In the frequency spectrum a band structure is seen in-between spikes of VC and its multiples. The fine-layered structure of the strange attractor is also clear from Poincarè map. For the chaotic region 2350 to 5640 rpm, the loss of stability is seen to be by the eigen values crossing  $+1$ . In this region, the period doubling bifurcations give way to chaos at about 2400 rpm and this chaotic region extends upto 5640 rpm. The chaotic solutions at 2500 rpm, 3800 rpm, 4000 rpm, 4050 rpm, 5100 rpm, 5200 rpm and 5500 rpm are shown in Figs. 4.44 to 4.50 respectively. The frequency spectrum has a dense band structure as shown in-between spikes of VC and its multiples. The orbits at this speed range do not repeat itself. The Poincarè maps of chaotic solutions have fractal structures that repeat as the maps are magnified. The time responses also show beat and chaos like behavior. It is clear that loss of periodicity is one characteristic feature of chaotic solution. The route to chaos by sudden loss of stability through a limit point has been shown by Sankarvelu (1994). Further increase in speed, causes the system return to stability in the speed range from 5700 to 6885 rpm.

The second region from 6915 to 10350 rpm has period doubling bifurcations as shown in Fig. 4.41. This is also a multi-valued region. Period-one solution becomes unstable from 6915 to 10350 rpm, because of period doubling bifurcations. The solution undergoes pitchfork bifurcations till 6950 rpm after which the chaotic solution is obtained at 6990 rpm. Figure 4.51 shows the nature of solution at 7000 rpm. In the frequency spectrum a band structure appears is seen in-between spikes of VC and its multiples. The dense structure of the strange attractor is also clear from Poincarè maps.

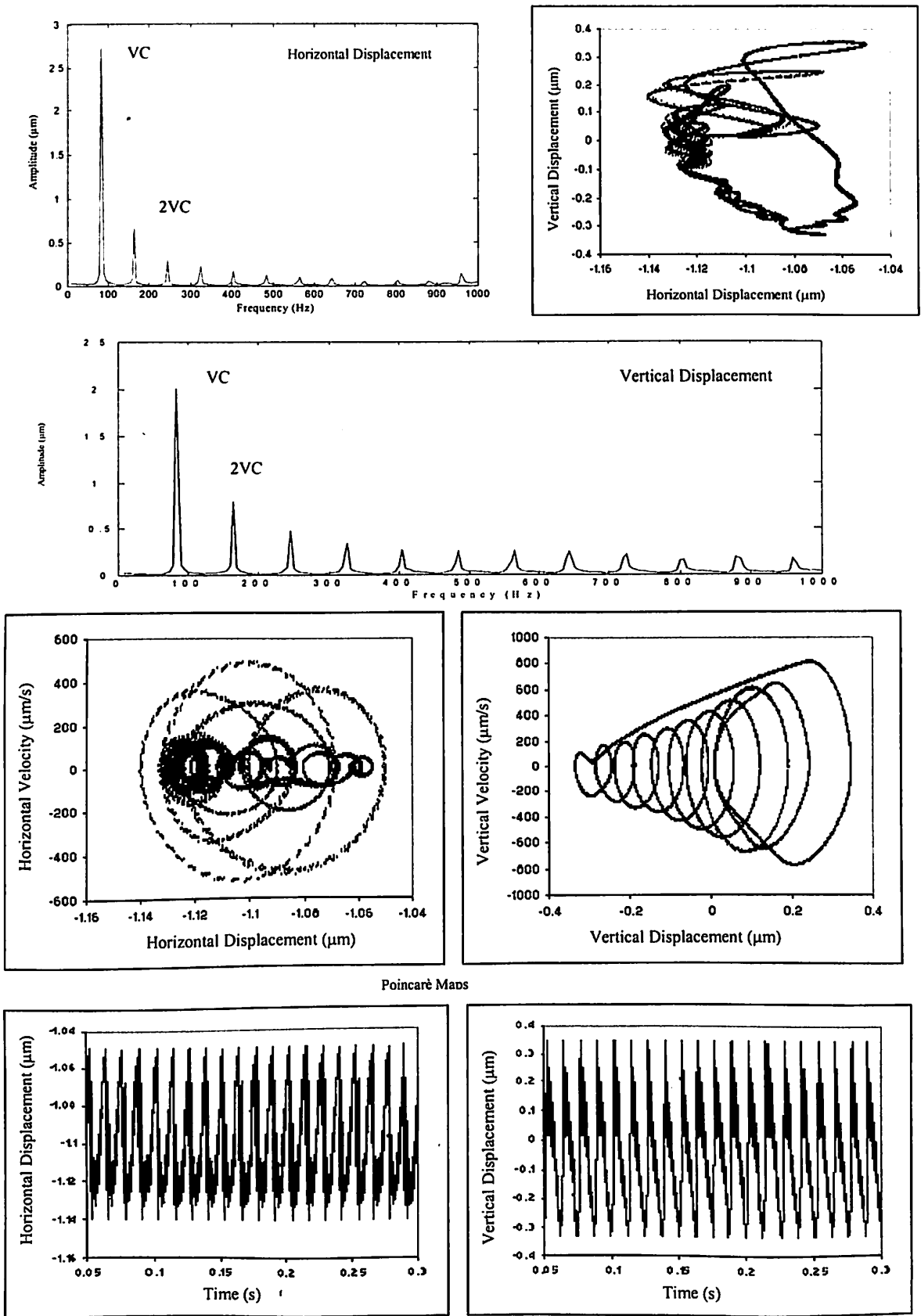
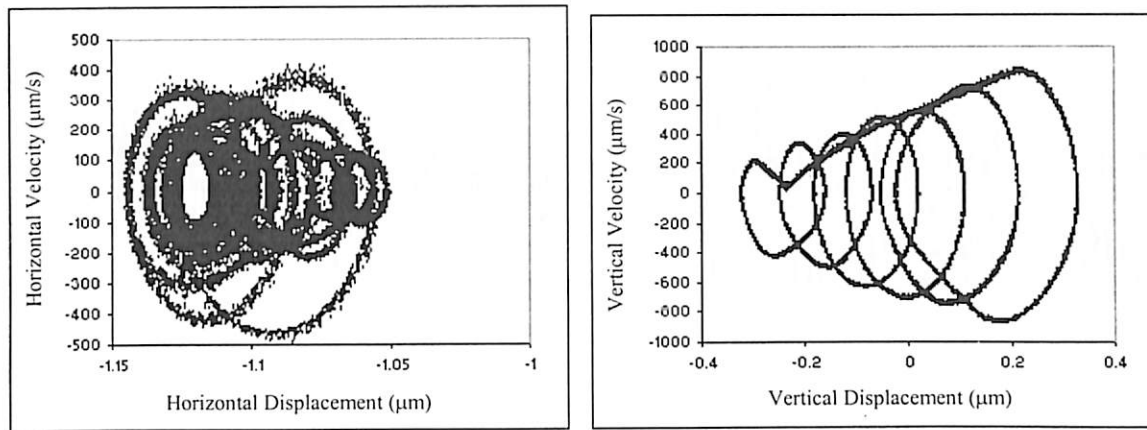


Fig. 4.42 Response at 1500 rpm for  $\gamma_0 = 1\mu\text{m}$ ,  $W = 6\text{N}$





Poincaré Maps

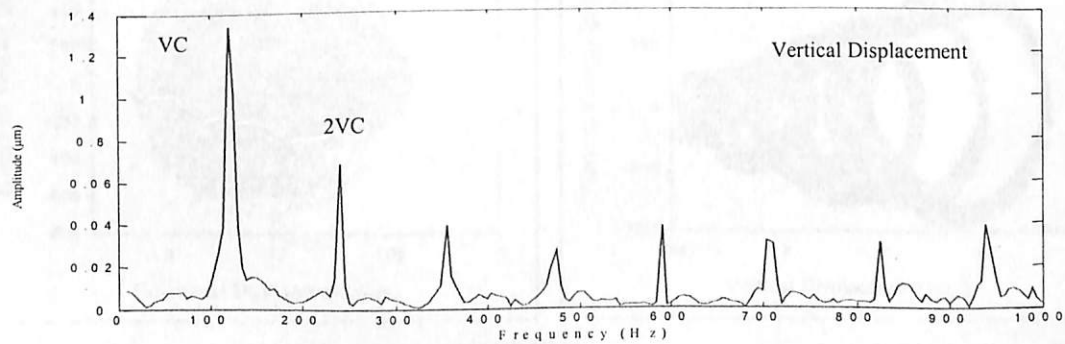
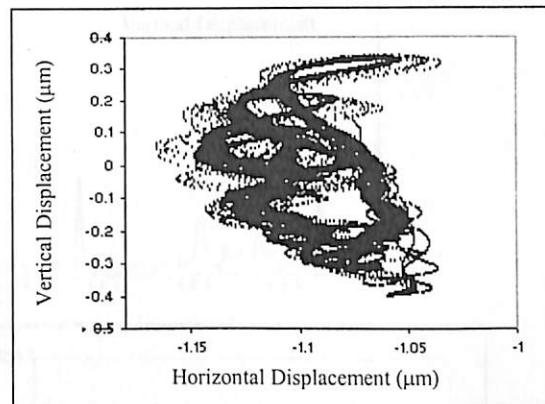
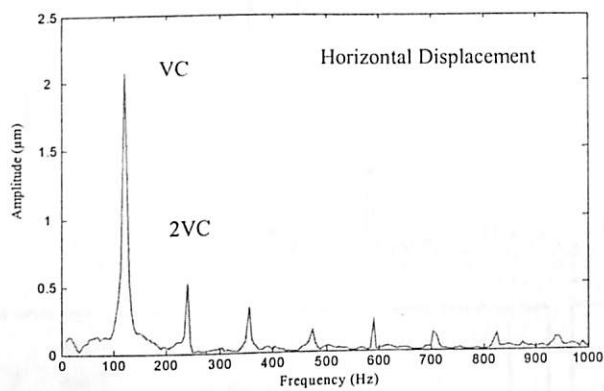
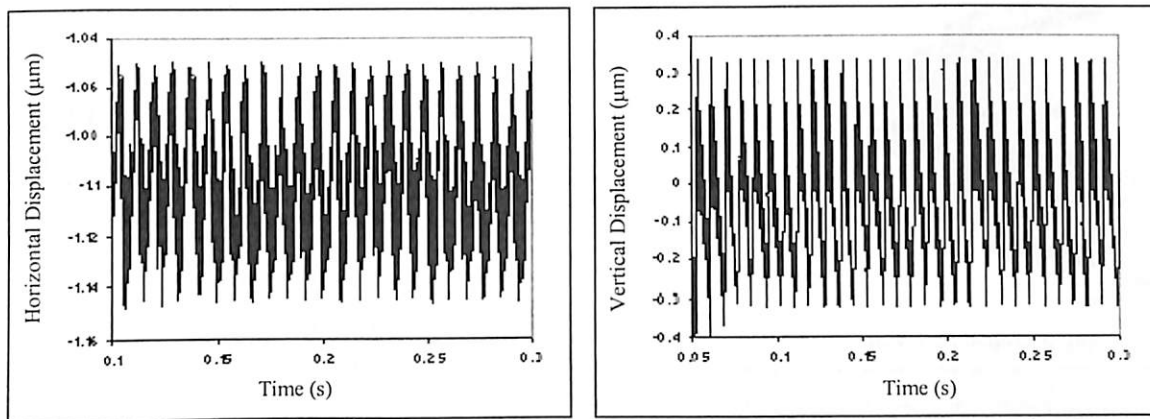
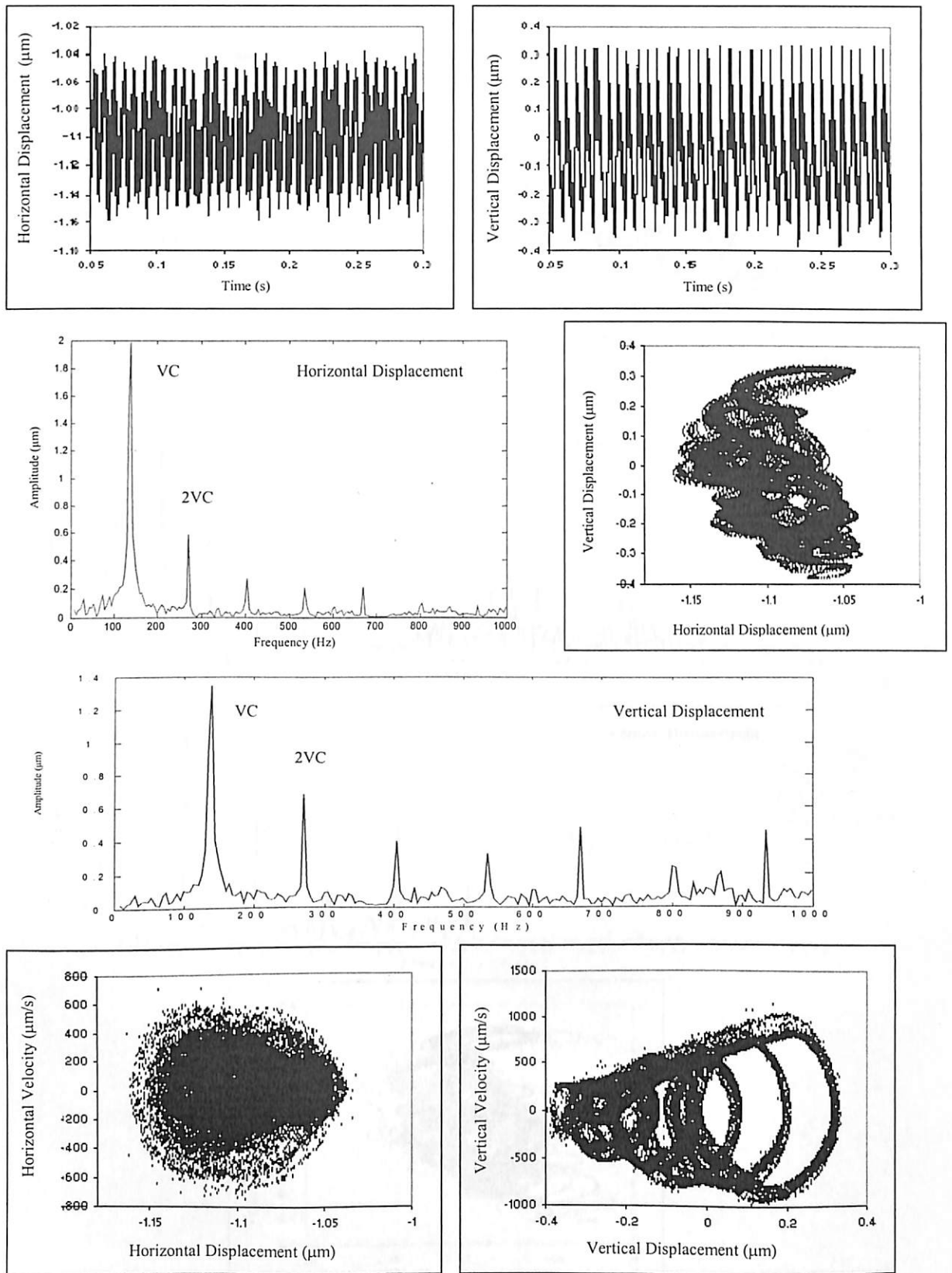
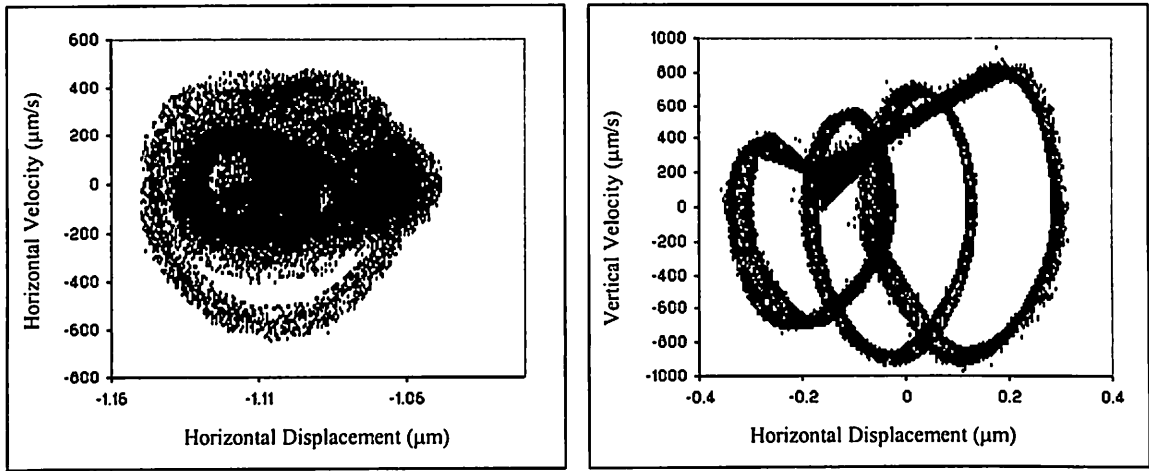


Fig. 4.43 Response at 2200 rpm for  $\gamma_0 = 1\mu\text{m}$ ,  $W = 6\text{N}$



Poincaré Maps

**Fig. 4.44** Response at 2500 rpm for  $\gamma_0 = 1\mu\text{m}$ ,  $W = 6\text{N}$



Poincaré Maps

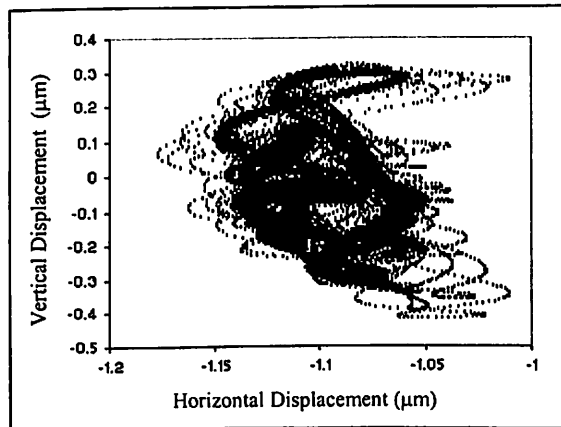
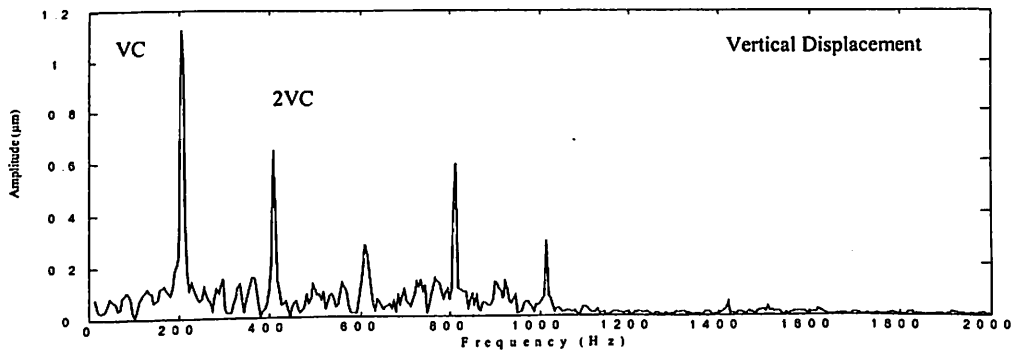
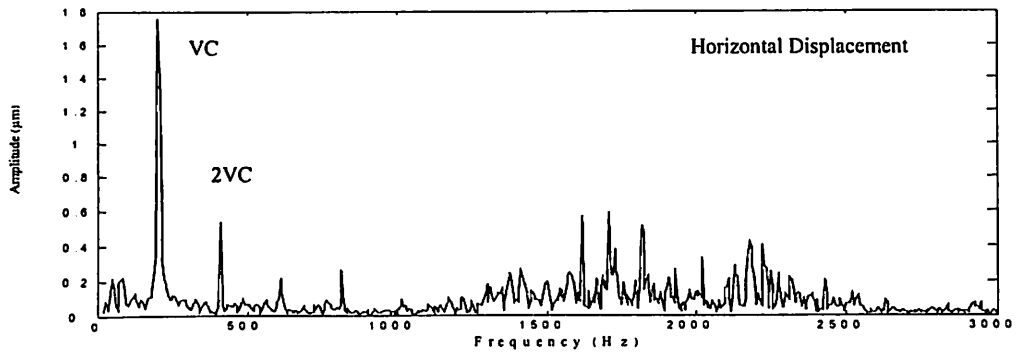
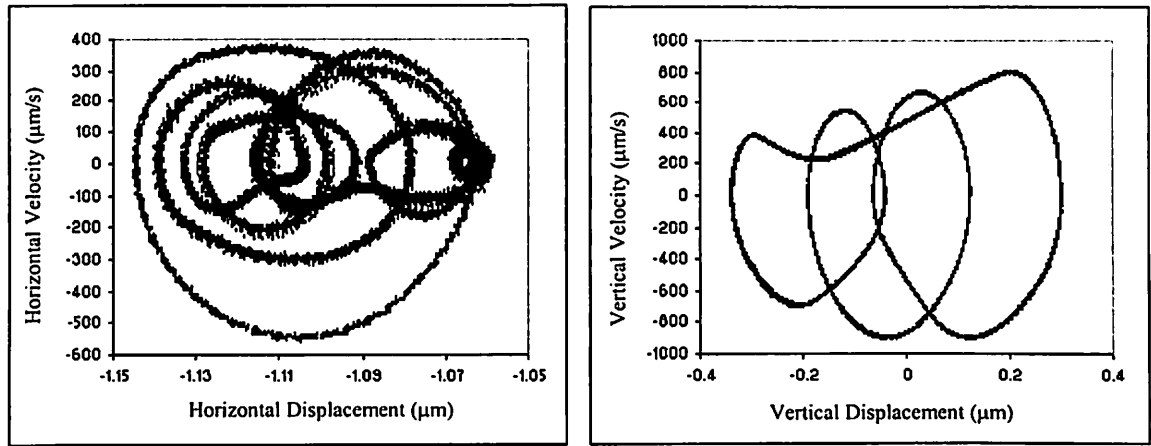


Fig. 4.45 Response at 3800 rpm for  $\gamma_0 = 1\mu\text{m}$ ,  $W = 6\text{N}$



Poincaré Maps

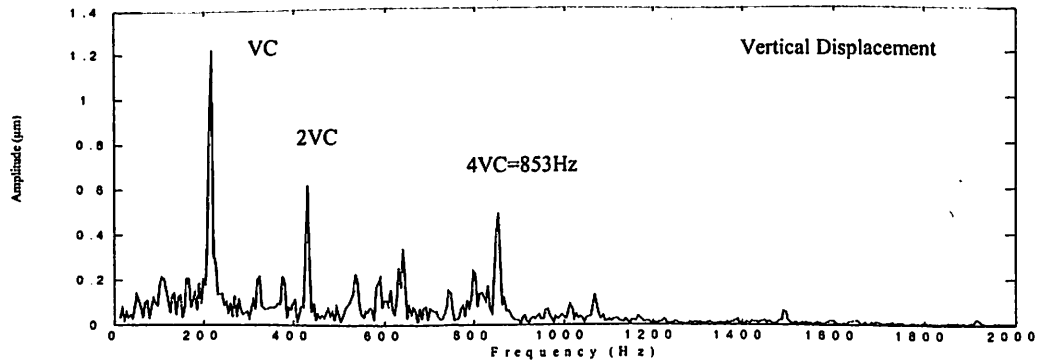
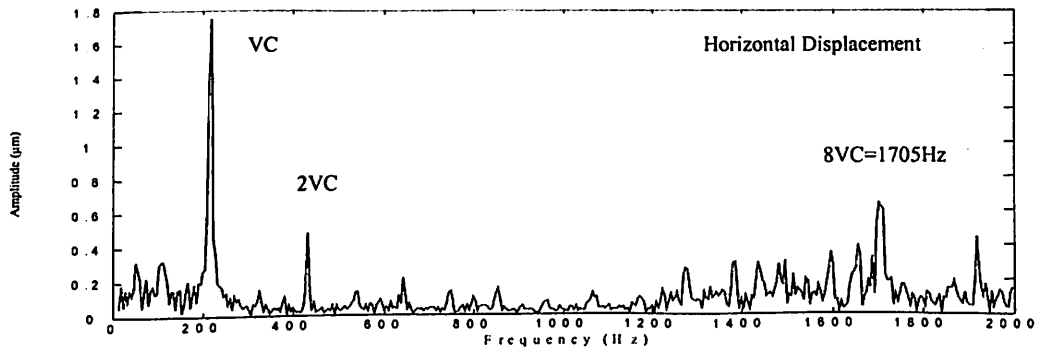
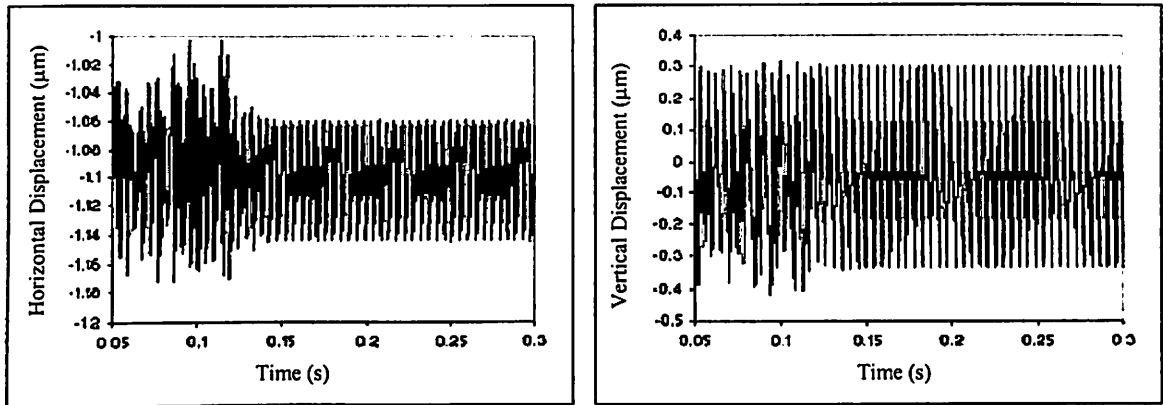
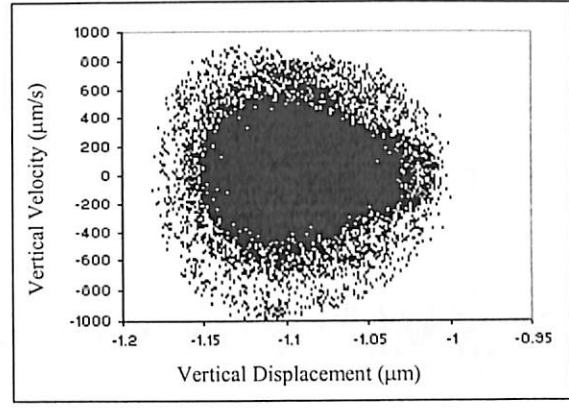
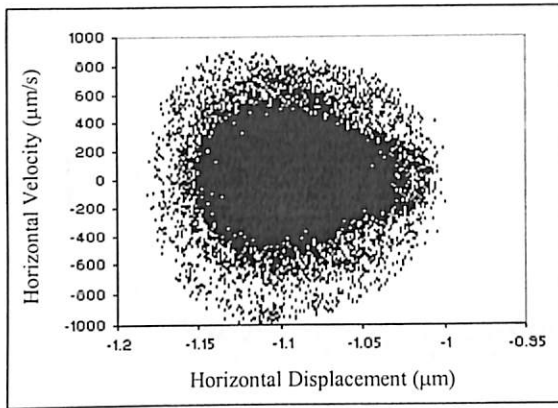
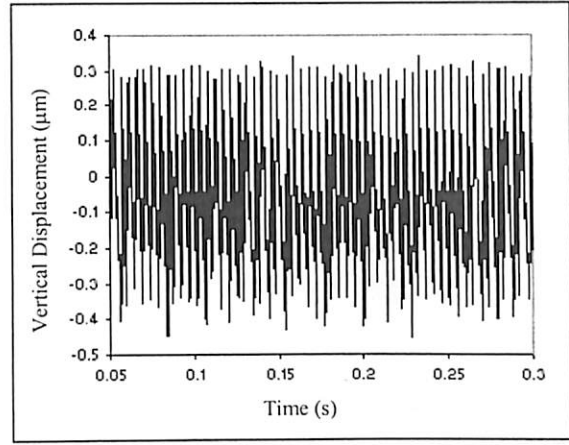
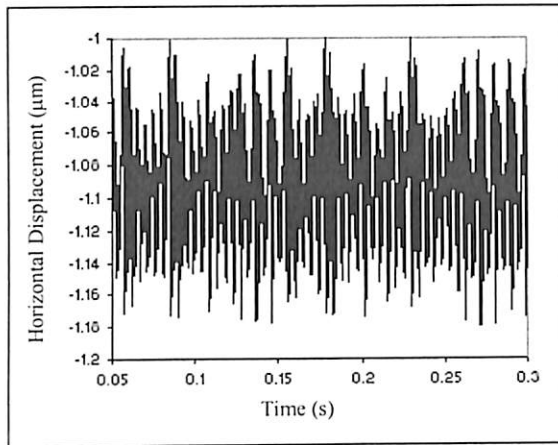


Fig. 4.46 Response at 4000 rpm for  $\gamma_0 = 1\mu\text{m}$ ,  $W = 6\text{N}$



Poincaré Maps

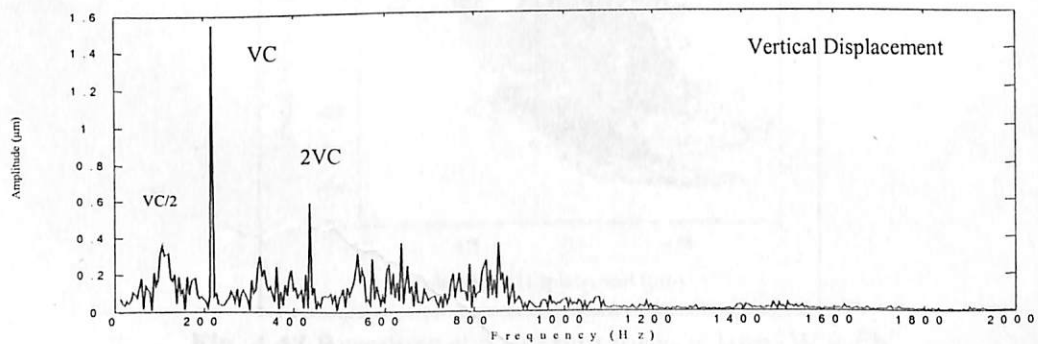
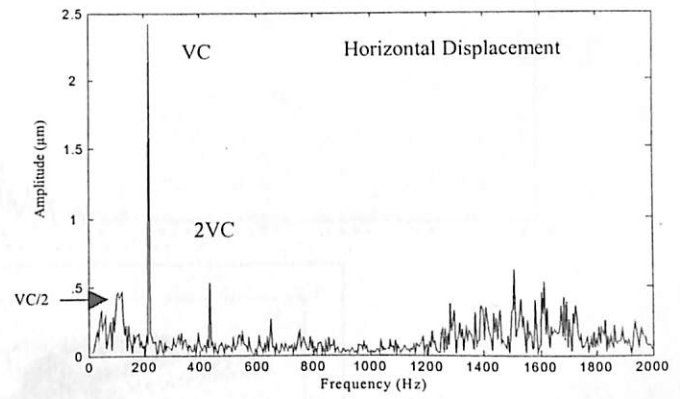
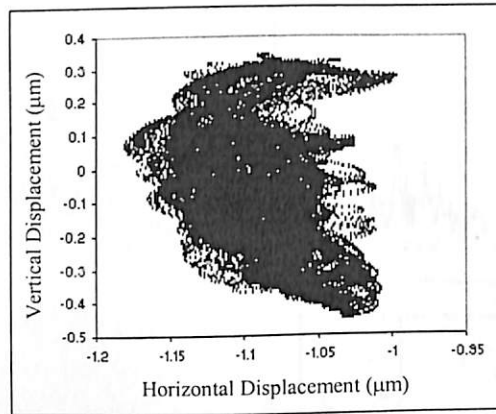
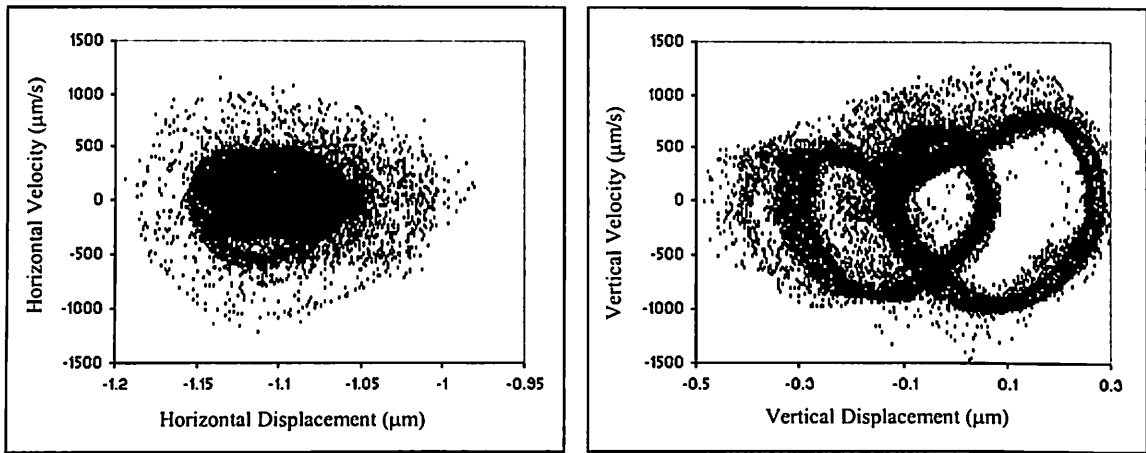


Fig. 4.47 Response at 4050 rpm for  $\gamma_0 = 1\mu\text{m}$ ,  $W = 6\text{N}$



Poincaré Maps

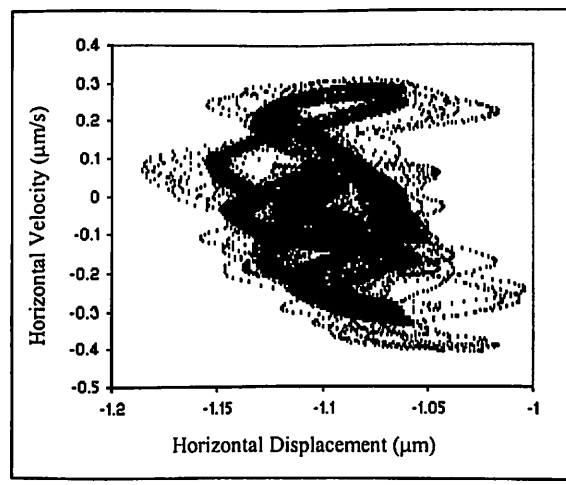
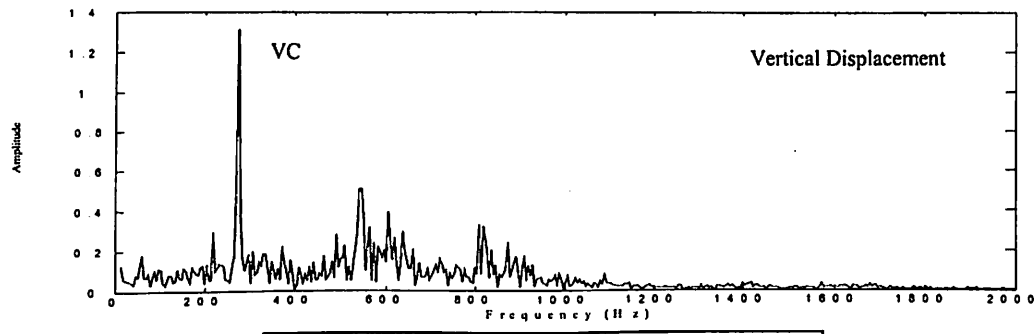
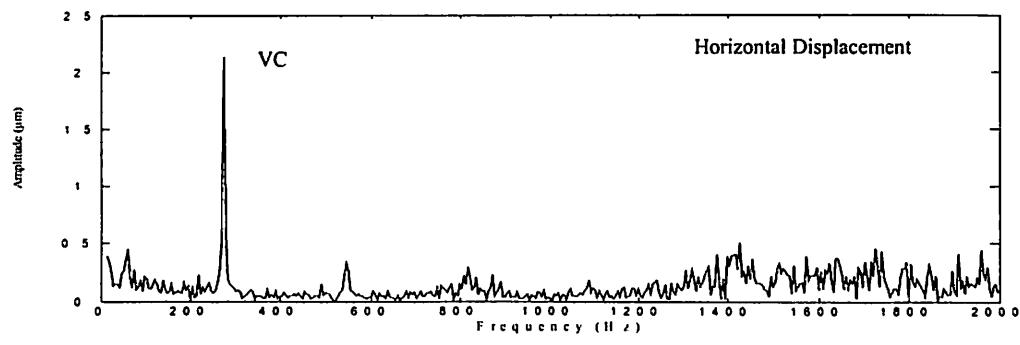


Fig. 4.48 Response at 5100 rpm for  $\gamma_0 = 1\mu\text{m}$ ,  $W = 6\text{N}$

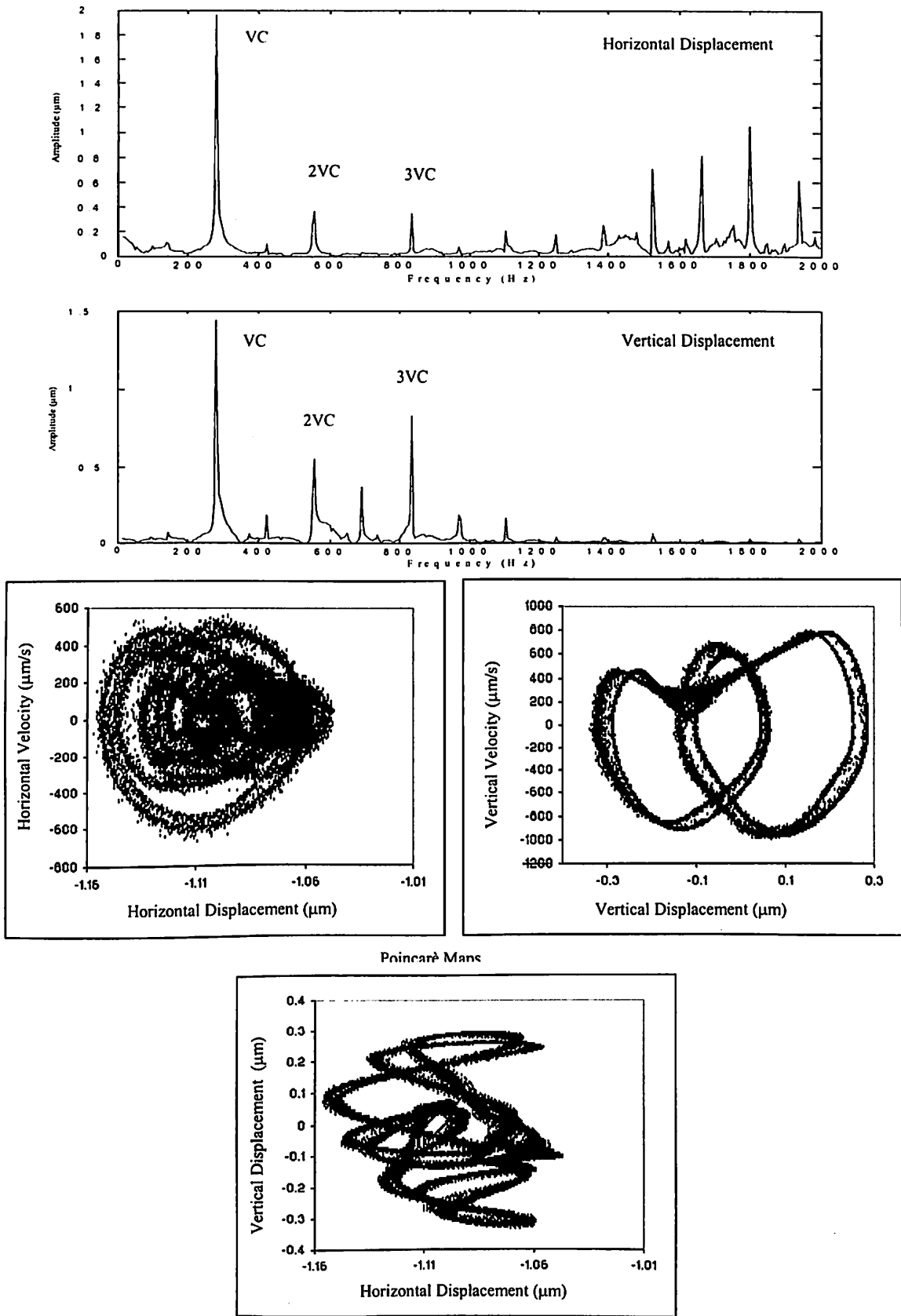
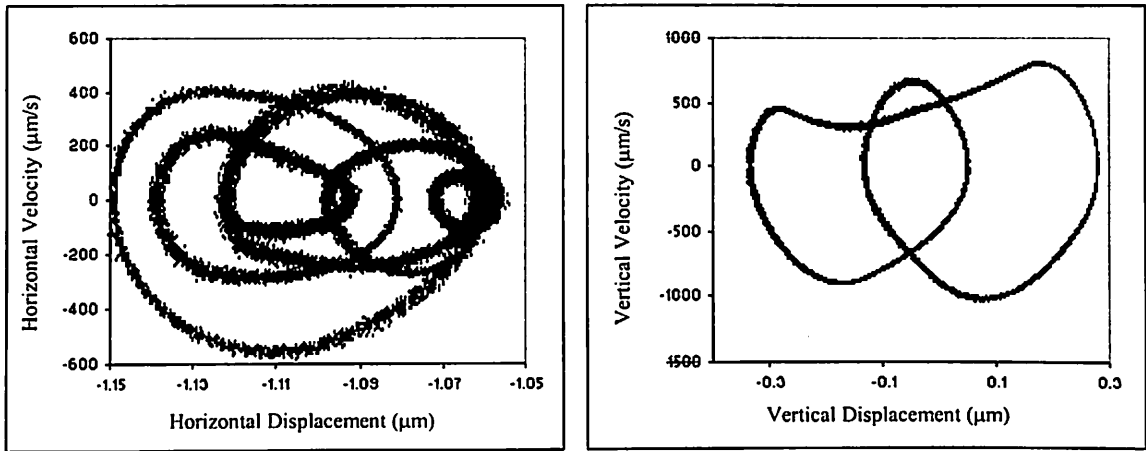


Fig. 4.49 Response at 5200 rpm for  $\gamma_0 = 1 \mu\text{m}$ ,  $W = 6\text{N}$



Poincaré Map

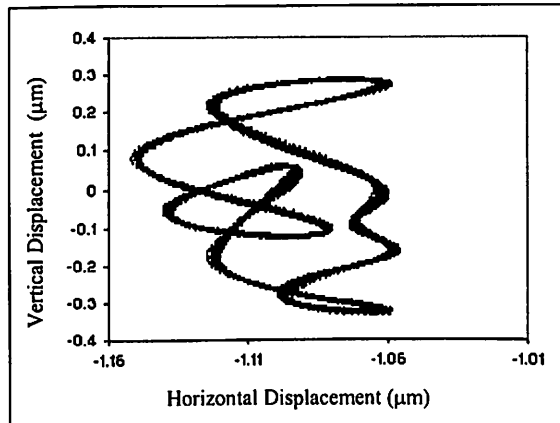
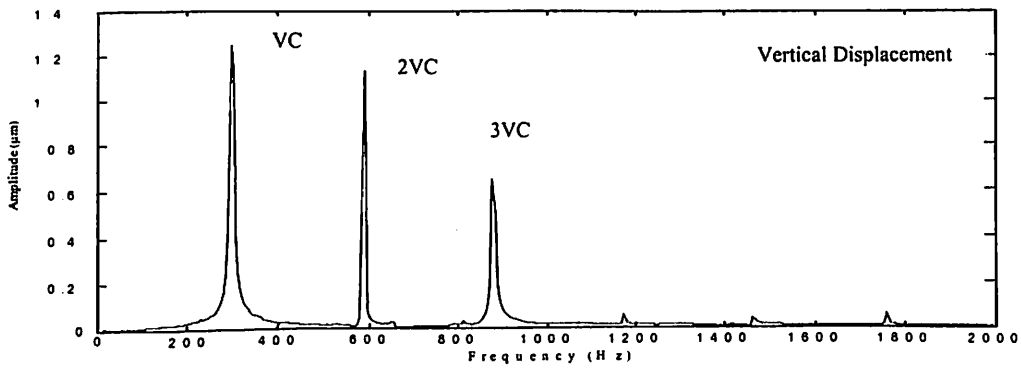
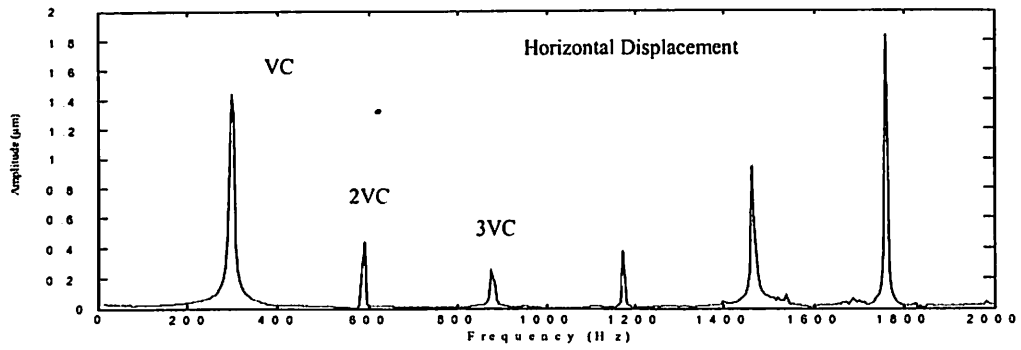
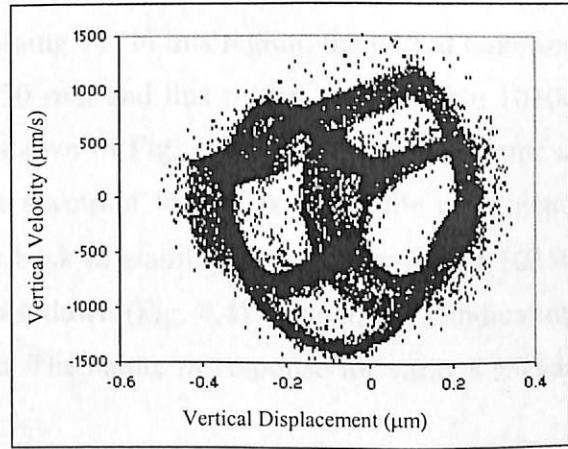
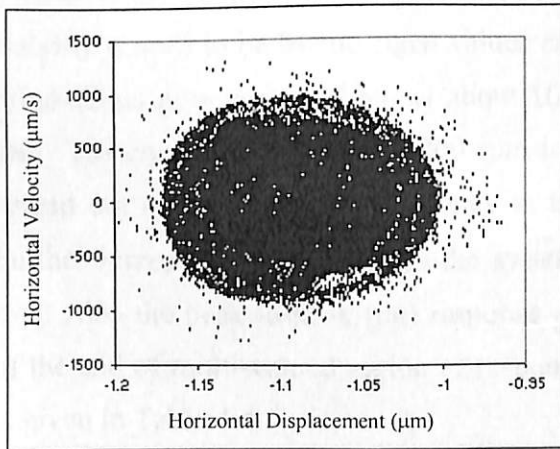
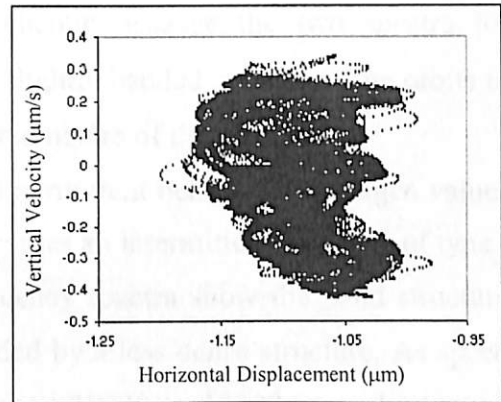
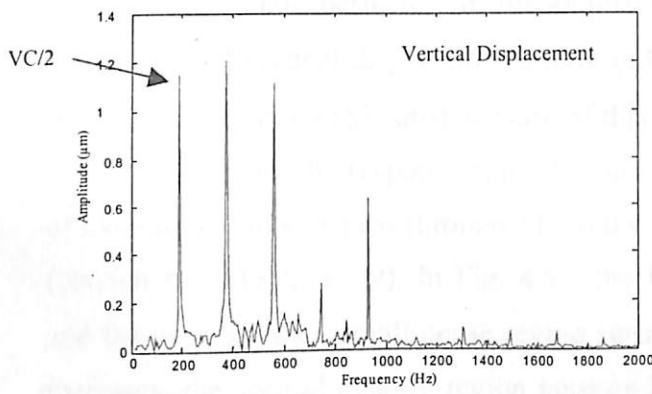
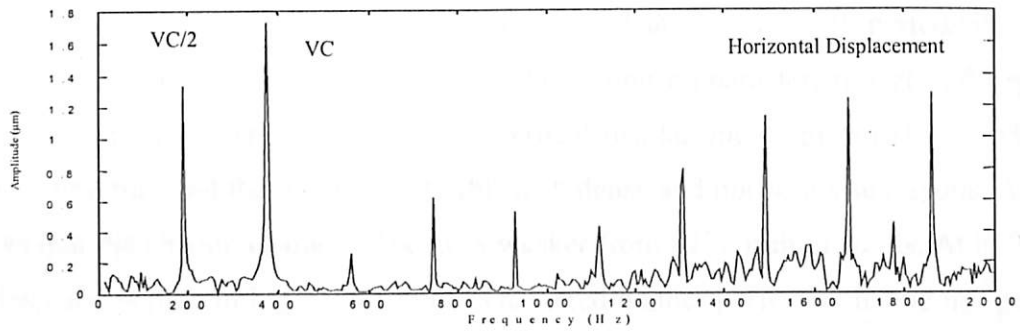
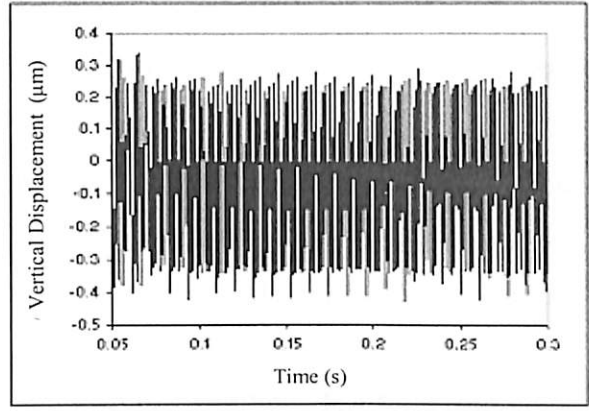
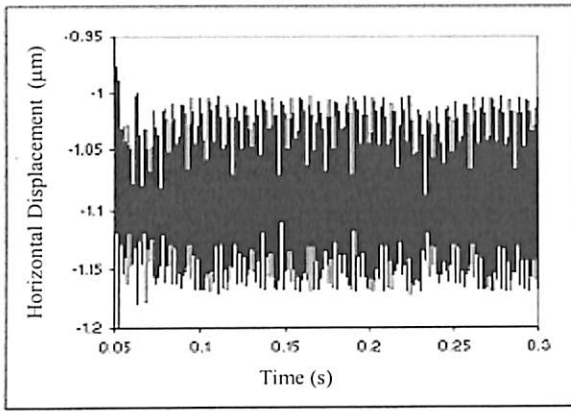


Fig. 4.50 Response at 5500 rpm for  $\gamma_0 = 1\mu\text{m}$ ,  $W = 6\text{N}$





Poincaré Maps

Fig. 4.51 Response at 7000 rpm for  $\gamma_0 = 1 \mu\text{m}$ ,  $W = 6\text{N}$

For the first chaotic region 7000 to 8270 rpm, the loss of stability is seen to be due to the eigen values crossing +1. In this region, the period doubling bifurcations give way to chaos at about 7000 rpm and this chaotic region extends upto 8270 rpm. The chaotic solutions at 7100, 7500 and 8000 rpm are shown in Figs. 4.52 to 4.54 respectively. The frequency spectrum has a dense band structure as seen in-between spikes of VC and its multiples. The fine-layered structure of the strange attractor is also clear from Poincarè maps. The orbit at this speed does not repeat itself. The Poincarè maps of chaotic solutions have fractal structures that repeat as the map is magnified. The time responses also show beat and chaos like behavior. It is clear that loss of periodicity is one characteristic feature of chaotic solution. The response characteristics at 8200 rpm are shown in Fig. 4.55. The horizontal and vertical displacement spectra (Fig. 4.55) have banded structure and there are closed orbit with dense and not so dense regions. Analysis shows that the chaotic character becomes weaker from 8270 rpm onwards. At 8500 rpm, the response shown in Fig. 4.56 can be considered neither perfectly chaotic nor perfectly periodic. It is not perfectly or predominantly chaotic because the two spectra for horizontal and vertical displacements have only a slightly banded structure. The orbits in Poincarè maps are complicated because of this mixed nature of the response.

At 10000 rpm, the response explodes into an intermittent behavior. The eigen values of monodromy matrix pass through +1, so this becomes an intermittent behavior of type I (Nayfeh and Mook, 1979). In Fig. 4.57, the frequency spectra show the band structure and the orbit shows a small dense region surrounded by a less dense structure. As speed increases, the second chaotic region appears between 10030 to 10300 rpm, the loss of stability is seen to be by the eigen values crossing +1. In this region, the period doubling bifurcations give way to chaos at about 10030 rpm and this region extends upto 10300 rpm. The chaotic solution at 10200 rpm is shown in Fig. 4.58. The chaotic attractor is spread out and the band of frequency in the spectrum formed is also quite prominent. Further increase in speed, brings the system back to stability beyond a speed of 10350 rpm. Also the peak-to-peak (pp) response goes down (Fig. 4.41), which is an indication of the end of multi-valued region of response. The nature of response for various speeds is given in Table 4.4.

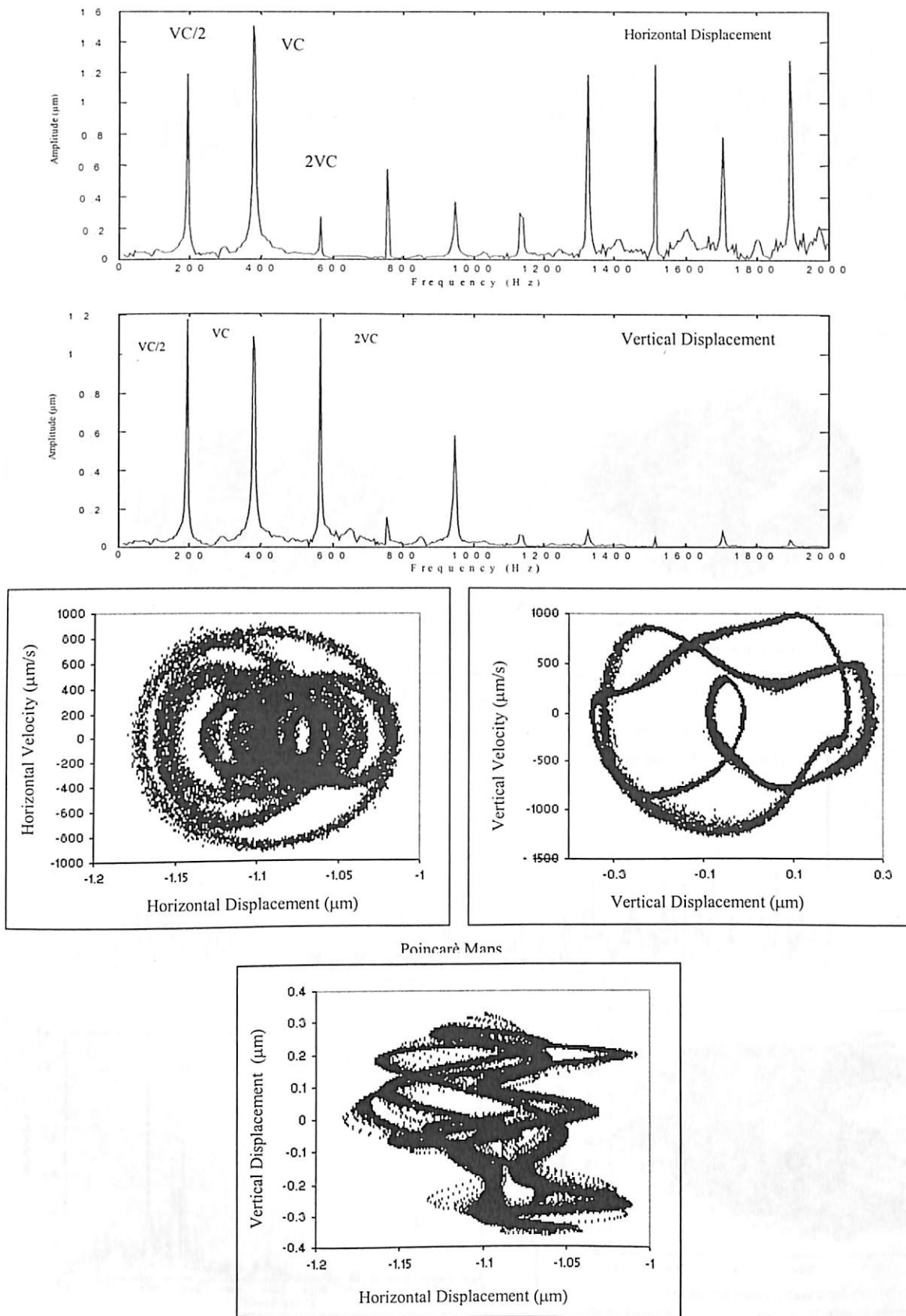
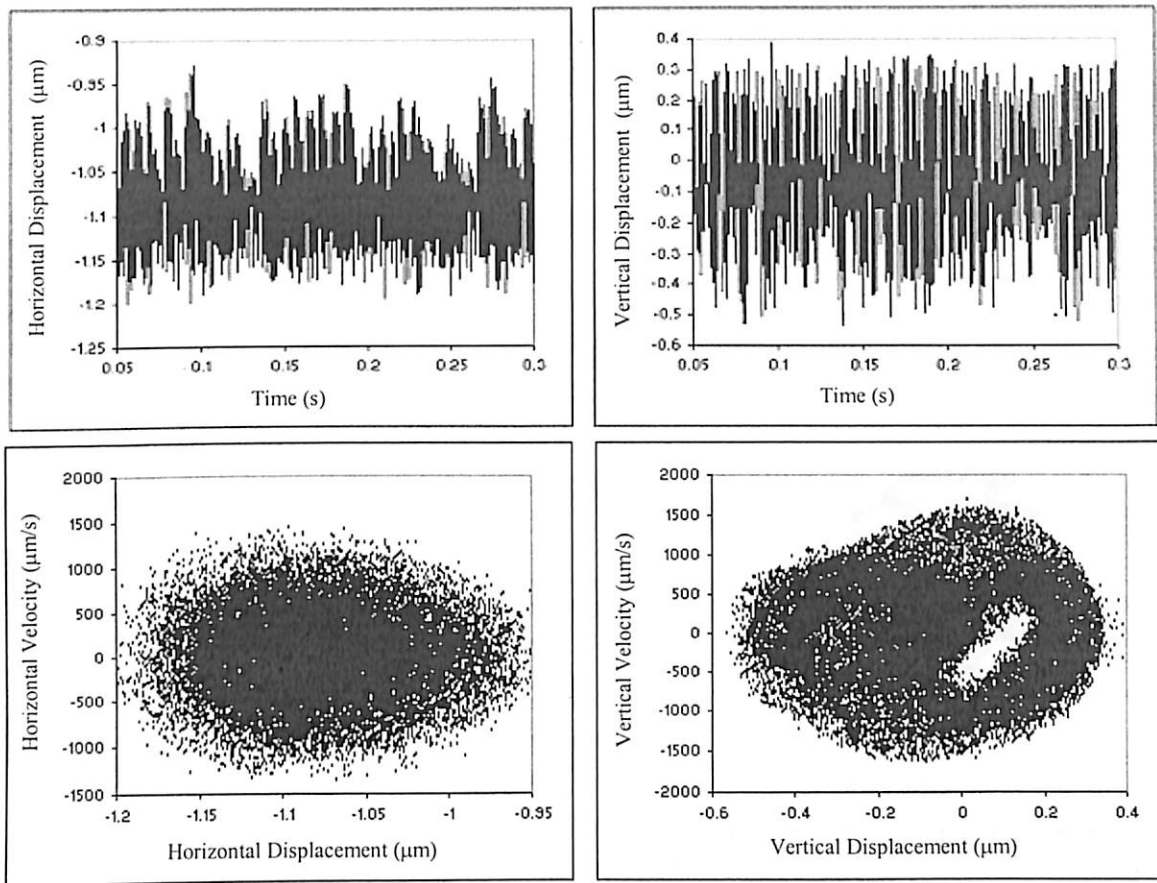


Fig. 4.52 Response at 7100 rpm for  $\gamma_0 = 1\mu\text{m}$ ,  $W = 6\text{N}$



Poincaré Maps

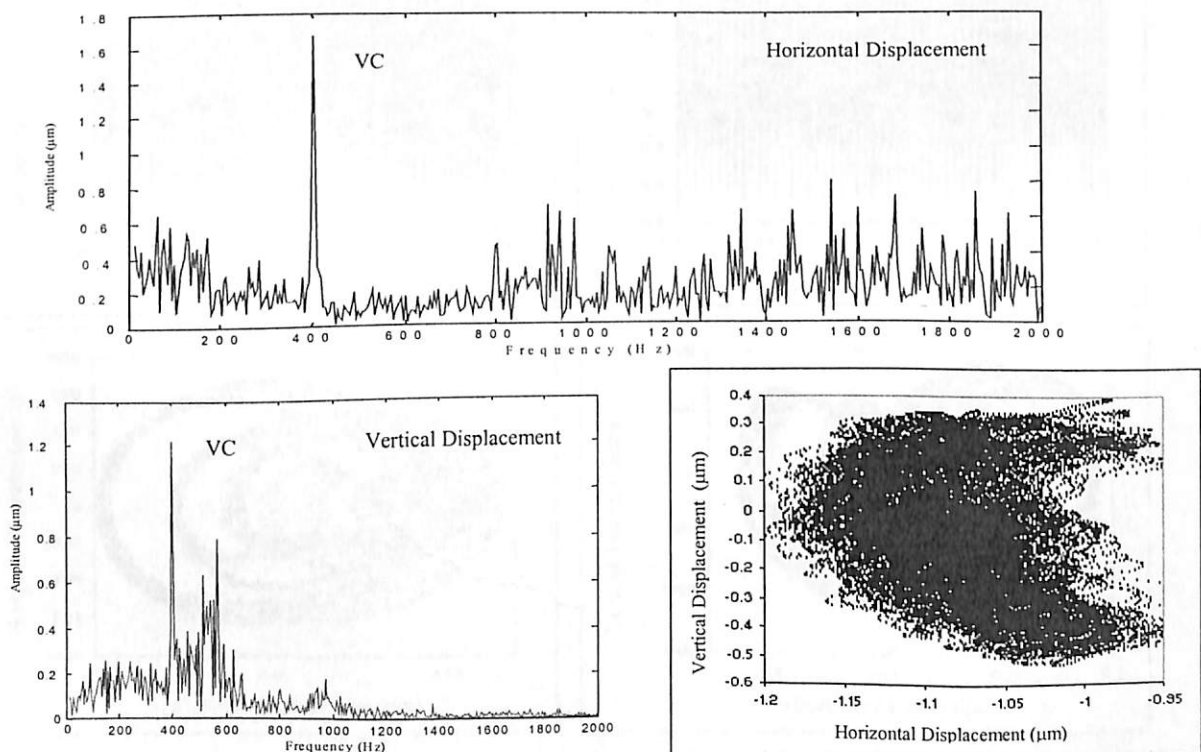
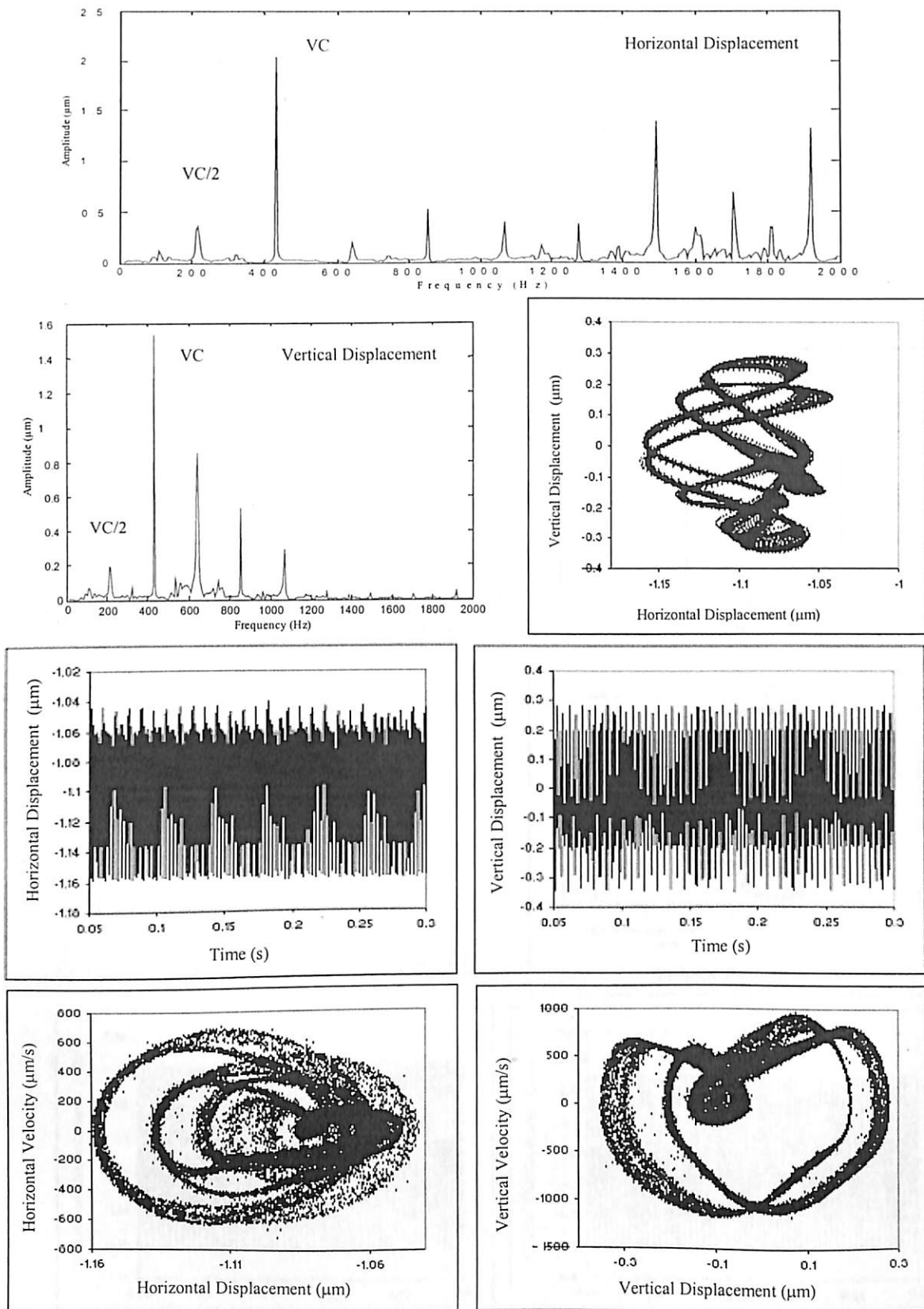
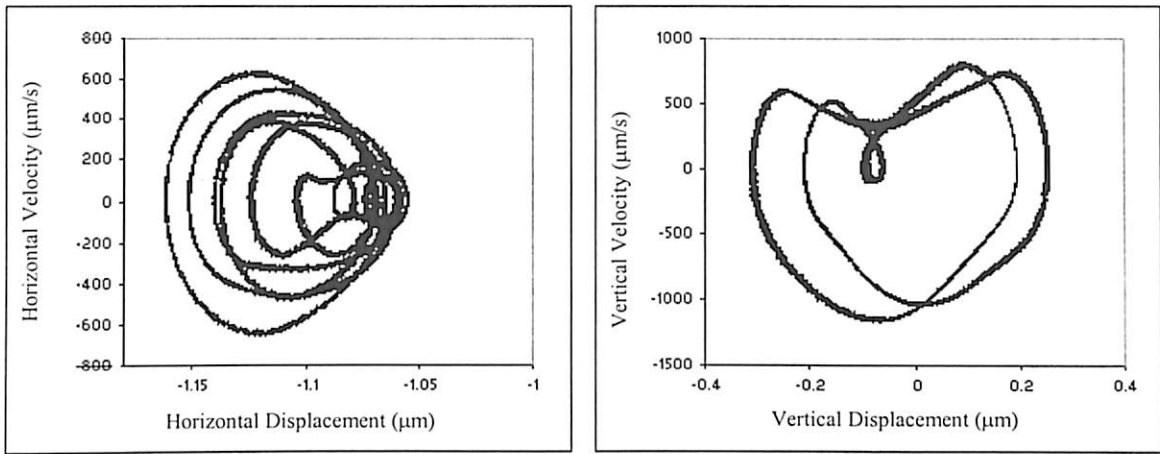


Fig. 4.53 Response at 7500 rpm for  $\gamma_0 = 1\mu\text{m}$ ,  $W = 6\text{N}$



Poincaré Maps

Fig. 4.54 Response at 8000 rpm for  $\gamma_0 = 1\mu\text{m}$ ,  $W = 6\text{N}$



Poincaré Maps

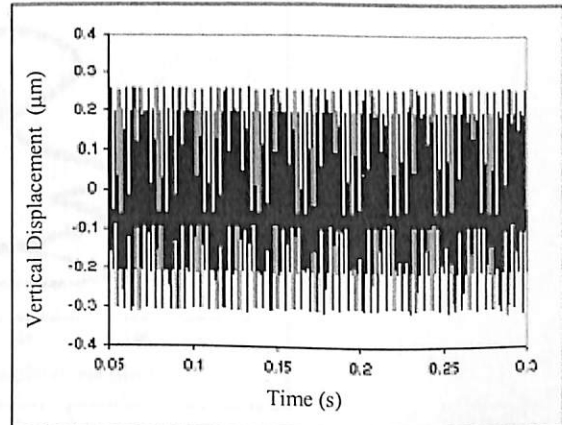
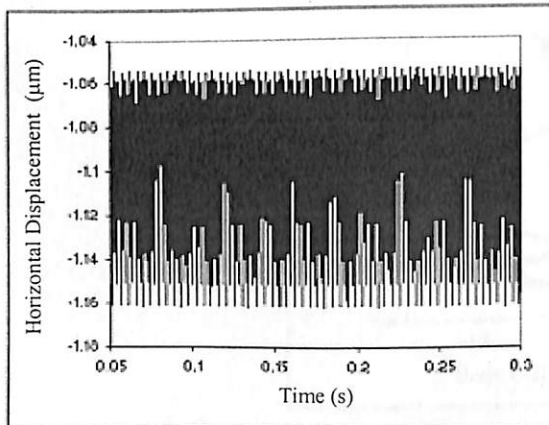
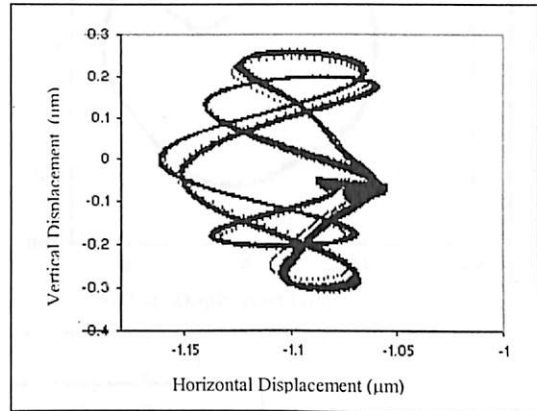
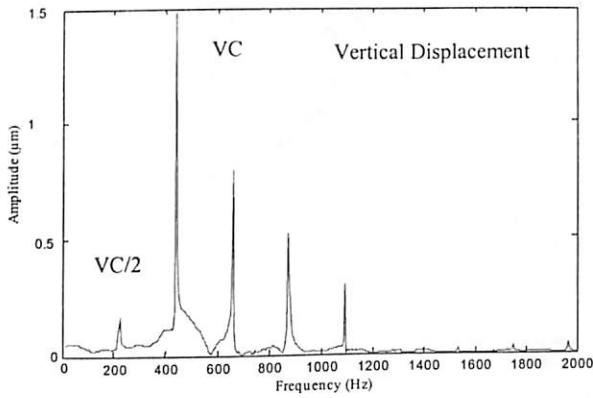
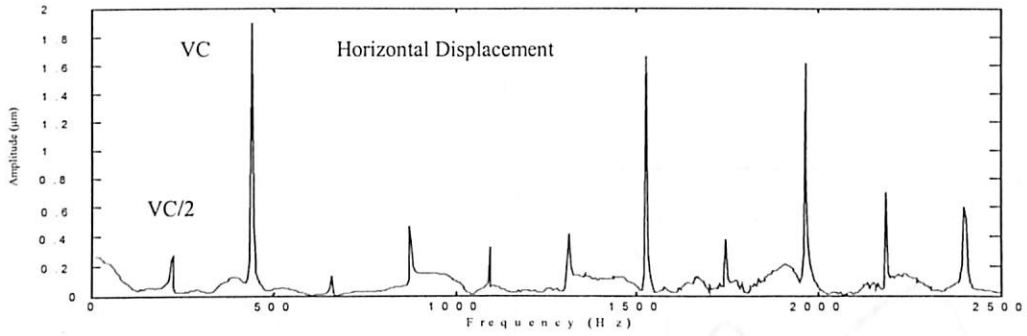


Fig. 4.55 Response at 8200 rpm for  $\gamma_0 = 1\mu\text{m}$ ,  $W = 6\text{N}$

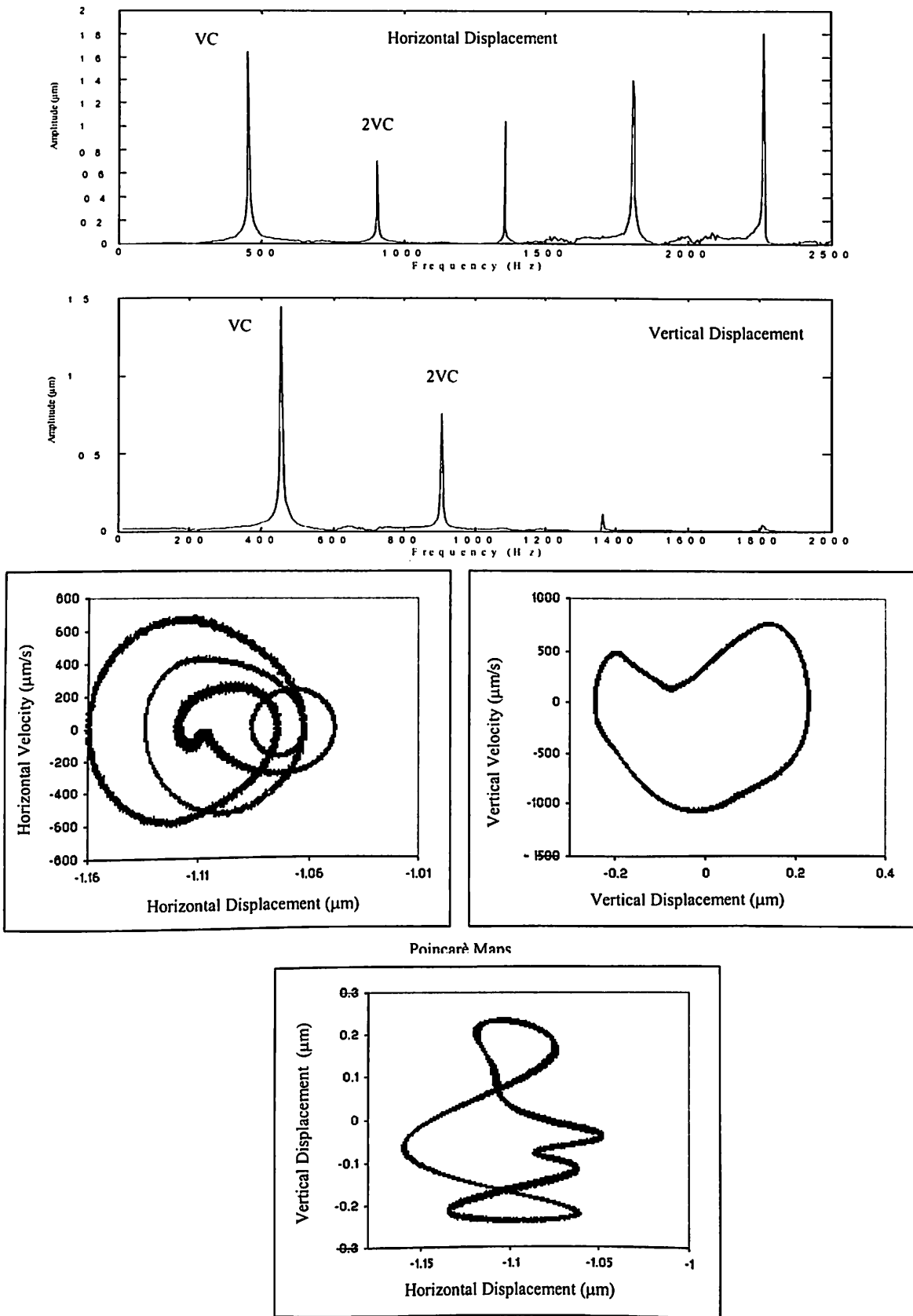


Fig. 4.56 Response at 8500 rpm for  $\gamma_0 = 1 \mu\text{m}$ ,  $W = 6\text{N}$

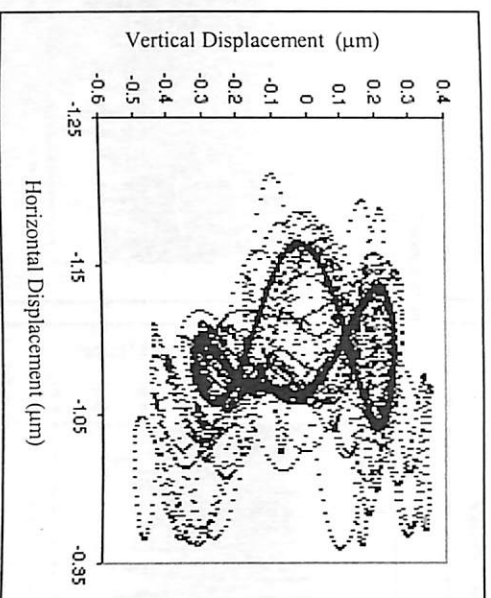
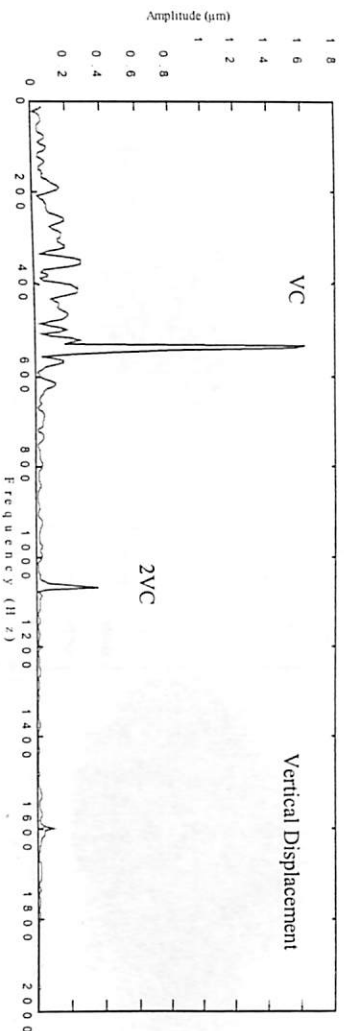
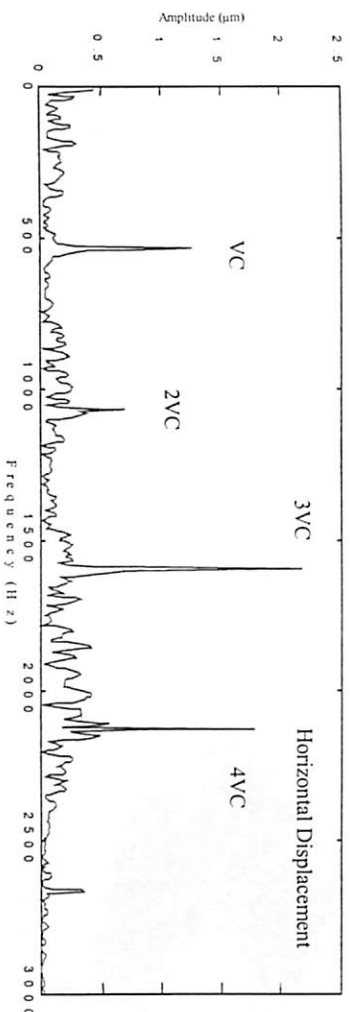
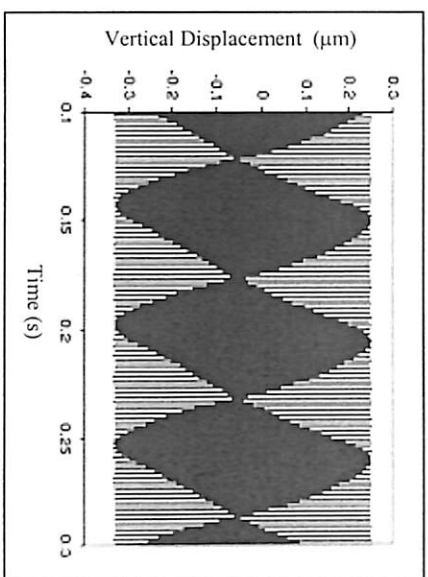
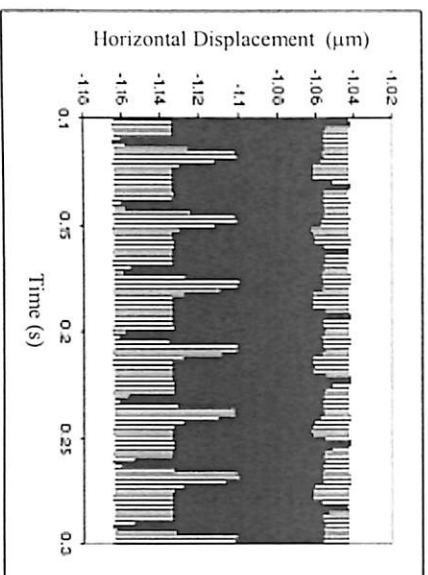


Fig. 4.57 Response at 10000 rpm for  $\gamma_0 = 1 \mu\text{m}$ ,  $W = 6\text{N}$



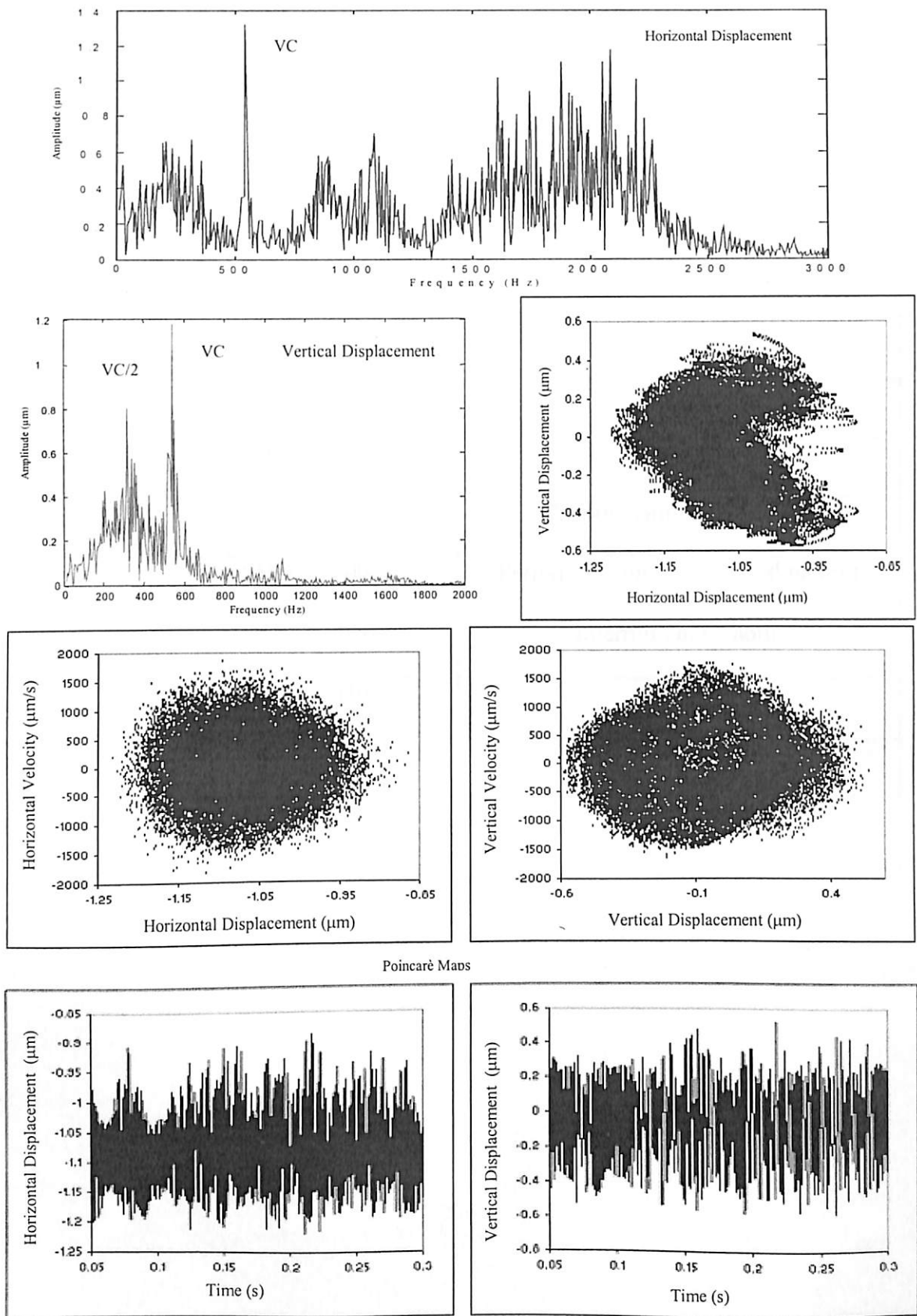


Fig. 4.58 Response at 10200 rpm for  $\gamma_0 = 1\mu\text{m}$ ,  $W = 6\text{N}$

**Table 4.4** Nature of solutions for  $\gamma_0 = 1\mu\text{m}$ ,  $W = 6N$ 

<b>Speed (RPM)</b>	<b>Nature of Response</b>
Upto 775	1T stable low amplitude
780 – 1900	Period-one unstable (at VC and harmonics)
1950 – 2200	Chaos developing
2350 – 5640	Chaotic
5700 – 6885	Periodic
6990 – 8170	Chaotic
8200	Chaotic natures decreasing
8500 – 9700	Period-one unstable (mixed nature)
9750 – 10020	Intermittent Chaotic
10030 – 10300	Chaotic
10350	Periodic

#### 4.5.2.5 Response for line contact at $\gamma_0 = 0.5 \mu\text{m}$ , $W = 6 \text{ N}$ and $F_u = 0$

The overall response plot of rolling element bearing for *line contact* with radial internal clearance of  $0.5 \mu\text{m}$  and radial load of  $6\text{N}$  is shown in Fig. 4.59. The overall response plot has a less rough appearance. Two regions can be identified which have high peak-to-peak (pp) response. These regions are shown in Fig. 4.59 bounded by lines A-A' and B-B'.

From Fig. 4.6 (b) of stiffness estimation in vertical and horizontal directions, it is seen that for radial internal clearance ( $\gamma_0$ ) of  $0.5 \mu\text{m}$  and  $1 \mu\text{m}$ , the stiffness values practically remain same. On analyzing the response plot for peak-to-peak amplitude against speed for the cases of radial internal clearance ( $\gamma_0$ ) of  $0.5 \mu\text{m}$  and  $1 \mu\text{m}$  (Fig. 4.41 and Fig. 4.59), it is seen that the peak (shown by P' in the Fig. 4.41) develops at a lower speed of  $3050 \text{ rpm}$ , for increased radial clearance ( $1 \mu\text{m}$ ). For  $0.5 \mu\text{m}$  radial clearance (Fig. 4.59), the peak develops at  $9300 \text{ rpm}$ . This shift in peak points to an increase in the value of stiffness as clearance decreases. A comparison of Figs. 4.41 and 4.59 shows that the period-one unstable regions shift towards lower speed as the clearance is increases.

Two regions of period-one unstable response are shown in Fig. 4.59. Three regions of chaotic behavior are seen in the first region of unstable response. Period-one solution becomes unstable from  $945$  to  $5500 \text{ rpm}$ , because of period doubling bifurcations. The solution undergoes pitchfork bifurcations till  $2015 \text{ rpm}$  after which the chaotic solution is obtained at  $2050 \text{ rpm}$ . Figure 4.60 shows the nature of solution at  $1800 \text{ rpm}$ . The VC and its harmonic (super-harmonic) character of the frequency spectra is also brought-out by the Poincarè map with the closed orbits. The presence of dense regions in the orbit is indicative of the onset of chaos.

For the first chaotic region  $2050$  to  $3600 \text{ rpm}$ , the loss of stability is seen to be by the eigen values crossing  $+1$ . In this region, the period doubling bifurcations give way to chaos at about  $2050 \text{ rpm}$  and this chaotic region extends upto  $3600 \text{ rpm}$ . The chaotic solutions at  $2800 \text{ rpm}$  and  $3500 \text{ rpm}$  are shown in Figs. 4.61 and 4.62, respectively. The frequency spectrum has a dense band structure as seen in-between spikes of VC and its multiples. The fine-layered structure of the strange attractor is also clear from Poincarè maps.

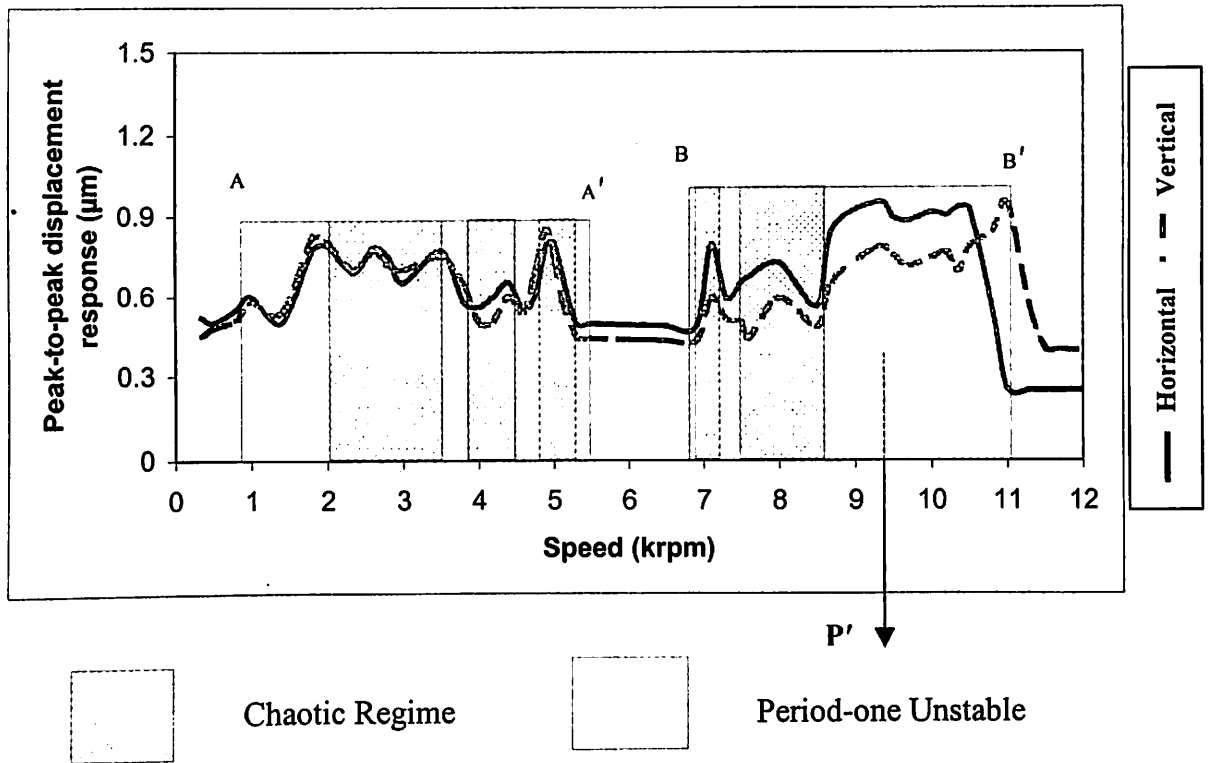


**Fig. 4.59** Response plot for  $\gamma_0 = 0.5 \mu\text{m}$  and  $W = 6\text{N}$

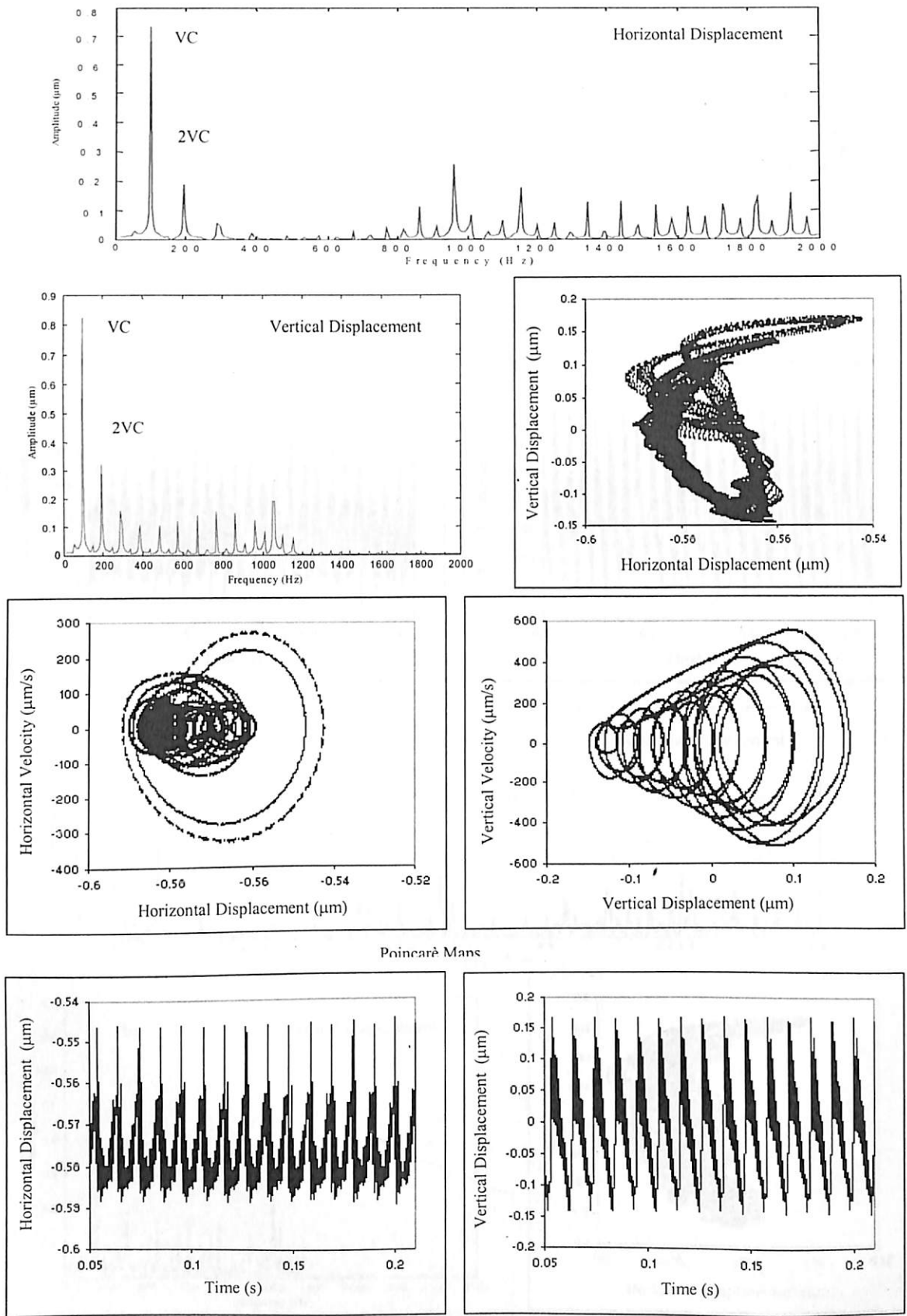
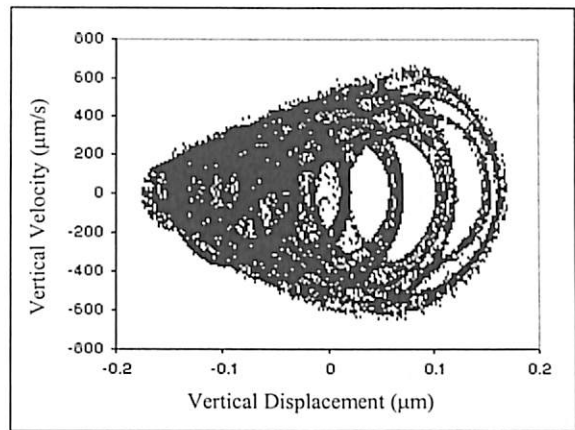
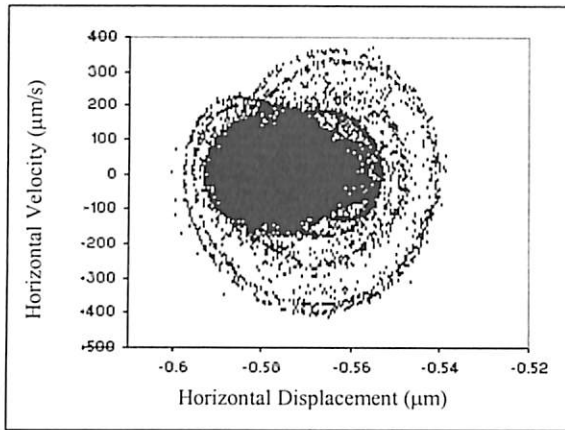


Fig. 4.60 Response at 1800 rpm for  $\gamma_0 = 0.5 \mu\text{m}$ ,  $W = 6\text{N}$



Poincaré Maps

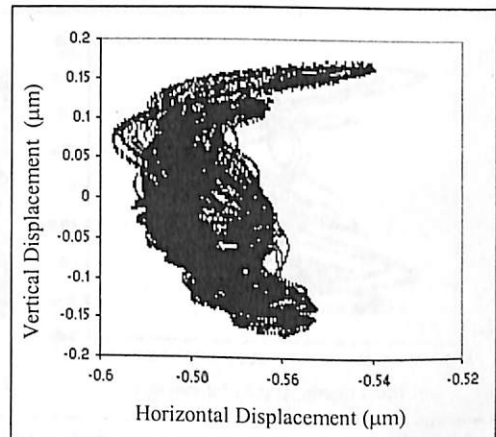
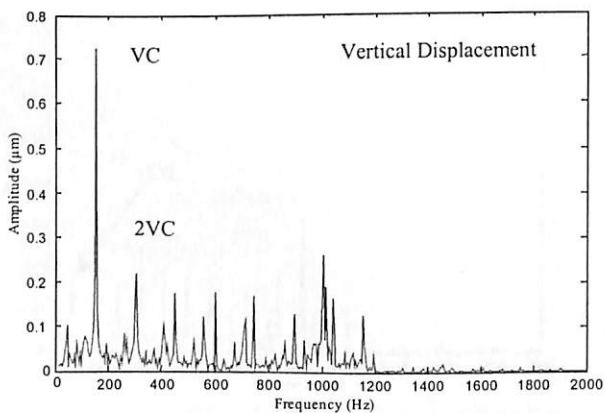
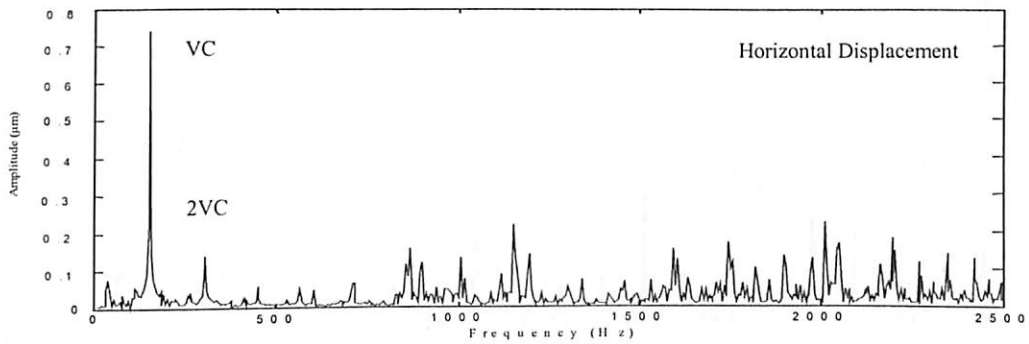
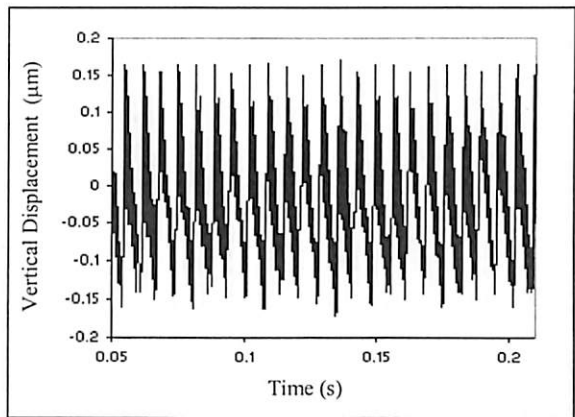
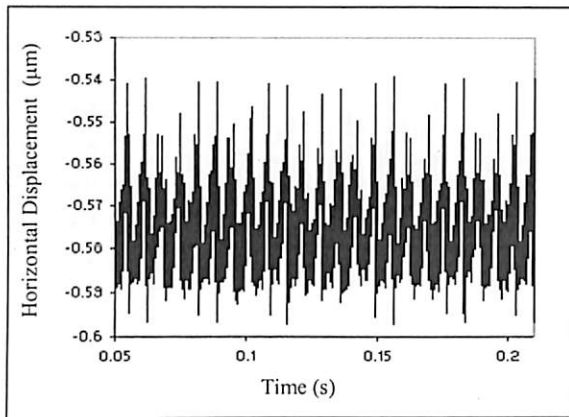


Fig. 4.61 Response at 2800 rpm for  $\gamma_0 = 0.5 \mu\text{m}$ ,  $W = 6\text{N}$

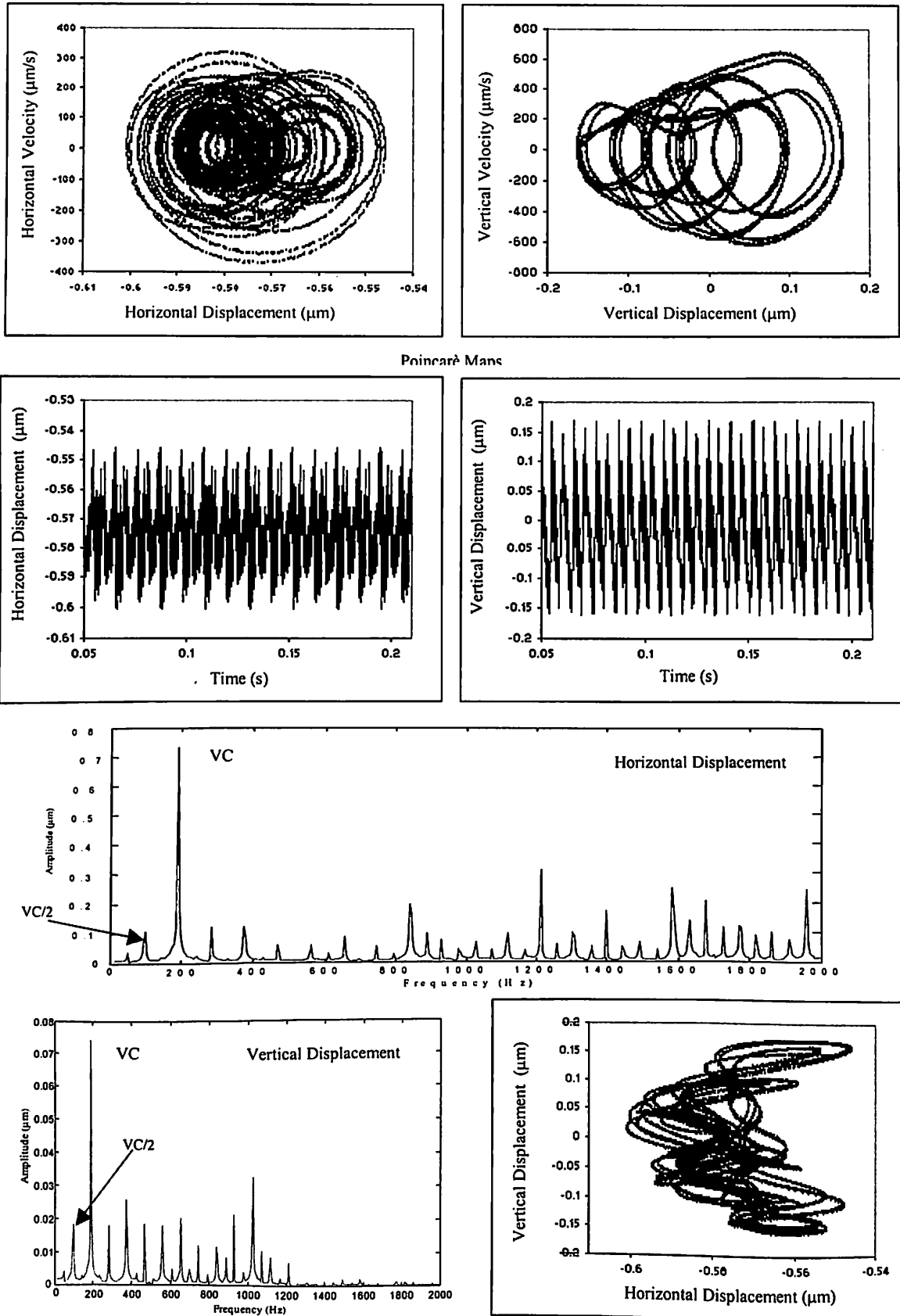


Fig. 4.62 Response at 3500 rpm for  $\gamma_0 = 0.5 \mu\text{m}$ ,  $W = 6\text{N}$

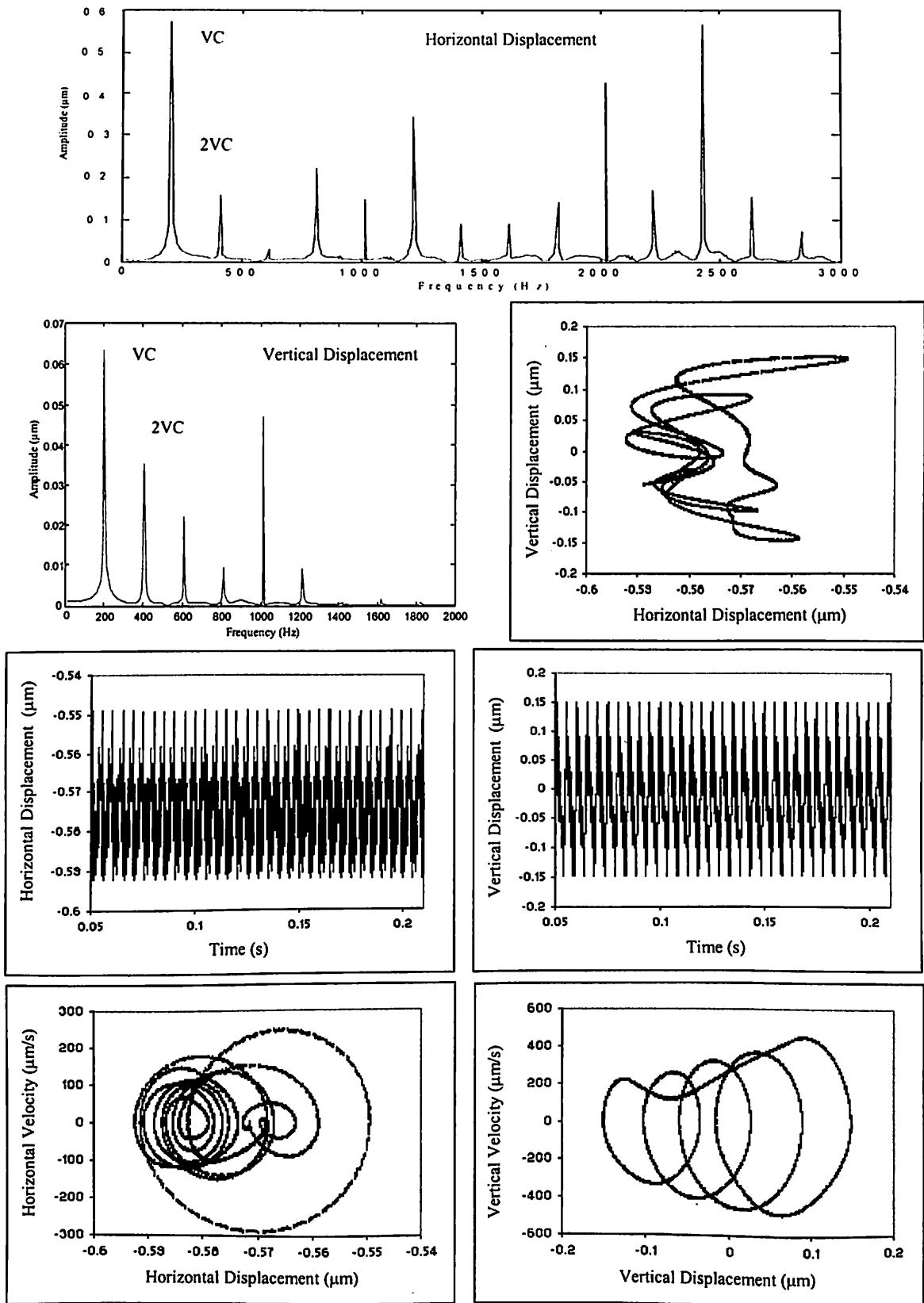
Further increase in speed causes a return of stability in the speed range from 3660 rpm to 3850 rpm. At 3800 rpm, the response becomes periodic as shown by the spectra of Fig. 4.63. The VC and its harmonic (super-harmonic) character of the frequency spectra is also brought-out by the Poincarè map with the multiloop orbit. The multiloop orbit also shows a periodic nature. The solution undergoes pitchfork bifurcations (1T) till 3850 rpm after which the second chaotic solution is obtained at 3915 rpm. Below 4000 rpm the response is period-one stable. Period doubling bifurcation gives way to chaos at 4000 rpm (Fig. 4.64). The chaotic attractor is spread out and the band of frequency in the spectrum formed is also quite prominent. This chaotic region extends upto 4350 rpm.

As speed increases, stability returns via a torus solution, which is clear from the multiloop orbit of Poincarè map at 4900 rpm as shown in Fig. 4.65. From 4920 rpm, again pitchfork bifurcation takes place leading to the occurrence of a third chaotic region from 4950 rpm to 5400 rpm. In this region, the period doubling bifurcations give way to chaos at about 5000 rpm as shown in Fig. 4.66 and this chaotic region extends upto 5400 rpm. Figure 4.67 shows the chaotic solution at 5100 rpm.

From 5450 rpm to 6850 rpm there is period-one stable response as shown earlier in Fig. 4.59. From 6900 rpm, pitchfork bifurcation takes place and again that leads to the first chaotic region from 6980 rpm to 7050 rpm. In this region, the period doubling bifurcations give way to chaos at about 7000 rpm as shown in Fig. 4.68. The chaotic nature is shown by the band structure of frequencies and also the layered structure of the Poincarè map at 7000 rpm. The presence of dense regions in the orbit is indicative of the onset of chaos. The chaotic region extends upto 7050 rpm after which the solution has a 2-T periodic response obtained at 7100 rpm as shown in Fig. 4.69.

The second chaotic region starts from 7215 rpm and extends upto 8620 rpm. The chaotic solutions at 7300, 7600 and 8500 rpm are shown in Figs. 4.70 to 4.72 respectively. The frequency spectrum has a dense band structure as seen in-between spikes of VC and its multiples. The fine-layered structure of the strange attractor is also clear from Poincarè maps. The orbit at this speed does not repeat itself. The Poincarè maps of chaotic solutions have fractal structures that repeat as the map is magnified. The time responses also show beat and chaos like behavior. It is clear that loss of periodicity is the characteristic feature of chaotic solution.





Poincaré Maps

Fig. 4.63 Response at 3800 rpm for  $\gamma_0 = 0.5 \mu\text{m}$ ,  $W = 6\text{N}$

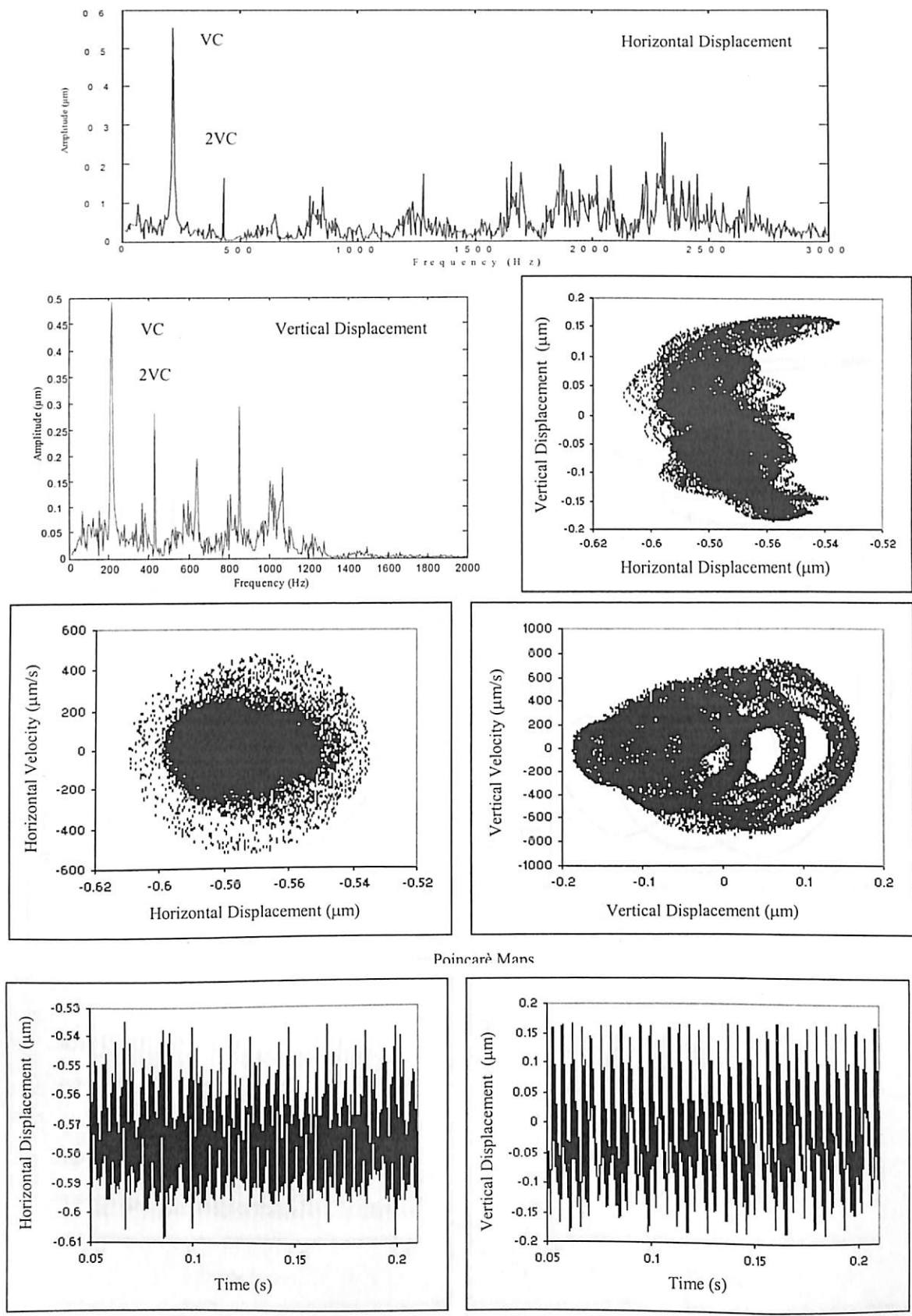


**Fig. 4.64** Response at 4000 rpm for  $\gamma_0 = 0.5 \mu\text{m}$ ,  $W = 6\text{N}$

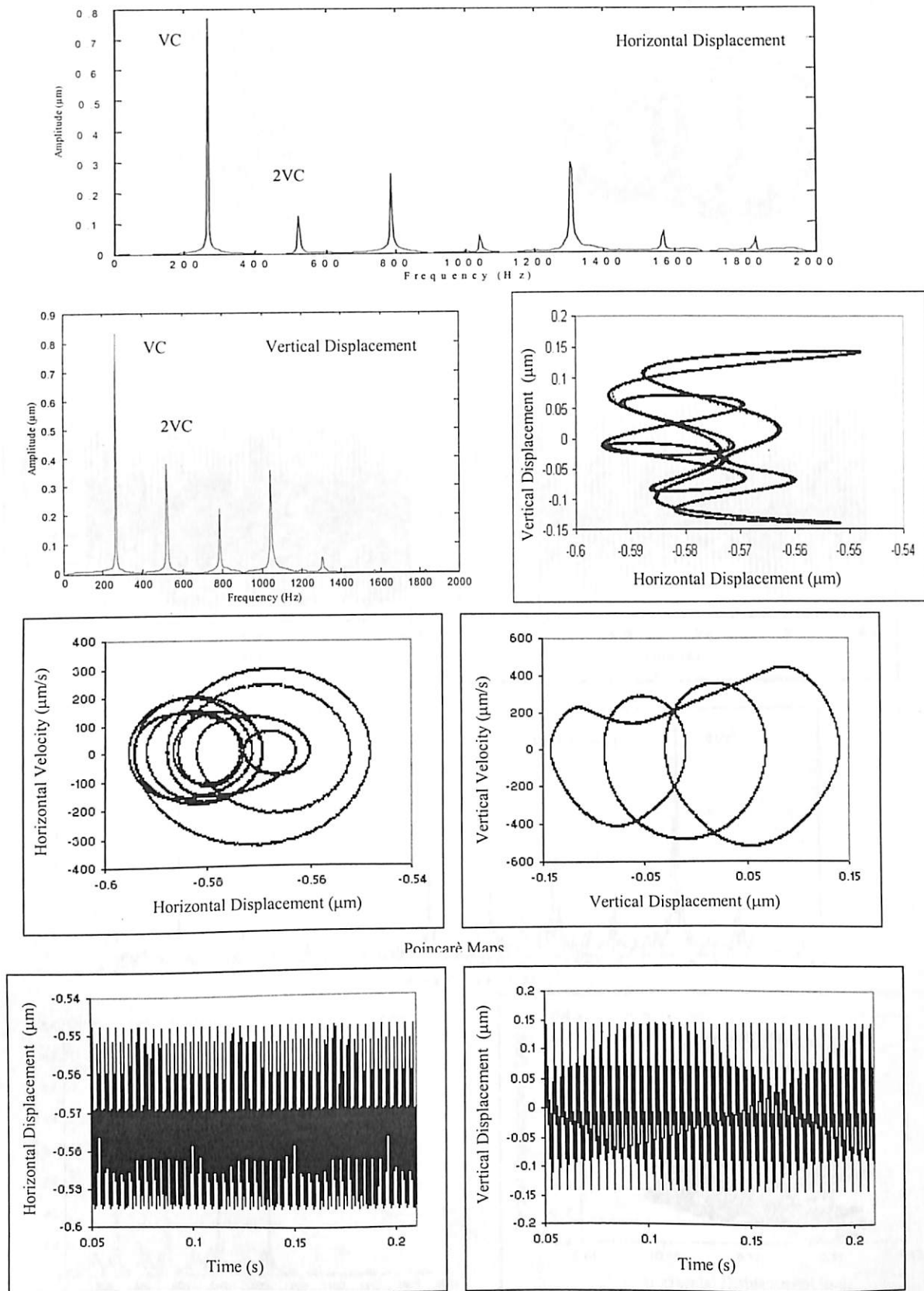
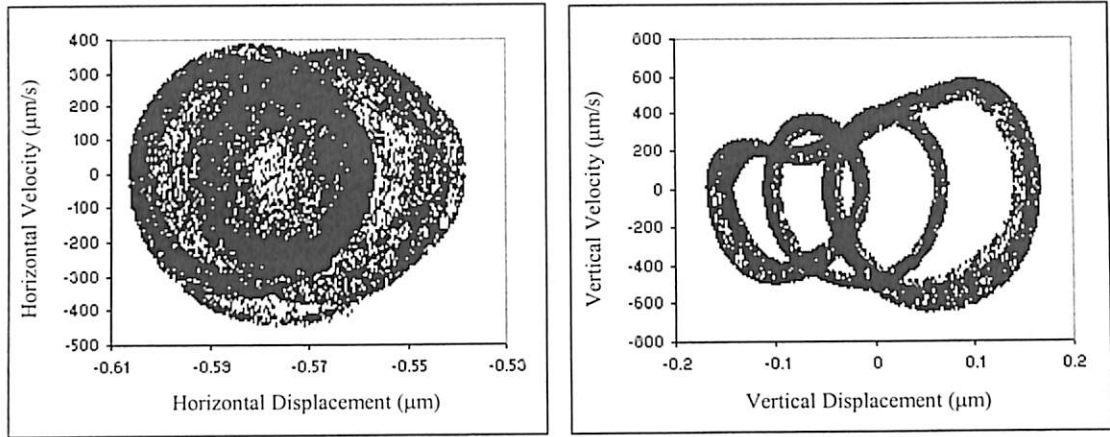


Fig. 4.65 Response at 4900 rpm for  $\gamma_0 = 0.5 \mu\text{m}$ ,  $W = 6\text{N}$



Poincaré Maps

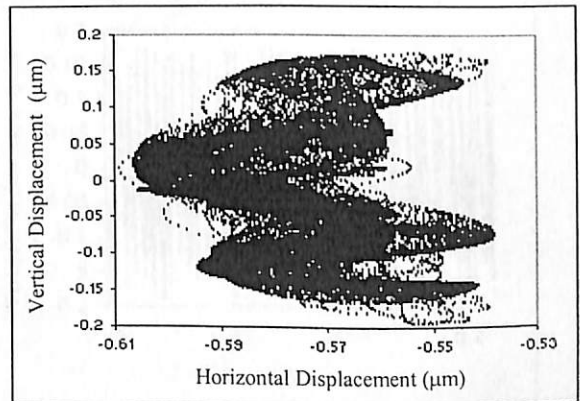
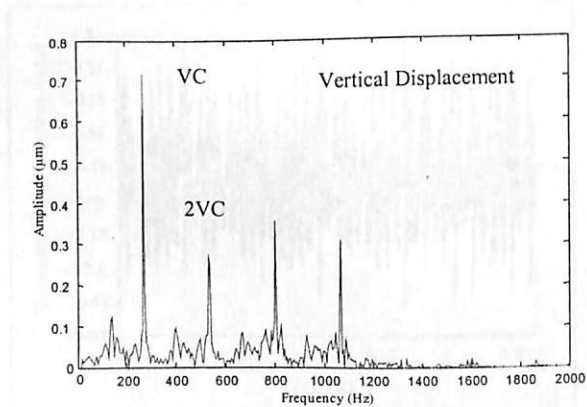
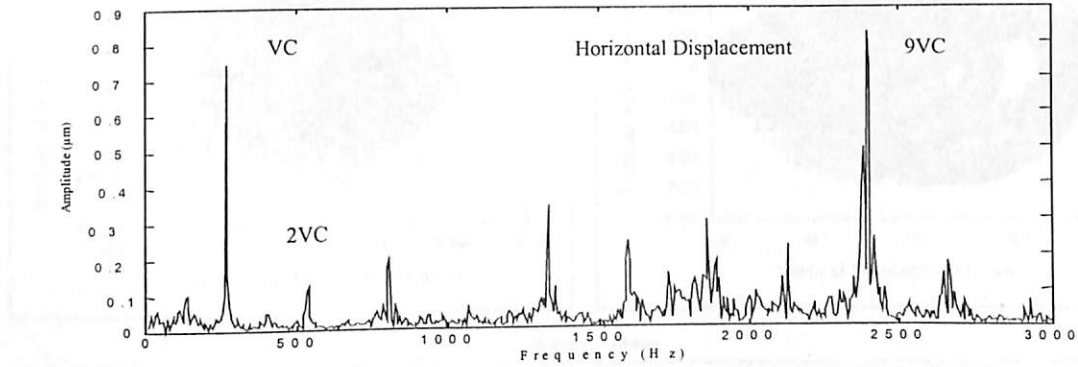
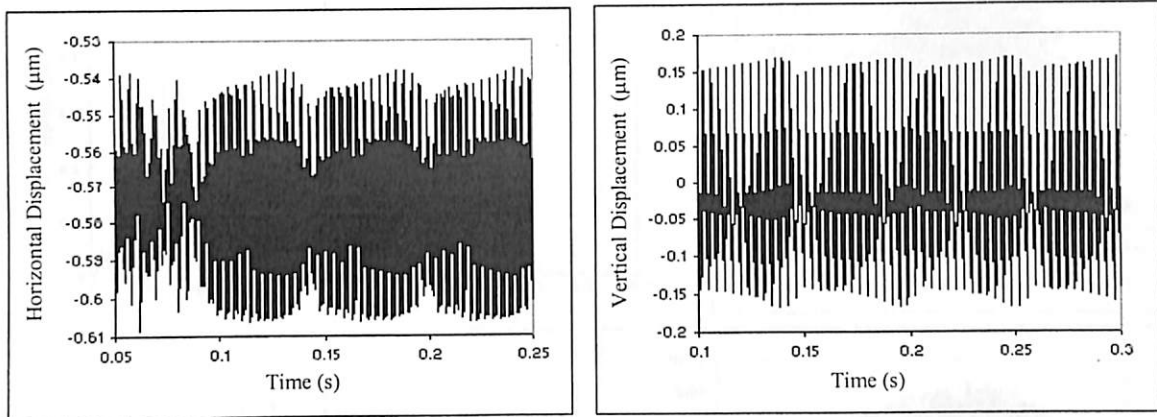


Fig. 4.66 Response at 5000 rpm for  $\gamma_0 = 0.5 \mu\text{m}$ ,  $W = 6\text{N}$

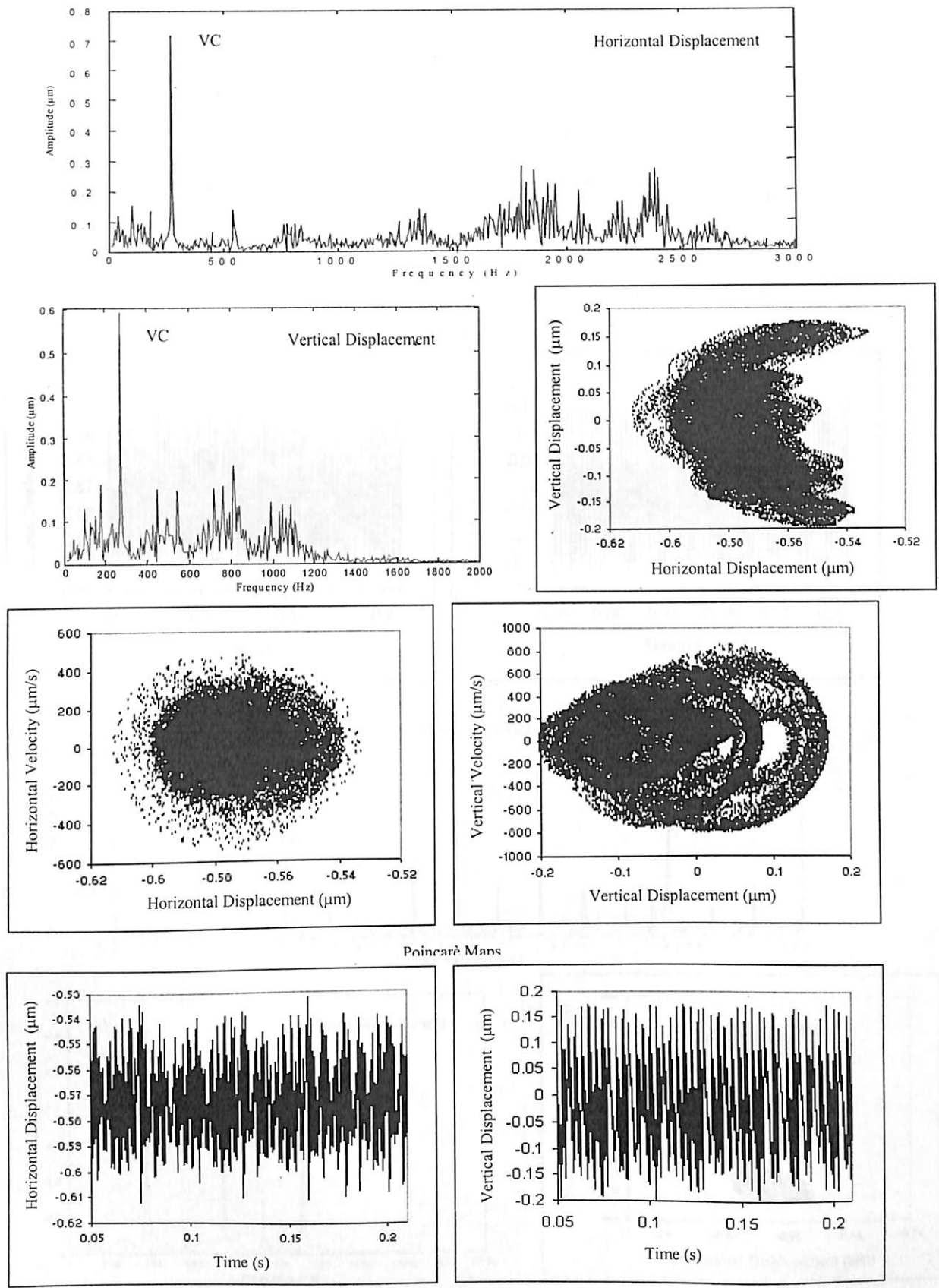
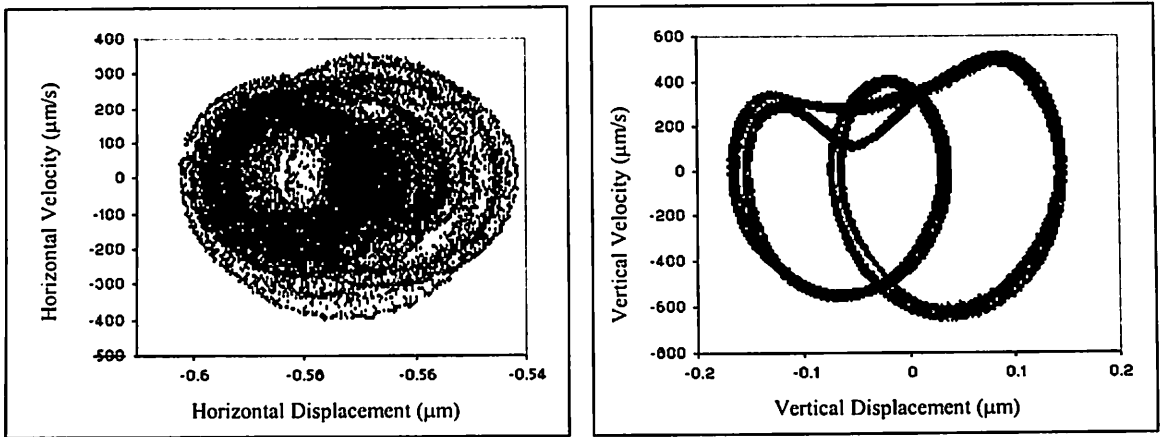


Fig. 4.67 Response at 5100 rpm for  $\gamma_0 = 0.5 \mu\text{m}$ ,  $W = 6\text{N}$



Poincaré Maps

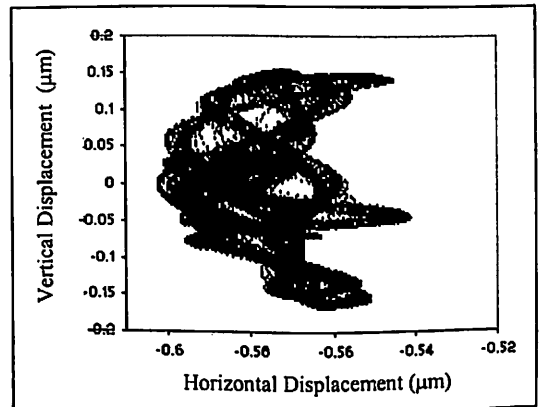
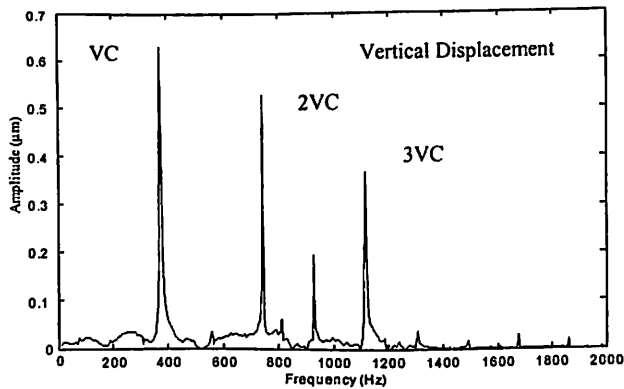
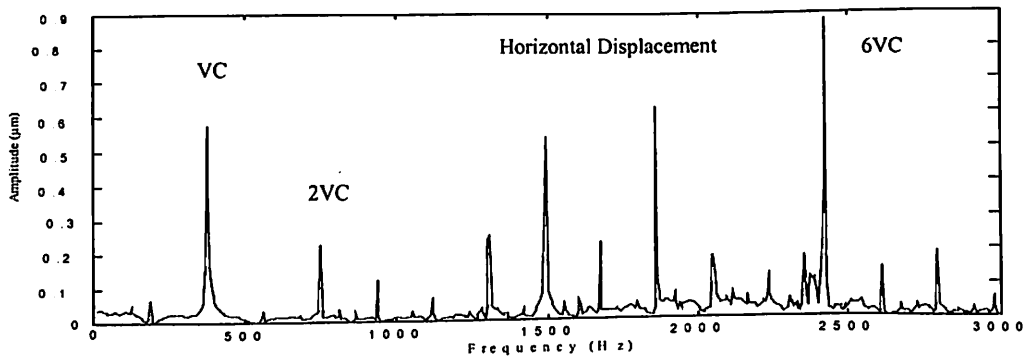
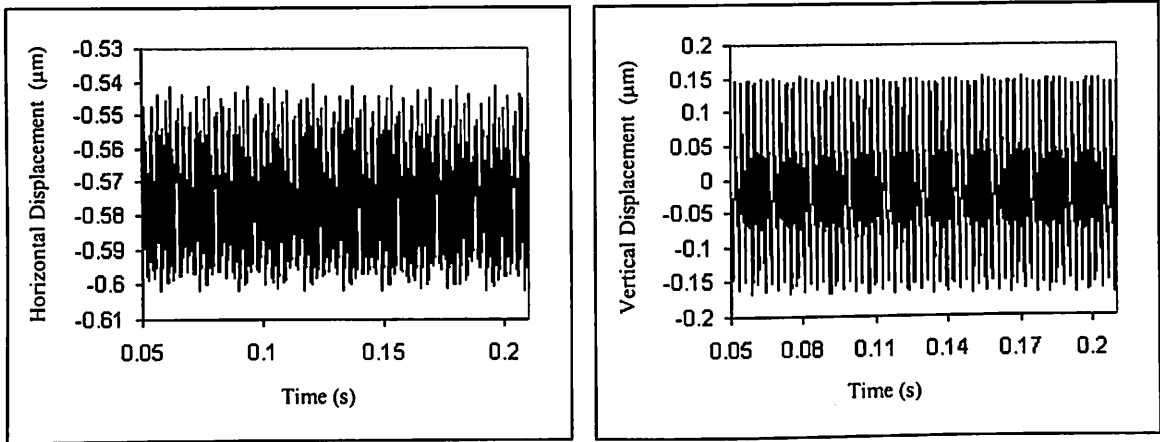
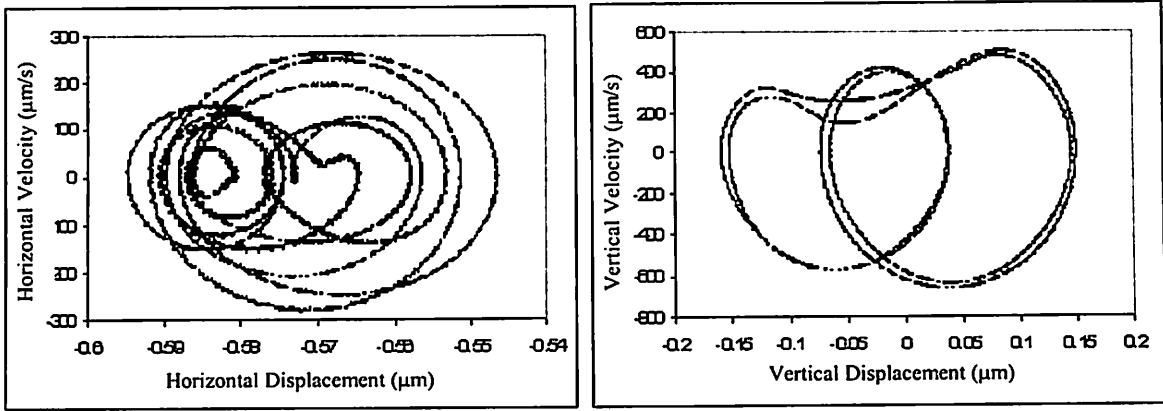


Fig. 4.68 Response at 7000 rpm for  $\gamma_0 = 0.5 \mu\text{m}$ ,  $W = 6\text{N}$



Poincaré Maps

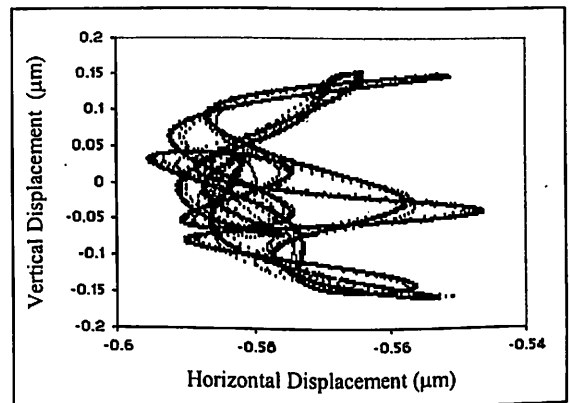
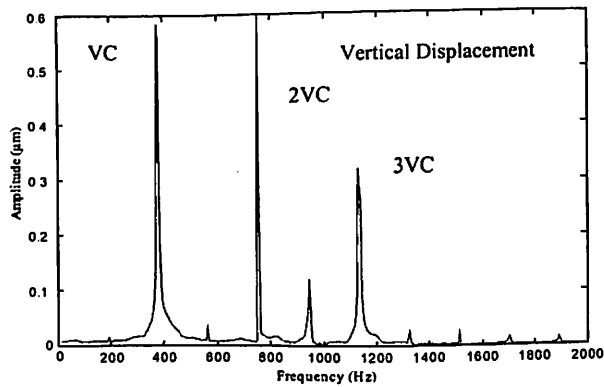
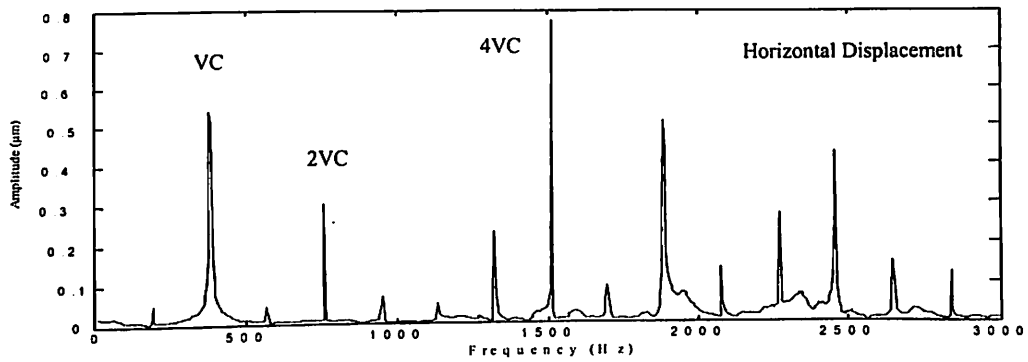
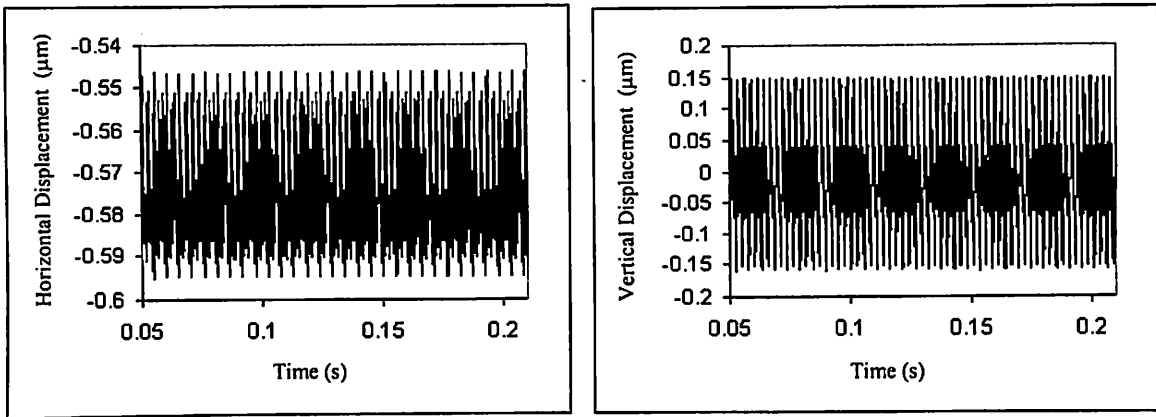
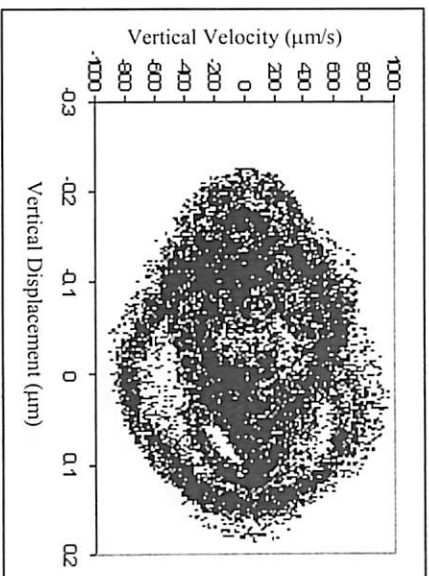
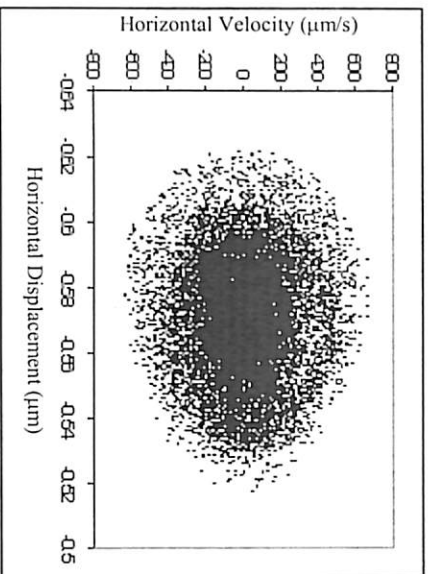


Fig. 4.69 Response at 7100 rpm for  $\gamma_0 = 0.5 \mu\text{m}$ ,  $W = 6\text{N}$



Poincaré Maps

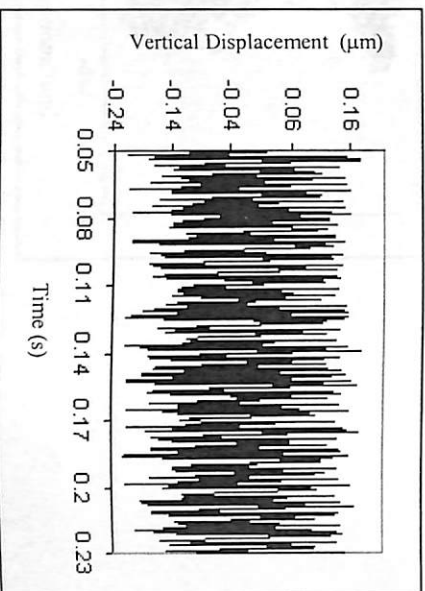
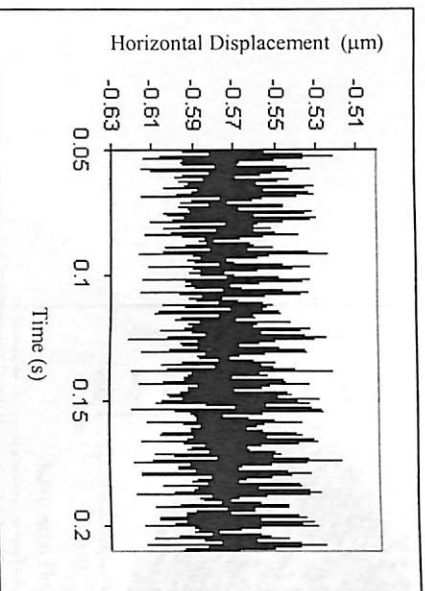
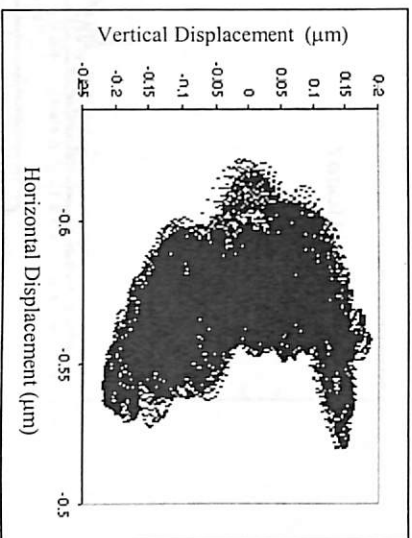
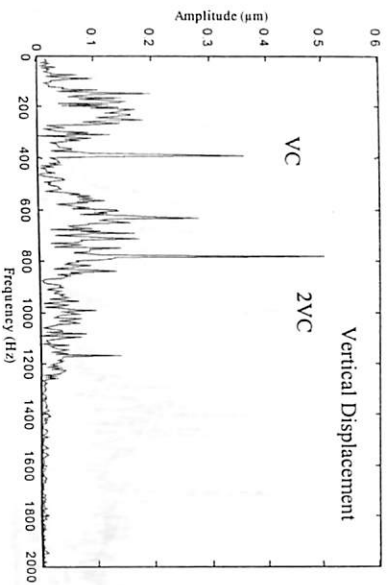
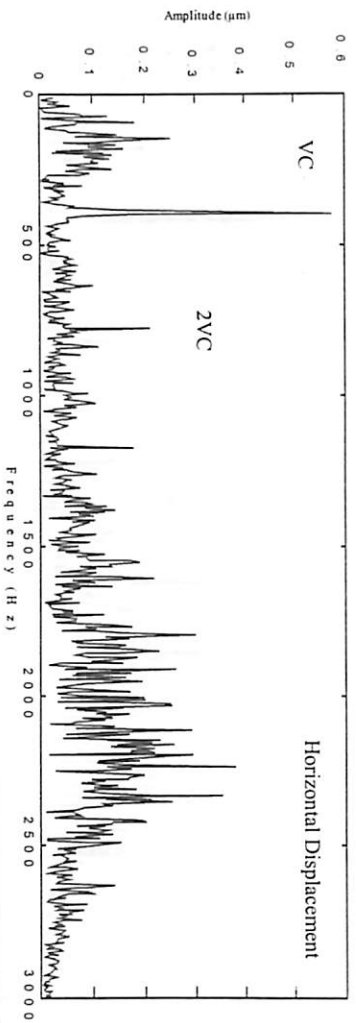
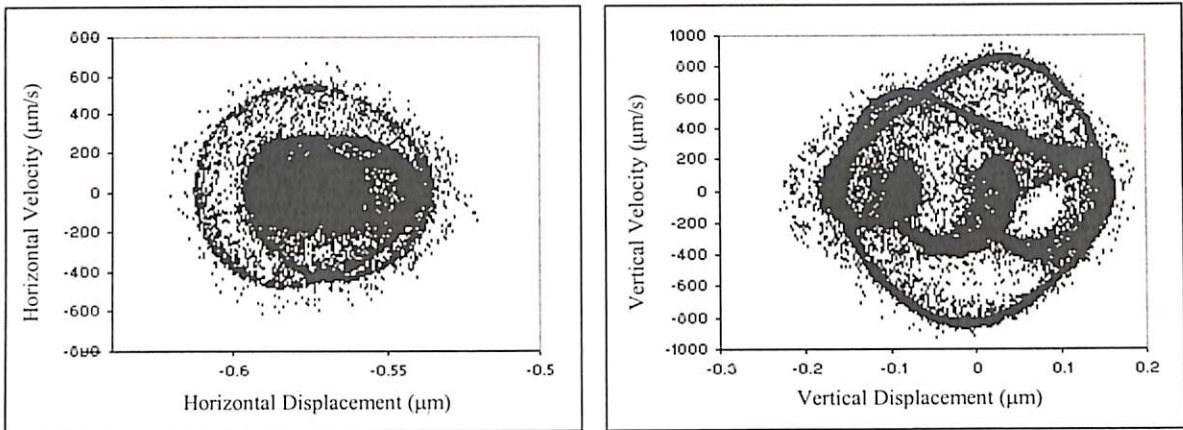


Fig. 4.70 Response at 7300 rpm for  $\gamma_0 = 0.5 \mu\text{m}$ ,  $W = 6\text{N}$





Poincaré Maps

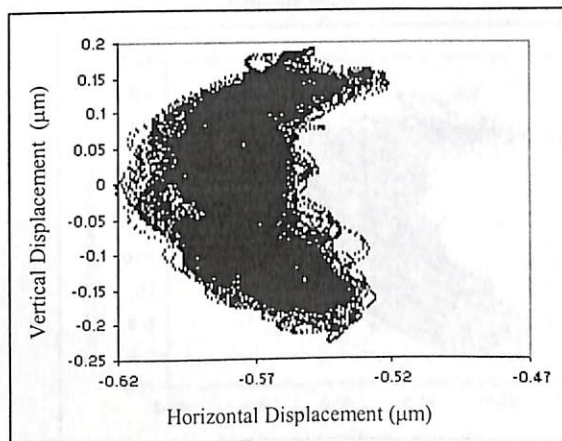
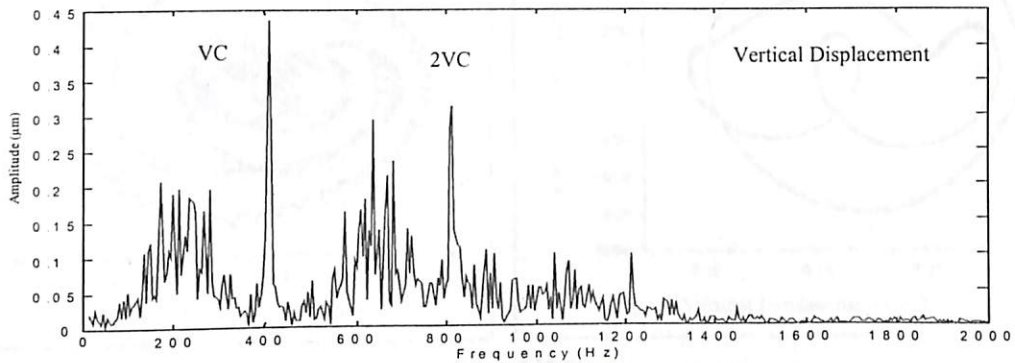
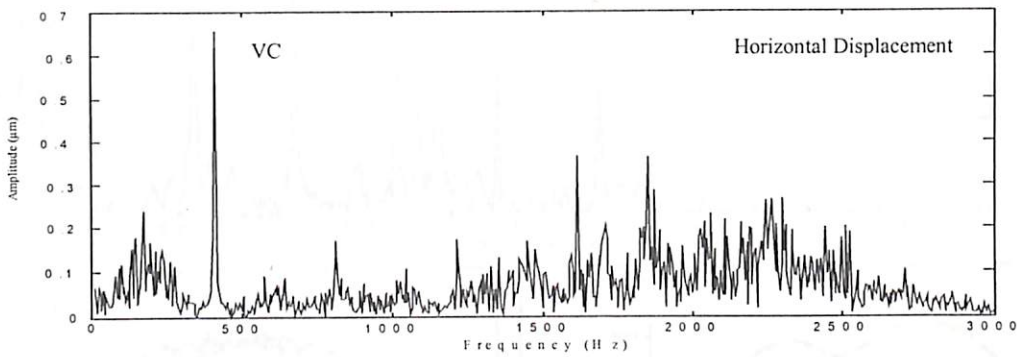


Fig. 4.71 Response at 7600 rpm for  $\gamma_0 = 0.5 \mu\text{m}$ ,  $W = 6\text{N}$

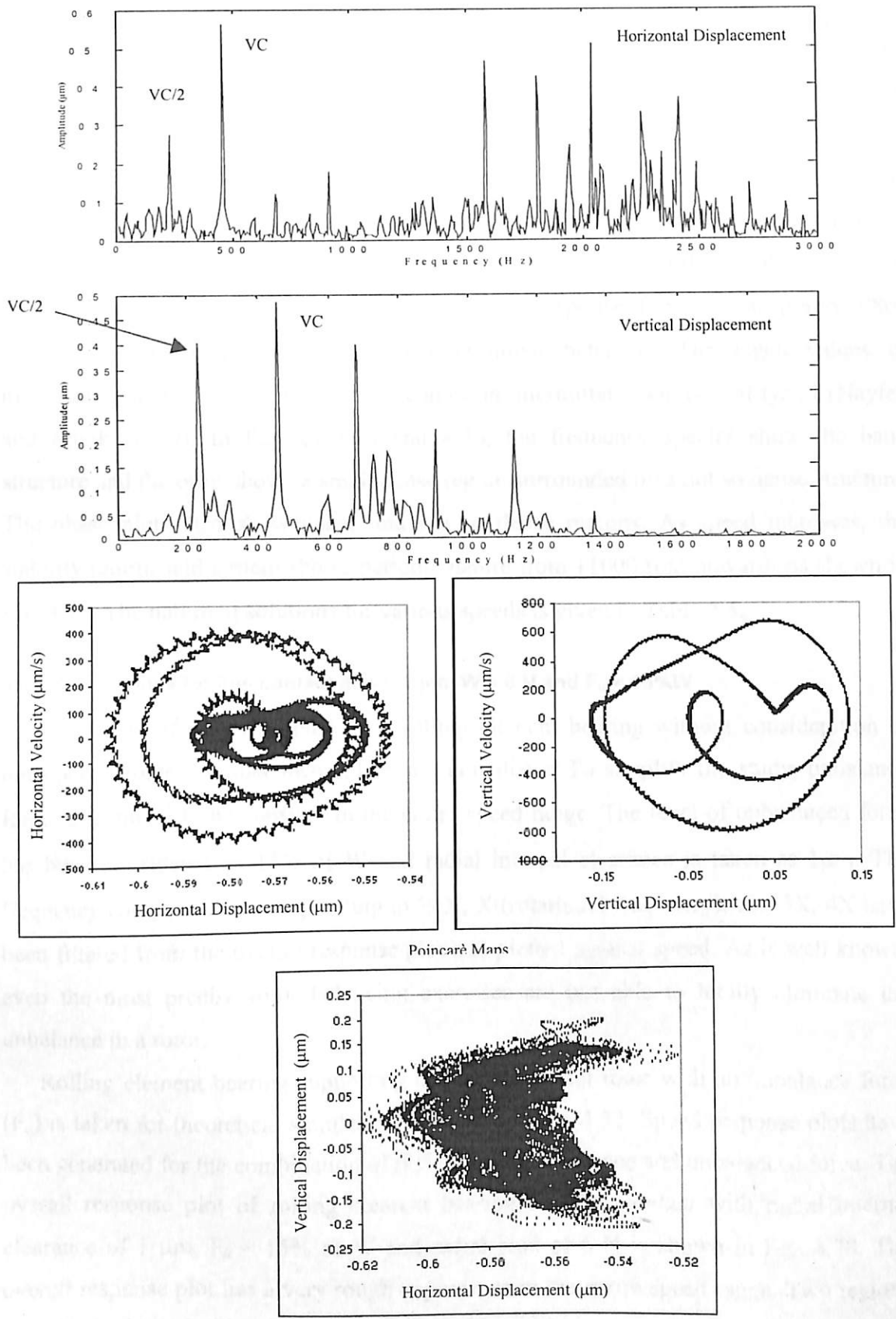


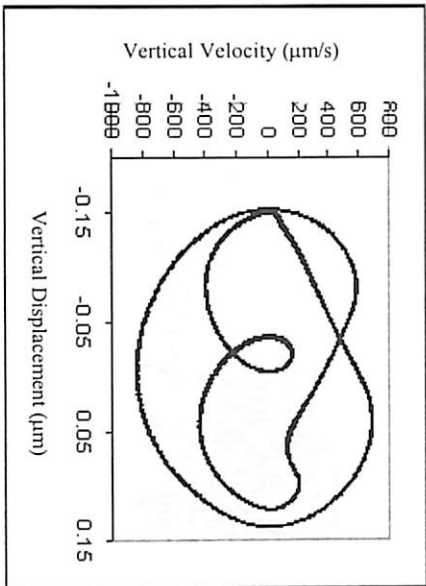
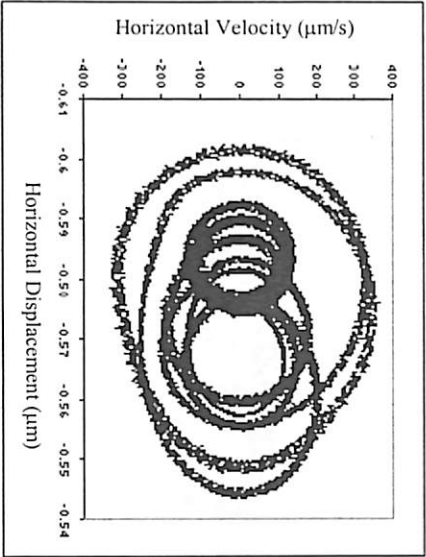
Fig. 4.72 Response at 8500 rpm for  $\gamma_0 = 0.5 \mu\text{m}$ ,  $W = 6\text{N}$

The response characteristics at 8700 rpm and at 9300 rpm are shown in Figures 4.73 and 4.74 respectively. The horizontal and vertical displacement spectra have band structure and closed orbits with dense and not so dense regions. Analysis has shown that the chaotic character becomes weaker from 8650 rpm to 9500 rpm. The responses shown in Figs. 4.73 and 4.74 can be considered neither perfectly chaotic nor perfectly periodic. It is not perfectly or predominantly chaotic because the two spectra for horizontal and vertical displacements have only a slightly banded structure. The orbits in Poincarè maps are complicated because of this mixed nature of the response. From 10500 rpm to 10800 rpm, the response explodes into an intermittent behavior. The eigen values of monodromy matrix cross +1, so this becomes an intermittent behavior of type I (Nayfeh and Mook, 1979). In Figures 4.75 and 4.76, the frequency spectra show the band structure and the orbit shows a small dense region surrounded by a not so dense structure. The phase plots also show dense and not so dense regions. As speed increases, the stability returns and system shows periodic nature from 11000 rpm onwards as shown in Fig. 4.77. The nature of solutions for various speeds is given in Table 4.5.

#### 4.5.2.6 Response for line contact at $\gamma_0 = 1 \mu\text{m}$ , $W = 6 \text{ N}$ and $F_u = 15\%W$

Any study of rotors supported on rolling element bearing without consideration of unbalanced force is rather incomplete and unrealistic. To simplify the study, unbalance force is assumed to be constant in the entire speed range. The level of unbalanced force has been considered as 15% of  $W$  and radial internal clearance is taken as  $1 \mu\text{m}$ . The frequency components corresponding to  $\frac{1}{2}X$ ,  $X$  (rotational frequency),  $2X$ ,  $3X$ ,  $4X$  have been filtered from the overall response plot and plotted against speed. As is well known, even the most precise rotor balancing exercises are not able to totally eliminate the unbalance in a rotor.

Rolling element bearing supporting a rigid horizontal rotor with an unbalance force ( $F_u$ ) is taken for theoretical simulation as shown in Fig. 4.32. Speed response plots have been generated for the combination of radial internal clearance and unbalanced force. The overall response plot of rolling element bearing for *line contact* with radial internal clearance of  $1 \mu\text{m}$ ,  $F_u = 15\%$  of  $W$  and radial load of  $6 \text{ N}$  is shown in Fig. 4.78. The overall response plot has a very rough appearance in the entire speed range. Two regions bounded by lines A-A' and B-B' are shown in Fig. 4.78.



Poincaré Maps

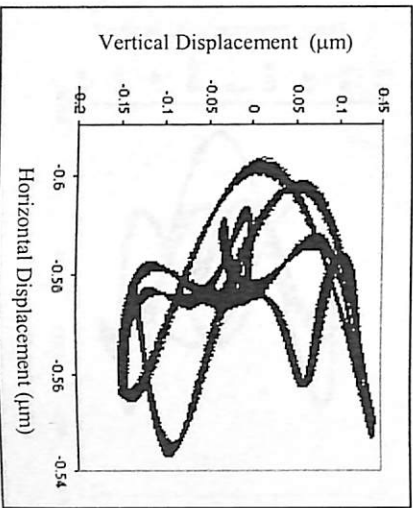
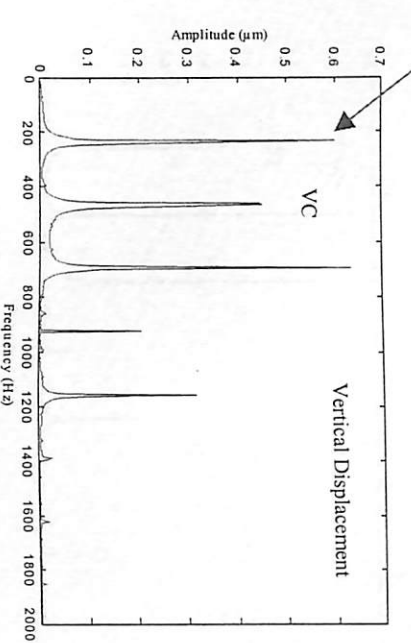
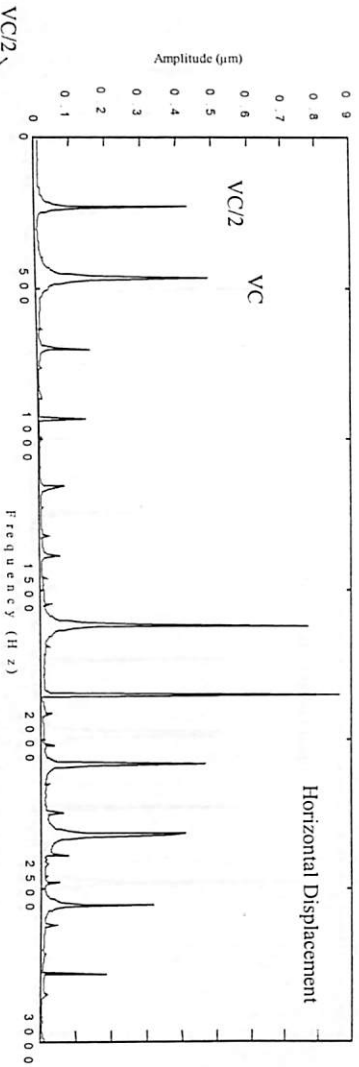
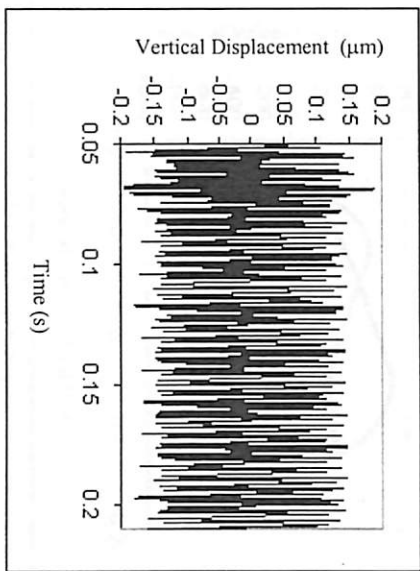
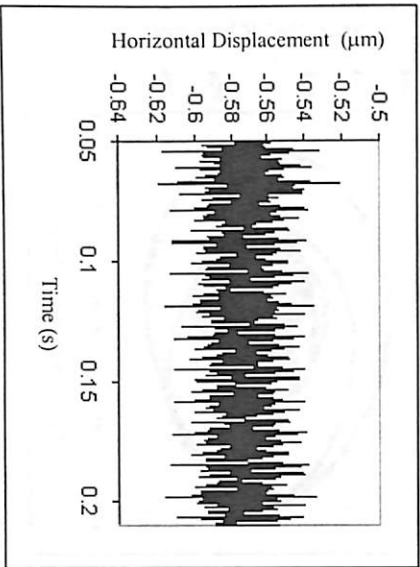
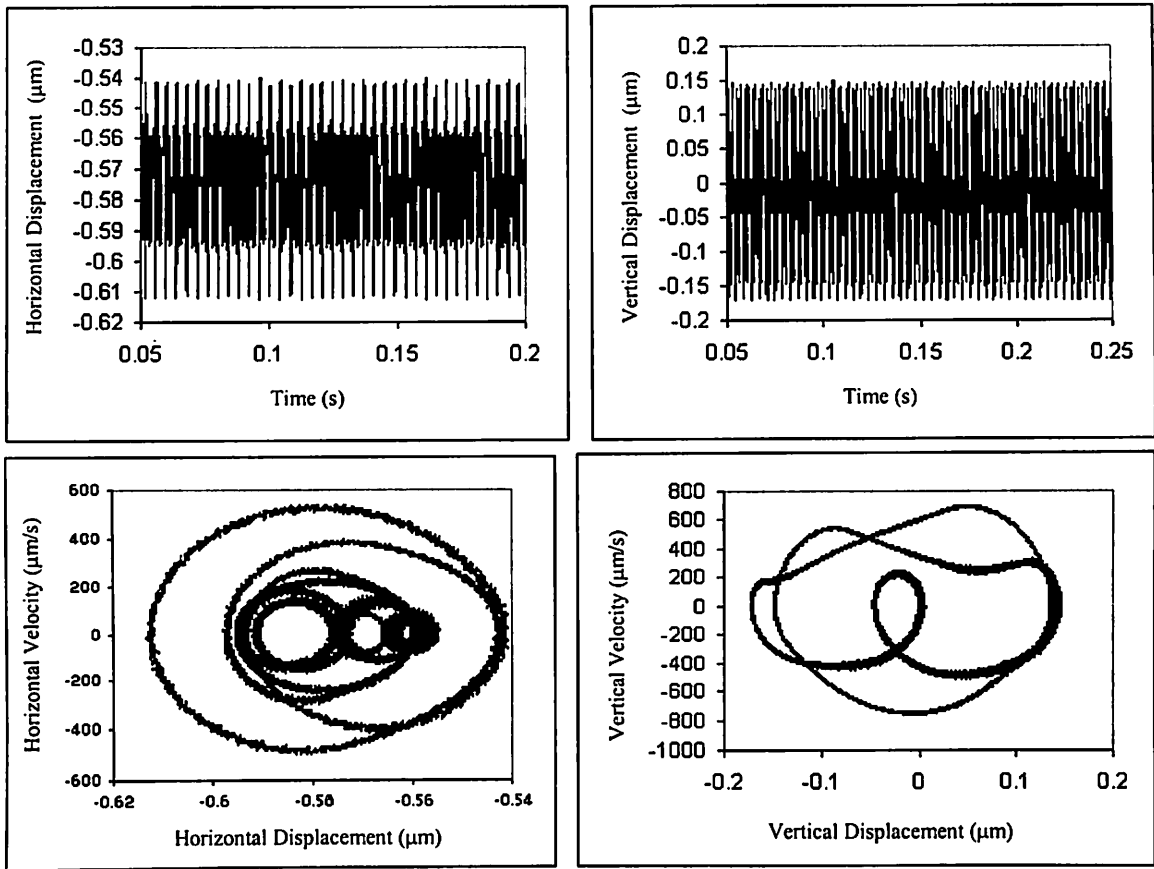


Fig. 4.73 Response at 8700 rpm for  $\gamma_0 = 0.5 \mu\text{m}$ ,  $W = 6\text{N}$



Poincaré Maps

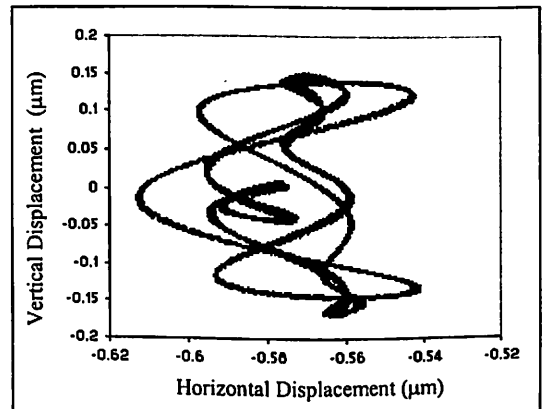
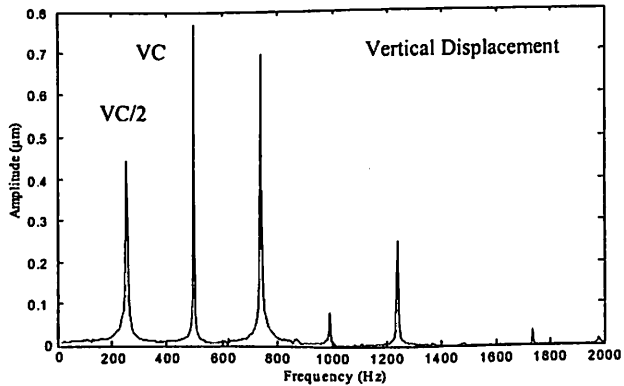
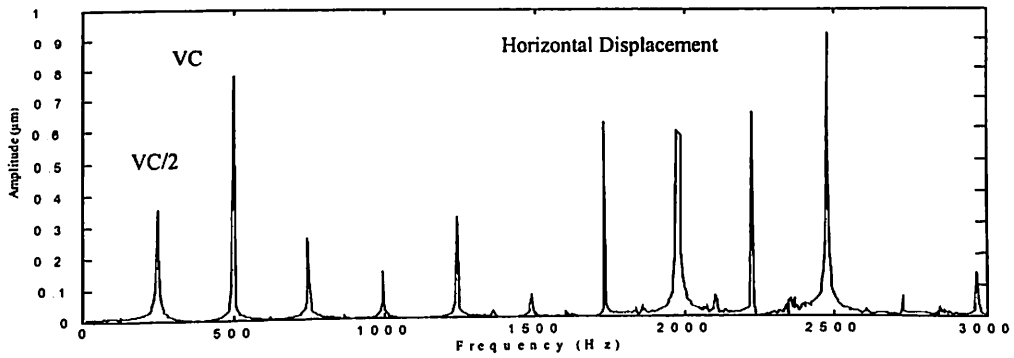
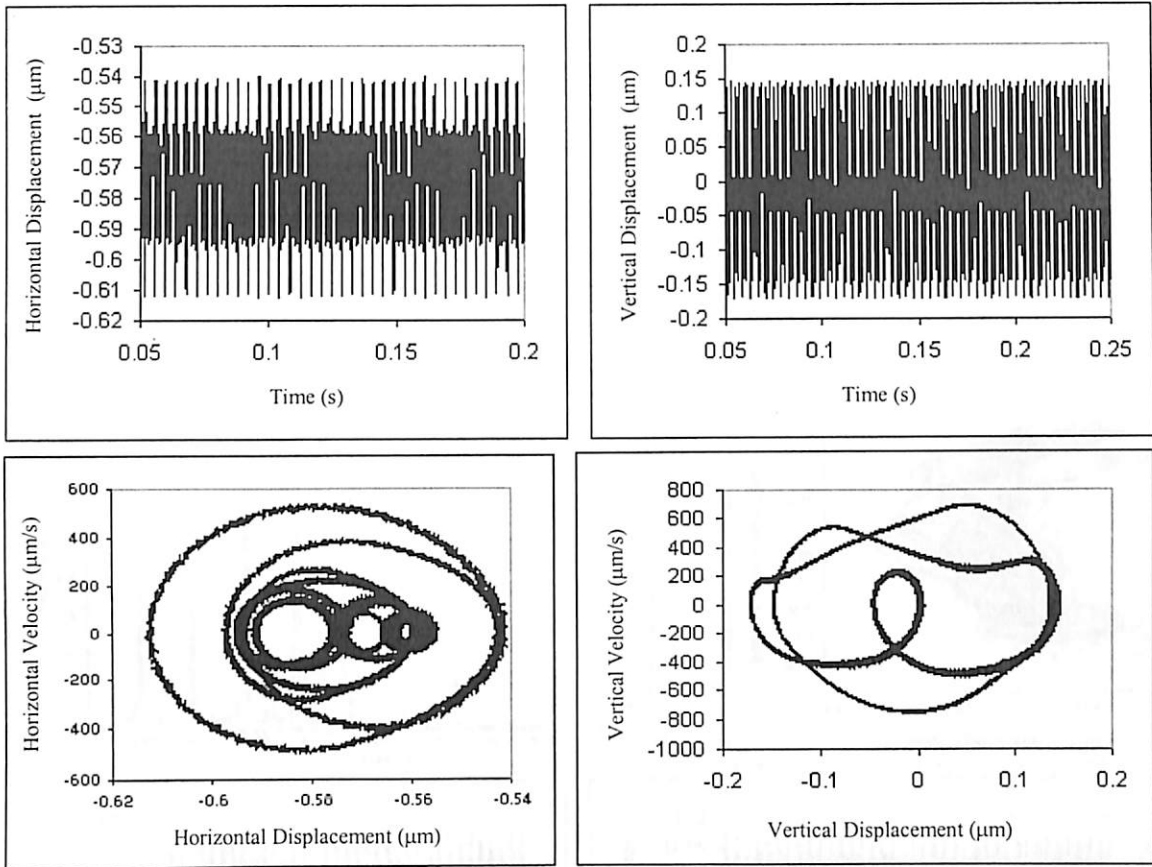


Fig. 4.74 Response at 9300 rpm for  $\gamma_0 = 0.5 \mu\text{m}$ ,  $W = 6\text{N}$



Poincaré Map

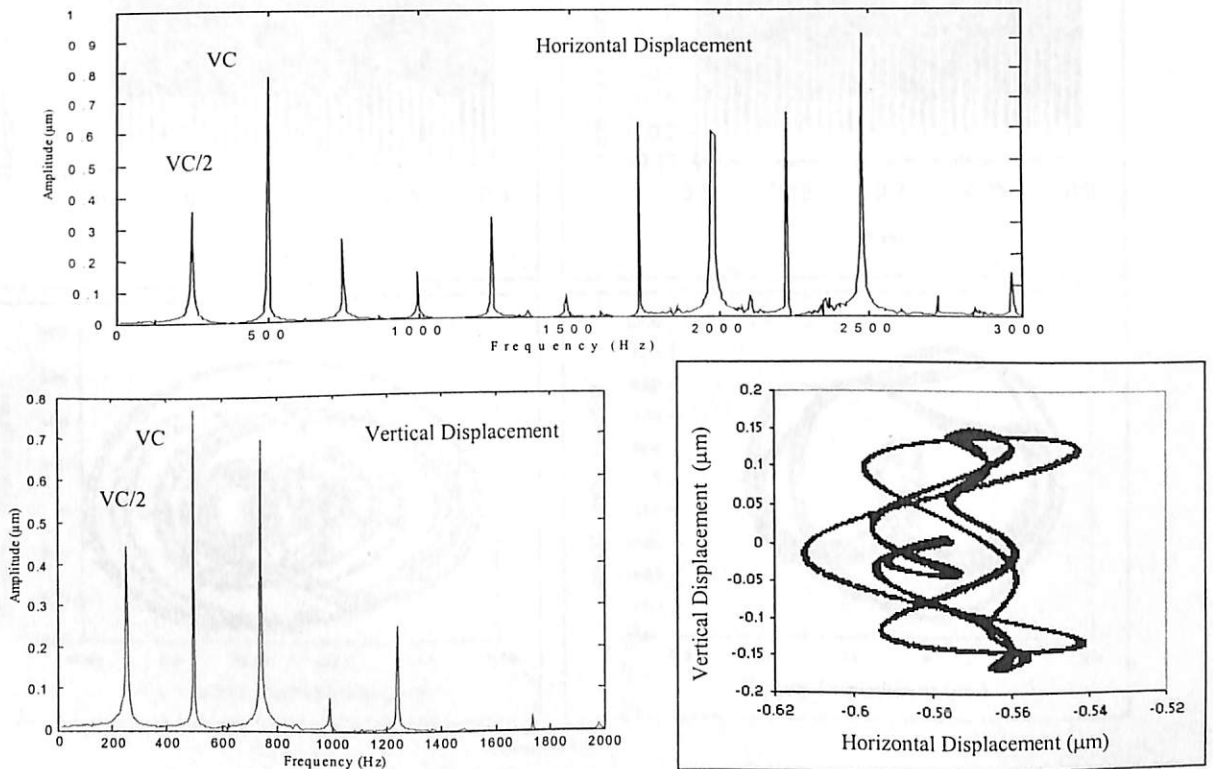
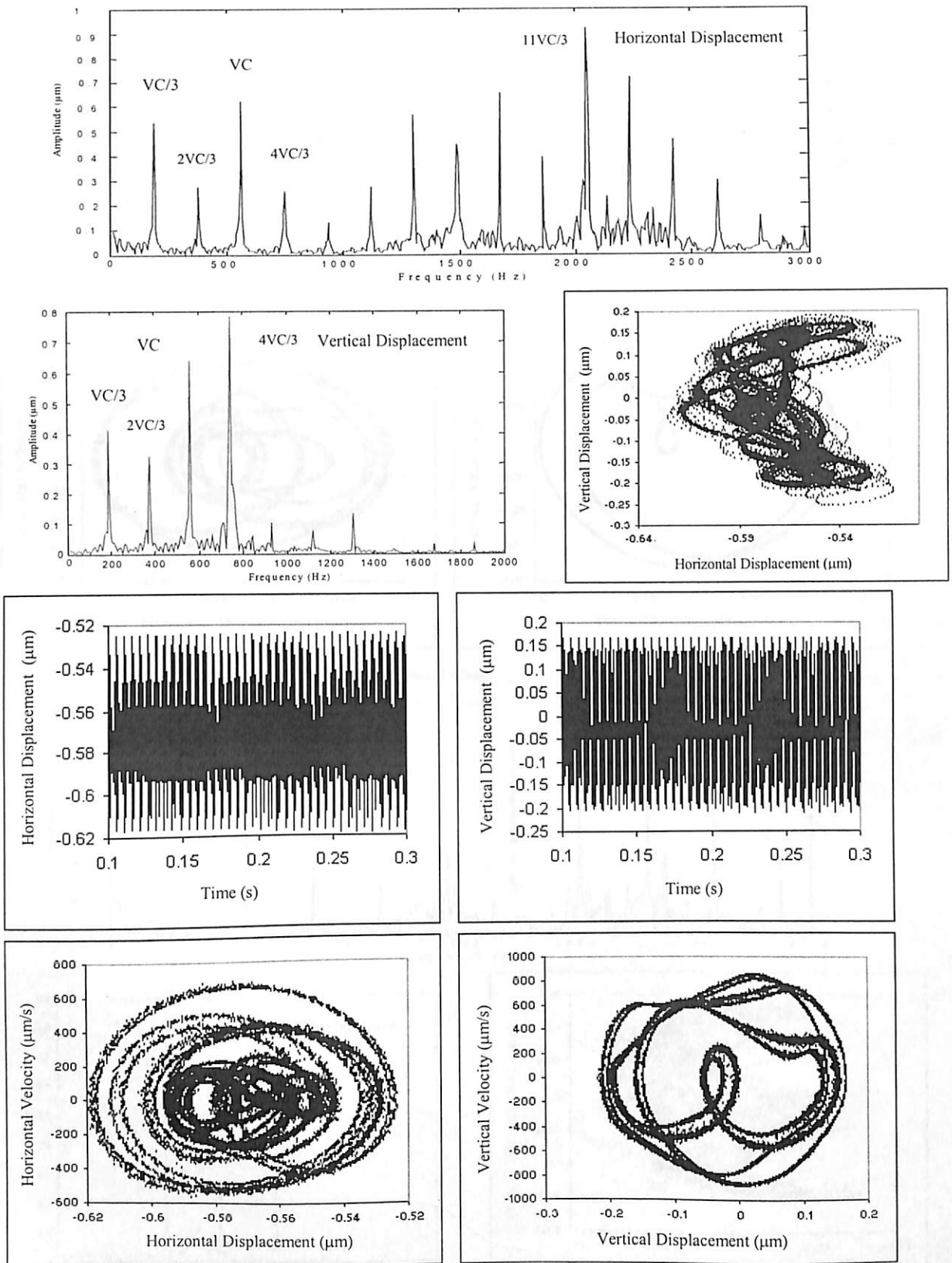
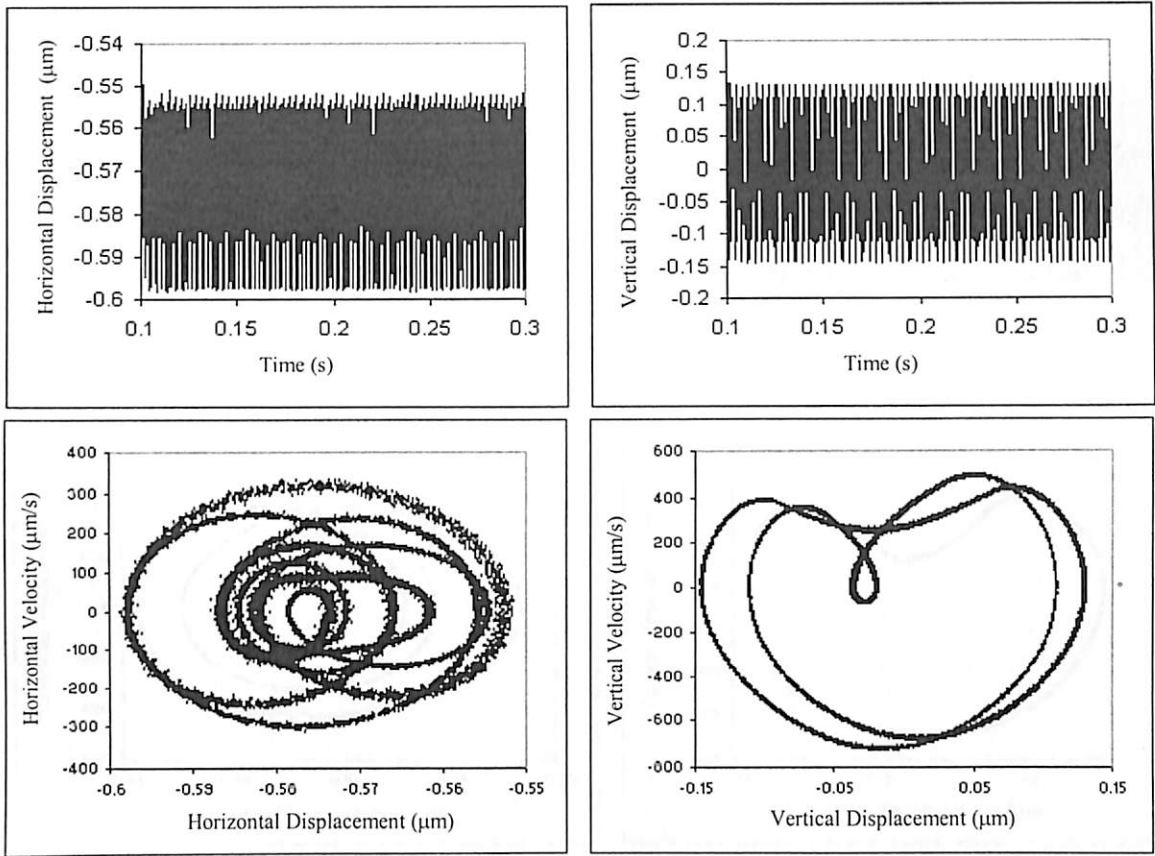


Fig. 4.74 Response at 9300 rpm for  $\gamma_0 = 0.5 \mu\text{m}$ ,  $W = 6\text{N}$



Poincaré Maps

Fig. 4.75 Response at 10500 rpm for  $\gamma_0 = 0.5 \mu\text{m}$ ,  $W = 6\text{N}$



Poincaré Maps

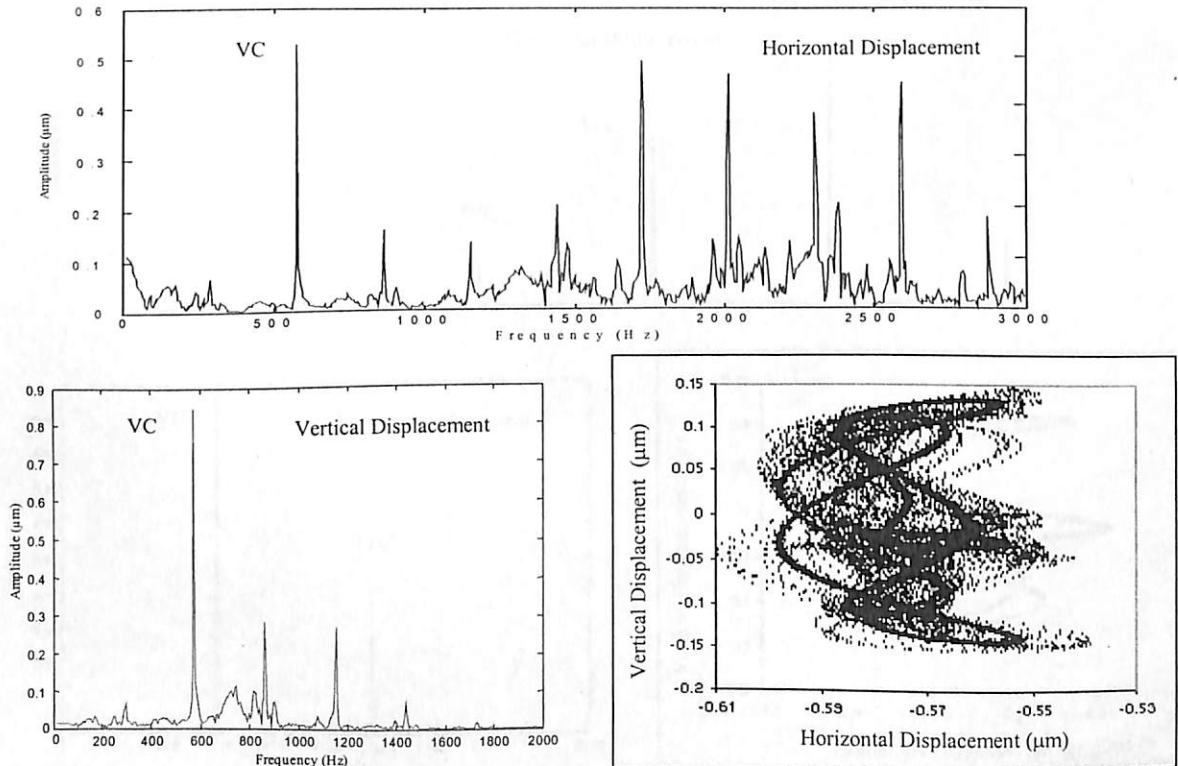
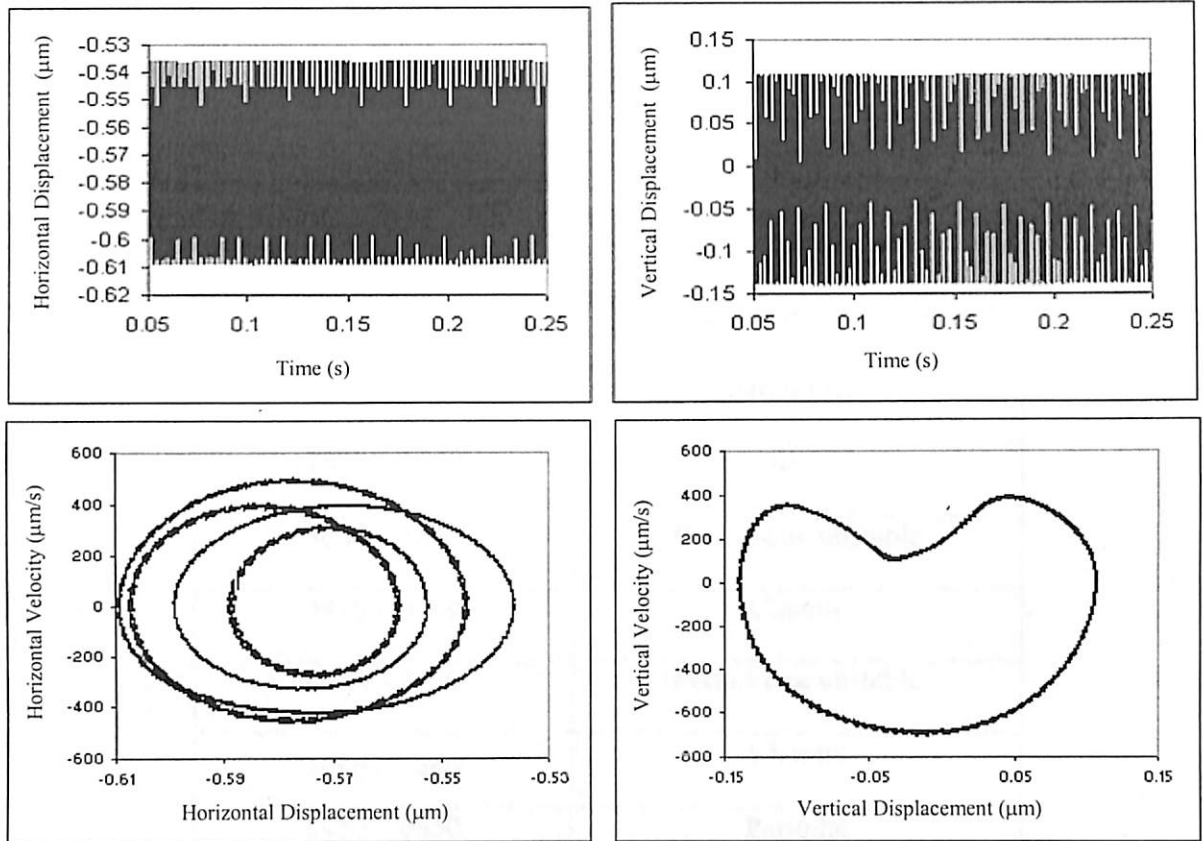


Fig. 4.76 Response at 10800 rpm for  $\gamma_0 = 0.5 \mu\text{m}$ ,  $W = 6\text{N}$





Poincaré Maps

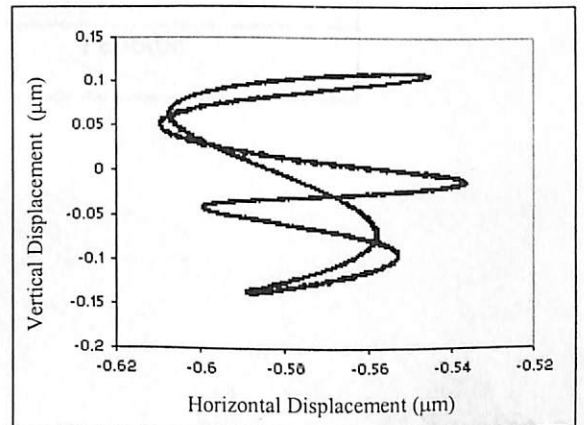
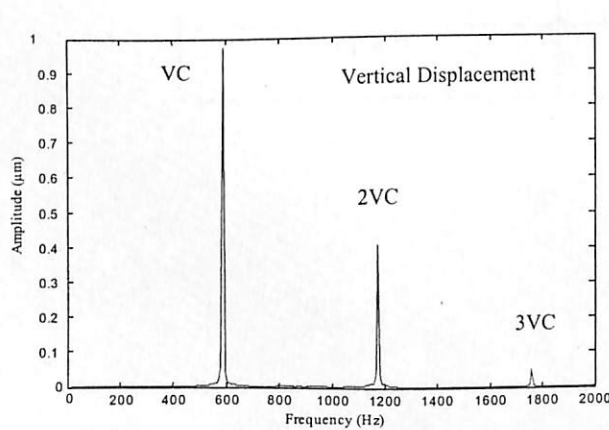
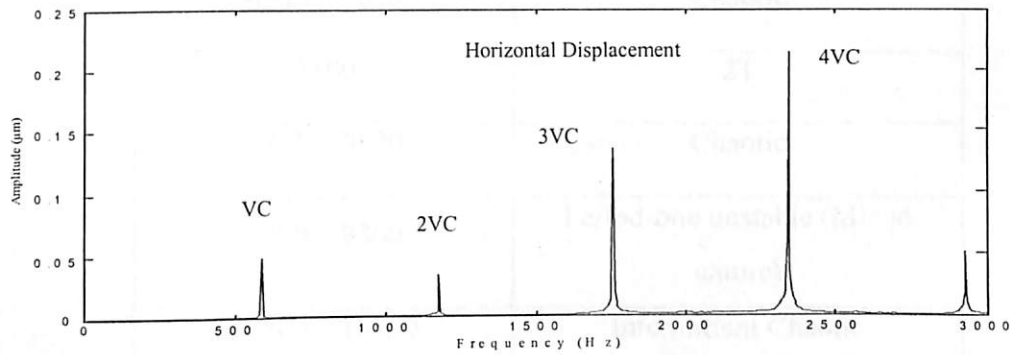


Fig. 4.77 Response at 11000 rpm for  $\gamma_0 = 0.5 \mu\text{m}$ ,  $W = 6\text{N}$

**Table 4.5 Nature of solutions for  $\gamma_0 = 0.5 \mu\text{m}$ ,  $W = 6\text{N}$**

<b>Speed (RPM)</b>	<b>Nature of Response</b>
Upto 925	1T stable low amplitude
945 – 2015	Period-one unstable (at VC and harmonics)
2050 – 3600	Chaotic
3660 – 3850	Period-one unstable
3915 – 4350	Chaotic
4400 – 4920	Period-one unstable
4950 – 5400	Chaotic
5450 – 6850	Periodic
6980 – 7050	Chaotic
7100	2T
7215 – 8620	Chaotic
8700 – 9500	Period-one unstable (Mixed nature)
10500 – 10800	Intermittent Chaotic
11000	Periodic

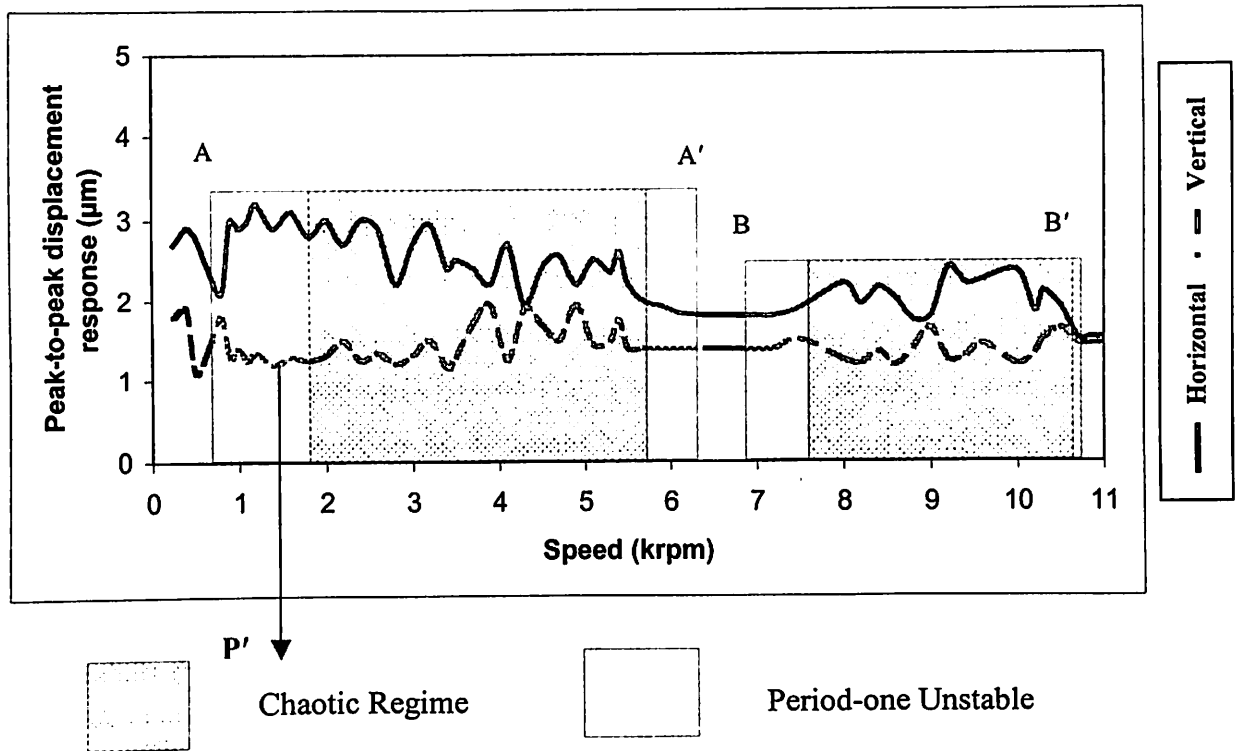


Fig. 4.78 Response plot for  $\gamma_0 = 1 \mu\text{m}$ ,  $W = 6 \text{ N}$  and  $F_u = 15\%W$

From Fig. 4.78, it is observed that the value of vertical displacement is less than that of horizontal displacement in the entire speed range. The response plot (Fig. 4.78) has a combination of the response due to varying compliance and other peaks (due to rotational speed) as a result of unbalanced force. The high amplitude region starting from 450 rpm has stable periodic orbit unlike the balanced case (as has been shown earlier in Fig. 4.41) where high amplitude region provides unstable period-one response. Due to unbalance rotor effect at 1200 rpm, the peak amplitude ( $P'$ ) appears in the response plot.

Period-one solution becomes unstable from 850 to 5950 rpm because of period doubling bifurcations. The solution undergoes pitchfork bifurcations till 1170 rpm after which the chaotic solution is obtained at 1200 rpm. At this speed chaos is at a developing stage. Figure 4.79 shows the nature of solution at 1200 rpm. The dense band of frequency spectrum shows the presence of both the rotational frequency ( $X = 20$  Hz) and the varying compliance frequency ( $VC = 65$  Hz). The presence of dense regions in the orbit is indicative of the onset of chaos. It cannot be considered perfectly periodic, since the two are not exactly line spectra. The orbit is complicated because of this mixed nature of the response as shown in Fig. 4.79.

For the first chaotic region 1700 to 6150 rpm, the loss of stability is seen to be by the eigen values crossing +1. The chaotic solutions at 3500, 3700, 4500 and 5500 rpm are shown in Figs. 4.80 to 4.83 respectively. The frequency spectrum has a band structure as seen in-between spikes of  $VC$ ,  $X/2$  and their multiples. Also, both the frequency components interact to produce sum and difference combination frequencies. The dense structures of the orbit are also clear from phase plots. The orbit at this speed does not repeat itself. The time responses also show beat and chaos like behavior. It is clear that loss of periodicity is a characteristic feature of chaotic solution.

The low amplitude region of unstable period solution starts from 6910 rpm and extends upto 10850 rpm. The large region of chaotic behavior is seen here. For the chaotic region between 7600 to 10750 rpm, the loss of stability is seen to be by eigen values crossing +1. In Figures 4.84 to 4.86, the chaotic responses at 8000, 9000 and 10700 rpm are shown by band structure of frequencies of frequency spectra. These band structures develop around  $X/2$  in the vertical and in the entire speed range for the horizontal displacement. The fine-layered structure of the strange attractor is also clear

from Poincarè maps. The presence of dense regions in the orbit is indicative of chaos. From 10900 rpm onwards the stability returns and system shows a periodic nature. The nature of response for various speeds is given in Table 4.6.

#### 4.6 CONCLUSIONS

The theoretical study of the balanced and unbalanced rotor supported by rolling element bearings for two levels of radial internal clearance of 20 $\mu\text{m}$  and 12 $\mu\text{m}$  (for *point contact*) and 1 $\mu\text{m}$  and 0.5 $\mu\text{m}$  (for *line contact*) and a level of unbalance force (15% of radial load (W)) has lead to the following conclusions:

1. The rotor bearing system has two high amplitude regions. The first region is one of period doubling response where the period-one response is unstable. This region also has bifurcations leading to 3 T, 5 T and 7 T responses. Chaotic response appears in this region, which has a weak attractor as compared to the chaotic behavior in other region. As Fukata et al. (1985) have shown this high amplitude region forms around critical speeds.
2. The second region appears for high radial internal clearance, which has not been predicted by previous studies. This region has unstable response due to Hopf bifurcation generating amplitude modulation and quasi-periodic response. The ratio of the carrier frequency (VC) to the modulating frequency decreases with the increase in speed. This leads to quasi-periodic and mode locked behavior.
3. Radial internal clearance is an important parameter for determining the dynamic response as it is observed that with increase in clearance, the regions of unstable and chaotic response become wider.
4. The peaks of amplitude shift down with increase in radial internal clearance, which points to decrease in the dynamic stiffness of the bearing with increasing clearance. This is not predicted in the stiffness estimates provided by Tamura (1985) and Datta and Farhang (1997).
5. Decrease in clearance, increases the linear characteristics of the rotor bearing system. There are no sub-harmonics formed or chaos as clearance decreases. The regions of unstable behavior decrease with decrease in magnitude of unbalanced rotor force.

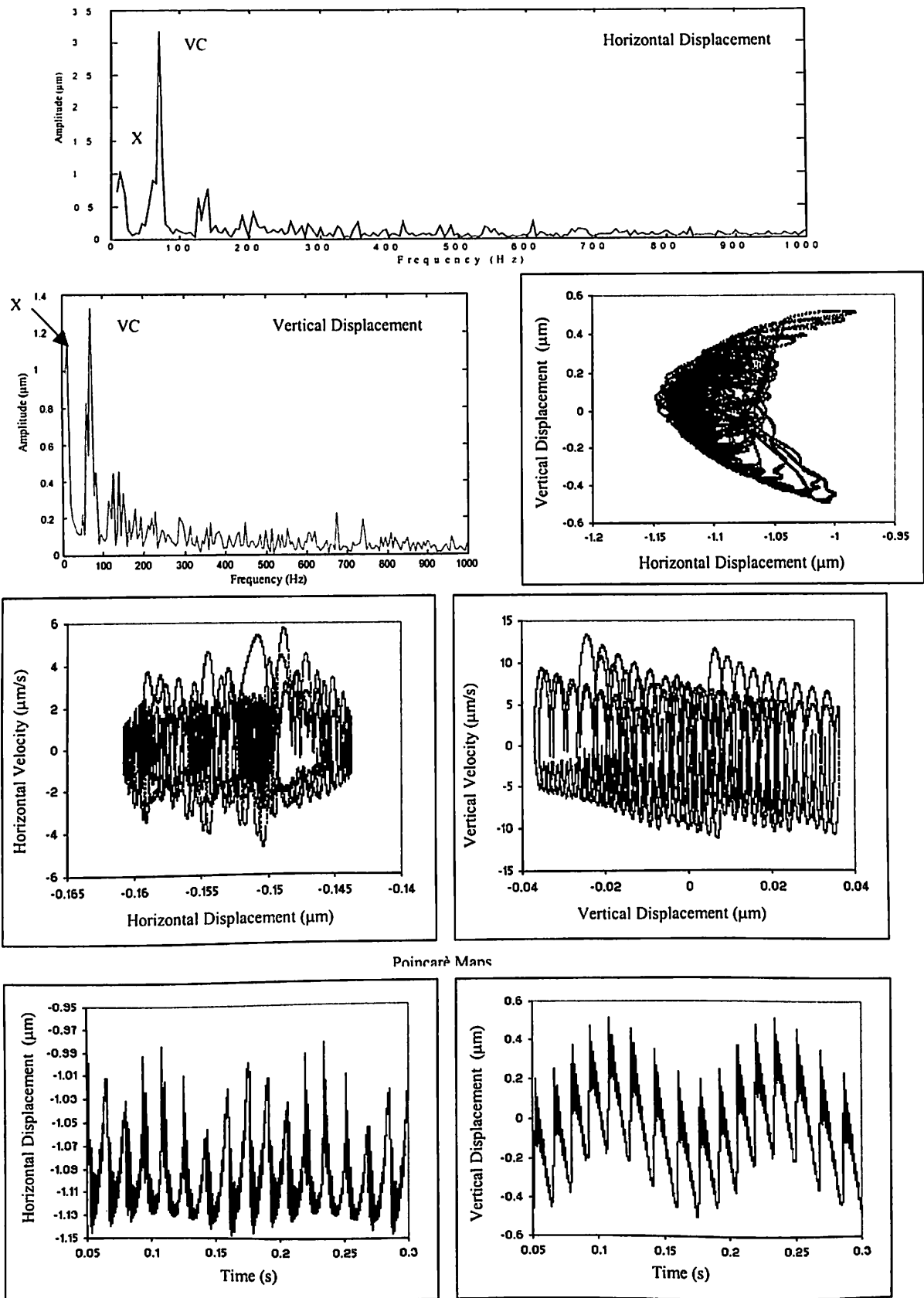
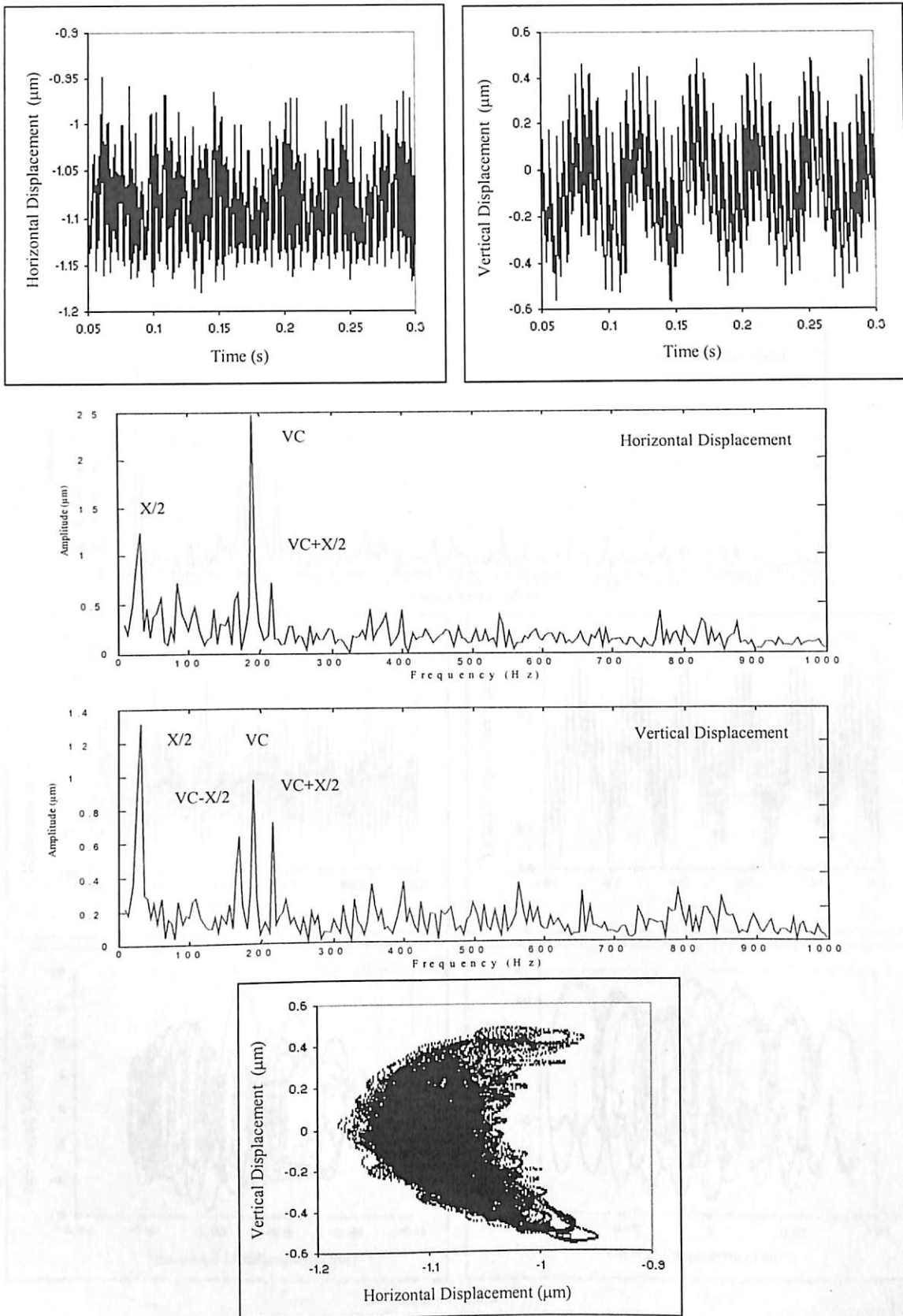
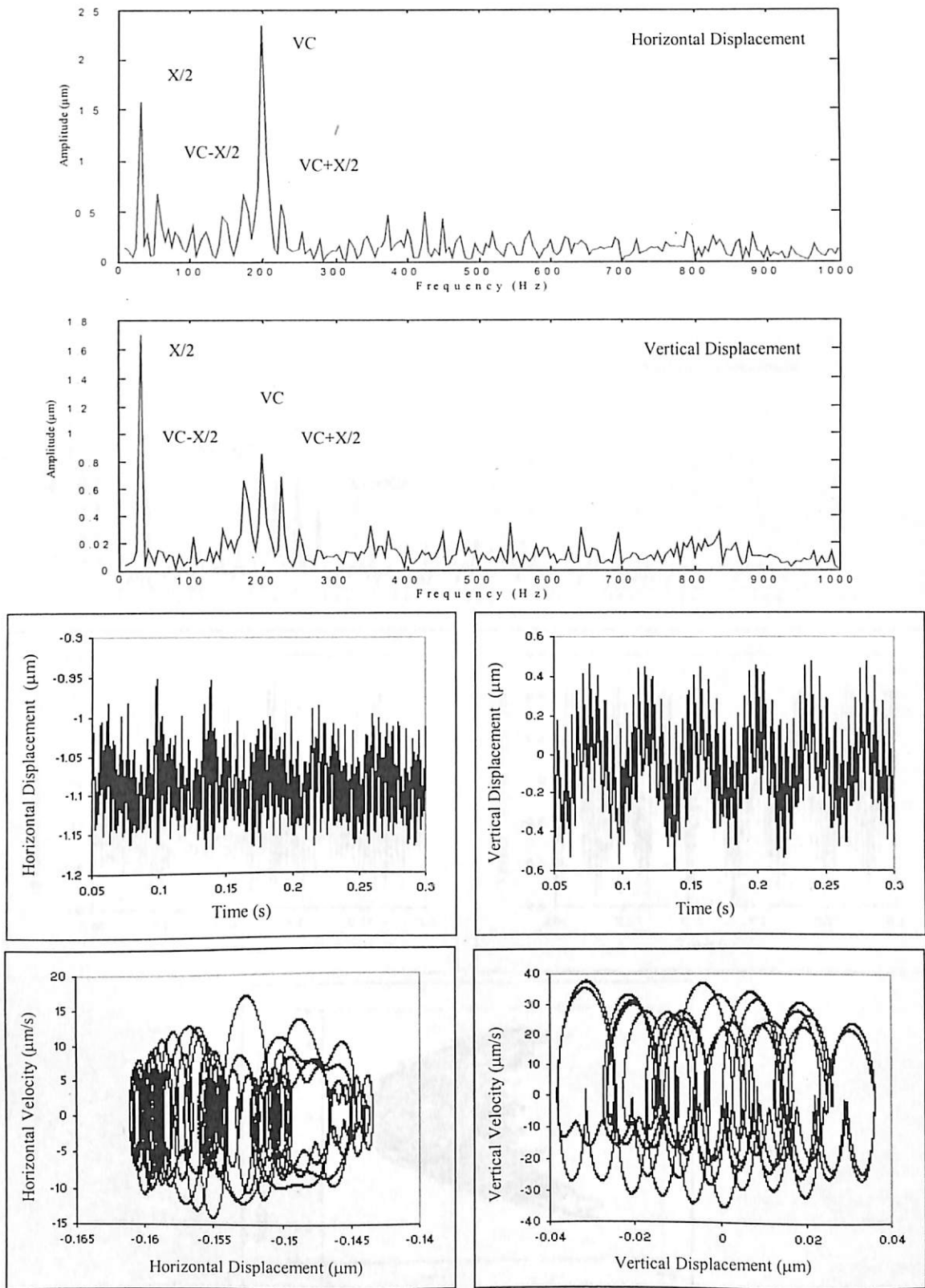


Fig. 4.79 Response at 1200 rpm for  $\gamma_0 = 1 \mu\text{m}$ ,  $W = 6 \text{ N}$  and  $F_u = 15\%W$



**Fig. 4.80** Response at 3500 rpm for  $\gamma_0 = 1 \mu\text{m}$ ,  $W = 6 \text{ N}$  and  $F_u = 15\%W$



Poincaré Maps

**Fig. 4.81** Response at 3700 rpm for  $\gamma_0 = 1 \mu\text{m}$ ,  $W = 6 \text{ N}$  and  $F_u = 15\%W$



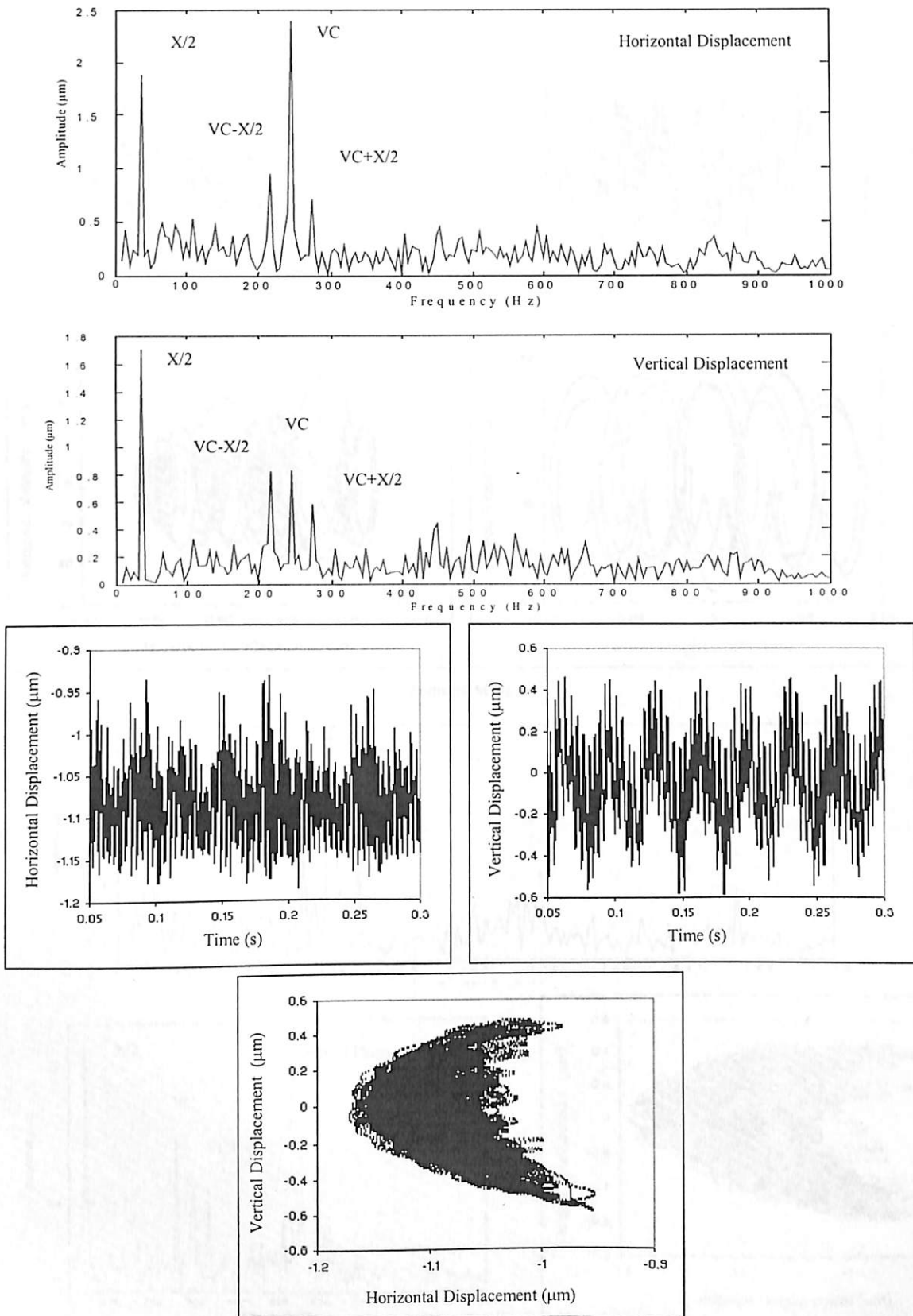
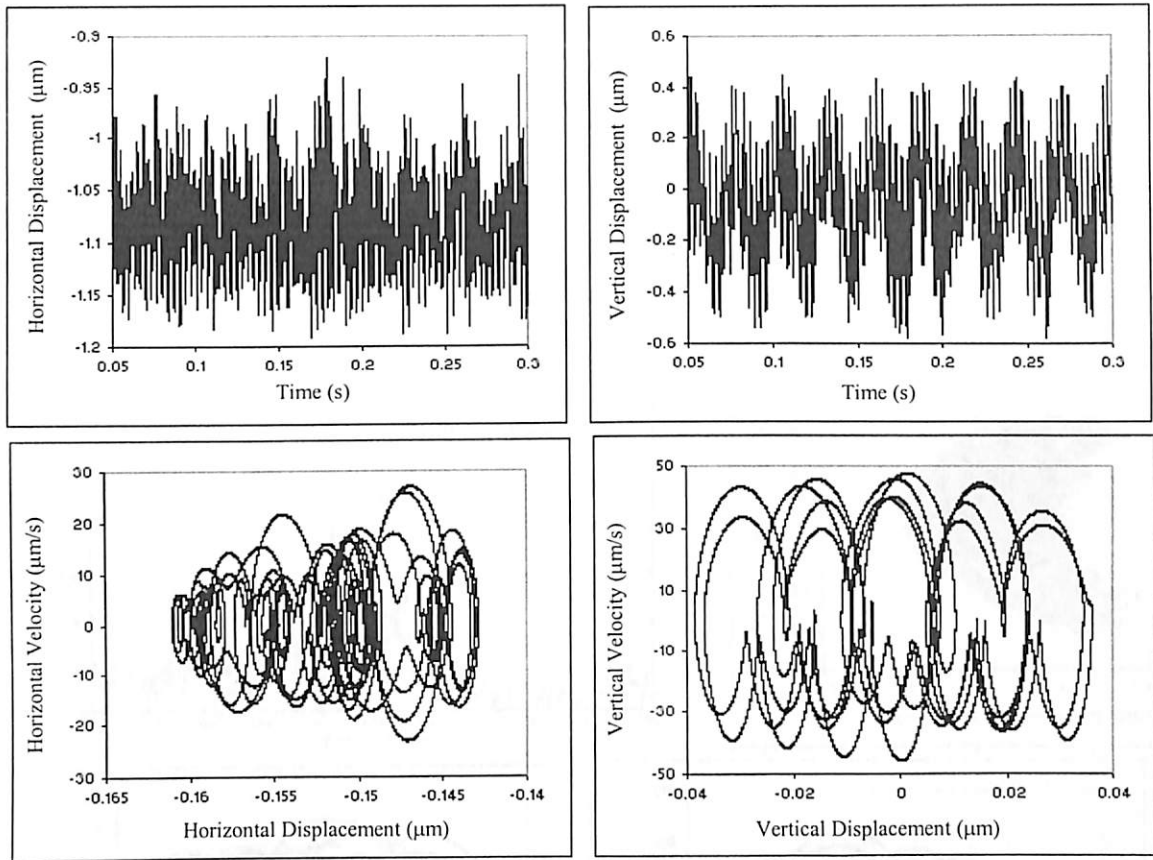


Fig. 4.82 Response at 4500 rpm for  $\gamma_0 = 1 \mu\text{m}$ ,  $W = 6 \text{ N}$  and  $F_u = 15\%W$



Poincaré Maps

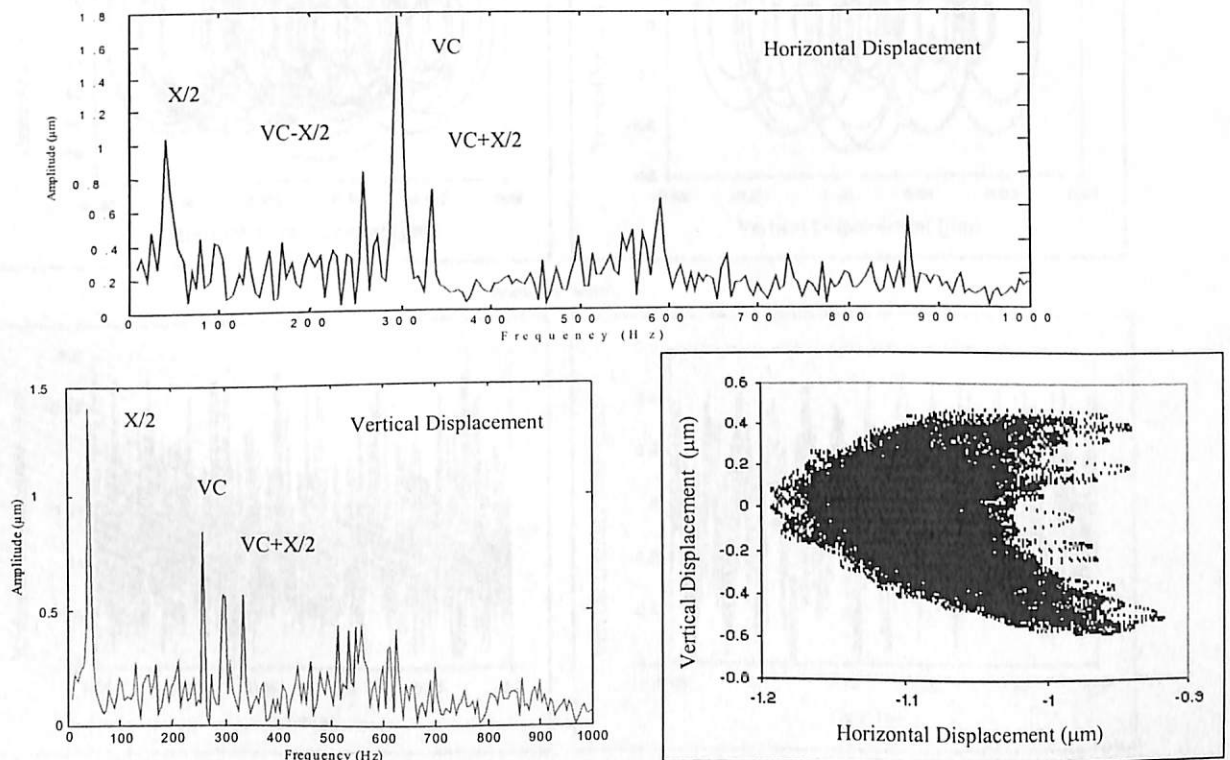
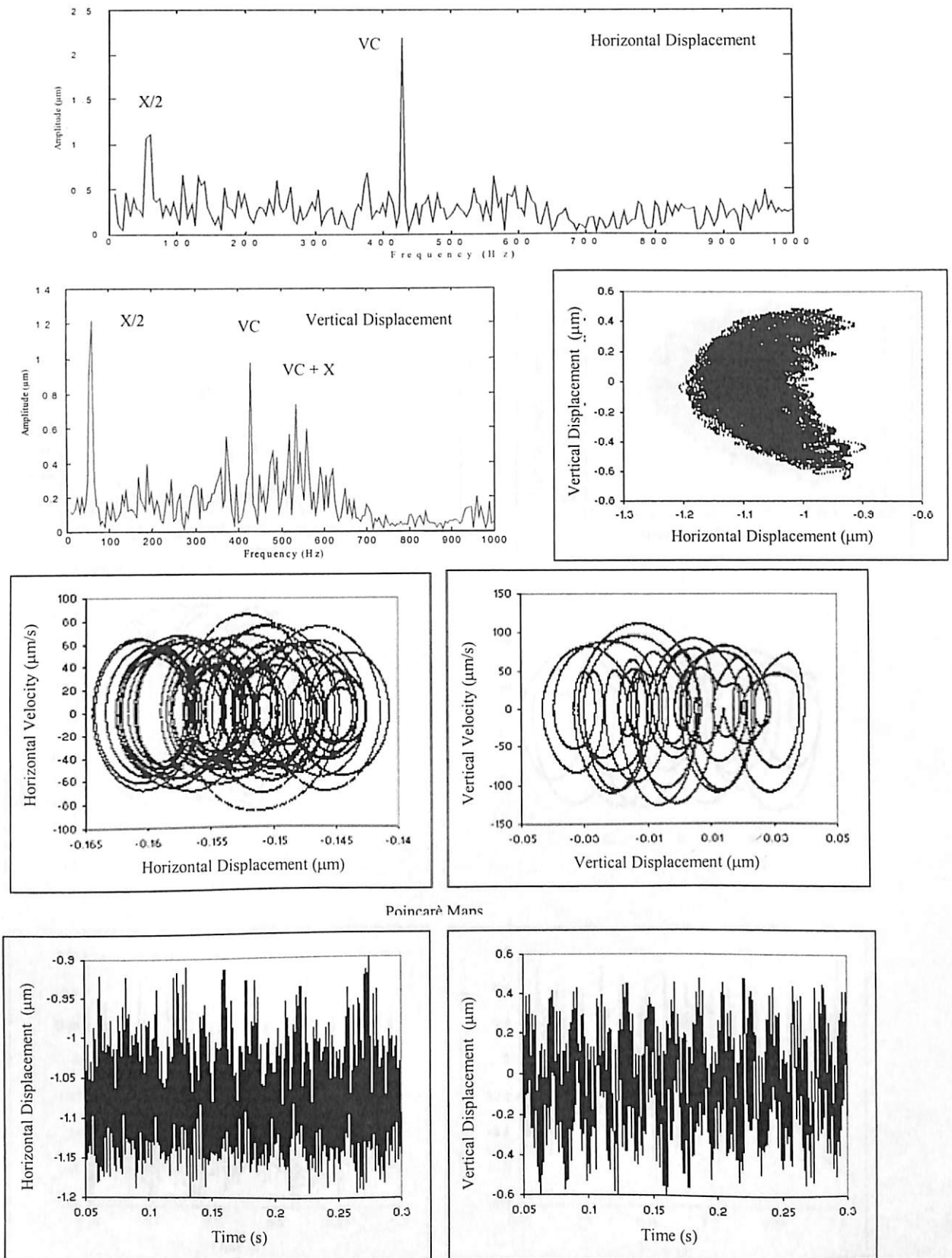
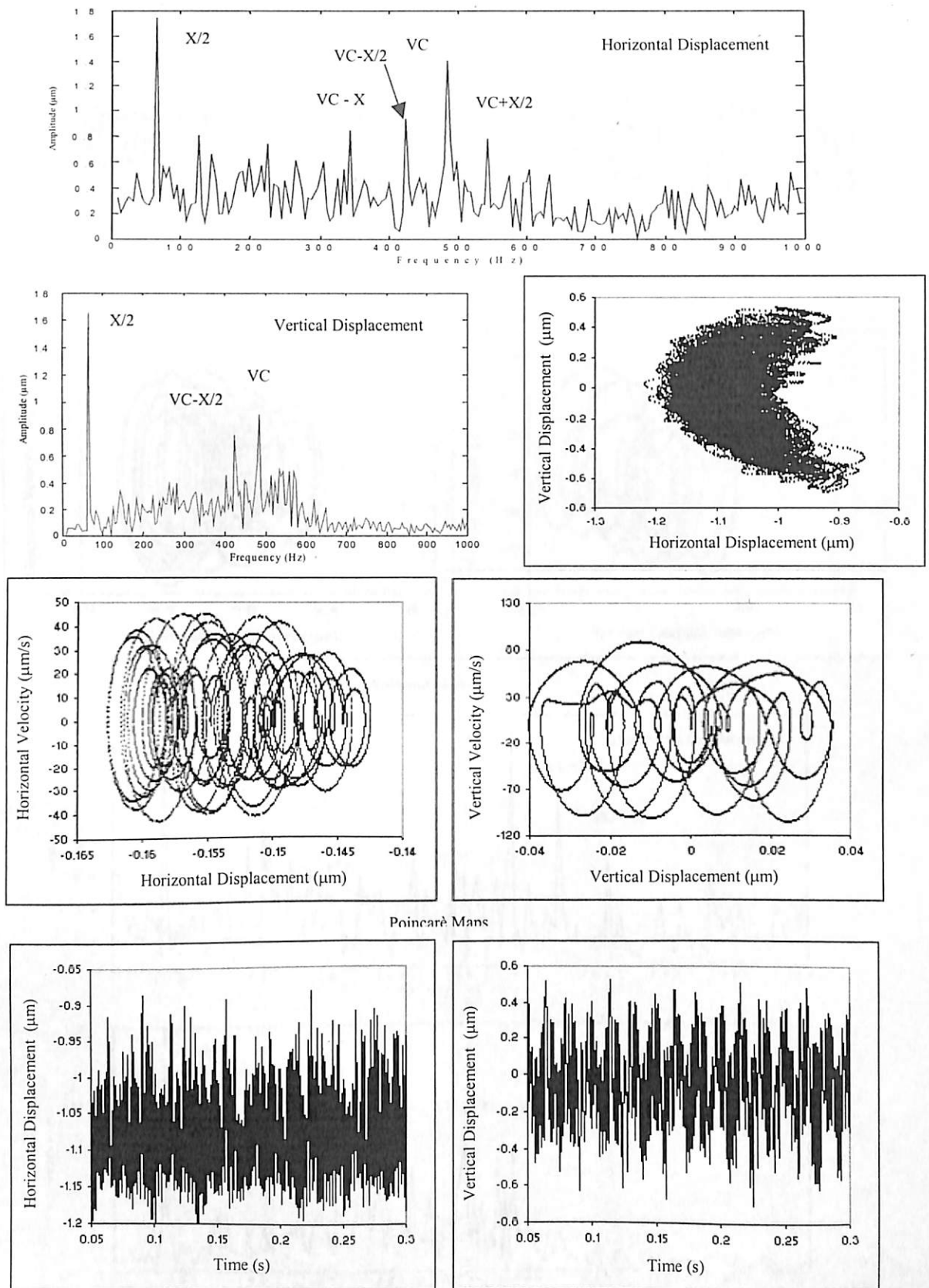


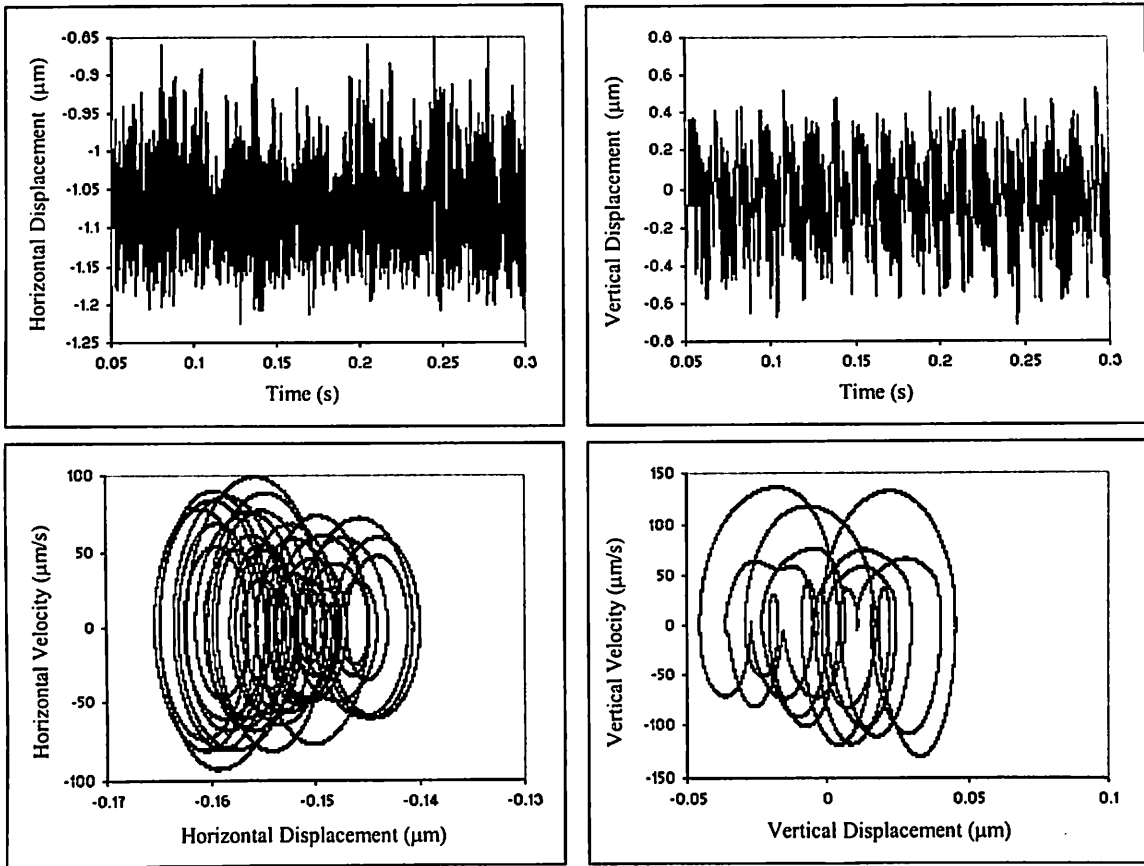
Fig. 4.83 Response at 5500 rpm for  $\gamma_0 = 1 \mu\text{m}$ ,  $W = 6 \text{ N}$  and  $F_u = 15\%W$



**Fig. 4.84** Response at 8000 rpm for  $\gamma_0 = 1 \mu\text{m}$ ,  $W = 6 \text{ N}$  and  $F_u = 15\%W$



**Fig. 4.85** Response at 9000 rpm for  $\gamma_0 = 1 \mu\text{m}$ ,  $W = 6 \text{ N}$  and  $F_u = 15\%W$



Poincaré Maps

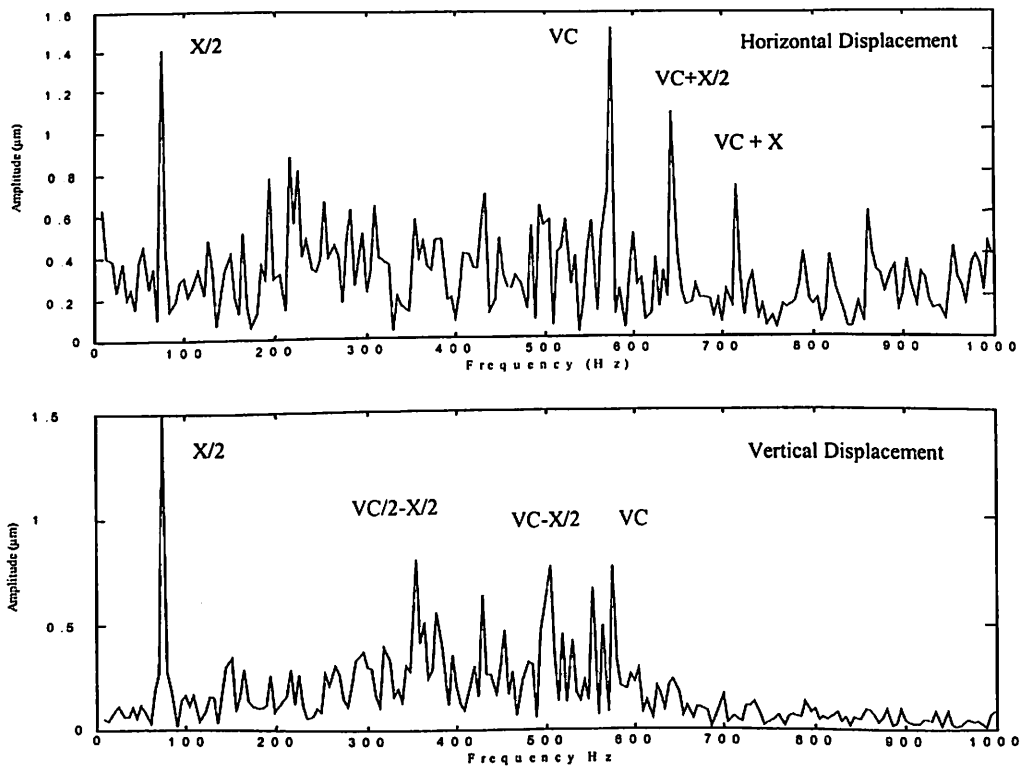


Fig. 4.86 Response at 10700 rpm for  $\gamma_0 = 1 \mu\text{m}$ ,  $W = 6 \text{ N}$  and  $F_u = 15\%W$

**Table 4.6** Nature of solutions for  $\gamma_0 = 1 \mu\text{m}$ ,  $W = 6\text{N}$  and  $F_u = 15\%W$

<b>Speed (RPM)</b>	<b>Nature of Response</b>
Upto 450	1T stable low amplitude
850 – 1170	Period-one unstable (at VC and harmonics)
1200	Chaos developing
1700 – 5850	Chaotic
5900 – 6300	Low amplitude region of unstable period
7600 - 10750	Chaotic
10900	Periodic

6. Due to the larger contact area, roller bearings are seen to have higher stiffness than ball bearings and the regions of unstable response are wider as shown by the speed response plots. The frequency of vibration for roller bearing is higher than that for ball bearing.
7. For unbalanced rotor condition, the study shows that the interaction of varying compliance and unbalanced force results in a response, which has regions of instability and chaos. The high amplitude regions are not necessarily regions of instability. The frequency spectrum displays multiples of rotational frequency ( $X$ ) as well as varying compliance ( $VC$ ) frequency and the linear combination of the two frequencies. This is an important result and similar results have also been reported by Ehrich (1988), who has shown the presence of sum and difference frequencies in the spectra.
8. The effect of unbalanced rotor results in larger unstable region in roller bearing as compared to ball bearing. The second region of unstable response also shows the occurrence of chaos for unbalanced rotor. Invariably, the route to chaos is seen to be intermittency mechanism by period doubling behavior.
9. Based on the characteristics of the dynamic behavior of the system, the responses may be put in three categories. (i) The system responses are periodic and are not sensitive to initial conditions or small variations of system parameters. This is a well-behaved region, which helps the designer to predict the trends accurately and without ambiguity. (ii) The system responses are chaotic but near quasi-periodic or sub-harmonic nature and are not sensitive to initial conditions but extremely sensitive to small variations of system parameters and operating conditions. For these responses, the hidden danger is the periodicity. The periodic response may lead designers to overlook its large sensitivity to small variations of system parameters or operating conditions. (iii) The responses are unpredictable, either periodic or chaotic and extremely sensitive to both the initial conditions and small variations in the system parameters.

## Chapter 5

# ***DYNAMIC ANALYSIS OF ROLLING ELEMENT BEARINGS WITH DISTRIBUTED DEFECTS***

In this chapter, the vibration response of rolling element bearing in a rotor bearing system due to distributed defects under radial load is investigated. The distributed defects considered are, the waviness of outer race, inner race and rolling elements and off-sized rolling element. Distributed defects existing in the rolling elements of a rolling element bearing have been regarded as excitation sources in the form of bearing frequencies, i.e. principal frequencies, their harmonics and side band frequencies. The excitation frequencies are proportional to the rotational speed of the shaft. The ratio between the excitation frequency and the shaft frequency is defined as excitation order. Most order numbers of excitations generated by the bearing are rational numbers so that they can easily be detected in the vibration spectrum. A comprehensive overview of the vibrations generated in rolling element bearings was given by Wardle (1988) and Yhland (1992).

However, these defects introduce the time varying components of the stiffness coefficients to change the natural vibration characteristics of the rotating system as well as response. Therefore, it is important to investigate the stability due to distributed defects in order to achieve their sound operation. The variation in contact force between rolling element and raceways due to the distributed defects causes an increase in the vibration level, which in turn results in premature surface fatigue leading to failure. The study of vibration response due to this category of defects is, therefore, important for quality inspection as well as for condition monitoring. These defects may result from manufacturing error and abrasive wear. Aktürk (1999), Tandon and Choudhury (2000) and Jang and Jeong (2002) have considered ball bearing waviness in their model. However, in their investigation, they did not apply these effects to the whole operating range, due to the inherent instability.

In the present investigation, the stability of rotor bearing systems due to distributed defects has been analyzed in detail. The present study also characterizes the vibration frequencies resulting from the distributed defects existing in rolling elements, the



harmonic frequencies resulting from the nonlinear load-deflection characteristics of the rolling element bearing and the sideband frequencies resulting from the defects interactions of the rolling element bearing.

## 5.1 INTRODUCTION

Rolling element bearing is one of the essential elements in the spindle system of the rotating machinery from the conventional power driven machines to the present sophisticated information storage devices. One important issue in rotor bearing application is the reduction of noise and vibration originating from the ball bearings. The rolling element bearing is composed of rolling elements, inner race, outer race and cages. One possible source of rolling element bearing vibration is the unbalance of the bearing force or the geometrical imperfections of the rolling elements. These geometrical imperfections are often called as “waviness,” and many researchers have investigated the vibration of a ball bearing resulting from the waviness.

Some researchers have investigated the vibration forces and frequencies originating from the waviness of the ball bearing. Yhland (1967) reported the axial and radial vibration frequencies due to the variation of waviness order through experiments. Wardle and Poon (1983) investigated the relation between the ball number and waviness order and they advocated that the ball bearing generates severe vibrations when the former matches with the latter. Wardle (1988) also predicted vibration frequencies resulting from the nonlinear load-deflection characteristics through his analytical model of the ball bearing to explain the relation between waviness and exciting forces. However, his model could not predict the vibration frequencies in the case where multiple waviness exists simultaneously in several components of the rolling elements of the ball bearing. However, the above studies did not include the dynamics of the rotor, so they could not explain the quantitative and qualitative characteristics of ball bearing vibration. Yhland (1992) used a linear theory to calculate the stiffness matrix of the ball bearing with waviness and investigated the effect of waviness through his rotor dynamic model. Yhland (1992) model however, could not explain the nonlinear load-deflection effect because it did not include the change of the relative positions of the rolling elements during rotation. Aktürk et al. (1997) proposed a vibration model of a ball bearing with

waviness considering three degrees of freedom, but they did not explain ball bearing vibration due to the effects of angular motion. Present study proposes a nonlinear model to analyze the ball bearing vibration resulting from the distributed defects in the rigid rotor supported by two or more ball bearings.

## 5.2 PROBLEM FORMULATION

For investigating the vibration characteristics of ball bearings, a model of a rotor-bearing assembly can be considered as a spring mass system, in which the outer race of the bearing is fixed in a rigid support and the inner race is fixed rigidly with the shaft. Elastic deformation between races and rollers gives a nonlinear force deformation relation, which is obtained by Hertzian theory. Other sources of stiffness variation are positive internal radial clearance, existence of a finite number of balls whose positions change periodically, the inner and outer race waviness and off-size rolling element. These cause periodic changes in stiffness of bearing assembly. Thus, the system undergoes nonlinear vibration under dynamic conditions.

In the mathematical modeling, the rolling element bearing is considered as a spring mass system and rolling elements act as nonlinear contact spring. Since, the Hertzian forces arise only when there is contact deformation, the springs are required to act only in compression. In other words, the respective spring force comes into play when the instantaneous spring length is shorter than its unstressed length, otherwise the separation between rolling element and the races takes place and the resultant force is set to zero. When there is an imperfection in a bearing, it causes additional deflection difference. This difference should also be considered in modeling. A detailed description about geometrical imperfections of bearing has already been given earlier in Chapter 3. Imperfection like 'waviness' may be caused by different manufacturing malfunctions such as uneven wear of the grinding wheel in various operations, variable interactions between the tool and work piece and vibrations of machine elements or movements of the work in the fixture. Waviness consists of sinusoidal shaped imperfections on the outer surface of the components. Furthermore, the wavelength is assumed to be much greater than the roller to race footprint width and the wave geometry itself, is assumed to be unaffected by contact distortion.

Some of the frequency components generated because of these defects are same as varying compliance frequency as reported by Sunnersjo et al. (1985), Tandon and Nakra (1993), Aktürk (1999) and Jang and Jeong (2002). In this study, we have considered the bearing as a whole. The balls are arranged equi-spaced within the bearing. They also move around the races with equal velocity, which is physically possible because of the cage. The waviness ( $\Pi$ ) exists at the outer surface of the bearing components. Hence, with the consideration of waviness ( $\Pi$ ), the contact deformations  $\delta_{in}$  and  $\delta_{out}$  at the inner and outer races respectively, may be estimated as,

$$\delta_{in} = \left[ \{r + \rho_r + \Pi\} - \chi_j \right] \quad (5.1)$$

$$\delta_{out} = \left[ R - \{\rho_j + \rho_r + \Pi\} \right] \quad (5.2)$$

In Eq. (5.1), if  $\{r + \rho_r + \Pi\} > \chi_j$ , compression takes place and a restoring force acts.

If  $\{r + \rho_r + \Pi\} < \chi_j$ , there is no compression and restoring force is set to zero

Likewise in Eq. (5.2), if  $R < \{\rho_j + \rho_r + \Pi\}$ , compression takes place and restoring force acts.

If  $R > \{\rho_j + \rho_r + \Pi\}$ , there is no compression and restoring force is set to zero.

After considering the distributed defects, the system equations of motion for the generalized coordinates  $\rho_j$ , may be written as,

$$m_j \ddot{\rho}_j + m_j g \sin \theta_j + m_j \rho_j \dot{\theta}^2 - (k_{in}) \left[ \{r + \rho_r + \Pi\} - \chi_j \right]_+ \frac{\partial \chi_j}{\partial \rho_j} + (k_{out}) \left[ R - (\rho_j + \rho_r + \Pi) \right]_+ \frac{\partial \chi_j}{\partial \rho_j} + \frac{1}{2} \frac{\partial k_{in}}{\partial \rho_j} \left[ \{r + \rho_r + \Pi\} - \chi_j \right]_+^2 + \frac{1}{2} \frac{\partial k_{out}}{\partial \rho_j} \left[ R - (\rho_j + \rho_r + \Pi) \right]_+^2 = 0; \quad j = 1, 2, \dots, N_b \quad (5.3)$$

For the generalized coordinate  $x_{in}$  the equation is:

$$(m_{in} + m_{rotor}) \ddot{x}_{in} - \sum_{j=1}^{N_b} k_{in} \left[ \{r + \rho_r + \Pi\} - \chi_j \right]_+ \frac{\partial \chi_j}{\partial x_{in}} = F_u \sin(\omega t) \quad (5.4)$$

For the generalized coordinate  $y_{in}$  the equation is:

$$(m_{in} + m_{rotor}) \ddot{y}_{in} + (m_{in} + m_{rotor}) g - \sum_{j=1}^{N_b} k_{in} \left[ \{r + \rho_r + \Pi\} - \chi_j \right]_+ \frac{\partial \chi_j}{\partial y_{in}} = W + F_u \cos(\omega t) \quad (5.5)$$

This is a system of  $(N_b + 2)$  second order, non-linear differential equations. No external radial force is allowed to act on the bearing system and no external mass is attached to the outer race. The “+” sign as subscript in these equations signifies that if the

expression inside the bracket is greater than zero, the rolling element at angular location  $\theta_j$  is loaded, giving rise to a restoring force. If the expression inside bracket is negative or zero, the rolling element is not in the load zone and restoring force is set to zero. For the balanced rotor condition, the unbalance rotor force ( $F_u$ ) is set to be zero.

### **5.3 RESULTS AND DISCUSSION**

Theoretical results are obtained for a rotor supported by rolling element bearing using the techniques already discussed in sections 4.3 and 4.4 of chapter 4. The results of the present work are presented and discussed in the subsequent paragraph

#### **5.3.1 Results of Theoretical Simulation**

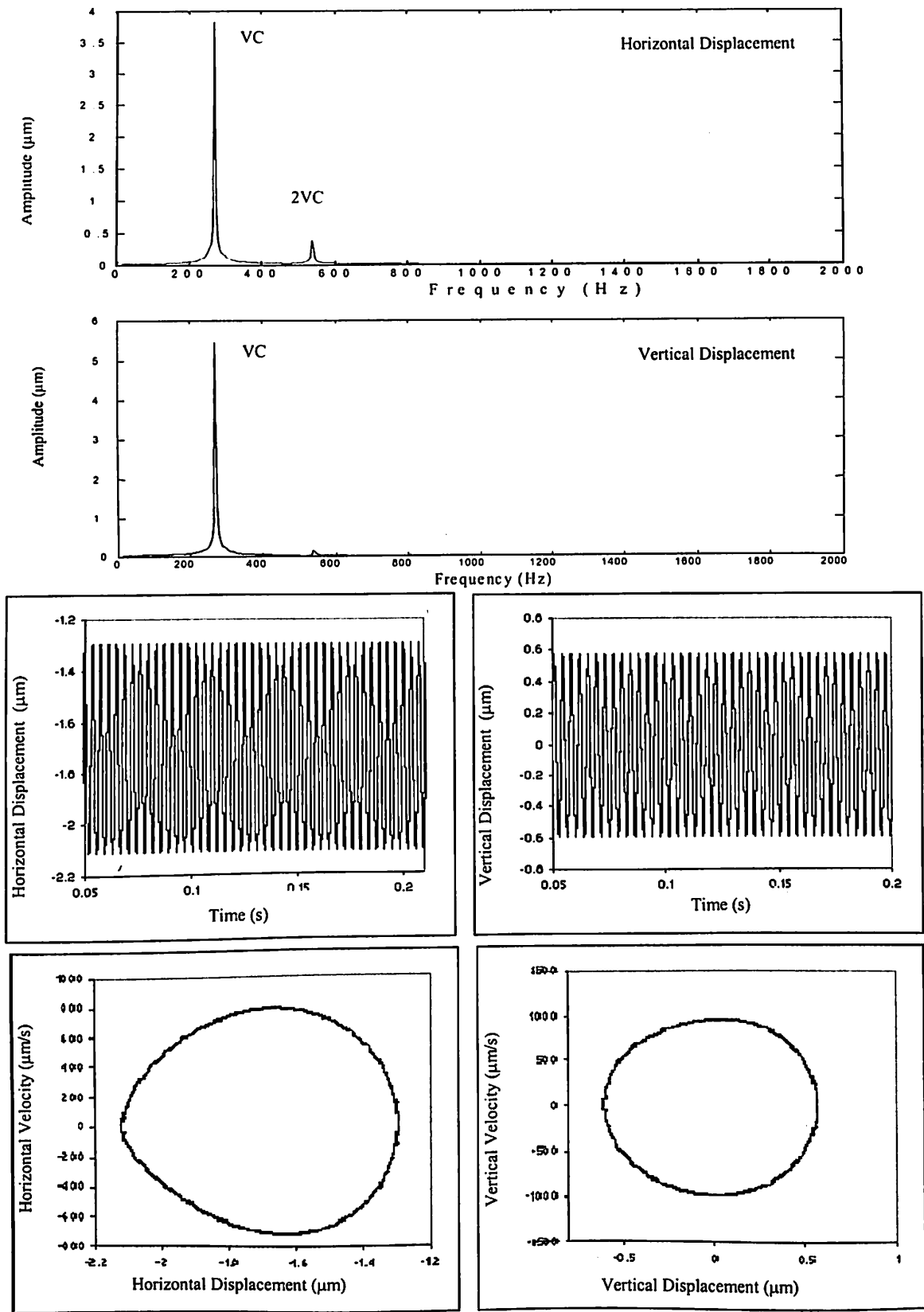
In order to study the effect of distributed defects in more detail, the rolling element bearing employed in this study is reduced to a radial ball bearing for this particular investigation is modeled as was shown earlier in Fig. 4.1. Balls are radially preloaded in order to ensure the continuous contact of all balls and the raceways, otherwise a chaotic behavior might be observed (Gad et al., 1984 (a)). In the simulation model, the rotor is assumed to be uniform, perfectly rigid and supported by radially loaded ball bearings. In order to see whether the predicted vibrations would occur in the mathematical model, surface waviness of the bearing components are considered separately. The outer races of all bearings are assumed to be wavy by the equal amount, so that the rotor would move in a cylindrical mode. The vibrations responses of a rotor, which is supported by bearings with 8 balls and rotating at a speed of 5000 rpm, are obtained. The waviness amplitude is set to 0.2  $\mu\text{m}$  and the number of waves around the circumference of races is allowed to vary for a bearing.

##### **5.3.1.1 Outer race waviness**

In order to see whether the predicted vibrations would occur in the simulation model, a set of results were obtained for selected number of waves. When the number of waves is 7, the peak amplitude of vibration appears in vibration spectra at the varying compliance frequency ( $\nu C = 266.7$  Hz) as shown in Fig. 5.1. The amplitude of peak is 4  $\mu\text{m}$  for horizontal and 5.5  $\mu\text{m}$  for vertical displacement response. Another peak appears at the super-harmonic ( $2\nu C = 533.3$  Hz) in the spectrum. The  $\nu C$  and its harmonic character of the frequency spectra is also brought-out by Poincarè map with the closed orbits.

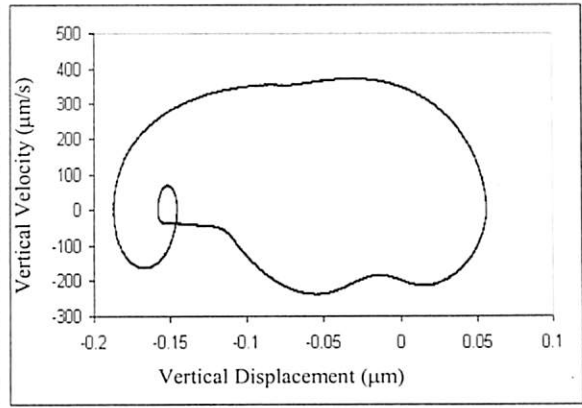
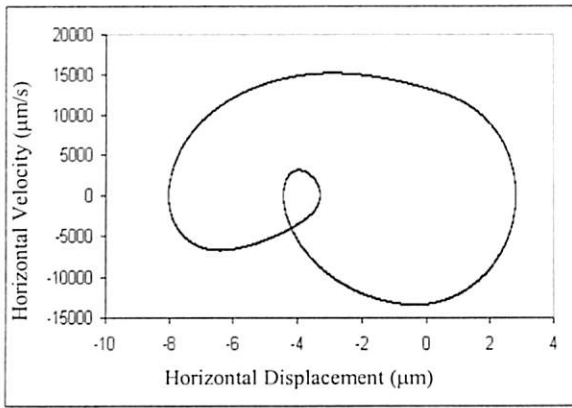
When the number of waves is 8, the dominant peak amplitude of vibration appears in the frequency spectra at the varying compliance frequency ( $\nu C = 266.7$  Hz) with the first super-harmonic at twice the varying compliance frequency ( $2\nu C = 533.3$  Hz) for vertical displacement as shown in Fig. 5.2. In the frequency spectra for horizontal displacement, the peak amplitude of vibration appears at  $2\nu C = 533.3$  Hz and the sub-harmonic appears at  $\nu C = 266.7$  Hz. The amplitude of the peak is  $3.7 \mu\text{m}$  for horizontal and  $0.9 \mu\text{m}$  for vertical displacement response. The other peaks appear in the frequency spectra at  $3\nu C = 800$  Hz and at  $4\nu C = 1066.7$  Hz. Figure 5.2 shows that the amplitude of the peak at the dominant frequency for  $N_b = 8$  is less than that observed for  $N_b = 7$  for the simulation model. Wardle (1988 (b)) has pointed out that severe vibrations occur for outer race waviness when the number of waves and balls are equal. Hence, severe vibration occurs when the waviness order ( $n$ ) equals  $N_b$ . Wardle (1988(a)) has also concluded from his linear model that the radial vibrations have larger amplitudes when  $n = qN_b \pm 1$ . The response obtained in the present study matches partially with his work.

When the number of waves is 12, peak amplitude of vibrations at twice of the varying compliance frequency ( $2\nu C = 533.3$  Hz) with first subharmonic at the varying compliance frequency ( $\nu C = 266.7$  Hz) as shown in Fig. 5.3. The amplitude of the peak is  $0.75 \mu\text{m}$  for horizontal and  $0.6 \mu\text{m}$  for vertical displacement response. Hence for  $N_w = 12$ , the vibrations are very small as also predicted by Aktürk (1999). The  $\nu C$  and its harmonics character of the frequency spectra is also brought-out by Poincarè map with the two closed orbits. The time displacement response also shows the sub-harmonic nature of the system.



Poincaré Maps

Fig. 5.1 Response plot for outer race waviness at  $N_w = 7$



Poincaré Maps

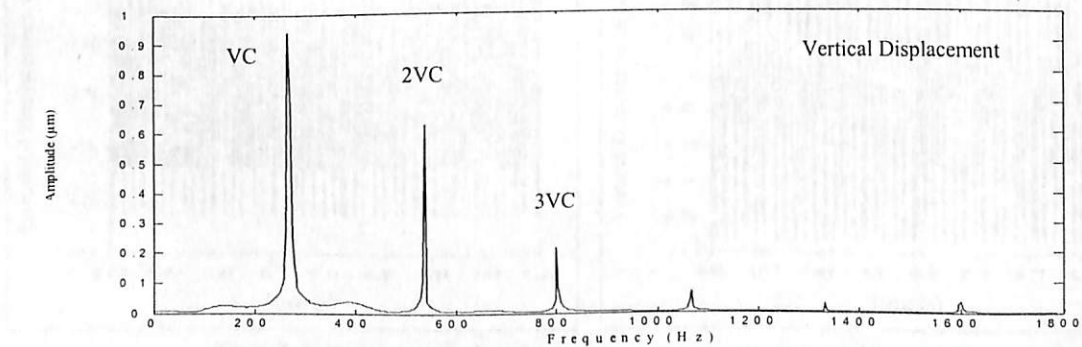
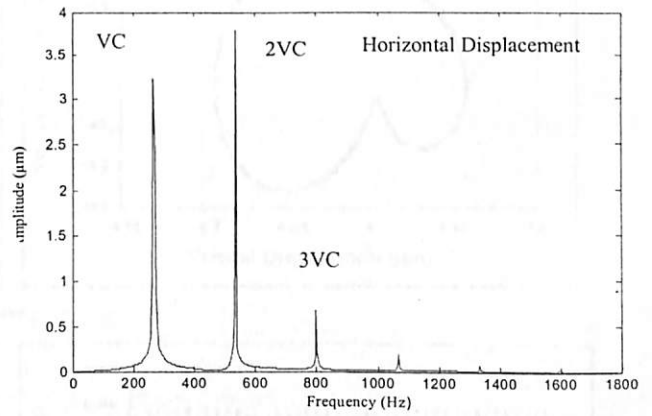
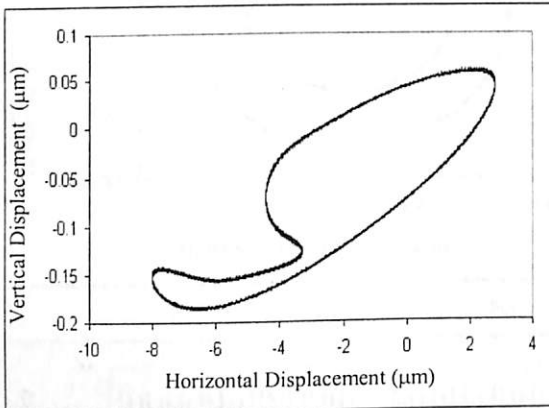
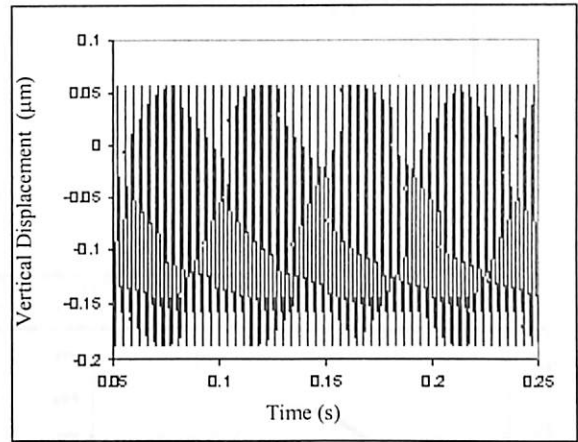
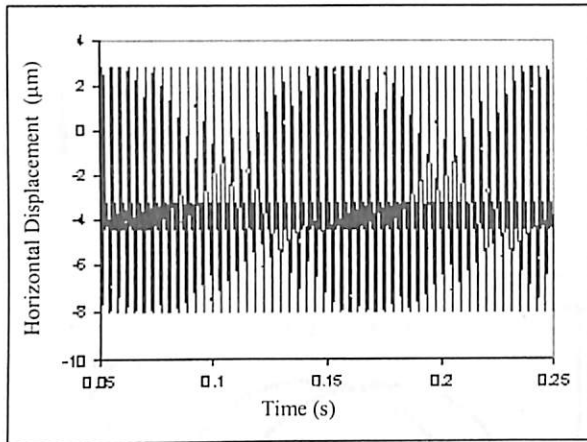


Fig. 5.2 Response plot for outer race waviness at  $N_w = 8$

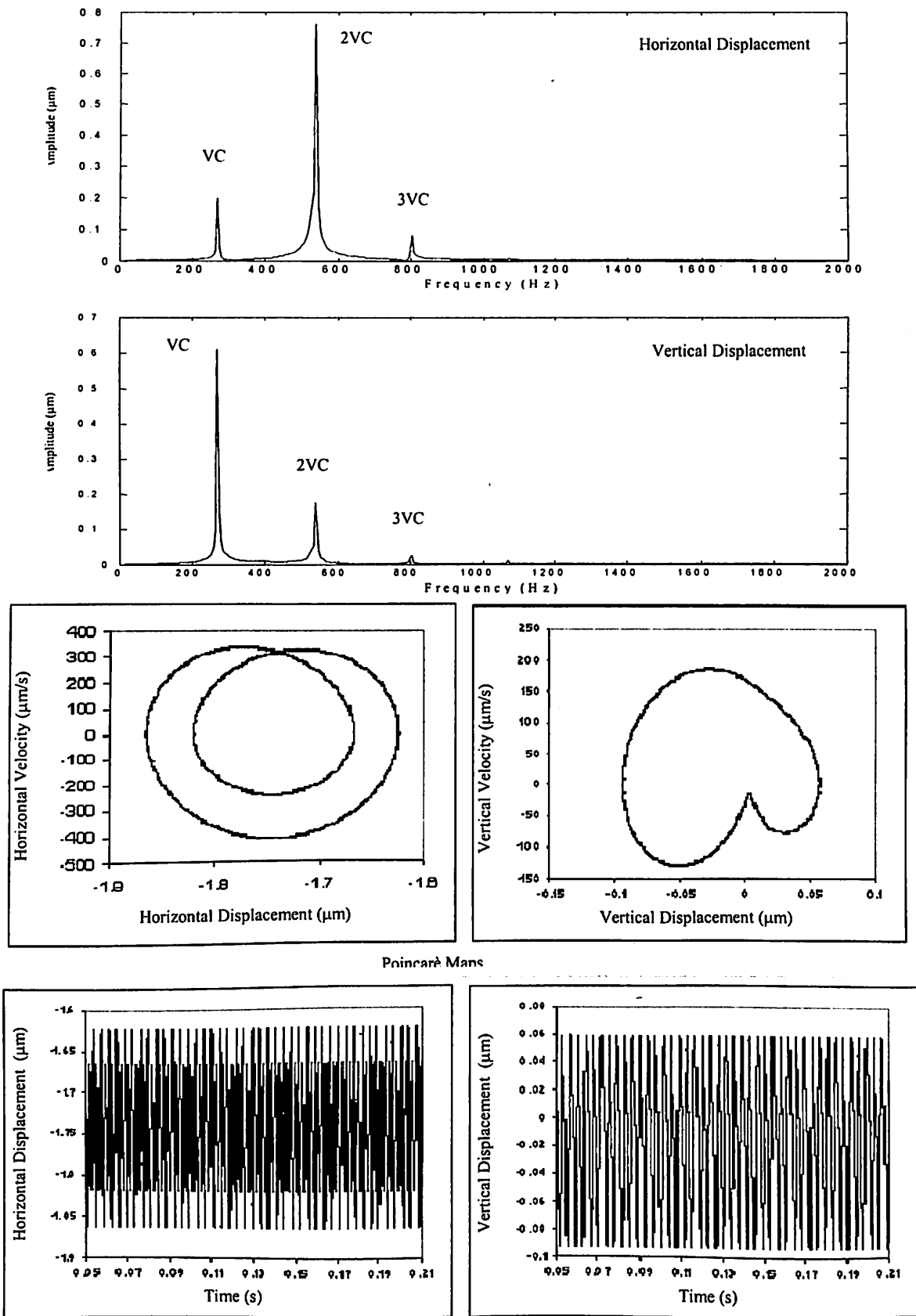


Fig. 5.3 Response plot for outer race waviness at  $N_w = 12$



When the number of waves is 16, the peak amplitude of vibrations appears at twice the varying compliance frequency ( $2VC = 533.3$  Hz) as shown in Fig. 5.4. The amplitude of peak is  $9 \mu\text{m}$  for horizontal and  $7 \mu\text{m}$  for vertical displacement response. A change of dominant vibration frequency from varying compliance frequency to twice the varying compliance frequency ( $2VC$ ) is of particular interest. A clear transformation from  $q = 1$  to  $q = 2$  can be observed in the resulting vibration spectrum. When the number of waves is 17, high amplitude of peak appears at twice the varying compliance frequency ( $2VC = 533.3$  Hz) as shown in Fig. 5.5. The amplitude of the peak is  $9 \mu\text{m}$  for horizontal and  $2 \mu\text{m}$  for vertical displacement response.

When the number of waves is 21, the peak amplitude of vibration appears in the spectrum at thrice the varying compliance frequency ( $3VC = 800.5$  Hz) as shown in Fig. 5.6. The amplitude of the peak is  $3 \mu\text{m}$  for horizontal and  $1.2 \mu\text{m}$  for vertical displacement response. In this case a change of dominant vibration frequency from twice the varying compliance frequency ( $2VC$ ) to thrice the varying compliance frequency ( $3VC$ ) is of particular interest. A clear transformation from  $q = 2$  to  $q = 3$  can be observed in the resulting vibration spectrum.

When the number of waves is 31, the peak amplitude of vibration appears in the spectrum at four times the varying compliance frequency ( $4VC = 1066.67$  Hz) as shown in Fig. 5.7. The amplitude of the peak is  $1.2 \mu\text{m}$  for horizontal and  $0.55 \mu\text{m}$  for vertical displacement response. One can observed a clear transformation from  $q = 3$  to  $q = 4$  in the resulting vibration spectrum.

From the obtained results for outer race waviness it can be inferred the severe vibrations occur when the number of balls and waves are equal. The waviness order for severe vibration is  $n = N_b$ . It is also observed from the obtained responses that small amplitude of waviness on the stationary outer race of a radial loaded bearing produces vibration, only at those frequencies that are harmonic of the ball to outer pass rate ( $N_b \times \omega_{cage}$ ).

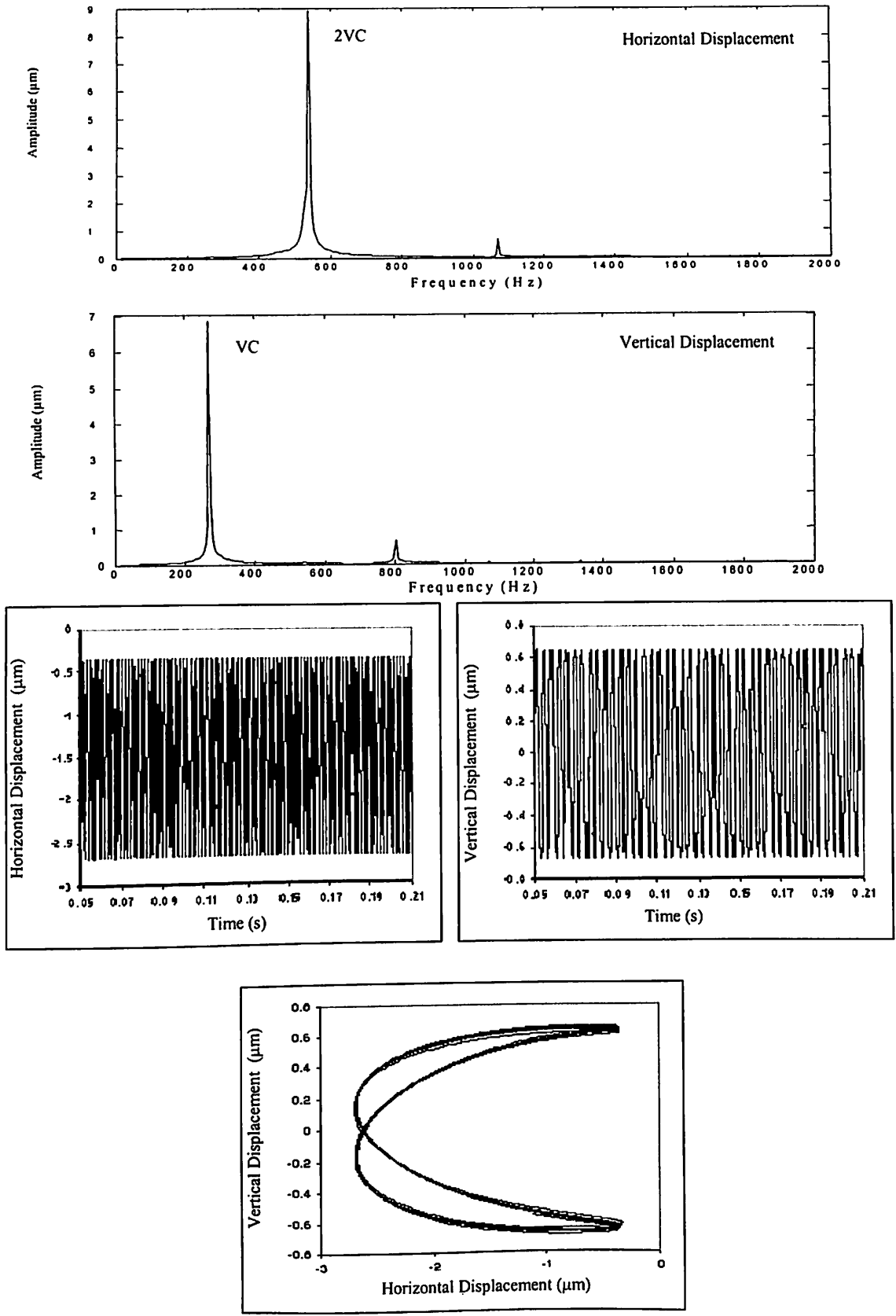


Fig. 5.4 Response plot for outer race waviness at  $N_w = 16$

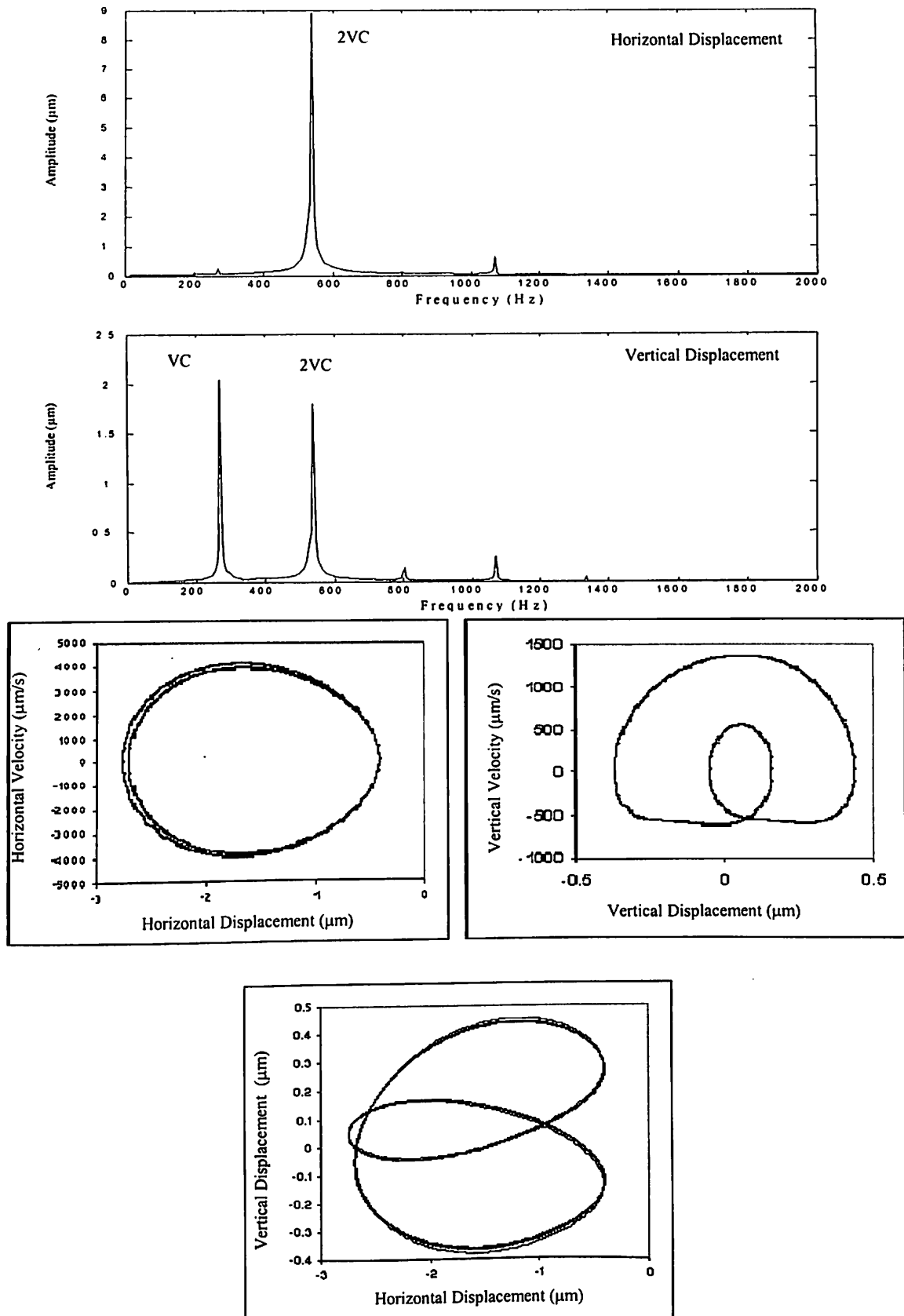
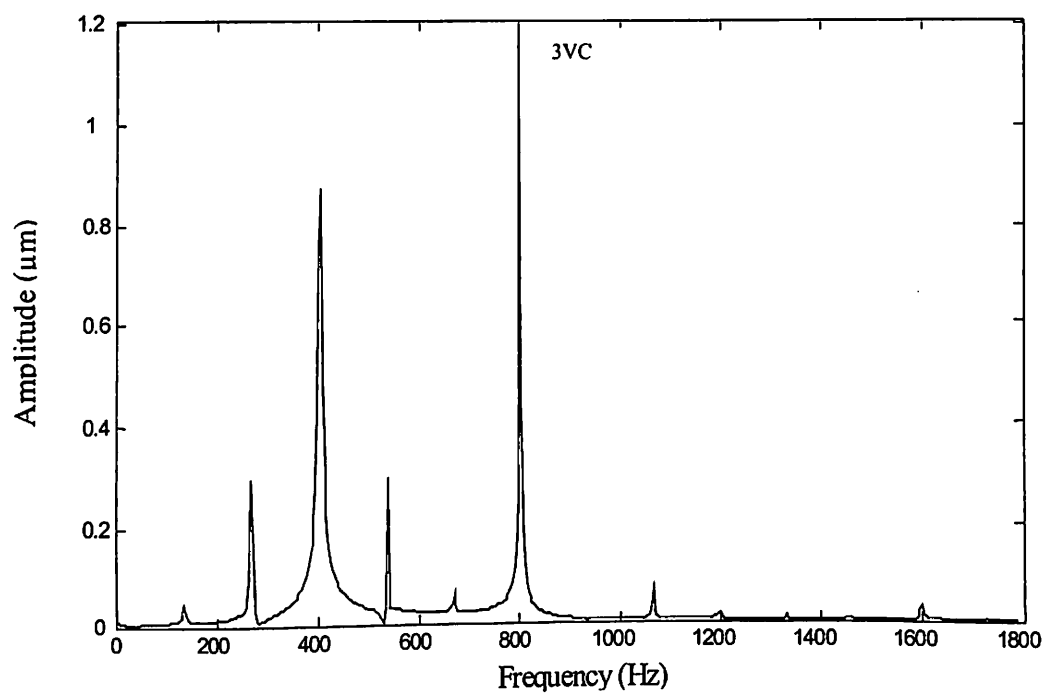
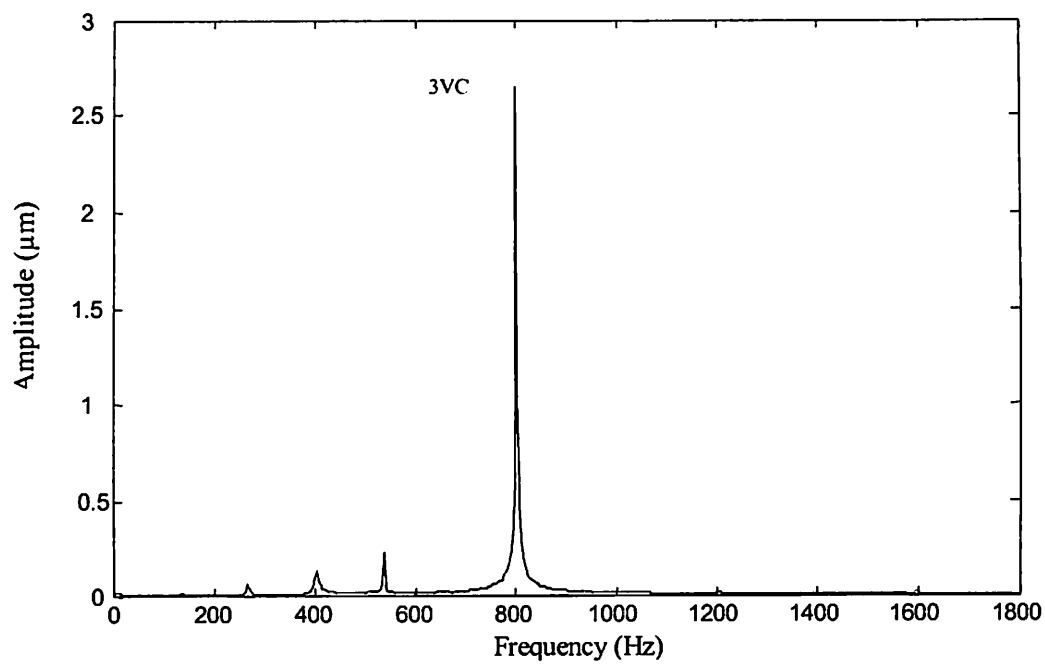


Fig. 5.5 Response plot for outer race waviness at  $N_w = 17$



**Fig. 5.6** Response plot for outer race waviness at  $N_w = 21$

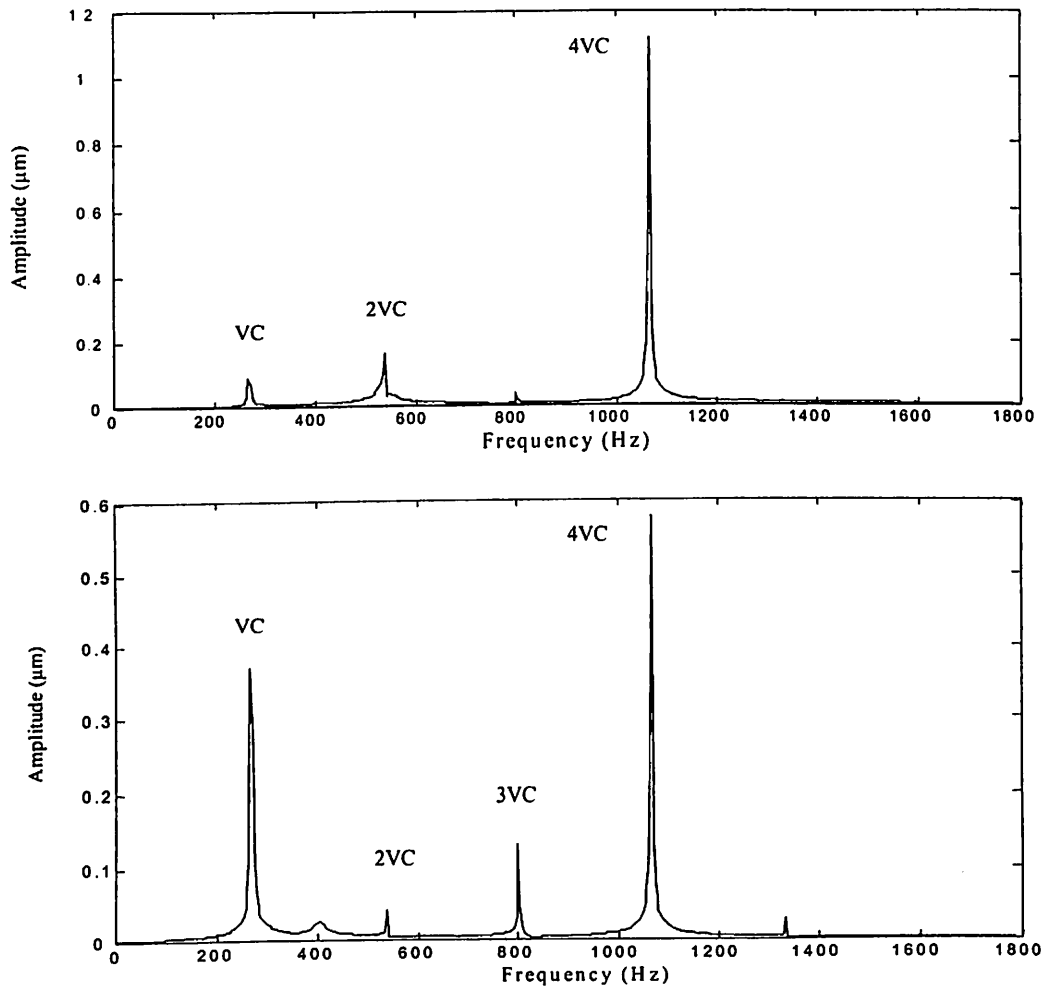


Fig. 5.7 Response plot for outer race waviness at  $N_w = 31$

Table 5.1 Summary of outer race waviness

Waviness Order (lobes / circumference)	Peak Amplitude at	Harmonic in Vibration Spectrum at
7	<i>VC</i>	<i>2VC</i>
8	<i>VC</i>	<i>2VC, 3VC, 4VC</i>
12	<i>2VC</i>	<i>VC, 3VC</i>
16	<i>2VC</i>	<i>VC, 4VC</i>
17	<i>2VC</i>	<i>VC, 4VC</i>
21	<i>3VC</i>	<i>VC, 2VC</i>
31	<i>4VC</i>	<i>VC, 2VC, 3VC</i>

A clear transformation from  $q = 1$  to  $q = 2$ ,  $q = 2$  to  $q = 3$  and  $q = 3$  to  $q = 4$  can be observed in the vibration spectrum as the number of waves increases. The amplitude of peak decreases also with increasing number of waves ( $N_w$ ). This has been theoretically proved by Wardle (1988(a)) and Aktürk (1999). The radial vibrations are produced when the number of waves per circumference is an integral multiple of the number of balls in the bearing. This has also been observed by Wardle (1988b) experimentally and by Yhland (1992) theoretically. Table 5.1 summarizes the relevant waviness orders, their peak amplitudes and harmonics in the bearing spectrum, ( $N_b \times \omega_{cage}$ ). The waviness order and vibration frequency for the outer race waviness are found to follow the relations given below.

Waviness order	Vibration caused by waviness	
$n = qN_b \pm k$	$qN_b \omega_{cage}$	(5.6)

#### 5.3.1.2 Inner race waviness

The vibrations produced by waviness on the rotating inner race exhibit a more complex spectrum than that produced by outer race waviness. In order to study the inner race waviness, the bearings of the simulation model are assumed to have waviness of the same order and magnitude. The amplitude of the waviness is  $0.2 \mu\text{m}$ , number of balls is 8 and rotor speed is 5000 rpm. As the inner races of the bearings are fitted to the rotor, they rotate at the rotor speed. Axial vibration occurs at frequencies that are harmonics of the ball to inner pass rate  $[-N_b(\omega_{cage} - \omega_{inner})]$ . The response has been obtained for different orders of waviness at inner race. For relatively low orders (in this case waviness is also called *out of roundness*), the vibration spectrum due to waviness was first experimentally studied in detail by Gustafsson et al. (1963). They reported that the number of waves times the inner race rotational speed dominates the vibration spectrum. The same conclusion has also been reported by Yhland (1967).

The predicted vibrations are clearly observed in case of 2 waves, as shown in Fig. 5.8. A dominant peak appears at  $2\omega_{inner} = 166.67 \text{ Hz}$  with the other peaks at super harmonics of the rotor speed  $4\omega_{inner} = 333.5 \text{ Hz}$ ,  $6\omega_{inner} = 500 \text{ Hz}$  and at the wave passage frequency (WPF)  $\omega_{wp} = N_b(\omega_{inner} - \omega_{cage}) = 400.3 \text{ Hz}$ . Other Peaks also appear which are

more complicated at  $\omega_{wp} - 2\omega_{inner} = 233.5$  Hz and at  $\omega_{wp} + 2\omega_{inner} = 567$  Hz. The major peaks of the frequency spectra are also brought-out by phase plot with the appearance of dense closed orbits. However, a more complicated response is observed for 3 waves. A dominant peak of relatively smaller amplitude is observed at  $3\omega_{inner} = 250$  Hz, implying a change of shape in the vibration spectrum. While the other peaks are observed at  $\omega_{wp} - 2\omega_{inner} = 233.6$  Hz,  $6\omega_{inner} = 498$  Hz,  $\omega_{wp} + \omega_{inner} = 483.6$  Hz,  $2\omega_{wp} - \omega_{inner} = 717$  Hz and at  $9\omega_{inner} = 750$  Hz as shown in Fig. 5.9.

For 4 waves, the peak amplitude appears in the spectrum at wave passage frequency ( $\omega_{wp}$ ) = 400.3 Hz and a relatively small peak appears at  $4\omega_{inner} = 333.3$  Hz. The vibrations due to waviness for vertical displacement are relatively small (0.5  $\mu$ m). The other peak amplitude appears at super-harmonic of the rotor speed  $2\omega_{wp} = 800.6$  Hz and this is confirmed by the presence of two dense closed orbits in phase plots as shown in Fig. 5.10.

For 6 waves, the frequency spectrum has a closer match with the given equation and from this waviness order onwards, the vibration spectrum is in better agreement with this equation. The waviness order and vibration frequency for inner race waviness follow the following relations,

Waviness order	Vibration caused by waviness	
$n = qN_b \pm k$	$qN_b (\omega_{inner} - \omega_{cage}) \pm k\omega_{inner}$	(5.7)

For 6 waves, the peak amplitude (2.5  $\mu$ m) appears in the vibration spectrum at  $\omega_{wp} - 2\omega_{inner} = 233.5$  Hz, where  $q = 1$  and  $k = 2$  in the Equation (5.7). However, there are other peaks also at  $\frac{1}{2}\omega_{wp} - \omega_{inner} = 117$  Hz,  $\frac{1}{2}\omega_{wp} + 2\omega_{inner} = 367$  Hz (where  $q = \frac{1}{2}$  and  $p = 2$ ),  $\omega_{wp} + \omega_{inner} = 484$  Hz and at  $\omega_{wp} + 6\omega_{cage} = 596$  Hz as shown in Fig. 5.11.

Wardle (1988(a)) has predicted from his linear equations of motion that the vibrations would take place only at waviness of order  $n = qN_b \pm 1$ . However, the vibrations for non-linear systems are relatively more complicated. Vibrations at the predicted speeds are the most severe ones and the equation given above matches with the simulation model for these values of waviness order.

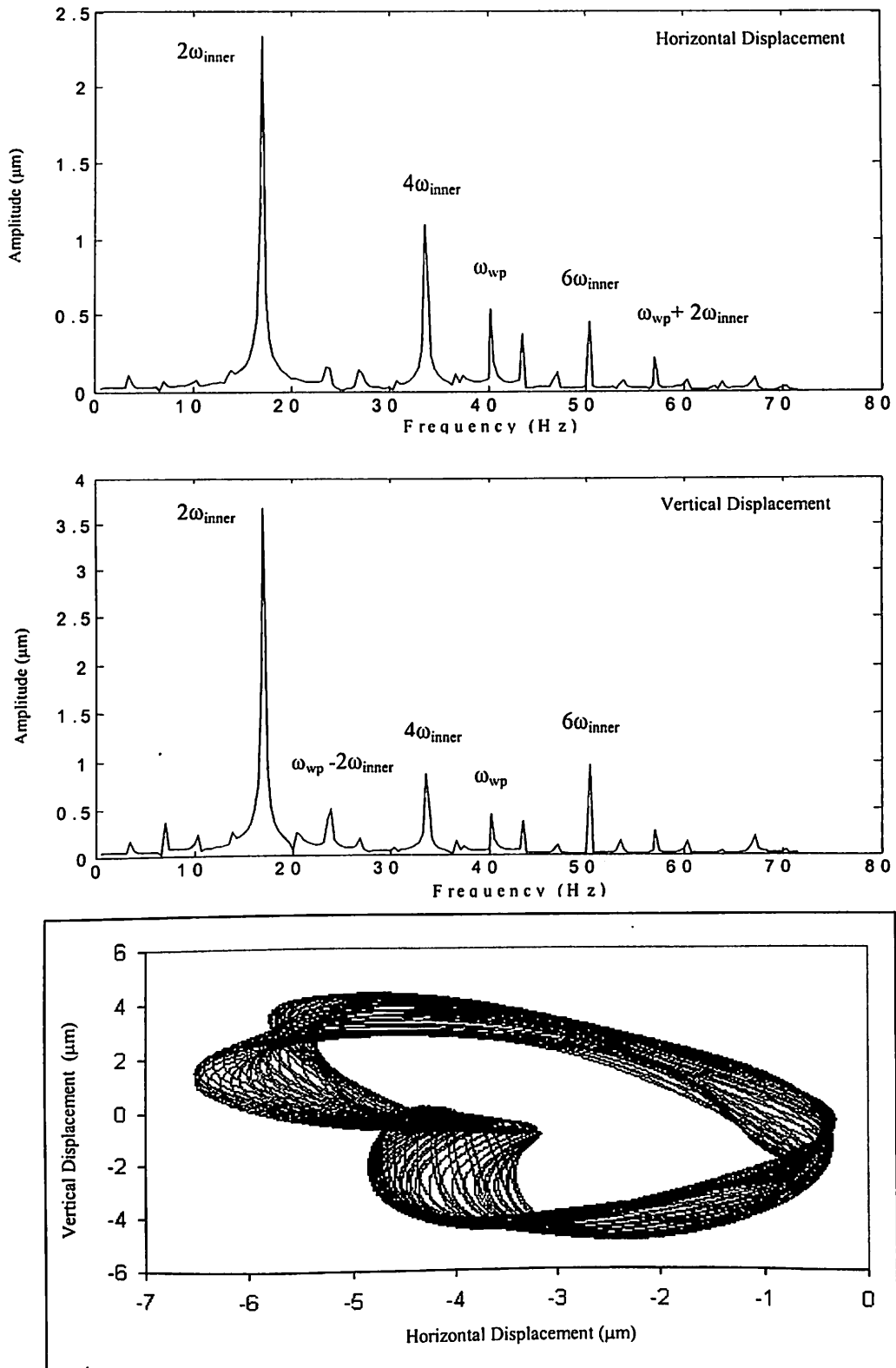


**Fig. 5.8** Response plot for inner race waviness at  $N_w = 2$



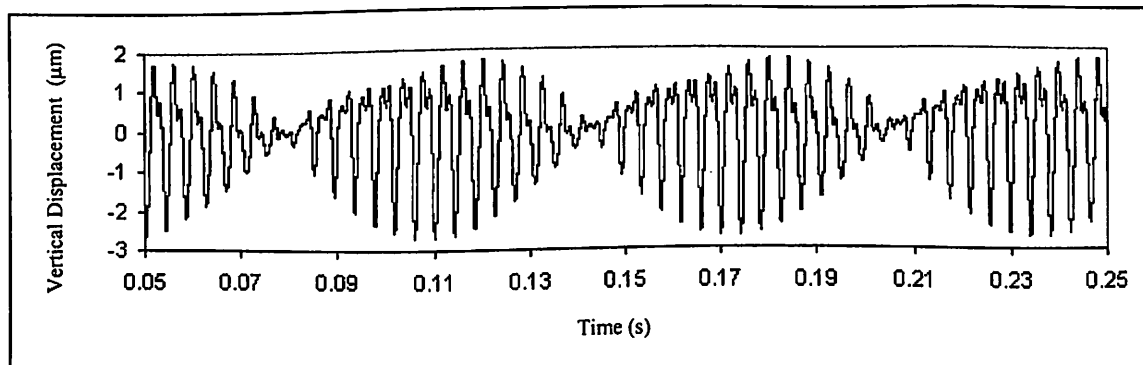
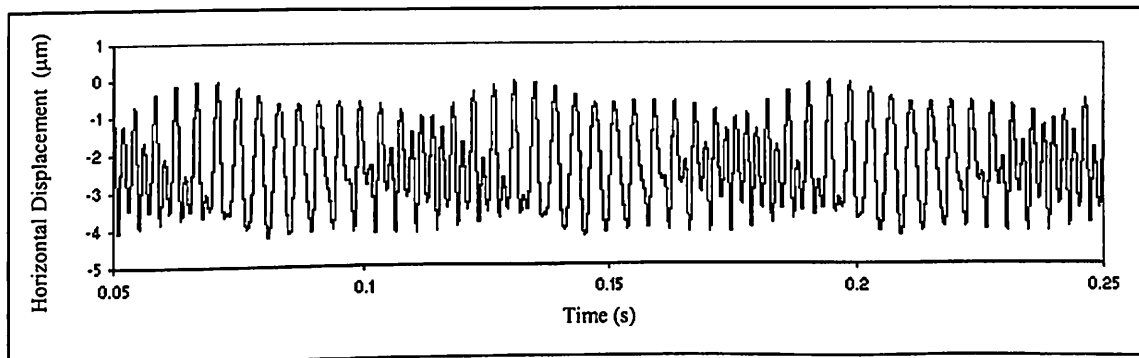
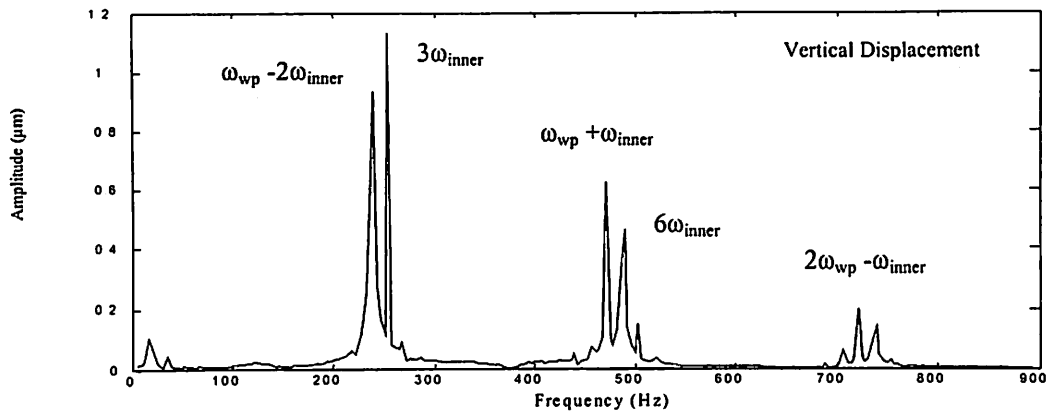
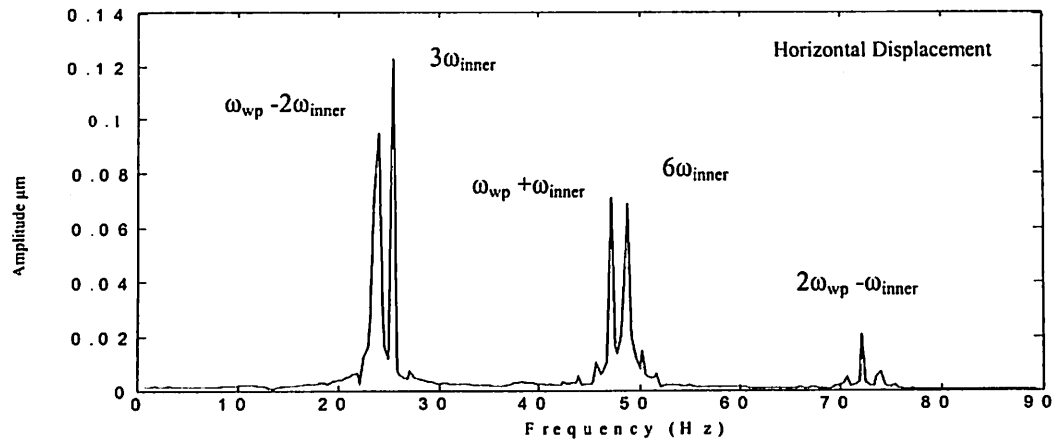
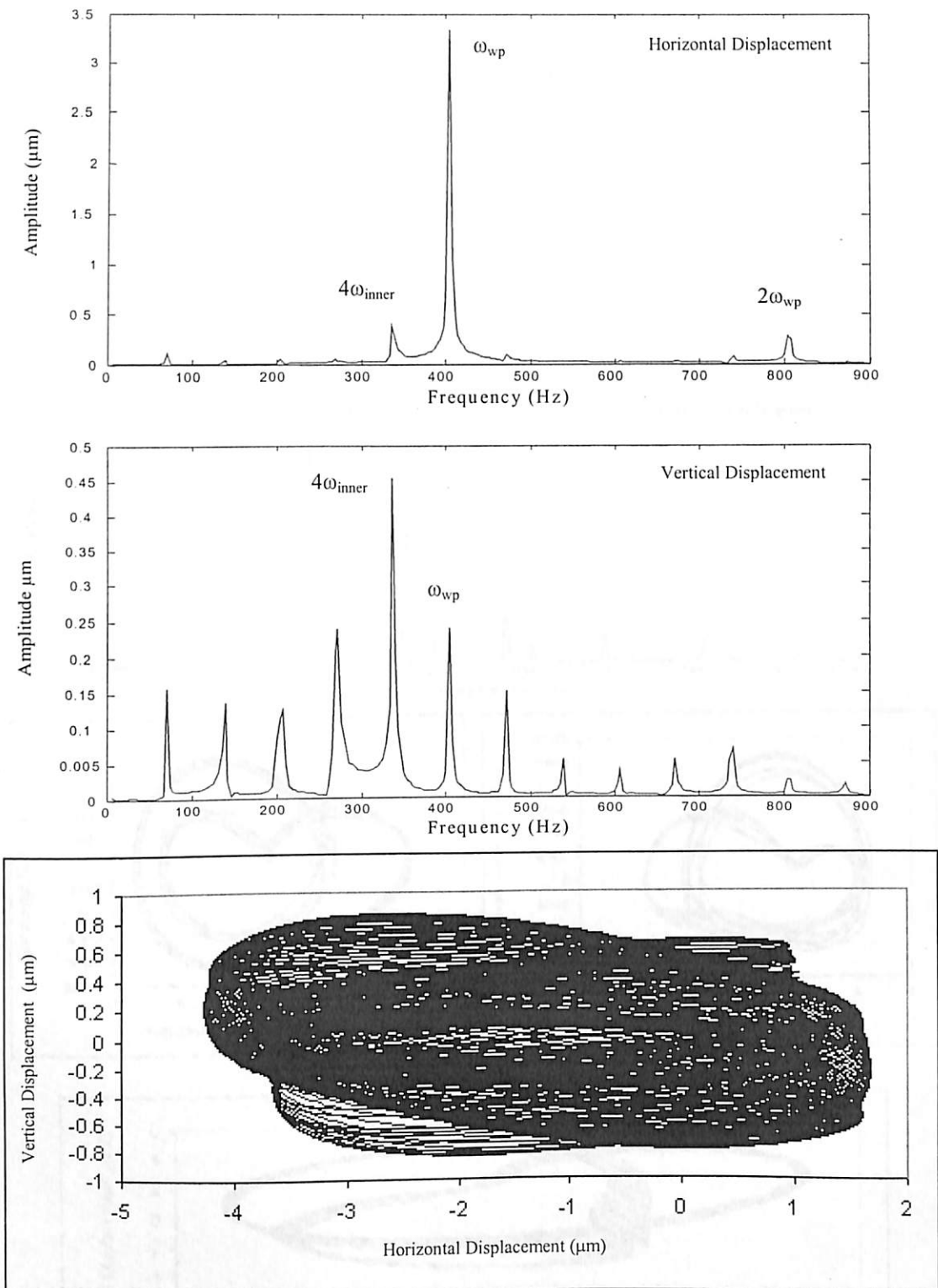


Fig. 5.9 Response plot for inner race waviness at  $N_w = 3$



**Fig. 5.10** Response plot for inner race waviness at  $N_w = 4$

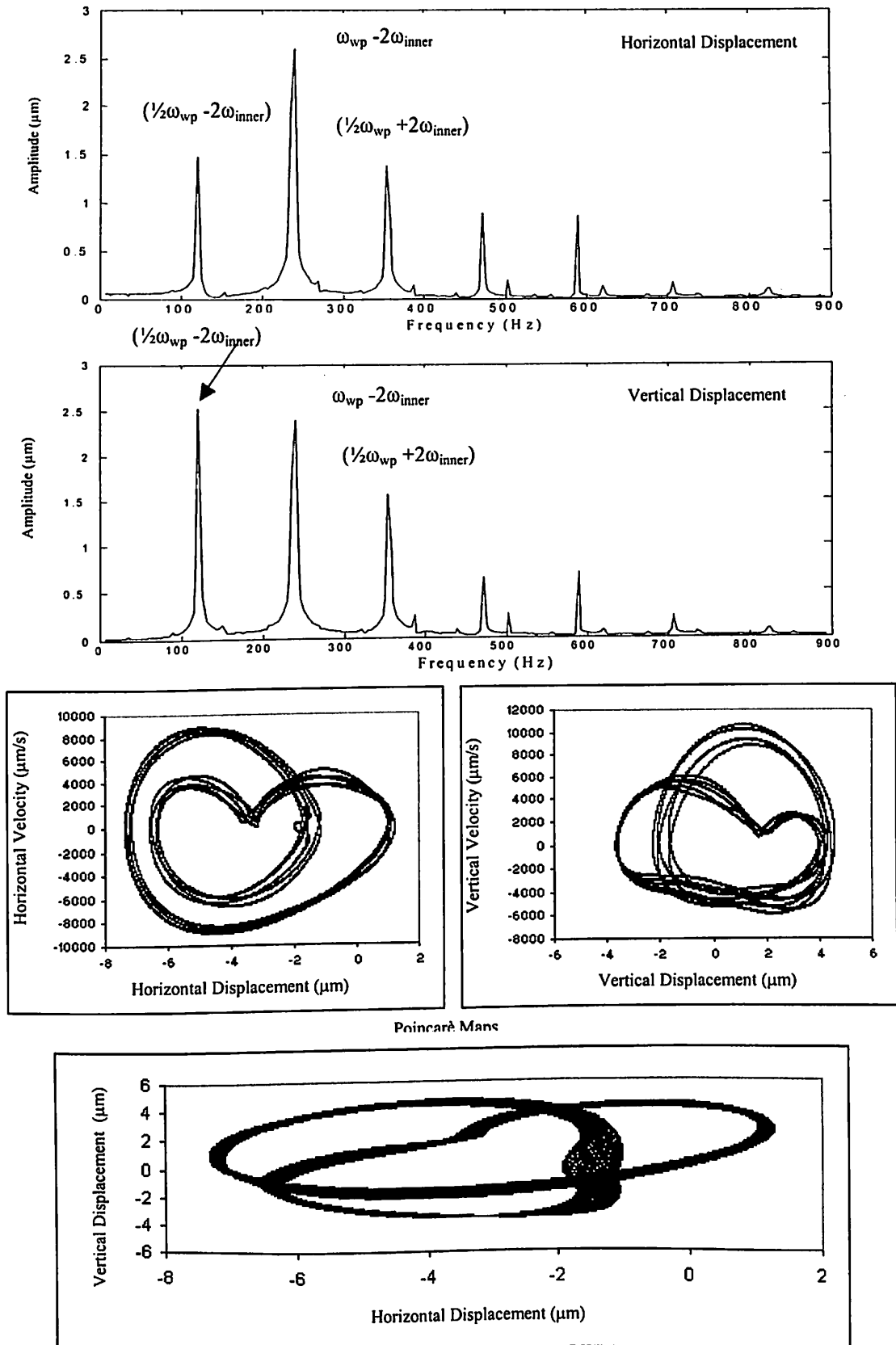


Fig. 5.11 Response plot for inner race waviness at  $N_w = 6$

For example, for 7 waves, there is a peak of high amplitude (11  $\mu\text{m}$ ) at  $\omega_{wp} - \omega_{inner} = 316$  Hz, where  $q = 1$  and  $k = 1$  in the Eq. (5.7). The other peak appears in the vibration spectrum at super-harmonic  $2\omega_{wp} - \omega_{inner} = 632$  Hz as shown in Fig. 5.12. For 9 waves, there is a peak of high amplitude (13  $\mu\text{m}$ ) at  $\omega_{wp} + \omega_{inner} = 483$  Hz, where  $q = 1$  and  $k = 1$  in the Eq. (5.7). The other peak of small amplitude appears in the vibration spectrum at super-harmonic  $2\omega_{wp} + \omega_{inner} = 966$  Hz as given in Fig. 5.14. From the relationship given in Eq. (5.7) for 8 waves, the vibrations are predicted at wave passage frequency ( $\omega_{wp}$ ) = 400.3 Hz, where  $q = 1$  and  $k = 0$  in the above equation and its super-harmonics at  $2\omega_{wp} = 800.6$  Hz as shown in Fig. 5.13. The amplitude of peak is 0.7  $\mu\text{m}$ . When the number of waves is 10, the peak amplitude of vibration appears in the spectrum at  $\omega_{wp} + 2\omega_{inner} = 566$  Hz where  $q = 1$  and  $k = 2$  in the Eq. (5.7) as shown in Fig.5.15. The amplitude of peak is 2  $\mu\text{m}$ . The other major peak is at  $\frac{1}{2}(\omega_{wp} + 2\omega_{inner}) = 283$  Hz. The amplitude of peak is 5.5  $\mu\text{m}$ .

For 11 waves, the peak amplitude of vibration appears in the spectrum at  $2\omega_{wp} - 5\omega_{inner} = 389$  Hz where  $q = 2$  and  $k = 5$  in the above equation as shown in Fig.5.16. The amplitude of peak is 0.4  $\mu\text{m}$ . The other major peak is at  $\frac{1}{2}(\omega_{wp} + 3\omega_{inner}) = 325$  Hz. The amplitude of peak is 4  $\mu\text{m}$ . For waviness of order 12, the predicted peak is either at  $\omega_{wp} + 4\omega_{inner}$  or at  $2\omega_{wp} - 4\omega_{inner}$  depending on the parameter  $q$  and  $k$  chosen in the Eq. 5.7. The peak for 12 waves are at  $2\omega_{wp} - 4\omega_{inner} = 467$  Hz where  $q = 2$  and  $k = 4$  in the above equation as shown in Fig. 5.17. Vibration amplitudes in the spectrum for 12 waves become negligible ( $< 1.5 \mu\text{m}$ ). However, there is another peak at  $\omega_{wp} + 4\omega_{inner} = 733.5$  Hz, where  $q = 1$  and  $k = 4$  in Eq. (5.7). A clear transformation from  $q = 1$  to  $q = 2$  can be observed in the vibration spectrum obtained for the waviness of order 12. When the number of waves is 13, the major peaks appear in the spectrum at  $2\omega_{wp} - 3\omega_{inner} = 550$  Hz and at  $\frac{1}{2}(2\omega_{wp} - 3\omega_{inner}) = 275$  Hz where  $q = 2$  and  $k = 3$  in the Eq. (5.7) as shown in Fig.5.18. Similar pattern is observed to appear in the vibration spectrum for 14 waves.

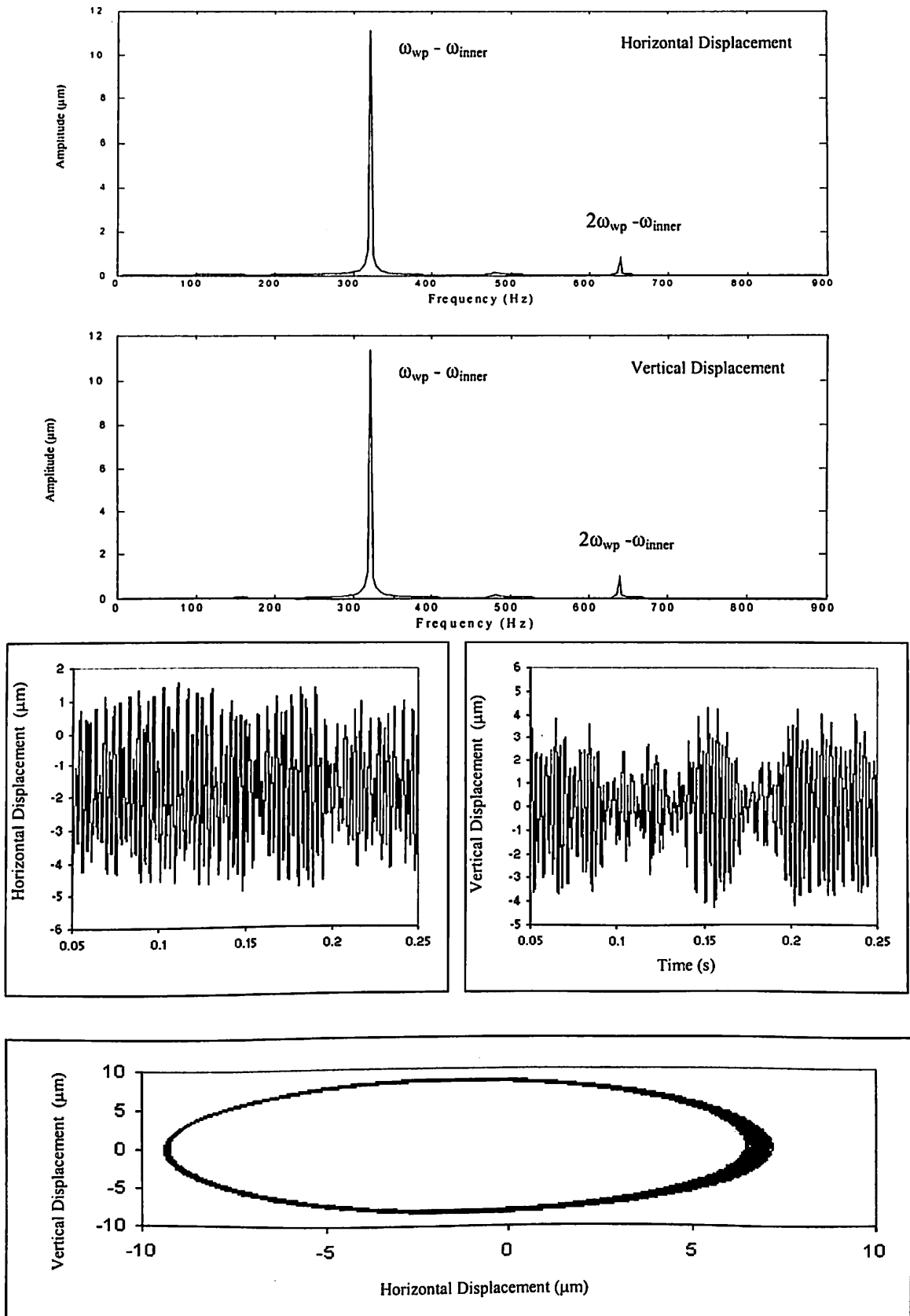
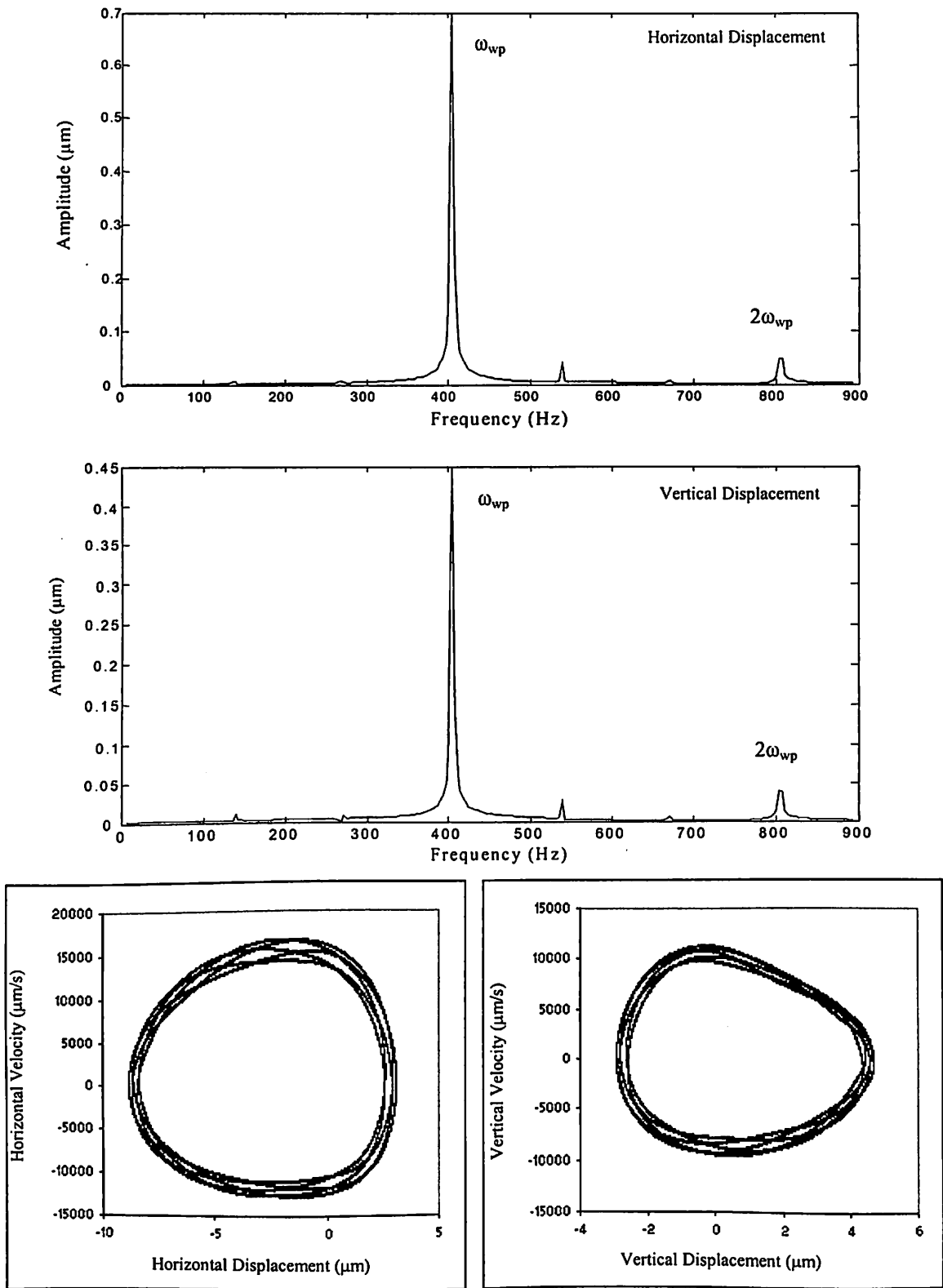


Fig. 5.12 Response plot for inner race waviness at  $N_w = 7$



Poincaré Maps

**Fig. 5.13** Response plot for inner race waviness at  $N_w = 8$

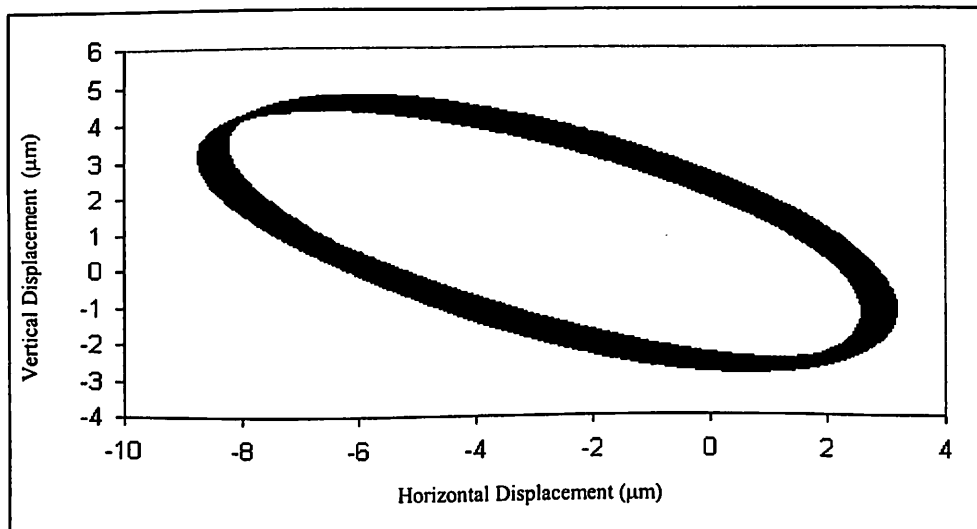
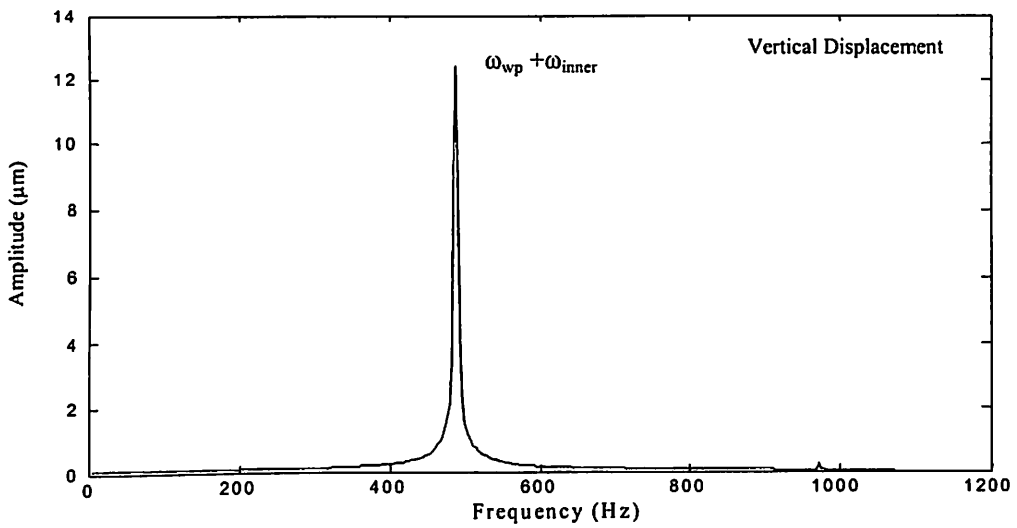
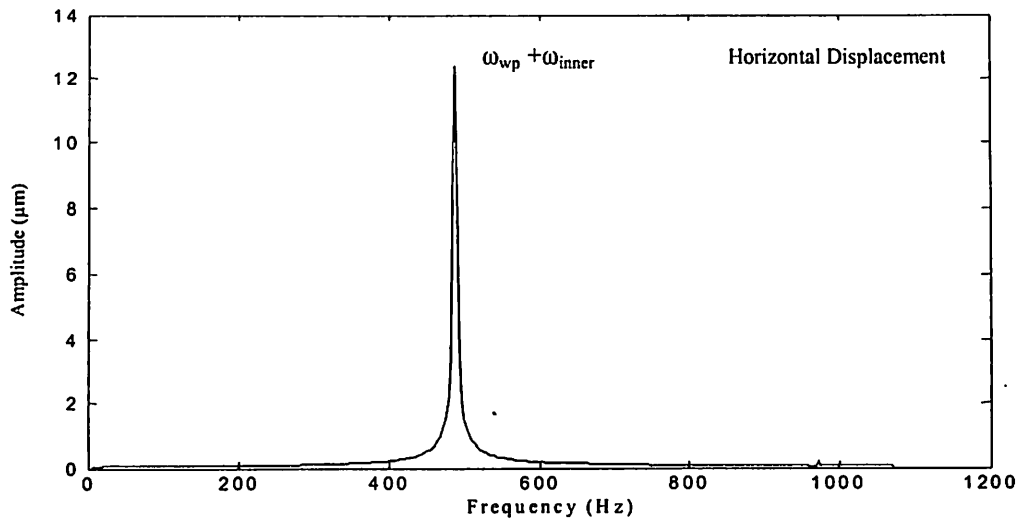


Fig. 5.14 Response plot for inner race waviness at  $N_w = 9$

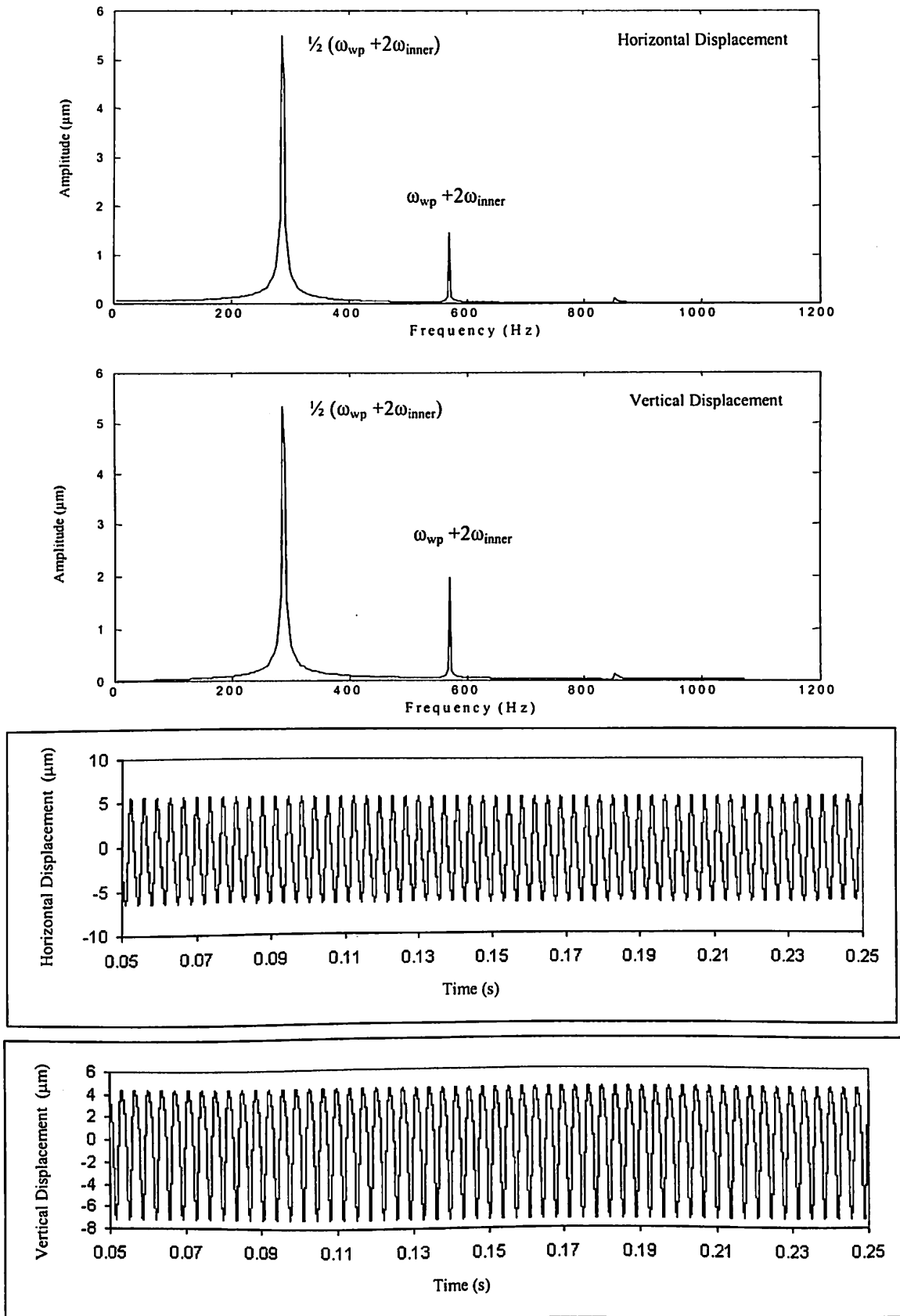
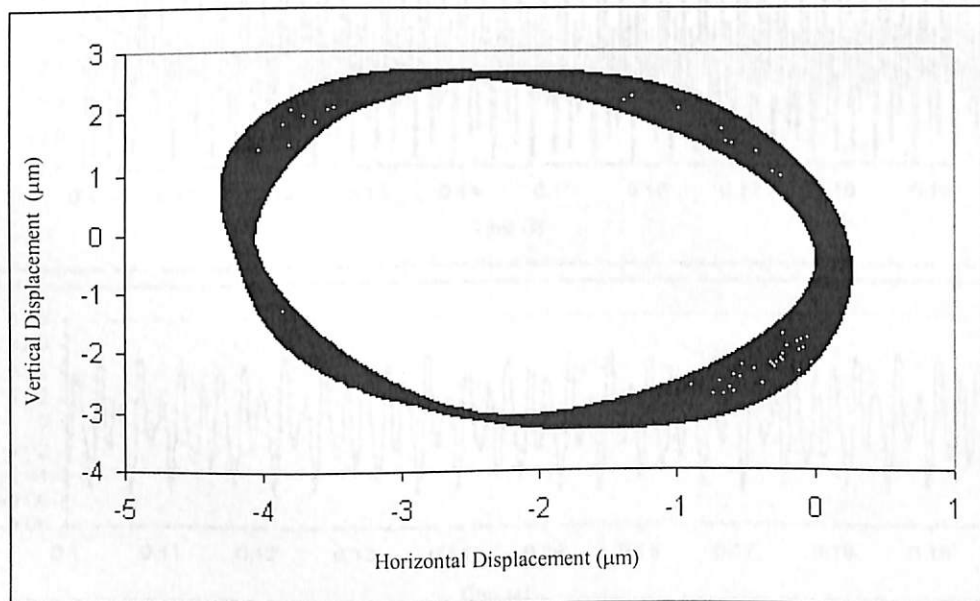
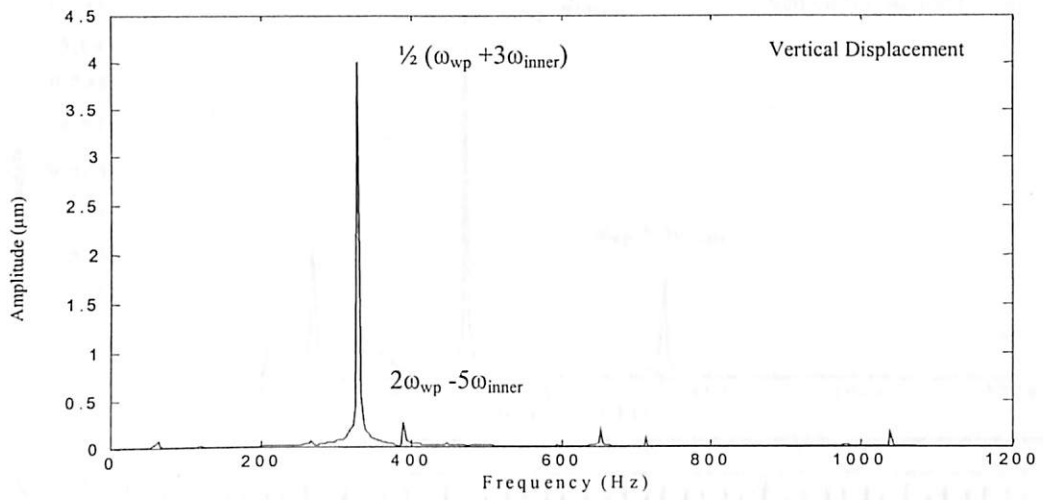
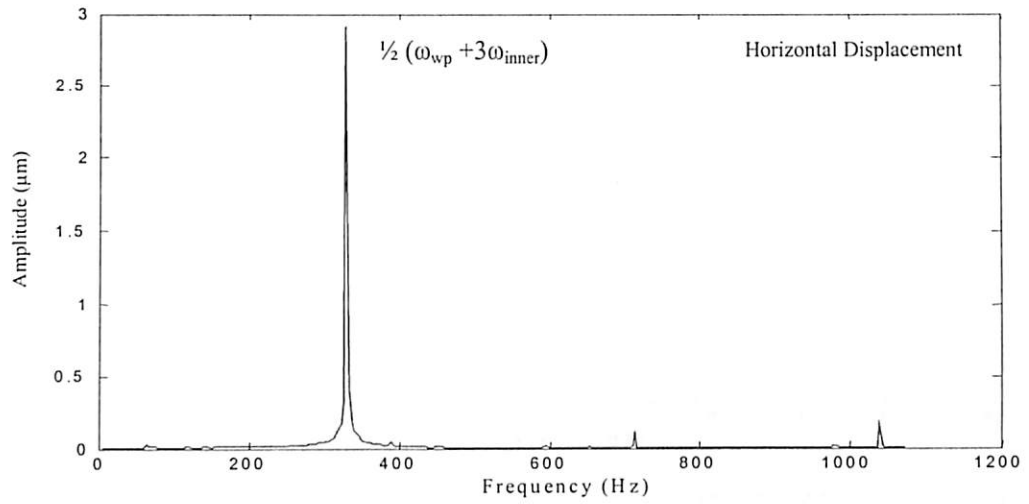


Fig. 5.15 Response plot for inner race waviness at  $N_w = 10$





**Fig. 5.16** Response plot for inner race waviness at  $N_w = 11$

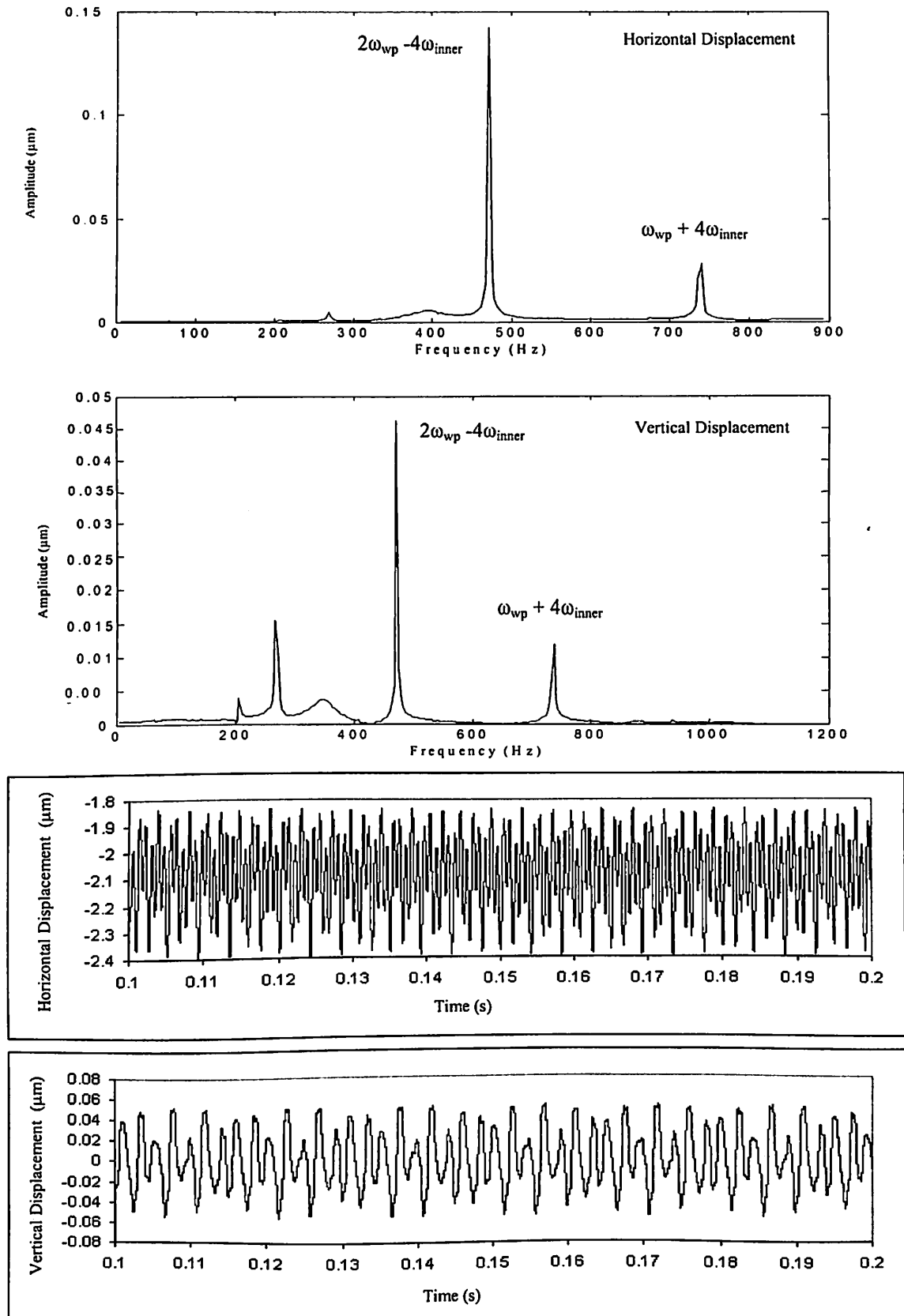
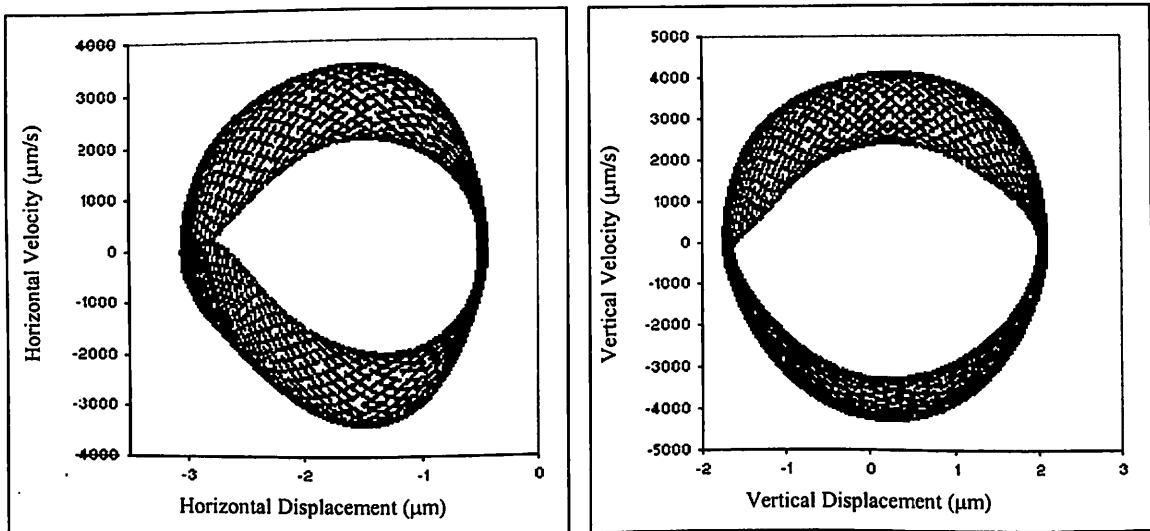
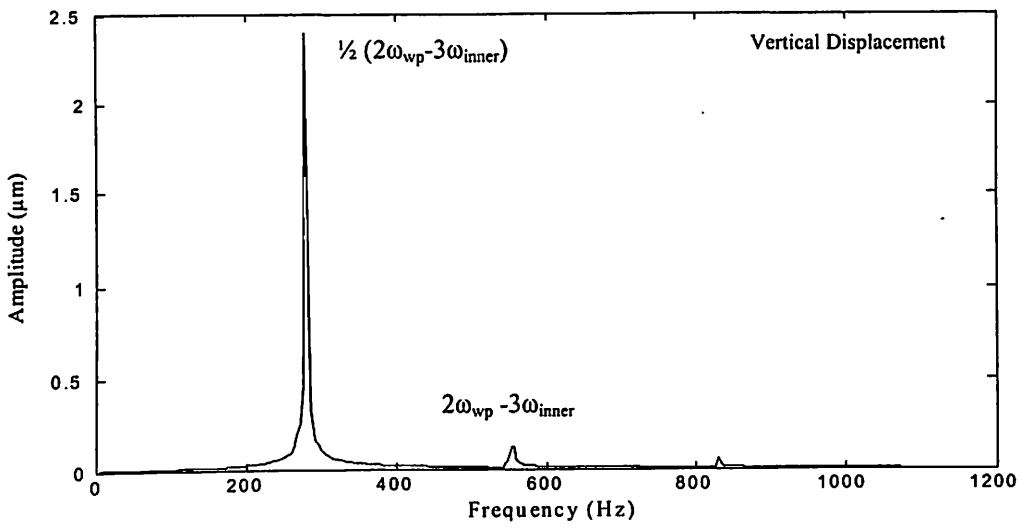
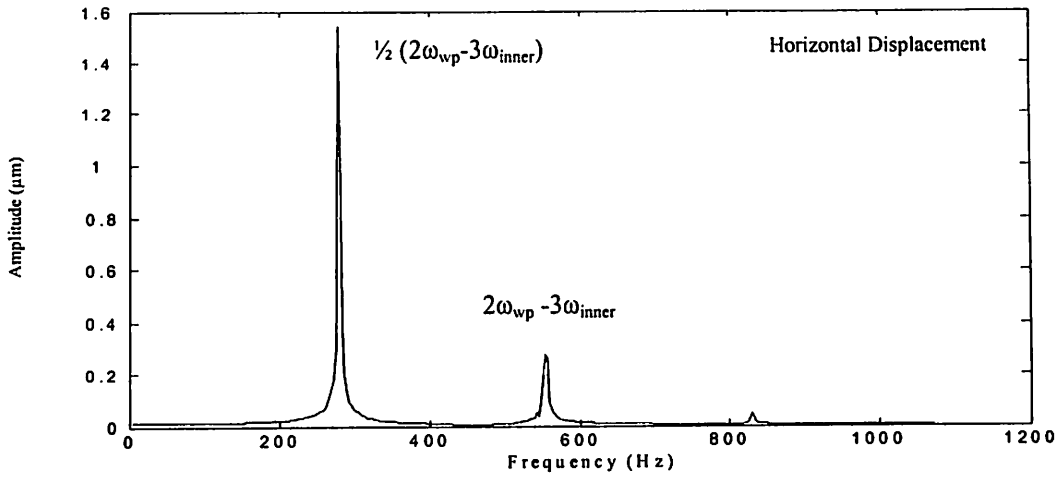
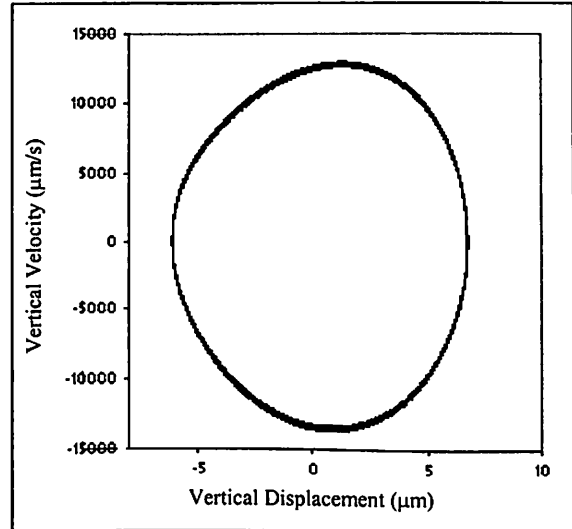
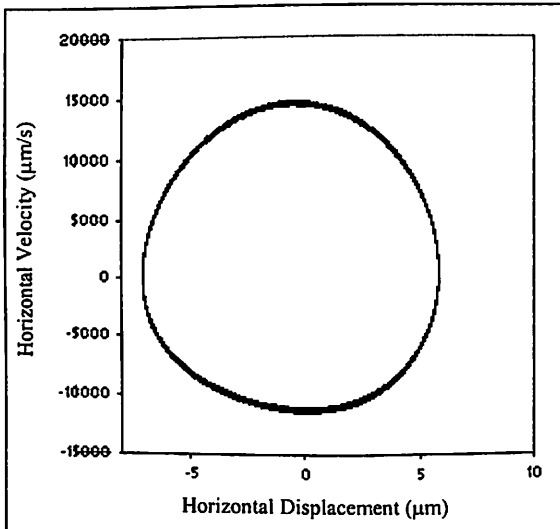
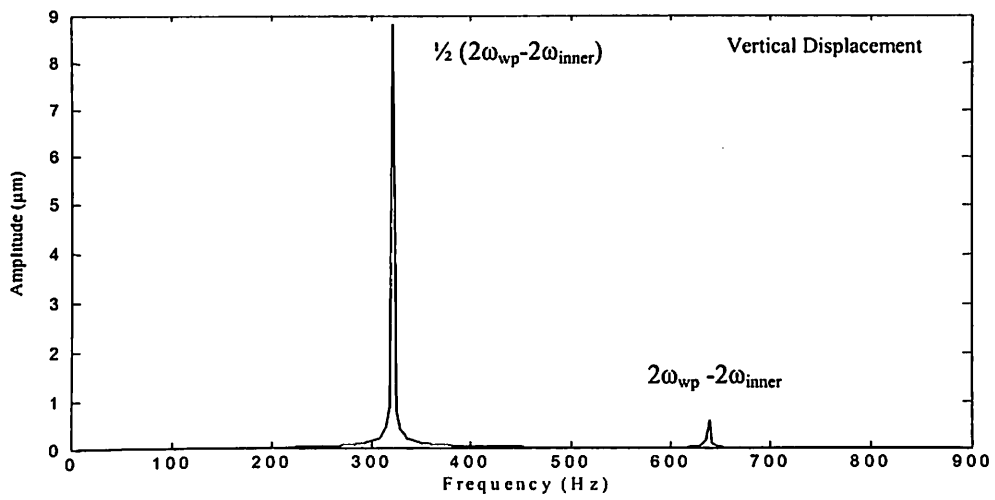
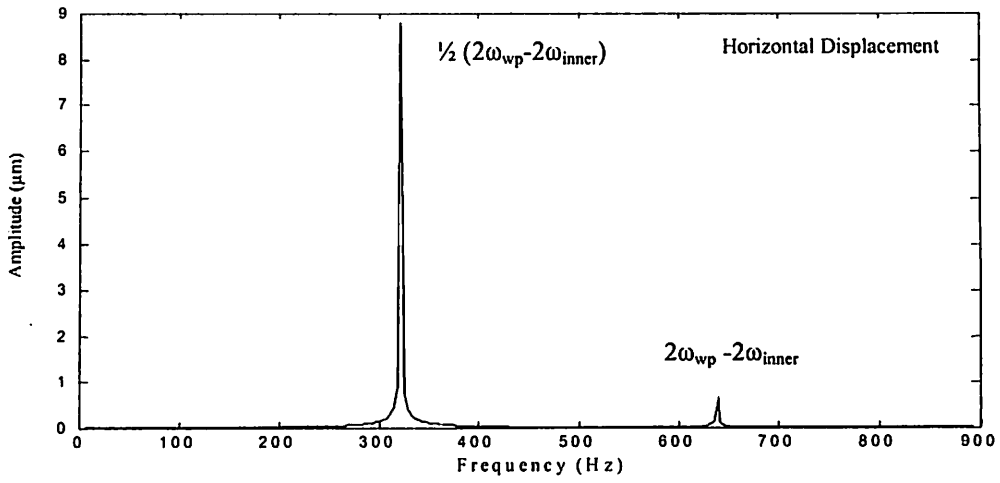


Fig. 5.17 Response plot for inner race waviness at  $N_w = 12$



Poincaré Maps

Fig. 5.18 Response plot for inner race waviness at  $N_w = 13$



Poincaré Maps

Fig. 5.19 Response plot for inner race waviness at  $N_w = 14$

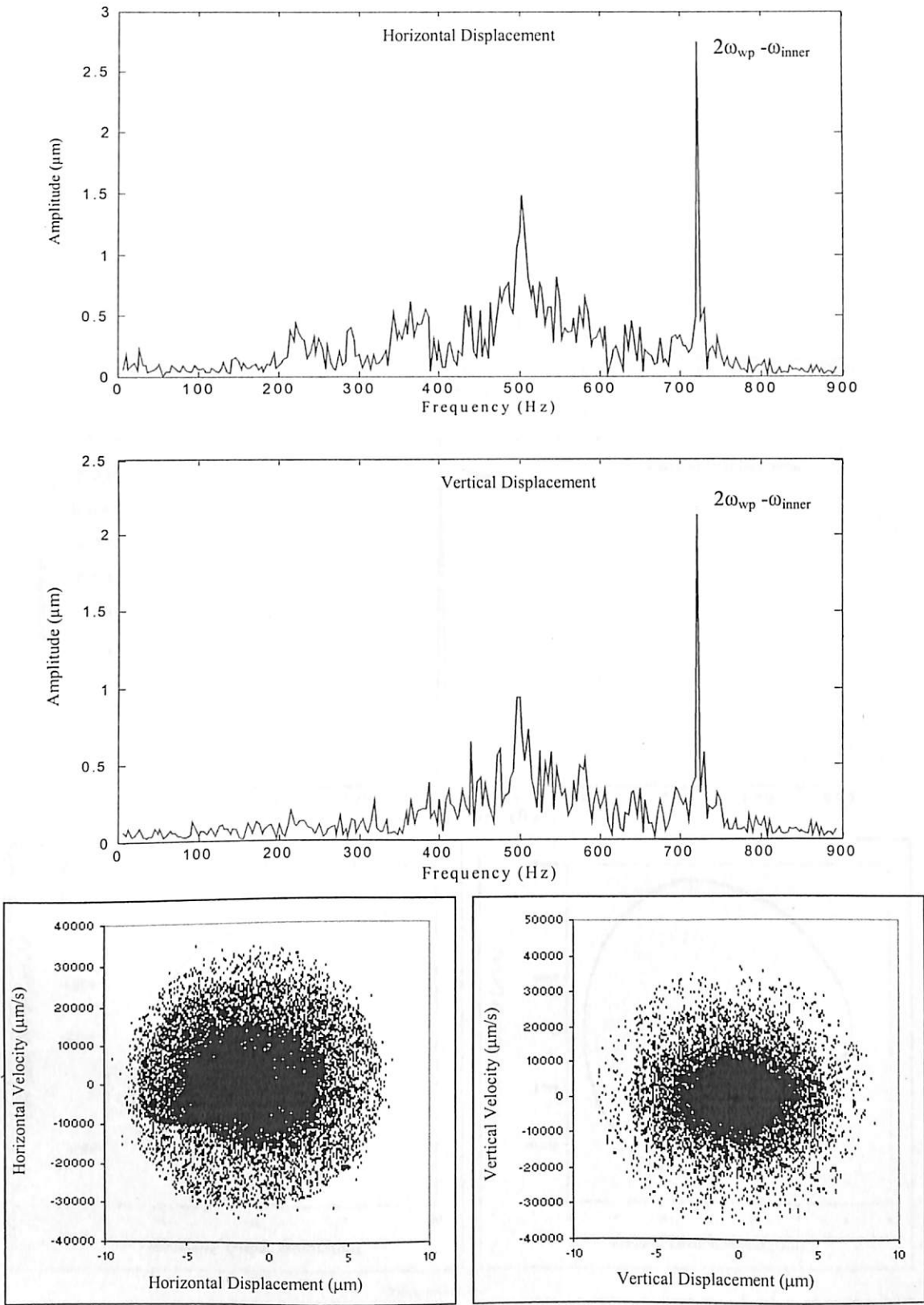
For 14 waves, the major peak amplitude of vibrations appears in the spectrum at  $2\omega_{wp} - 2\omega_{inner} = 633.5$  Hz and at  $\frac{1}{2}(2\omega_{wp} - 2\omega_{inner}) = 316.5$  Hz where  $q = 2$  and  $k = 2$  in the Eq. (5.7) as shown in Fig.5.19. For 15 waves, severe vibration exists as predicted by Wardle (1988(a)). The peak amplitude of dense vibration appears at  $2\omega_{wp} - \omega_{inner} = 717$  Hz, where  $q = 2$  and  $k = 1$  in the Eq. (5.7) as shown in Fig.5.20. The nature of solution for 15 waves is chaotic. The frequency spectrum has a band structure in between spikes of  $(2\omega_{wp} - \omega_{inner})$  and its multiples. The amplitude of peak is  $2.5 \mu\text{m}$ . The fine-layered structure of the strange attractor is also clear from Poincarè maps. The orbit does not repeat itself at this speed. The Poincarè maps of chaotic solutions have fractal structures that repeat as the map is magnified. It is clear that loss of periodicity is the characteristic feature of chaotic solution.

When the number of waves is 16, the stability returns and the peak amplitude of vibration appears at  $2\omega_{wp} = 800.5$  Hz where  $q = 2$  and  $k = 0$  in Eq. (5.7) as shown in Fig.5.21. The amplitude of peak is  $1.4 \mu\text{m}$ . For waviness order of 17, the peaks are at  $2\omega_{wp} + \omega_{inner} = 884$  Hz,  $\frac{1}{2}(2\omega_{wp} + \omega_{inner}) = 442$  Hz,  $2\omega_{wp} - 6\omega_{cage} = 598$  Hz and at  $2\omega_{wp} - \omega_{inner} = 717$  Hz as shown in Fig. 5.22. The amplitude of peak is  $7 \mu\text{m}$ . The system shows high non-linearity for 15 and 17 waves, while for 16 waves a periodic nature is observed. Hence, severe vibrations would take place only at waviness of order  $n = qN_b \pm 1$  as also predicted by Wardle (1988(a)), where  $q = 2$  in this equation.

In the present results, four different stages are observed. From  $N_w = 2$  to  $N_w = 5$ , small amplitude of peak in vibration spectrum exists. From  $N_w = 7$  to  $N_w = 9$ , the predicted vibrations are for  $q = 1$  in the Eq. (5.7). From  $N_w = 11$  to  $N_w = 13$ , there is a transformation from  $q = 1$  to  $q = 2$  in Eq. (5.7) and from  $N_w = 14$  to  $N_w = 17$  the predicted vibrations are again for  $q = 2$ . A similar trend is also expected for larger orders of waviness. Table 5.2 shows the summary of the inner race waviness.

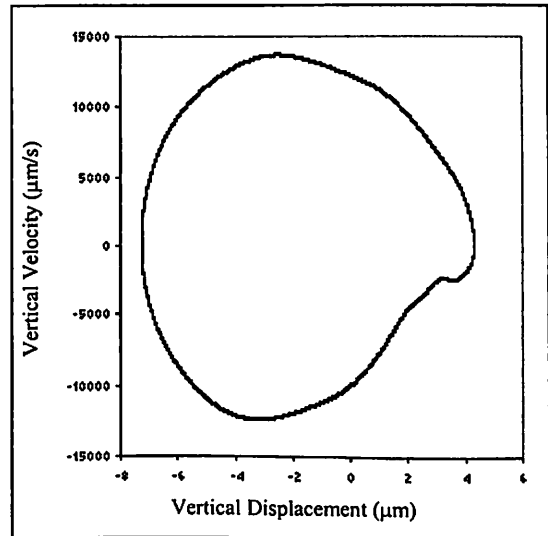
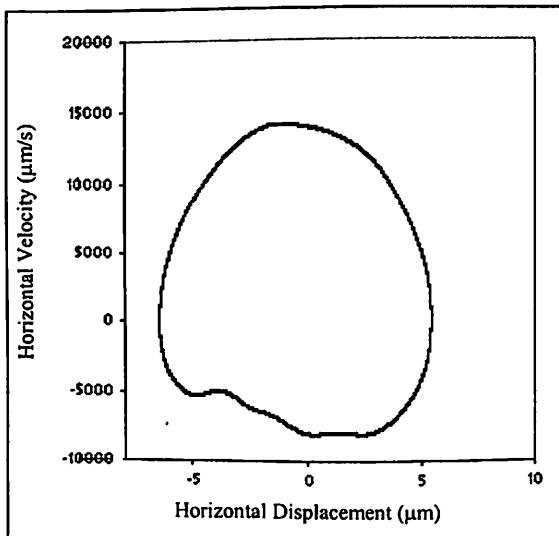
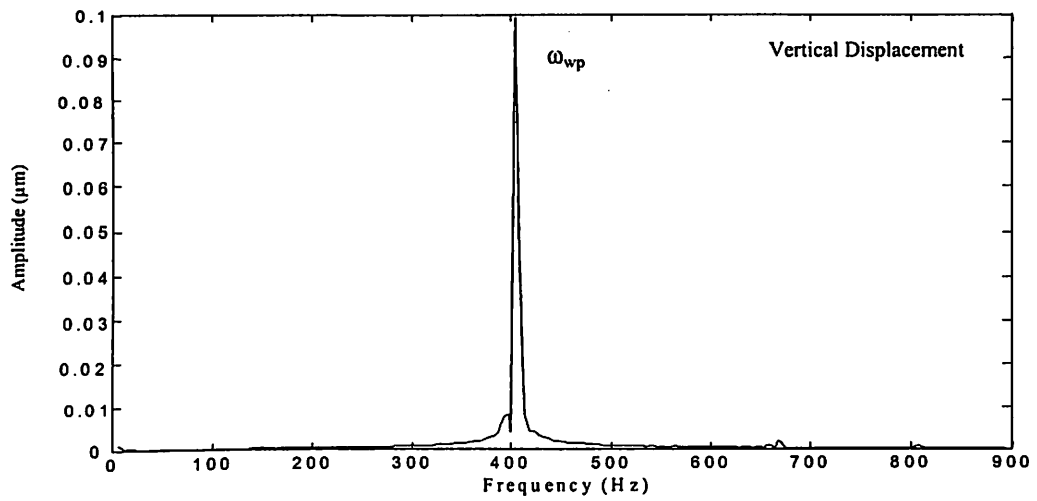
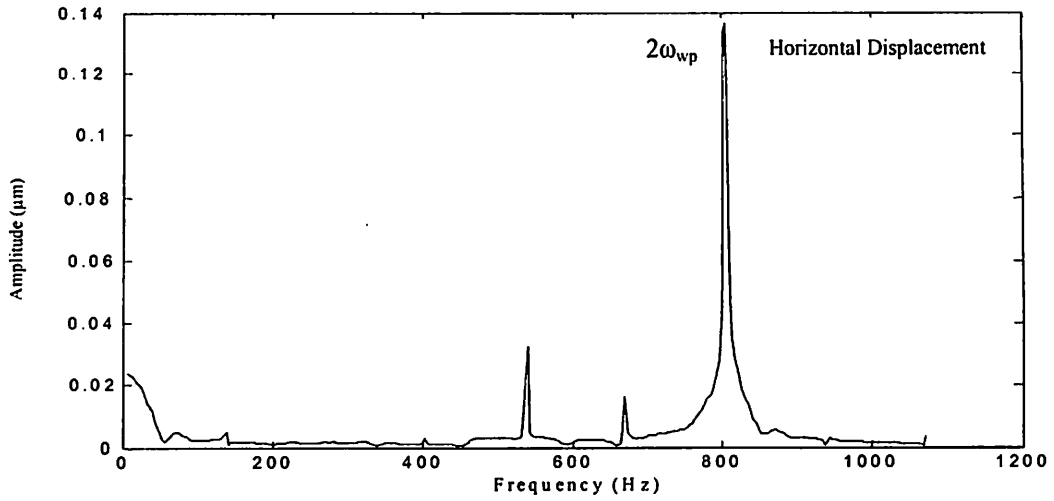
### 5.3.1.3 Ball waviness

In order to study the effect of ball waviness, the ball is assumed to have wavy surface. The case is further simplified by assuming that the ball rotates about an axis passing through its center and parallel to the bearing axis.



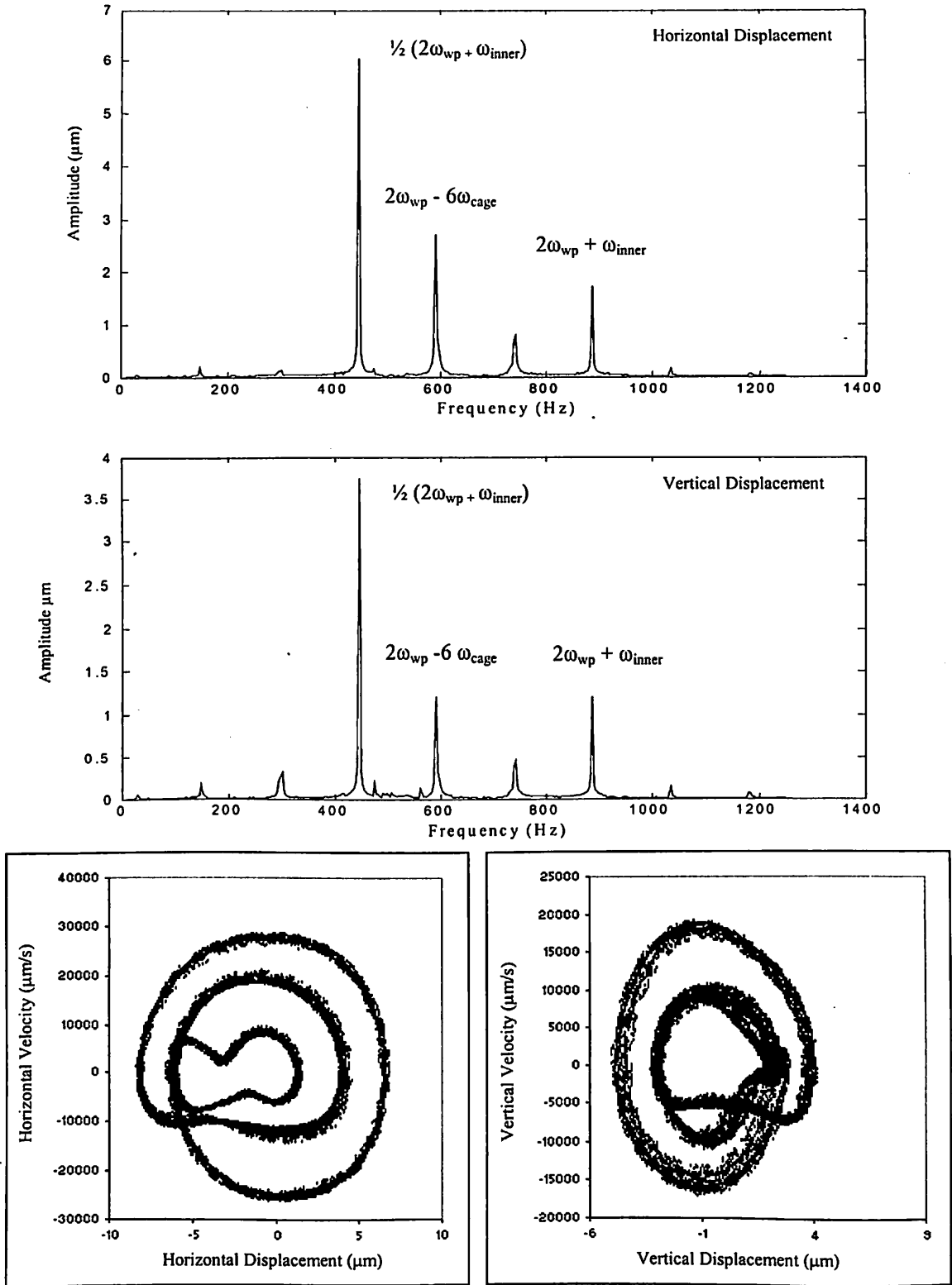
Poincaré Maps

Fig. 5.20 Response plot for inner race waviness at  $N_w = 15$



Pnincarè Mans

Fig. 5.21 Response plot for inner race waviness at  $N_w = 16$



Poincaré Maps  
**Fig. 5.22** Response plot for inner race waviness at  $N_w = 17$



**Table 5.2 Summary of inner race waviness**

<b>Waviness Order (lobes / circumference)</b>	<b>Peak Amplitude at</b>	<b>Harmonic in Vibration Spectrum at</b>
2	$2 \omega_{inner}$	$4 \omega_{inner}, 6 \omega_{inner}, \omega_{wp}, \omega_{wp} - 2\omega_{inner}, \omega_{wp} + 2\omega_{inner}$
3	$3 \omega_{inner}$	$6 \omega_{inner}, 9 \omega_{inner}, \omega_{wp} - 2\omega_{inner}, \omega_{wp} + \omega_{inner}, 2\omega_{wp} - \omega_{inner}$
4	$4 \omega_{inner}$	$2 \omega_{wp}$
6	$\omega_{wp} - 2\omega_{inner}$	$\frac{1}{2} \omega_{wp} - \omega_{inner}, \frac{1}{2} \omega_{wp} + 2\omega_{inner}, \omega_{wp} + \omega_{inner}, \omega_{wp} + 6\omega_{cage}$
7	$\omega_{wp} - \omega_{inner}$	$2 \omega_{wp} - \omega_{inner}$
8	$\omega_{wp}$	$2 \omega_{wp}$
9	$\omega_{wp} + \omega_{inner}$	$2 \omega_{wp} + \omega_{inner}$
10	$\omega_{wp} + 2\omega_{inner}$	$\frac{1}{2} (\omega_{wp} + 2\omega_{inner})$
11	$2\omega_{wp} - 5\omega_{inner}$	$\frac{1}{2} (\omega_{wp} + 3\omega_{inner})$
12	$\omega_{wp} + 4\omega_{inner}$ or $2\omega_{wp} - 4\omega_{inner}$	$\omega_{wp} + 4\omega_{inner}$
13	$2\omega_{wp} - 3\omega_{inner}$	$\frac{1}{2} (2\omega_{wp} - 3\omega_{inner})$
14	$2\omega_{wp} - 2\omega_{inner}$	$\frac{1}{2} (2\omega_{wp} - 2\omega_{inner})$
15	$2\omega_{wp} - \omega_{inner}$	$\frac{1}{2} (2\omega_{wp} - \omega_{inner})$
16	$2\omega_{wp}$	$\omega_{wp}$
17	$2\omega_{wp} + \omega_{inner}$	$\frac{1}{2} (2\omega_{wp} + \omega_{inner}), 2\omega_{wp} - 6\omega_{cage}, 2\omega_{wp} - \omega_{inner}$

The amplitude of the waviness is 0.2  $\mu\text{m}$ , number of balls is 8 and rotor speed is 5000 rpm. In the case of ball waviness, there are two important frequencies. The ball set rotates at the cage speed around the inner race and the ball with wavy surface acts like an oversized ball. Since the ball set comes to the same position after one cage rotation, the system undergoes vibrations at the cage speed ( $\omega_{cage}$ ). Other important frequency is ball rotation frequency (or, wave passage frequency) occurring at ball rotation speed ( $\omega_{wp} = N_w \omega_{roll}$ ). When the ball rotates, the position of the balls will repeat itself after each  $\frac{2}{N_w}$ , where  $N_w$  is the number of waves per circumference of the ball. Therefore, the vibration due to ball waviness will take place at the speed of  $N_w \omega_{roll}$ .

Figure 5.23 shows the vibrations for bearing with a ball having waviness of order 2. The rotor rotates at a speed of 5000 rpm. The wave passage frequency ( $N_w \omega_{roll}$ ) for  $N_w = 2$  is 166.7 Hz. A dominant peak appears in the vibration spectrum at  $2\omega_{roll} = \omega_{wp} = 166.7$  Hz with the other peaks occurring at  $2\omega_{roll} - 2\omega_{cage} = 100.5$  Hz,  $2\omega_{roll} + 3\omega_{cage} = 266.6$  Hz,  $2\omega_{roll} + 8\omega_{cage} = 433$  Hz and at  $2\omega_{roll} + 13\omega_{cage} = 600$  Hz. The high amplitude of peak appears in the frequency spectra for horizontal displacement only at the wave passage frequency. The vertical displacement response shows a fairly dense structure with small amplitudes of peaks. The phase plane plot in Fig. 5.23, gives an indication of a quasi-static response because of the 'net' structure.

For 4 waves, the peak appears at  $4\omega_{roll} = \omega_{wp} = 333.3$  Hz in horizontal displacement response as shown in Fig. 5.24. Other peaks are at  $\frac{1}{4}\omega_{wp} = 83.3$  Hz,  $4\omega_{roll} - 2\omega_{cage} = 266.5$  Hz,  $4\omega_{roll} + 2\omega_{cage} = 400$  Hz and at  $4\omega_{roll} + 8\omega_{cage} = 600$  Hz. The quasi-periodic nature of the system is seen to be continuing with this waviness order also. Figure 5.25 shows the vibrations for bearing with a ball having waviness of order 6. A dominant peak appears in the vibration spectrum at  $6\omega_{roll} = \omega_{wp} = 500$  Hz with the other peaks occurring at  $6\omega_{roll} - 8\omega_{cage} = 234$  Hz,  $6\omega_{roll} - 7\omega_{cage} = 266.6$  Hz,  $6\omega_{roll} - \omega_{cage} = 466.7$  Hz and at  $6\omega_{roll} + 8\omega_{cage} = 767$  Hz. For 8 waves, the peak appears at  $8\omega_{roll} = \omega_{wp} = 666.7$  Hz in horizontal displacement response as shown in Fig. 5.26. Other peak is at  $\frac{1}{2}\omega_{wp} = 333.3$  Hz. The system shows periodic nature for 8 waves.

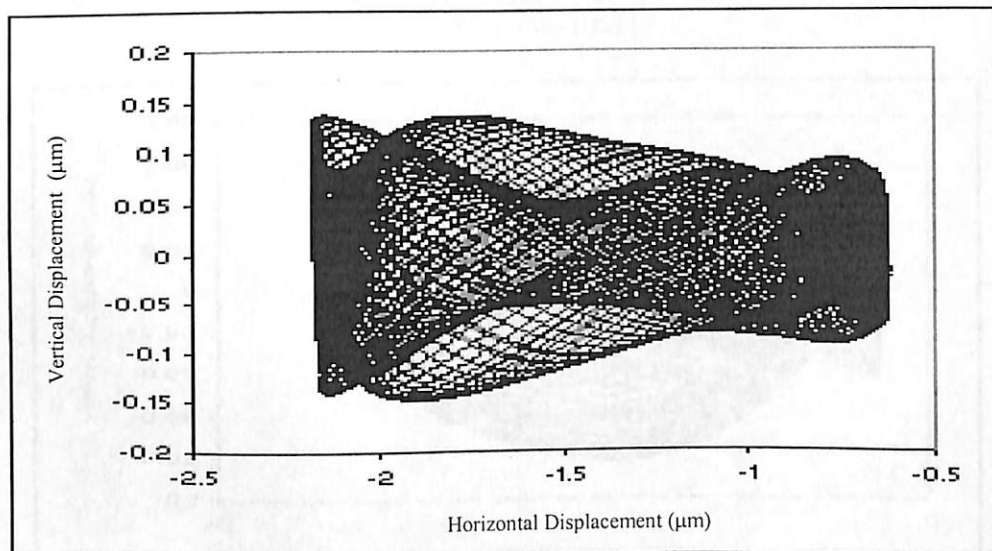
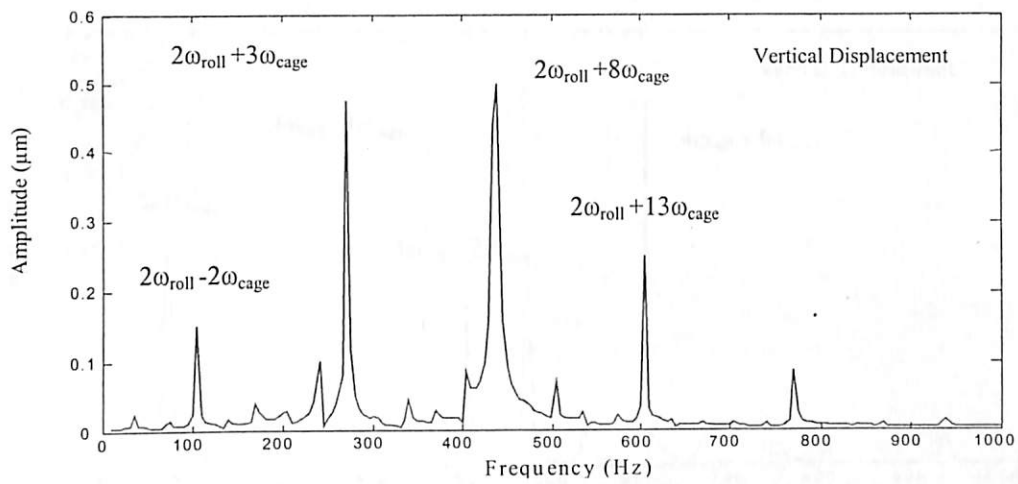
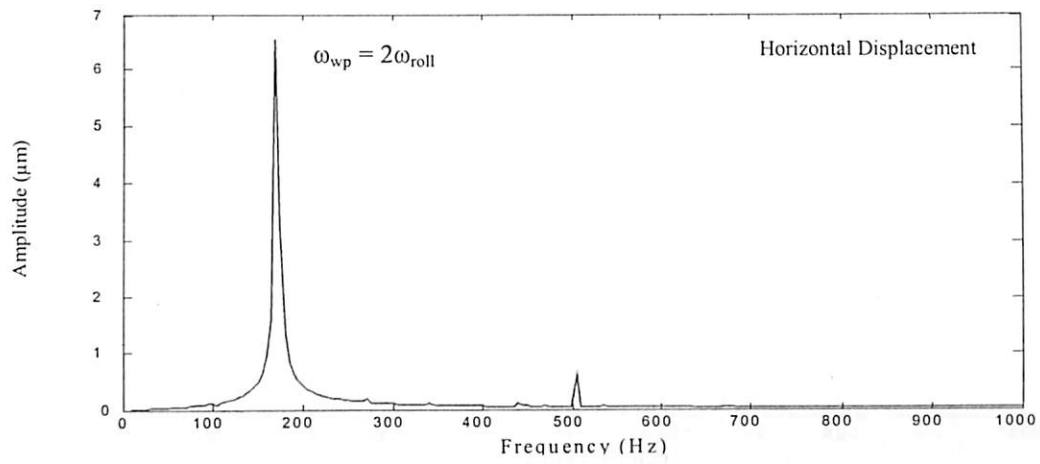


Fig. 5.23 Response plot for ball waviness at  $N_w = 2$

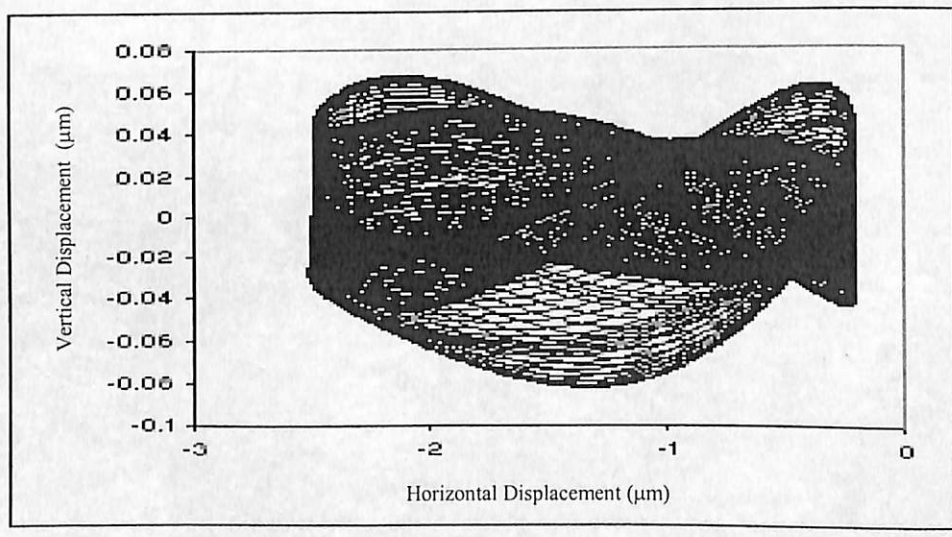
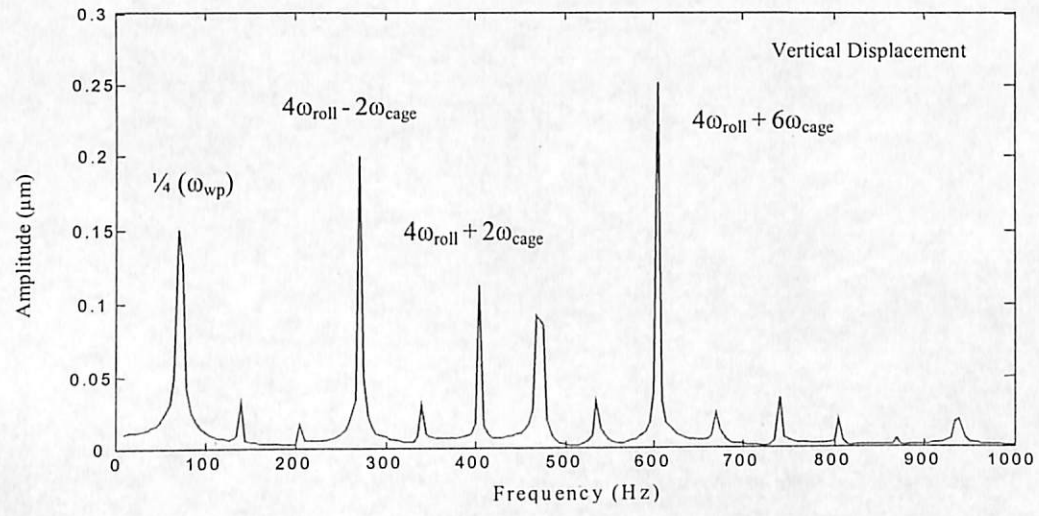
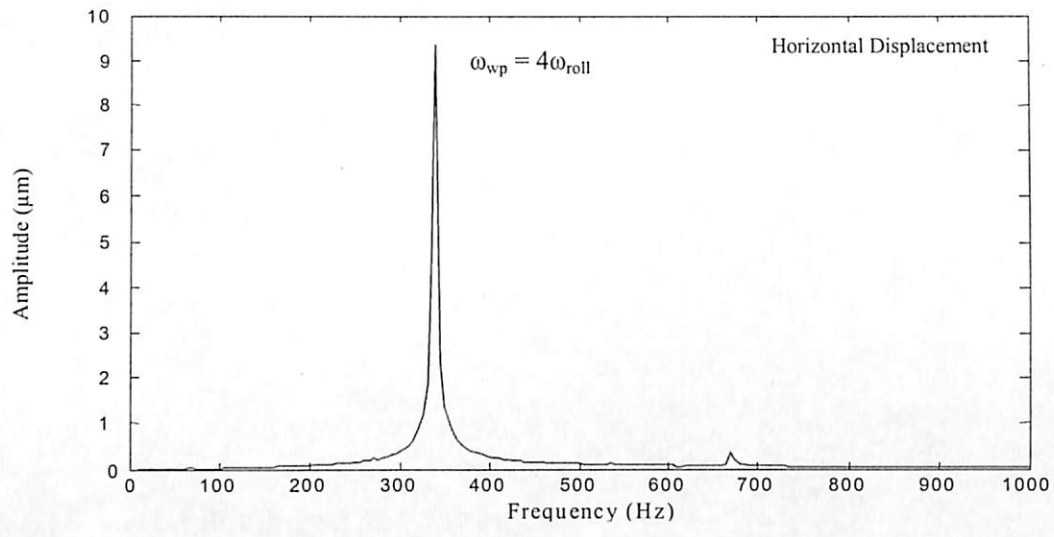


Fig. 5.24 Response plot for ball waviness at  $N_w = 4$

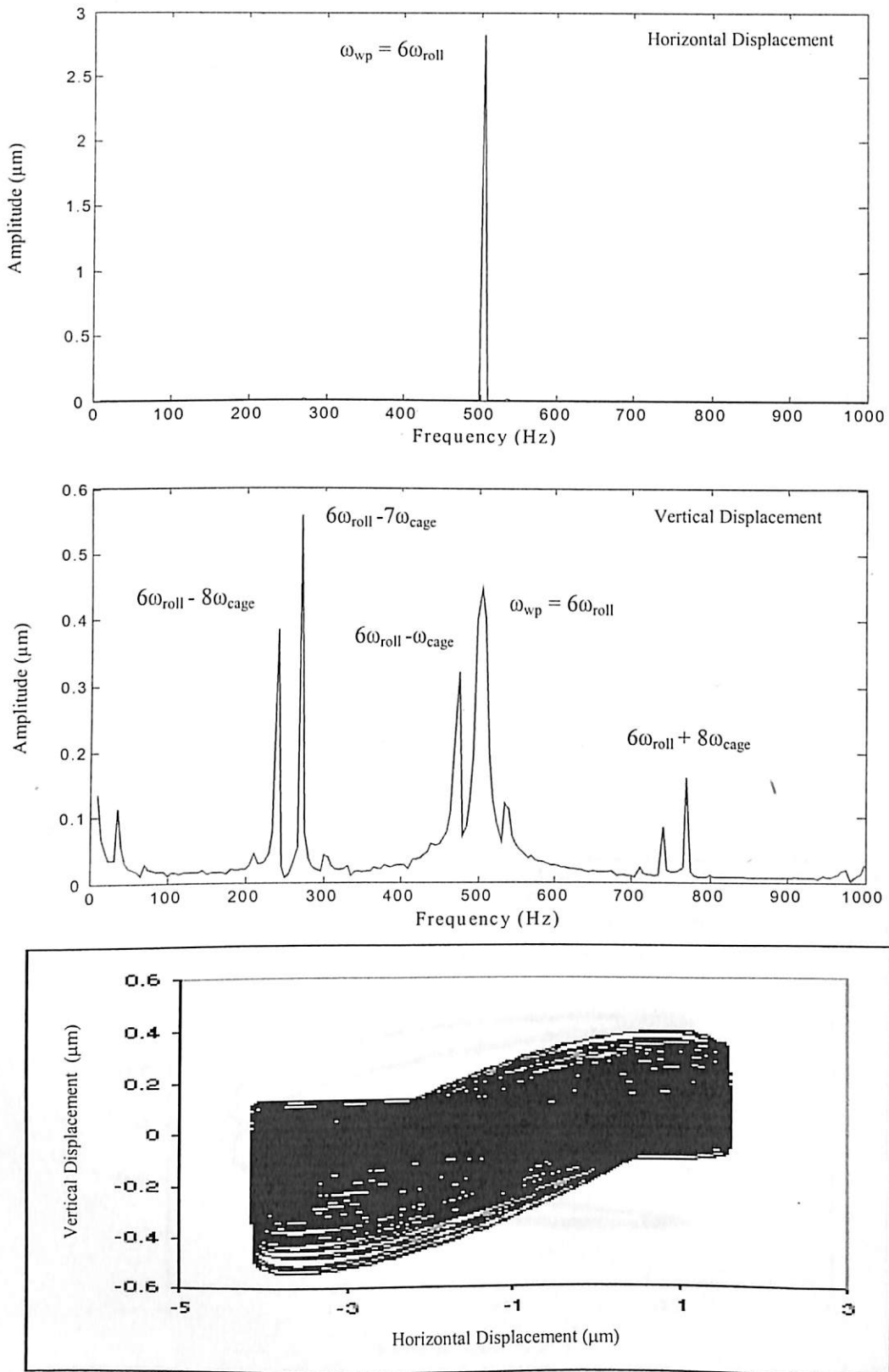


Fig. 5.25 Response plot for ball waviness at  $N_w = 6$

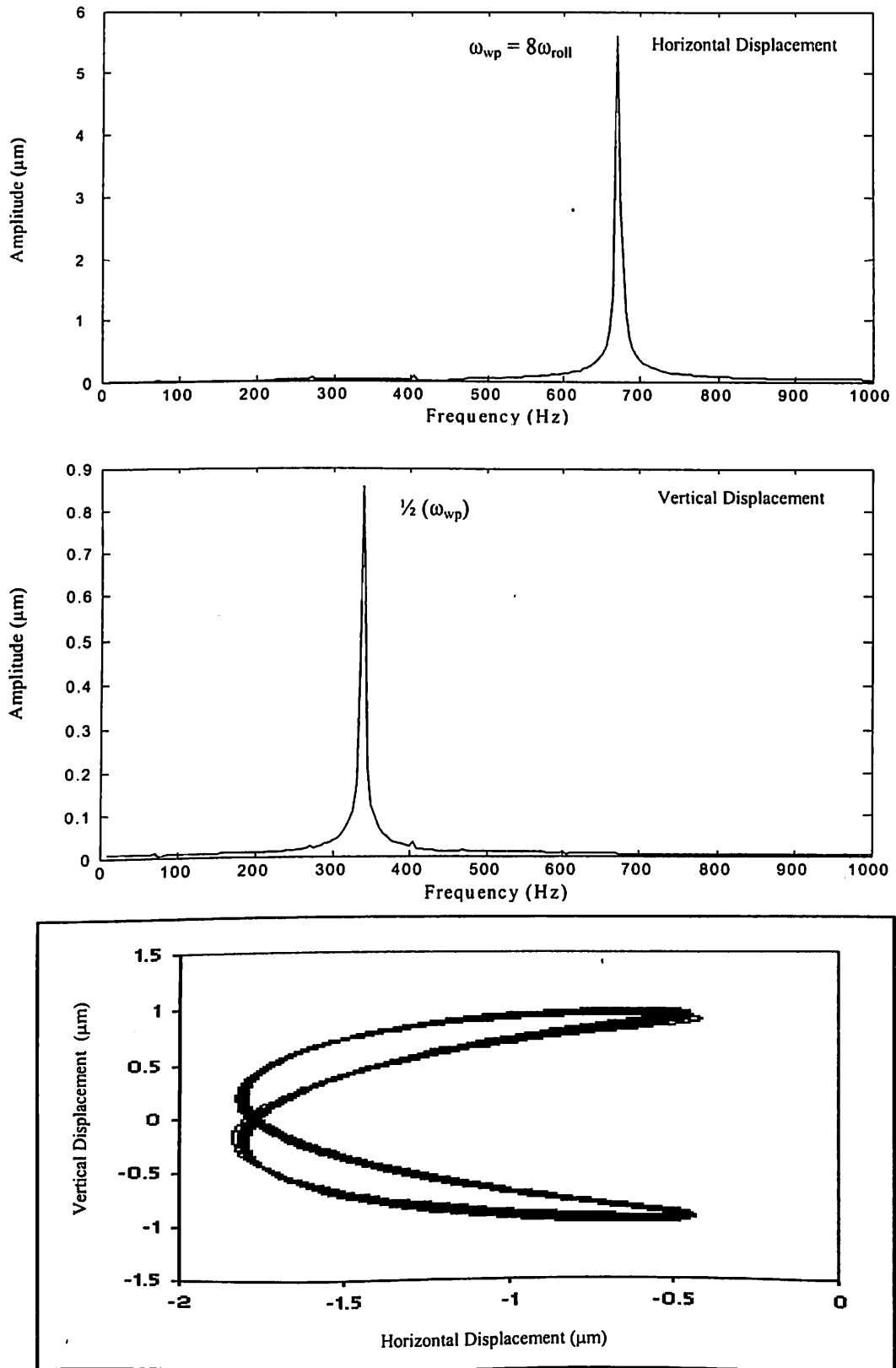


Fig. 5.26 Response plot for ball waviness at  $N_w = 8$

For 10 waves, the peak amplitude of vibration appears at  $10\omega_{roll} = \omega_{wp} = 833$  Hz and at  $\frac{1}{2} \omega_{wp} = 417$  Hz as shown in Fig. 5.27. The periodic nature of the system continues with 10 waves also. Figure 5.28 shows the vibrations for bearing with a ball having waviness of order 12. A dominant peak appears in the vibration spectrum at  $\frac{1}{2} (12\omega_{roll} = \omega_{wp}) = 500$  Hz with the other peaks are at  $\omega_{wp} = 1000$  Hz. For 14 waves, the peak amplitude of vibration appears at  $14\omega_{roll} = \omega_{wp} = 1166$  Hz and at  $8\omega_{cage} = 267$  Hz as shown in Fig. 5.29.

Hence, it is observed from the vibration spectrum that the peak amplitude of vibrations due to ball waviness appear at the wave passage frequency ( $N_w \omega_{roll}$ ). Increasing the number of waves means making the ball smoother with a larger diameter. When the  $N_w \omega_{roll} \pm k\omega_{cage}$  coincides with the natural frequency of the system severe vibrations take place. Increasing the order of waviness will diminish the vibrations at the  $N_w \omega_{roll} \pm k\omega_{cage}$  and only vibrations at the wave passage frequency and at cage speed will remain in the spectrum. The axial vibrations are produced when the number of waves per circumference is an integral multiple of the ball rotation frequency in the bearing, which was proved experimentally by Wardle (1988b) and Yhland (1972).

#### 5.3.1.4 Ball size variation

Due to the different ball diameters, the race is deformed into a complex shape that turns with the rotational speed of the cage. The off-sized balls were located symmetrically in bearings such that they moved in the same direction simultaneously (i.e. the balls are assumed to be in phase). Firstly, two balls are assumed to be  $0.2 \mu\text{m}$  oversized. The responses are obtained for the bearing with varying ball size and for different number of balls. The rotor rotates at 5000 rpm. The ball set rotates at the cage speed around the inner race and the oversized ball. Since the ball set comes to the same position after one cage rotation, the system undergoes vibrations at a frequency that is equal to the number of balls times the cage speed ( $N_b \omega_{cage}$ ) i.e. at the system excitation frequency (varying compliance frequency ( $N_b \omega_{cage} = VC$ )). Table 5.3 shows the summary of the ball waviness.

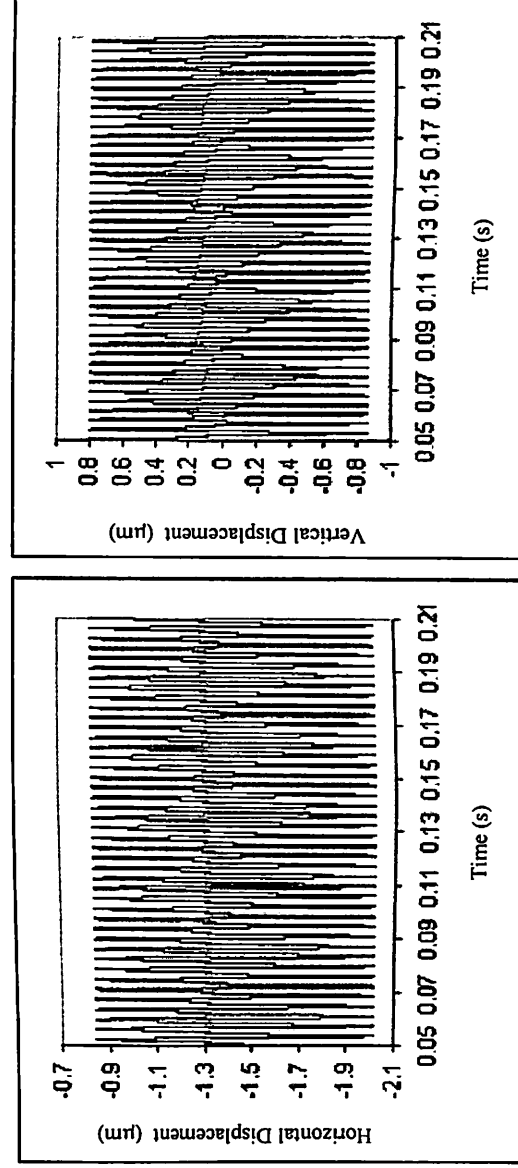
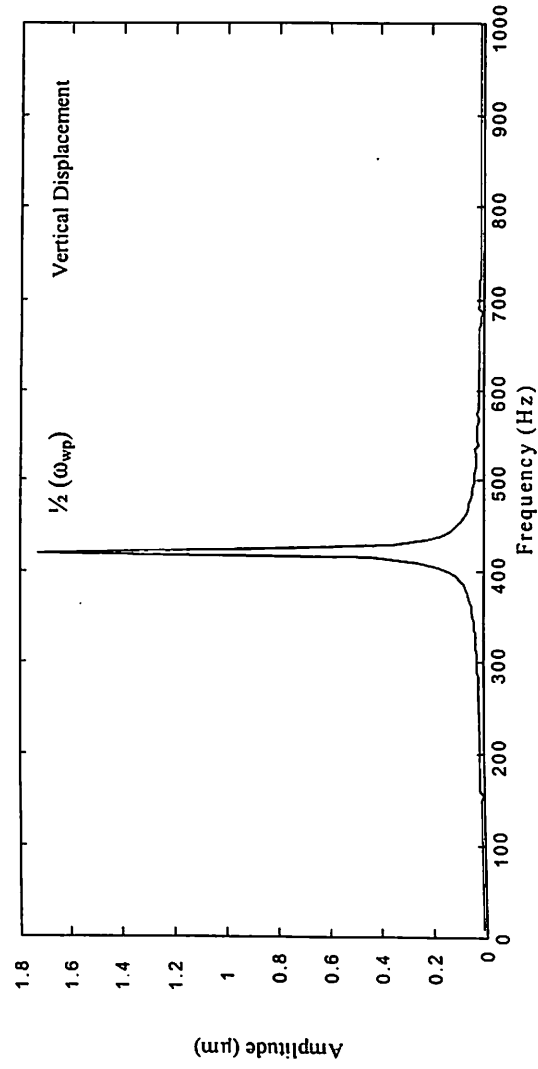
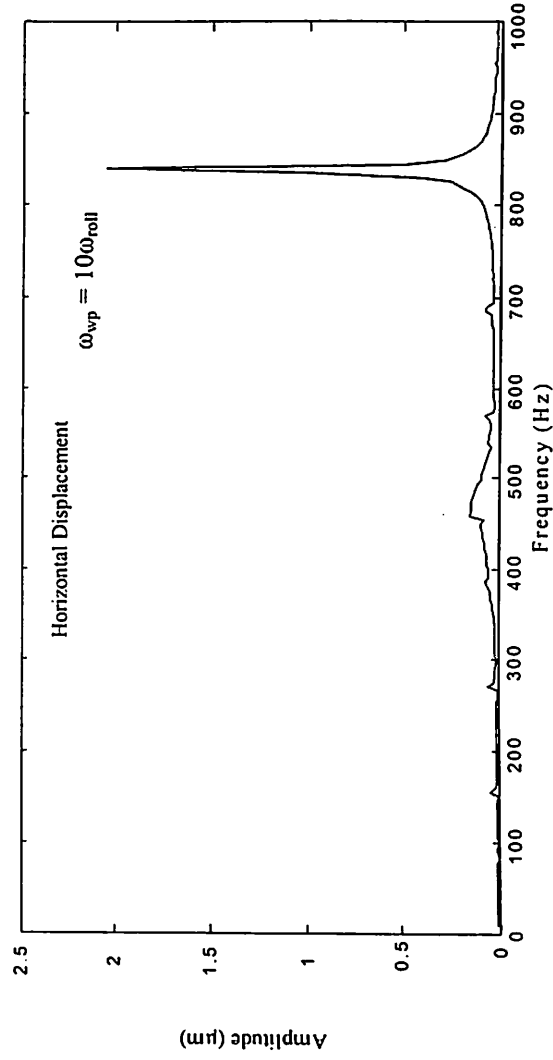


Fig. 5.27 Response plot for ball waviness at  $N_w = 10$



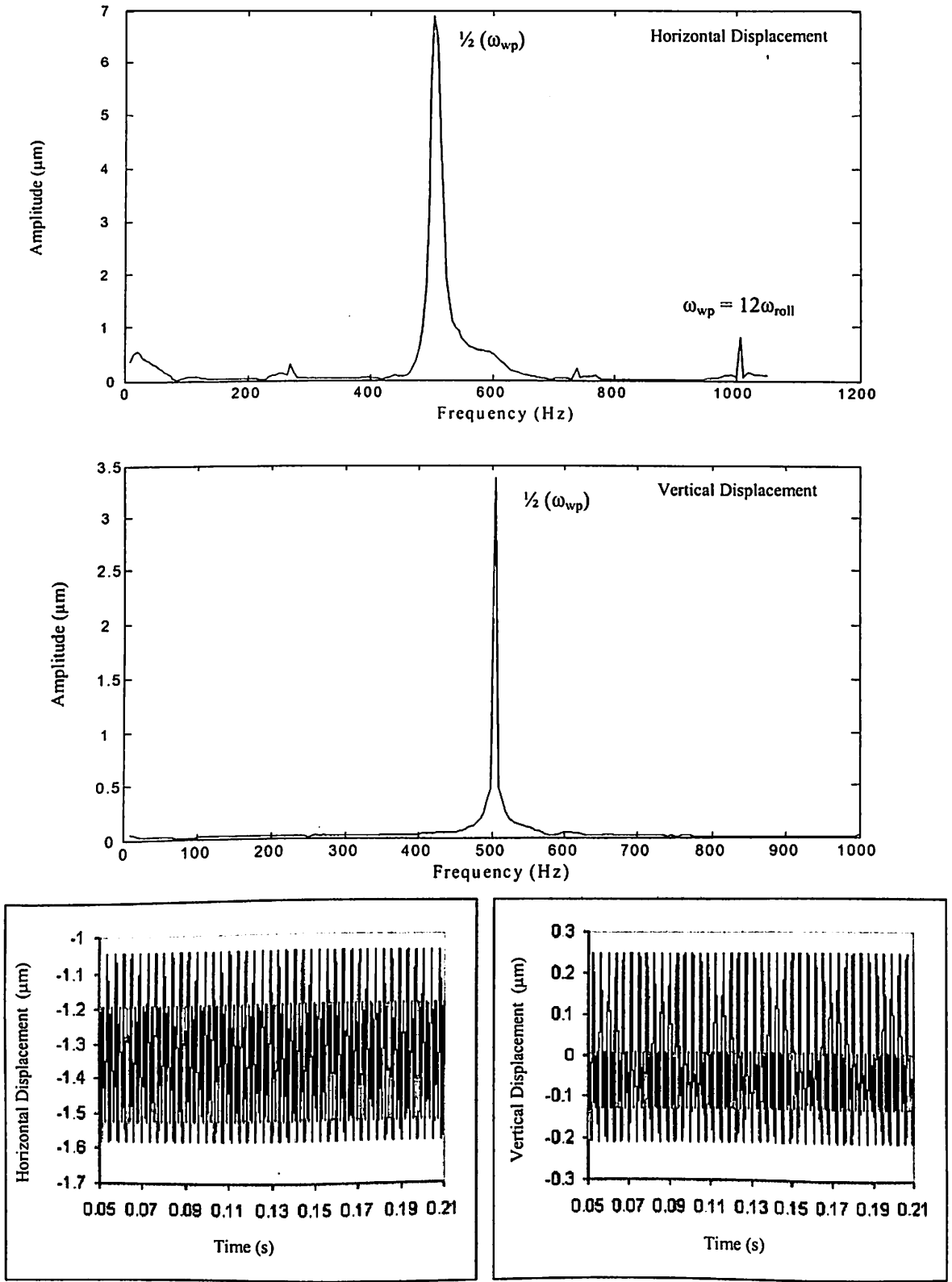


Fig. 5.28 Response plot for ball waviness at  $N_w = 12$

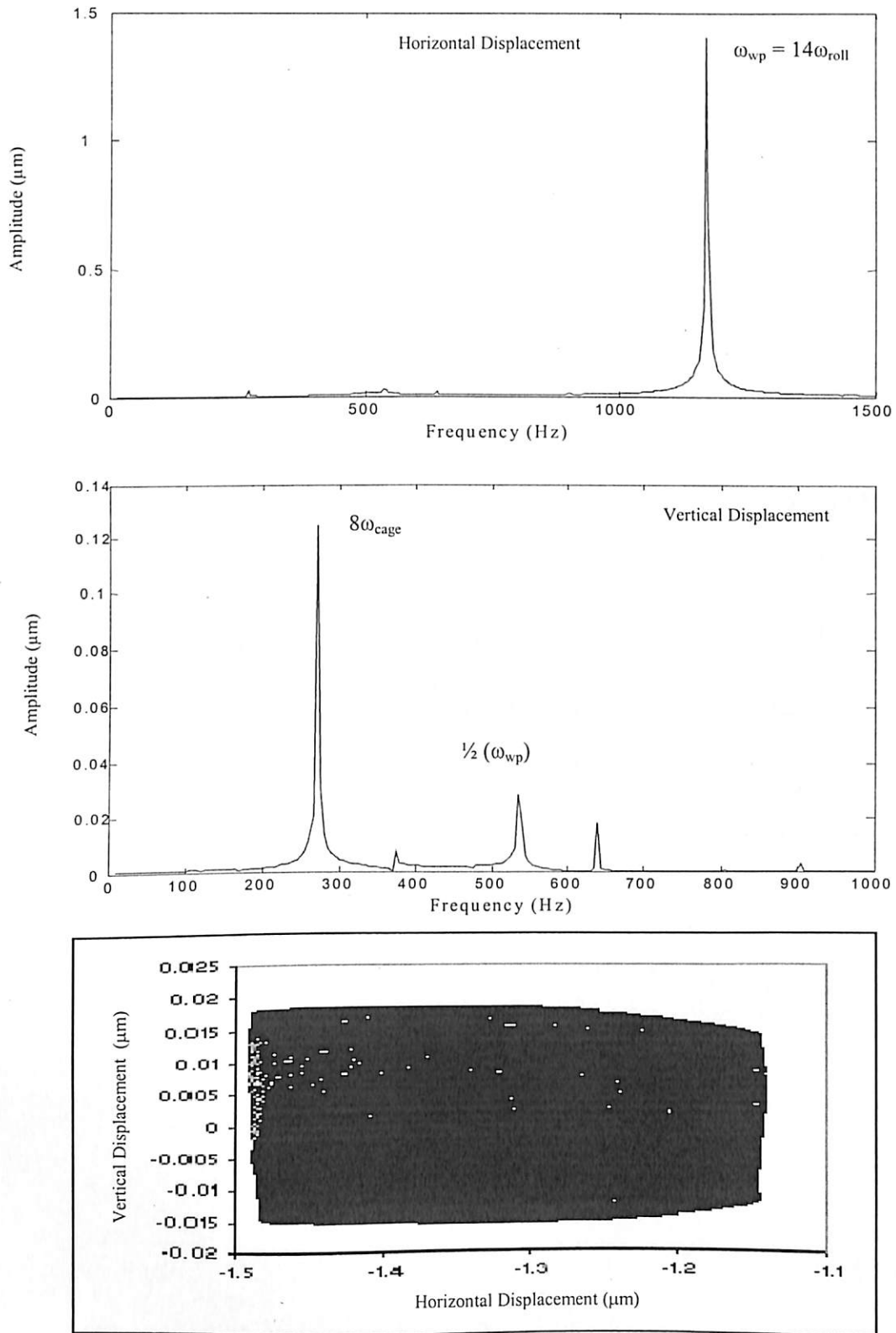


Fig. 5.29 Response plot for ball waviness at  $N_w = 14$

**Table 5.3 Summary of ball waviness**

Waviness Order (lobes / circumference)	Peak Amplitude at	Harmonic in Bearing Spectrum at
2	$2\omega_{roll} = \omega_{wp}$	$2\omega_{roll} - 2\omega_{cage}$ , $2\omega_{roll} + 3\omega_{cage}$ , $2\omega_{roll} + 8\omega_{cage}$ , $2\omega_{roll} + 13\omega_{cage}$
4	$4\omega_{roll} = \omega_{wp}$	$\frac{1}{4}\omega_{wp}$ , $4\omega_{roll} - 2\omega_{cage}$ , $4\omega_{roll} + 2\omega_{cage}$ , $4\omega_{roll} + 8\omega_{cage}$
6	$6\omega_{roll} = \omega_{wp}$	$6\omega_{roll} - 8\omega_{cage}$ , $6\omega_{roll} - 7\omega_{cage}$ , $6\omega_{roll} - \omega_{cage}$ , $6\omega_{roll} + 8\omega_{cage}$
8	$8\omega_{roll} = \omega_{wp}$	$\frac{1}{2}(\omega_{wp})$
10	$10\omega_{roll} = \omega_{wp}$	$\frac{1}{2}(\omega_{wp})$
12	$\frac{1}{2}(12\omega_{roll} = \omega_{wp})$	$\omega_{wp}$
14	$14\omega_{roll} = \omega_{wp}$	$8\omega_{cage}$

**Table 5.3 Summary of ball waviness**

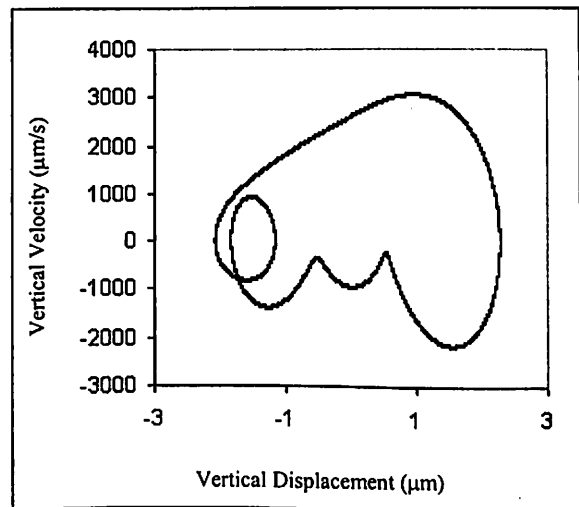
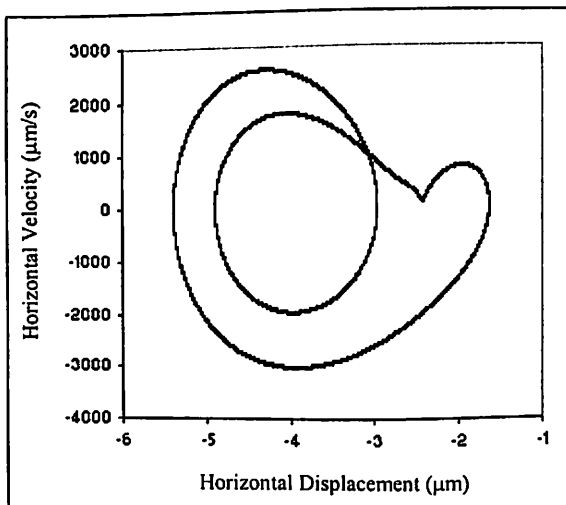
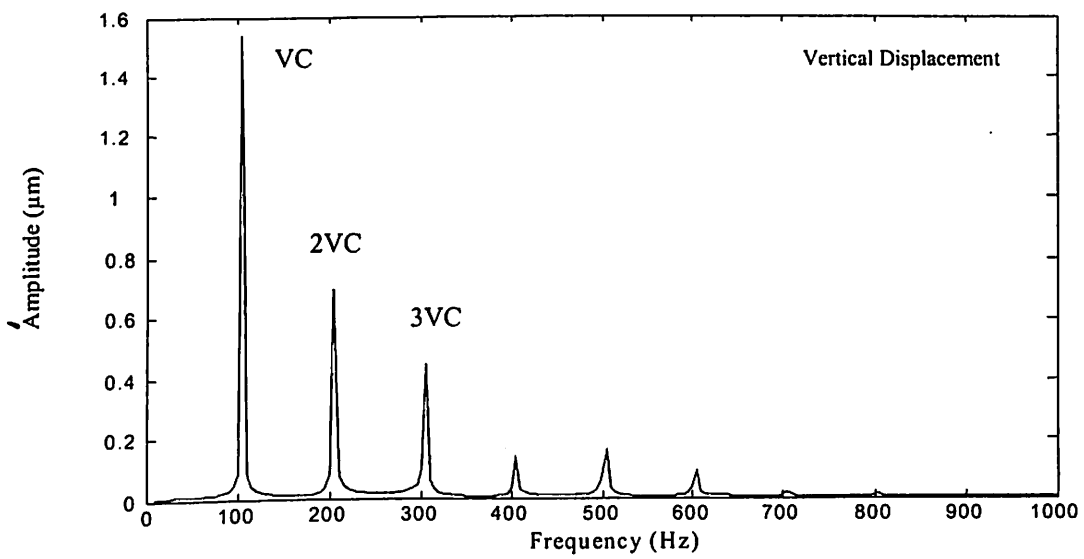
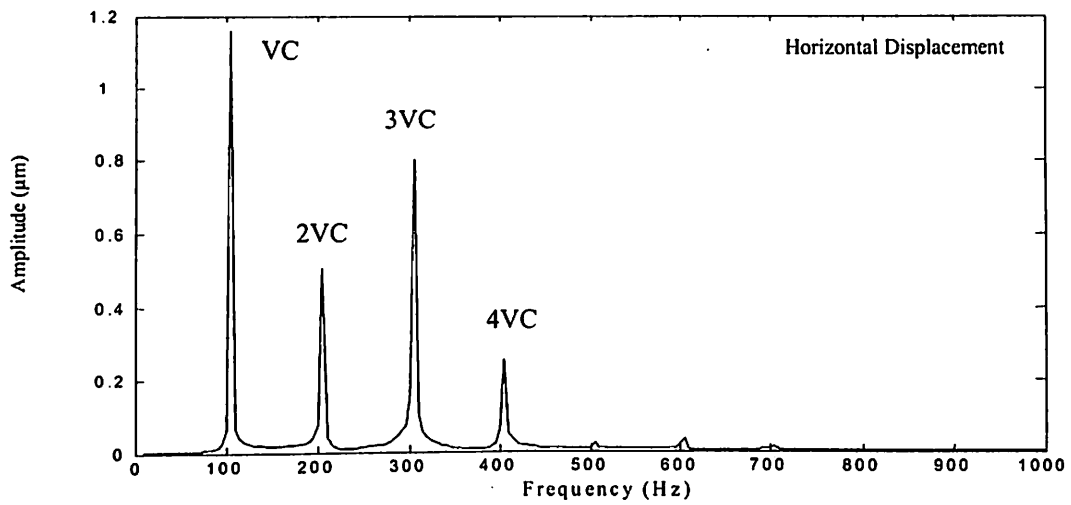
Waviness Order (lobes / circumference)	Peak Amplitude at	Harmonic in Bearing Spectrum at
2	$2\omega_{roll} = \omega_{wp}$	$2\omega_{roll} - 2\omega_{cage}$ , $2\omega_{roll} + 3\omega_{cage}$ , $2\omega_{roll} + 8\omega_{cage}$ , $2\omega_{roll} + 13\omega_{cage}$
4	$4\omega_{roll} = \omega_{wp}$	$\frac{1}{4}\omega_{wp}$ , $4\omega_{roll} - 2\omega_{cage}$ , $4\omega_{roll} + 2\omega_{cage}$ , $4\omega_{roll} + 8\omega_{cage}$
6	$6\omega_{roll} = \omega_{wp}$	$6\omega_{roll} - 8\omega_{cage}$ , $6\omega_{roll} - 7\omega_{cage}$ , $6\omega_{roll} - \omega_{cage}$ , $6\omega_{roll} + 8\omega_{cage}$
8	$8\omega_{roll} = \omega_{wp}$	$\frac{1}{2}(\omega_{wp})$
10	$10\omega_{roll} = \omega_{wp}$	$\frac{1}{2}(\omega_{wp})$
12	$\frac{1}{2}(12\omega_{roll} = \omega_{wp})$	$\omega_{wp}$
14	$14\omega_{roll} = \omega_{wp}$	$8\omega_{cage}$

When the number of balls is 3, the peak amplitude of vibration appears in the spectrum at the varying compliance frequency  $VC = 3\omega_{cage} = 100.5$  Hz as shown in Fig. 5.30. Other major peaks at super harmonics of vibration appear at integral multiples of the varying compliance frequency, i.e. at  $2VC = 201$  Hz,  $3VC = 301.5$  Hz and  $4VC = 402$  Hz. The peak amplitude of vibration is  $1.5 \mu\text{m}$ . The  $VC$  and its harmonics (super-harmonic) character of the frequency spectra is also brought out by the Poincarè Maps with the closed orbits.

When the number of balls is 4, the peak amplitude of vibration appears in the spectrum at the varying compliance frequency  $VC = 4\omega_{cage} = 133.3$  Hz as shown in Fig. 5.31. Other major peaks at super harmonics of vibration appear at integral multiples of the varying compliance frequency, i.e., at  $2VC = 266.5$  Hz and  $3VC = 399.6$  Hz. The  $VC$  and its harmonics (super-harmonic) character of the frequency spectra is also brought out by the Poincarè Maps with the closed orbits.

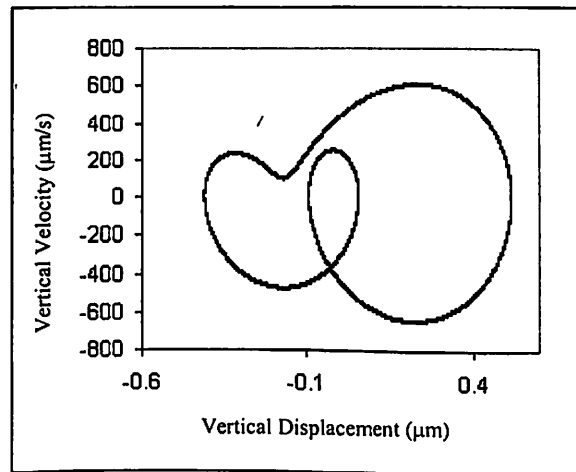
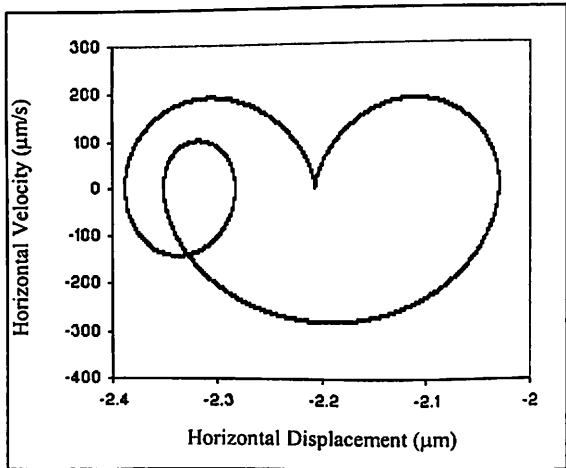
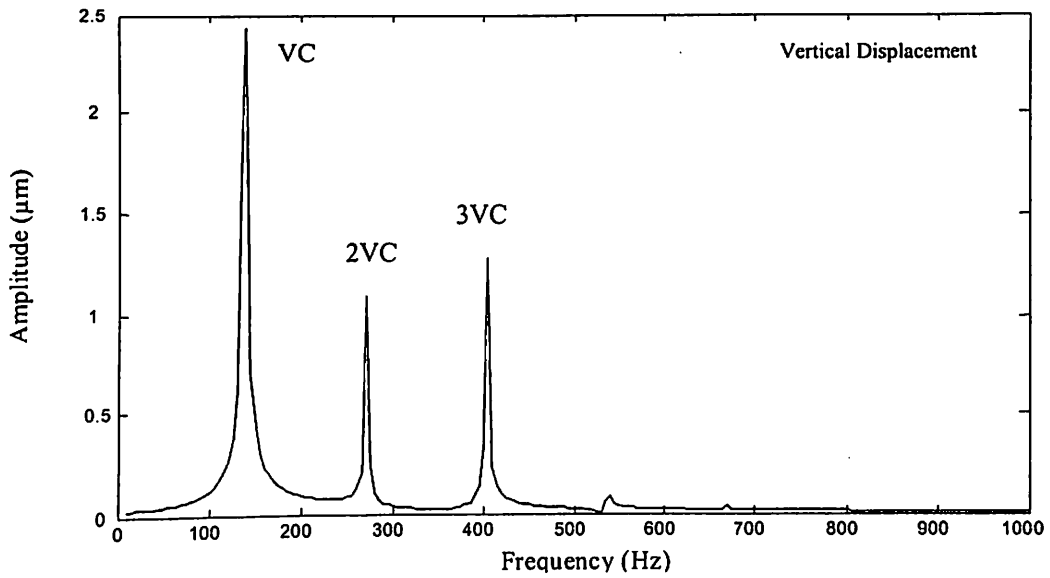
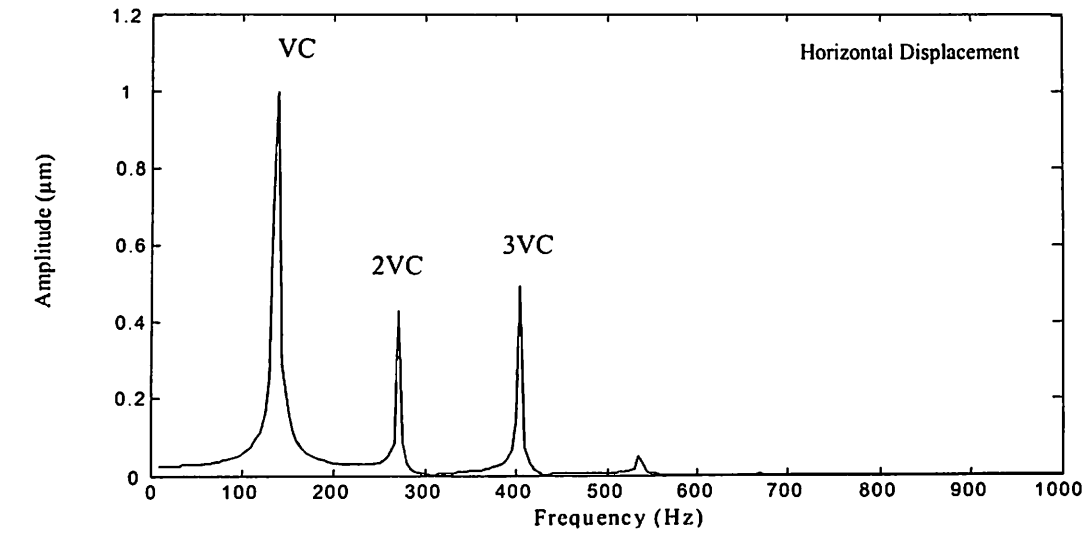
For 5 balls, the peak amplitude of vibration appears in the spectrum at  $VC = 5\omega_{cage} = 166.5$  Hz as shown in Fig. 5.32. The system shows its periodic nature for 5 balls. One major peak at super harmonics of vibration appears at an integral multiple of the varying compliance frequency i.e. at  $2VC = 333$  Hz. When the number of balls is 6, the peak amplitude of vibration appears in the spectrum at the varying compliance frequency  $VC = 6\omega_{cage} = 200$  Hz as shown in Fig. 5.33. Other major peak at super harmonics of vibration appears at integral multiples of the varying compliance frequency, i.e., at  $2VC = 400$  Hz and  $3VC = 600$  Hz. The  $VC$  and its harmonics (super-harmonic) character of the frequency spectra is also brought out by the Poincarè Maps with the closed orbits.

For 7 balls, the peak amplitude of vibration appears in the spectrum at  $VC = 7\omega_{cage} = 233.1$  Hz as shown in Fig. 5.34. Other major peaks at super harmonics of vibration appear at an integral multiple of the varying compliance frequency i.e. at  $2VC = 466.2$  Hz and at  $2VC + \omega_{cage} = 500$  Hz. For 8 balls, the peak amplitude of vibration appears in the spectrum at  $VC = 8\omega_{cage} = 266.4$  Hz as shown in Fig. 5.35. Other major peak at super harmonics of vibration appears at an integral multiple of the varying compliance frequency i.e. at  $2VC = 532.8$  Hz.



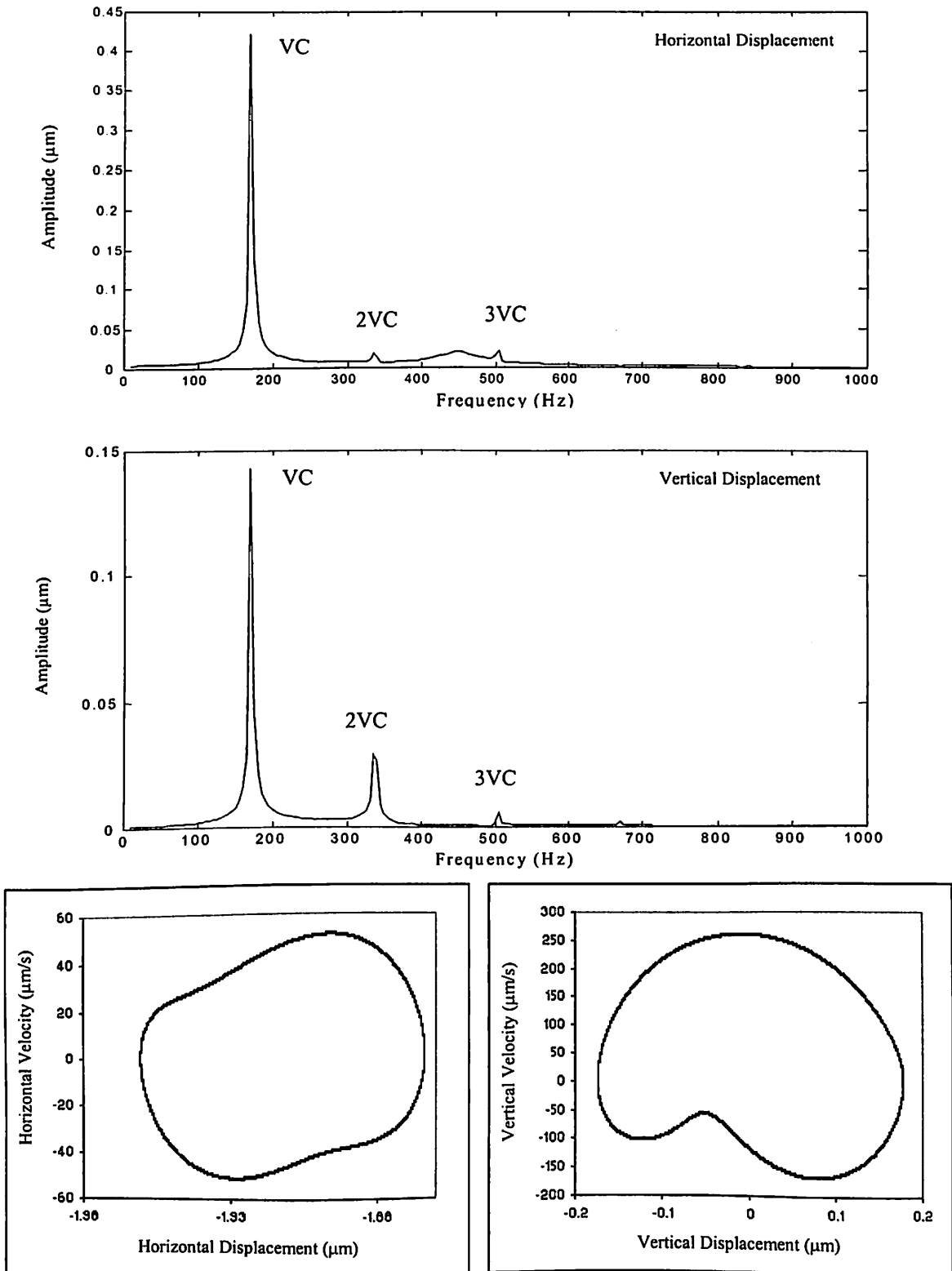
Poincaré Maps

Fig. 5.30 Response plot for ball size variation at  $N_b = 3$



Poincaré Maps

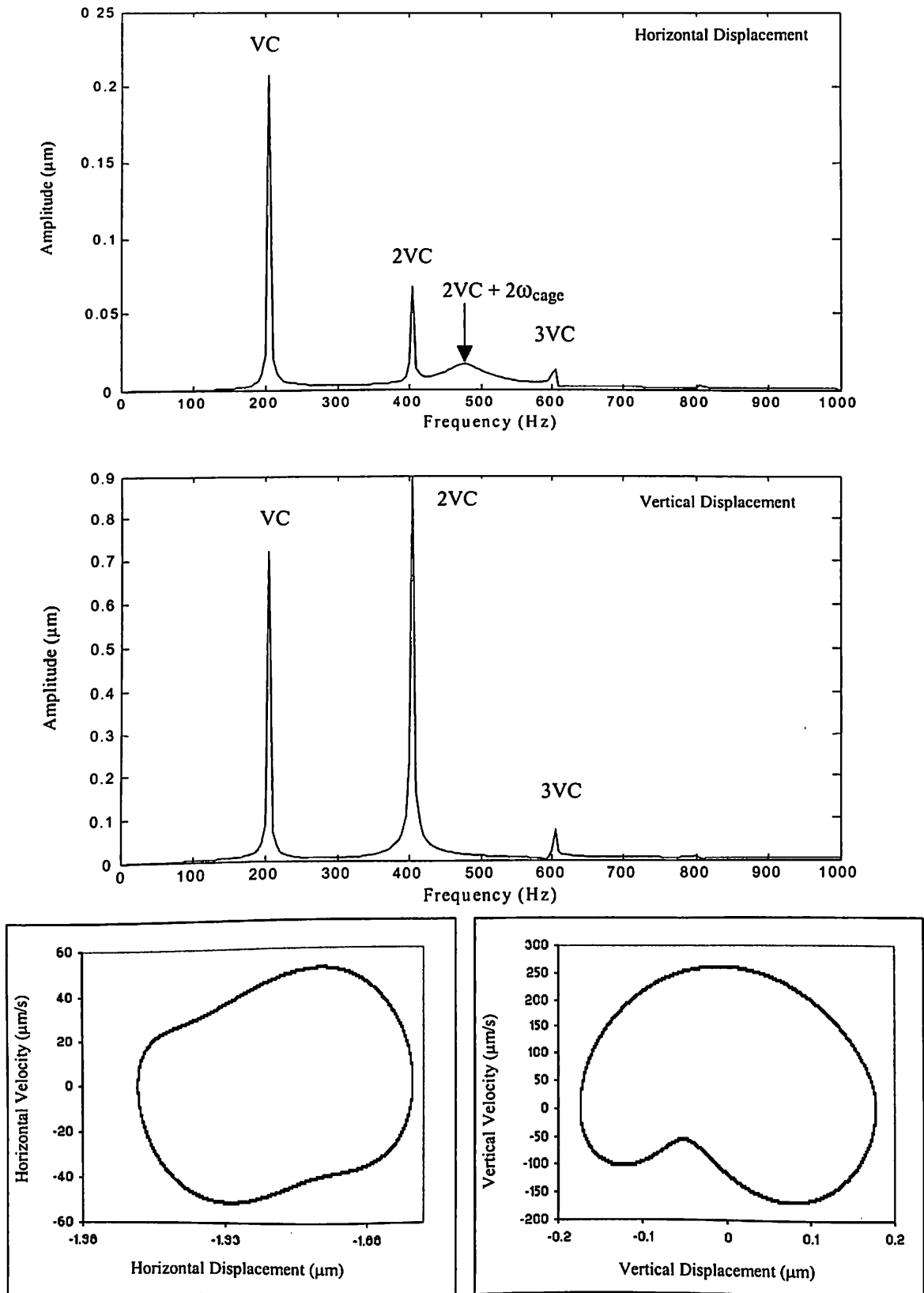
Fig. 5.31 Response plot for ball size variation at  $N_b = 4$



Poincaré Maps

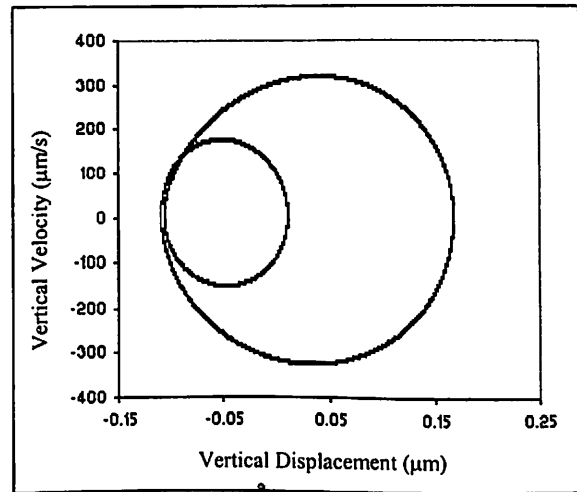
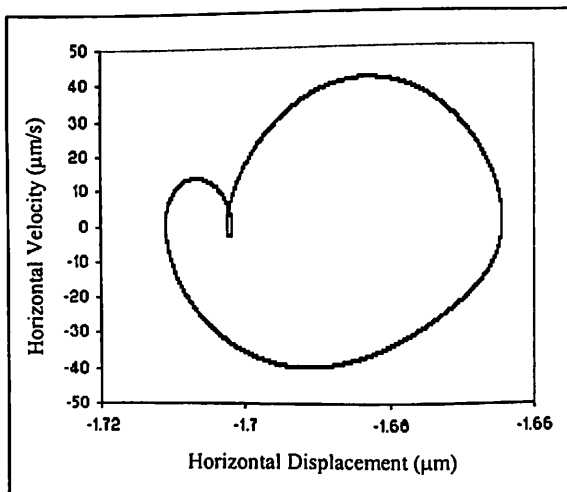
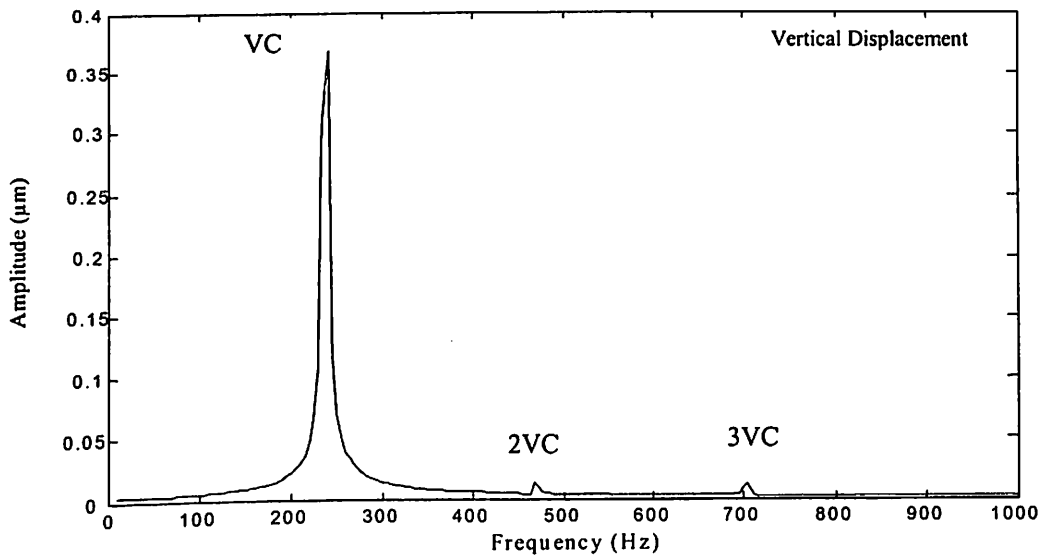
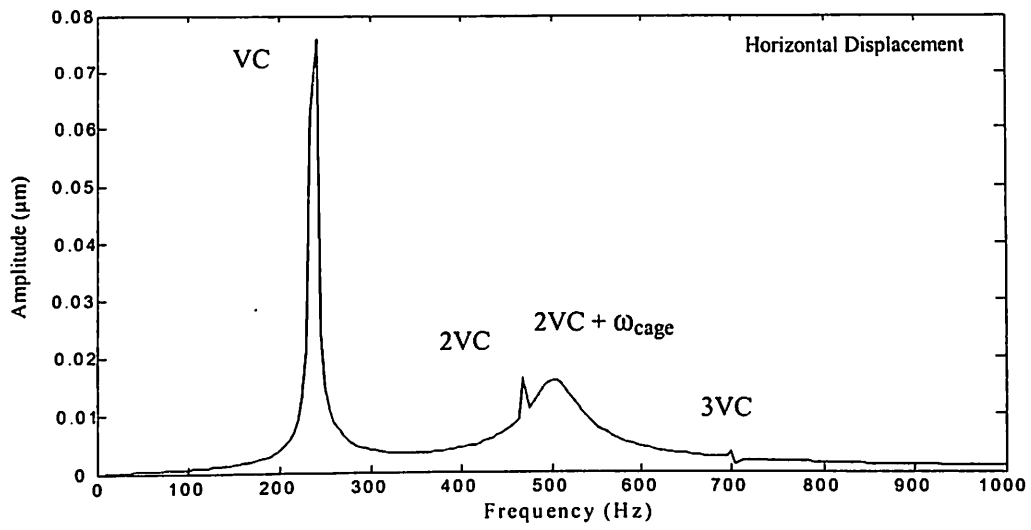
Fig. 5.32 Response plot for ball size variation at  $N_b = 5$





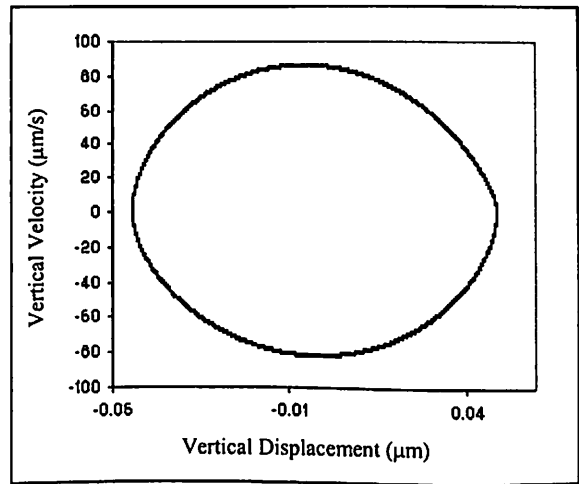
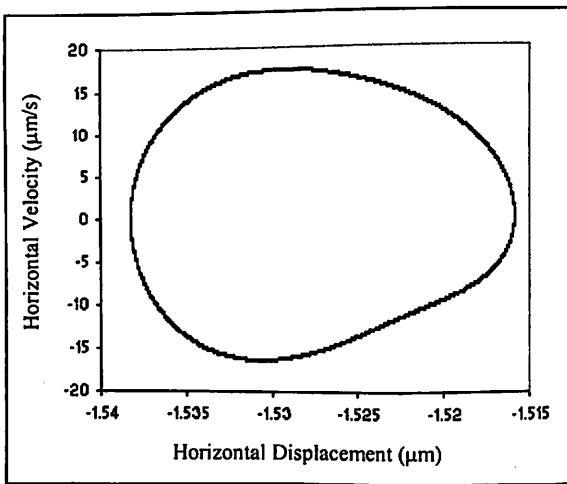
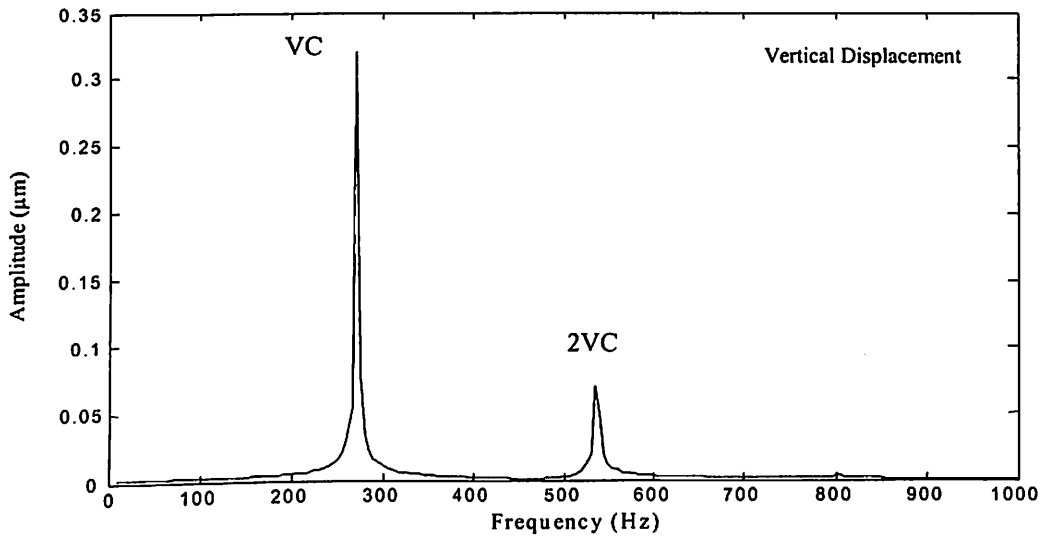
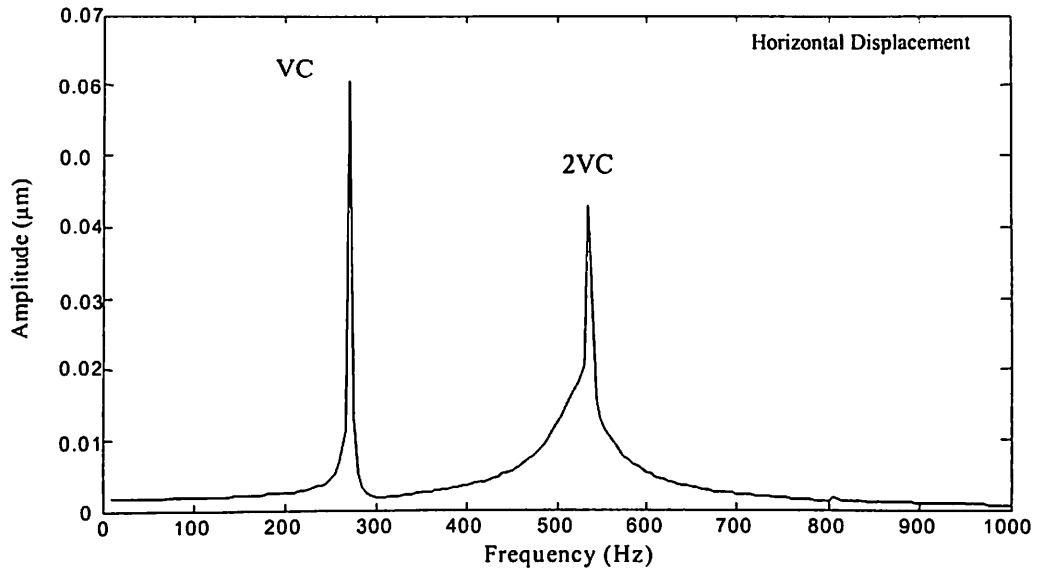
Poincaré Maps

**Fig. 5.33** Response plot for ball size variation at  $N_b = 6$



Poincaré Maps

Fig. 5.34 Response plot for ball size variation at  $N_b = 7$



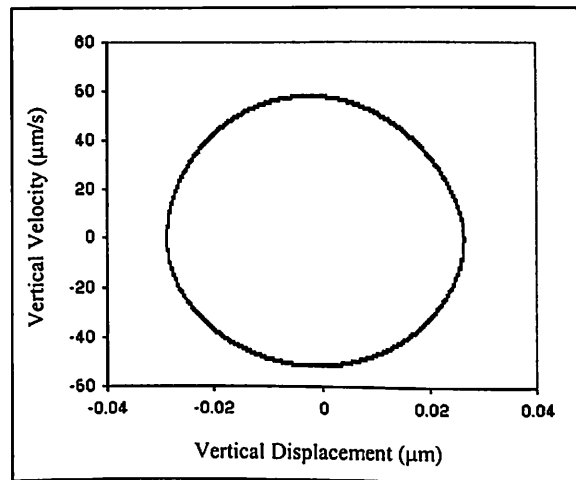
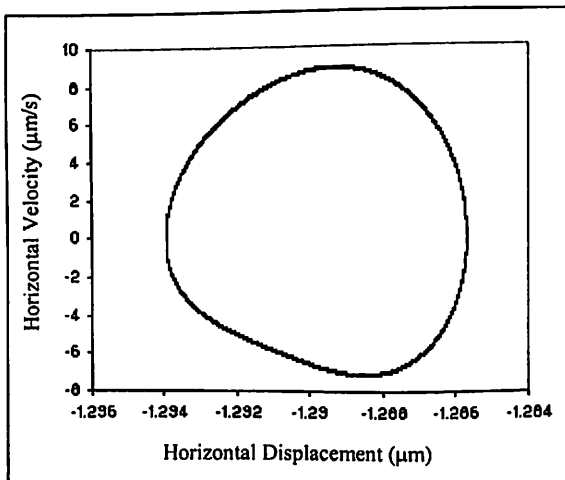
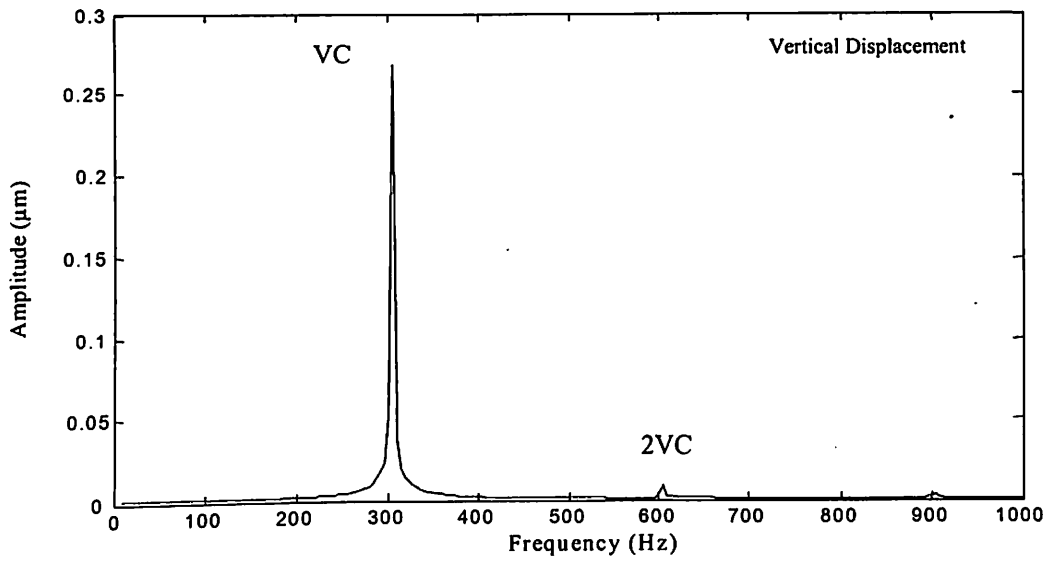
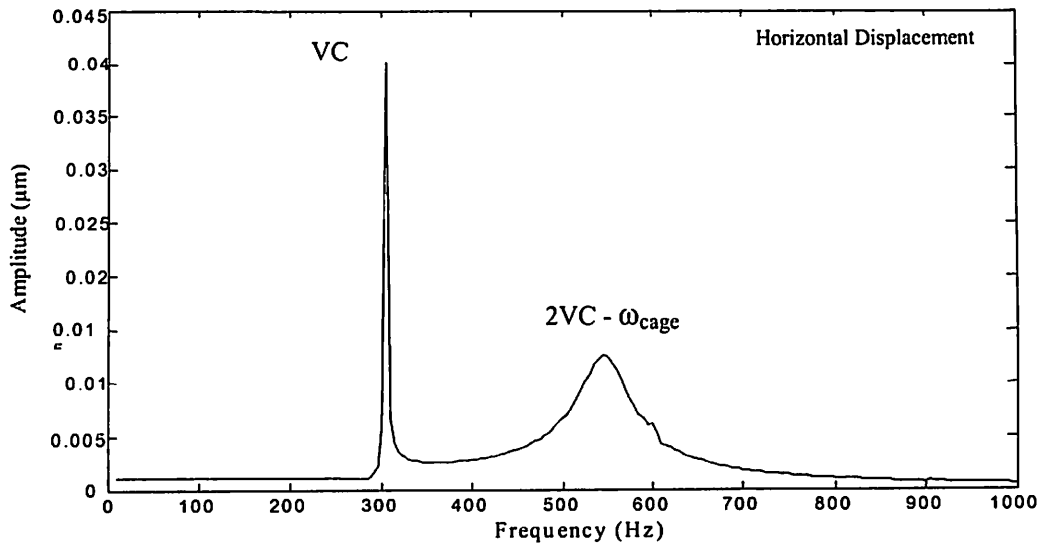
Poincaré Maps

**Fig. 5.35** Response plot for ball size variation at  $N_b = 8$

For 9 balls, the peak amplitude of vibration appears in the spectrum at  $VC = 9\omega_{cage} = 300$  Hz as shown in Fig. 5.36. The system shows a periodic nature for 9 balls. One major peak at super harmonics of vibration appears at an integral multiple of the varying compliance frequency i.e. at  $2VC - \omega_{cage} = 566$  Hz. For 10 balls, the peak amplitude of vibration appears in the spectrum at  $VC = 10\omega_{cage} = 333$  Hz as shown in Fig. 5.37. The  $VC$  and its harmonics (super-harmonic) character of the frequency spectra is also brought out by the Poincarè Maps with the closed orbits. Other major peaks at super harmonics of vibration appear at an integral multiple of the varying compliance frequency i.e. at  $2VC = 666$  Hz and at  $2VC - 3\omega_{cage} = 566$  Hz. For 11 balls, the peak amplitude of vibration appears in the spectrum at  $VC = 11\omega_{cage} = 366$  Hz as shown in Fig. 5.38. The system shows its periodic nature for 11 balls. One major peak at super harmonics of vibration appears at an integral multiple of the varying compliance frequency i.e. at  $2VC - 4\omega_{cage} = 600$  Hz.

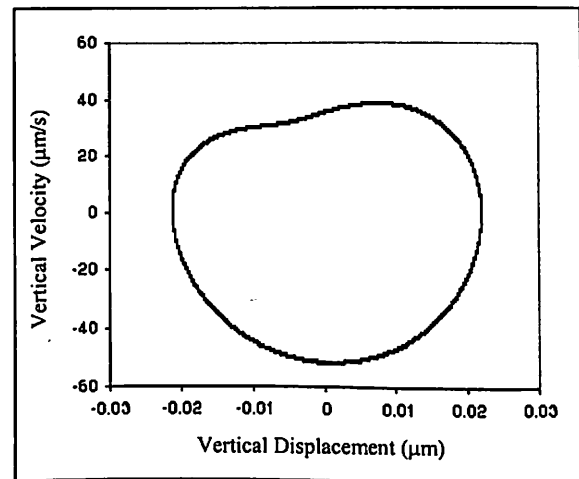
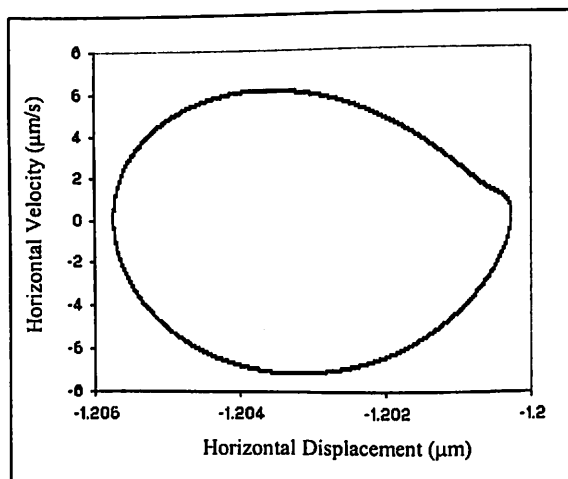
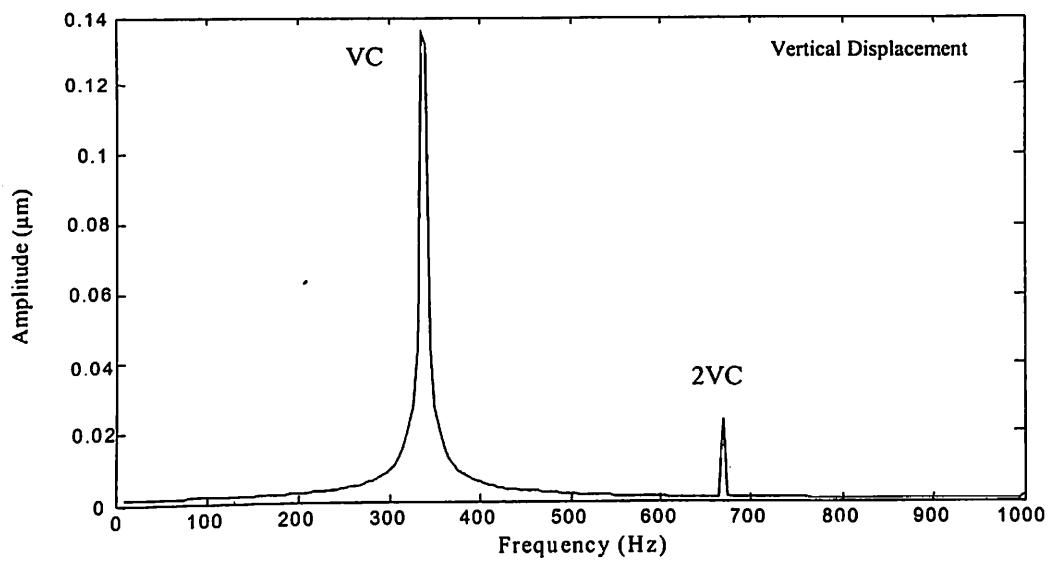
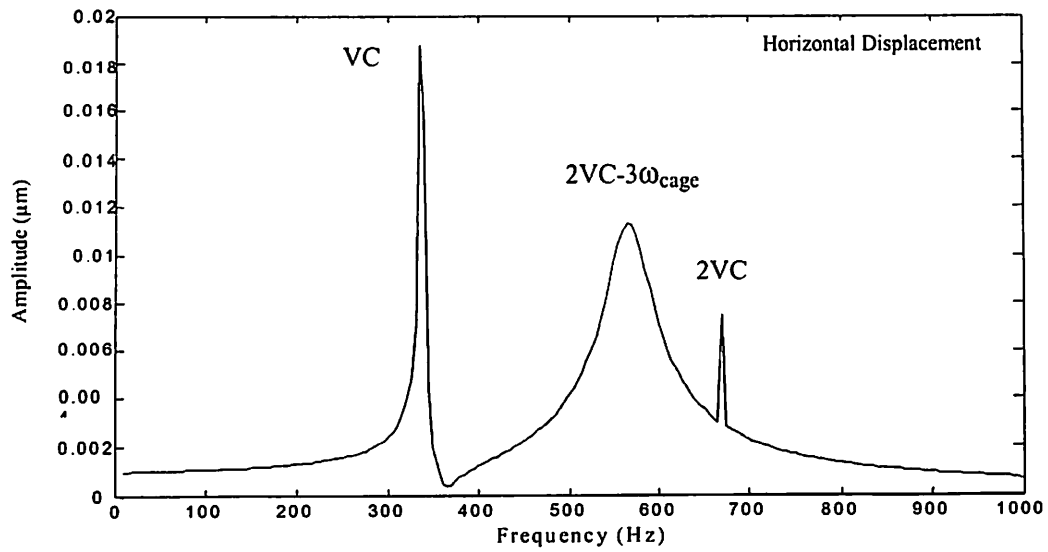
For 13 balls, the peak amplitude of vibration appears in the spectrum at  $VC = 13\omega_{cage} = 433$  Hz for vertical displacement response as shown in Fig. 5.39. While for horizontal displacement response, the major peak appears at  $2VC - 7\omega_{cage} = 633$  Hz. For 16 balls, the peak amplitude of vibration appears in the spectrum at  $VC = 16\omega_{cage} = 533$  Hz for vertical displacement response as shown in Fig. 5.40. While for horizontal displacement response, the major peak appears at  $2VC - 12\omega_{cage} = 666$  Hz. Table 5.4 shows the Summary of variation due to number of off-sized balls.

All the results show that off-sized balls in the bearing cause vibrations at the varying compliance frequency and its harmonics, depending on their arrangement within the bearing. The other vibrations due to ball size variation also occur at  $VC \pm k\omega_{cage}$ , where  $k$  is a constant.



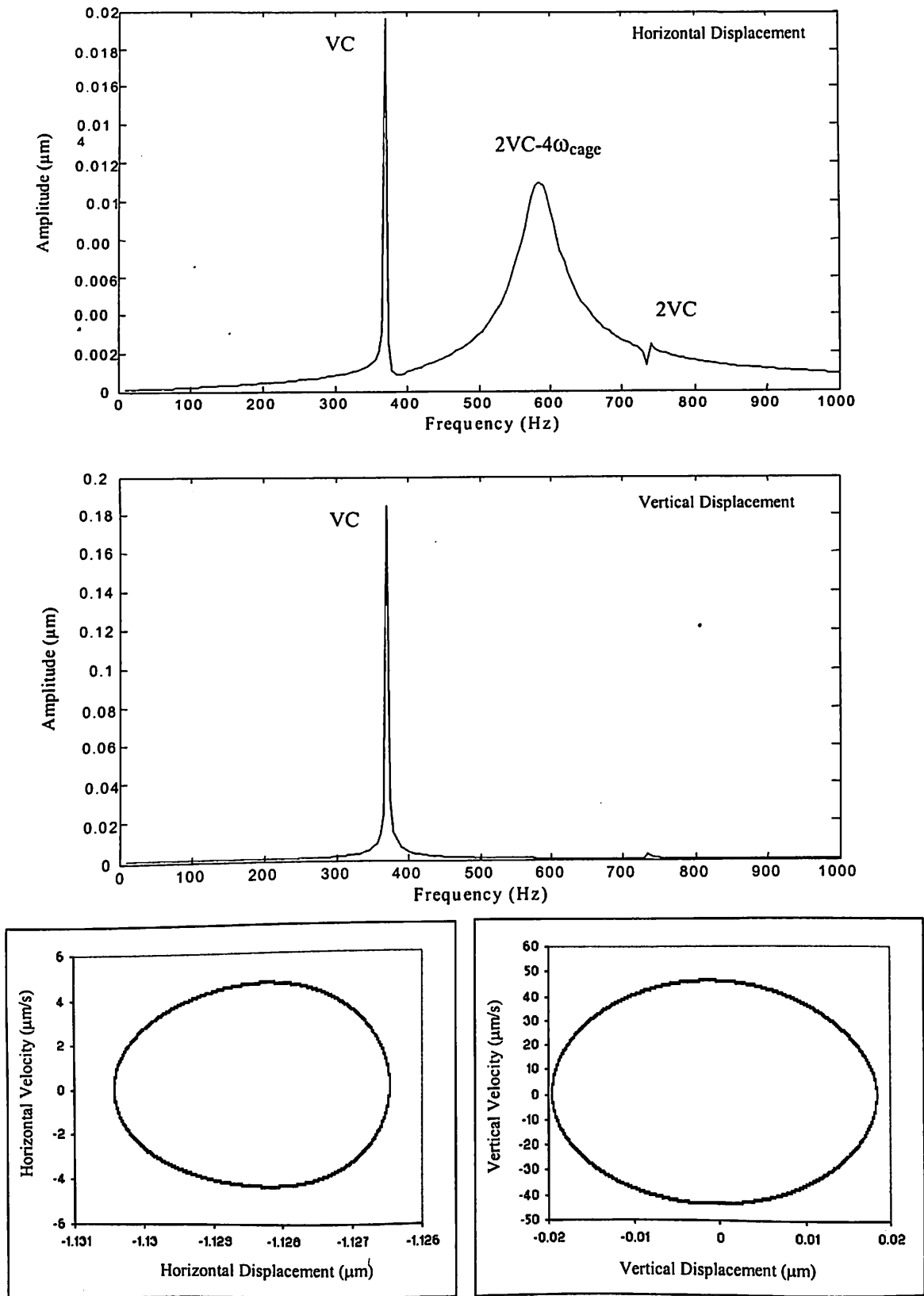
Poincaré Maps

Fig. 5.36 Response plot for ball size variation at  $N_b = 9$



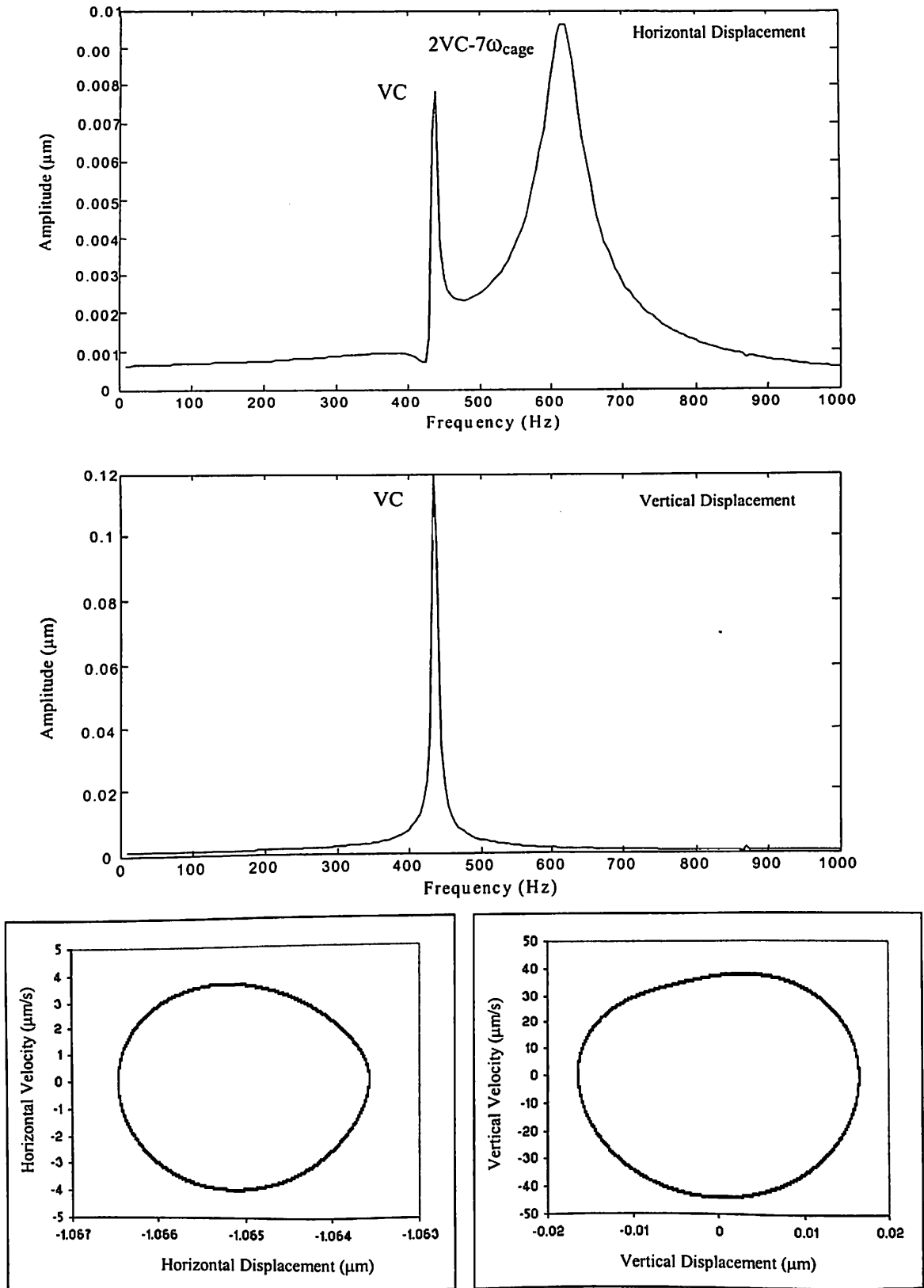
Poincaré Maps

Fig. 5.37 Response plot for ball size variation at  $N_b = 10$



Poincaré Maps

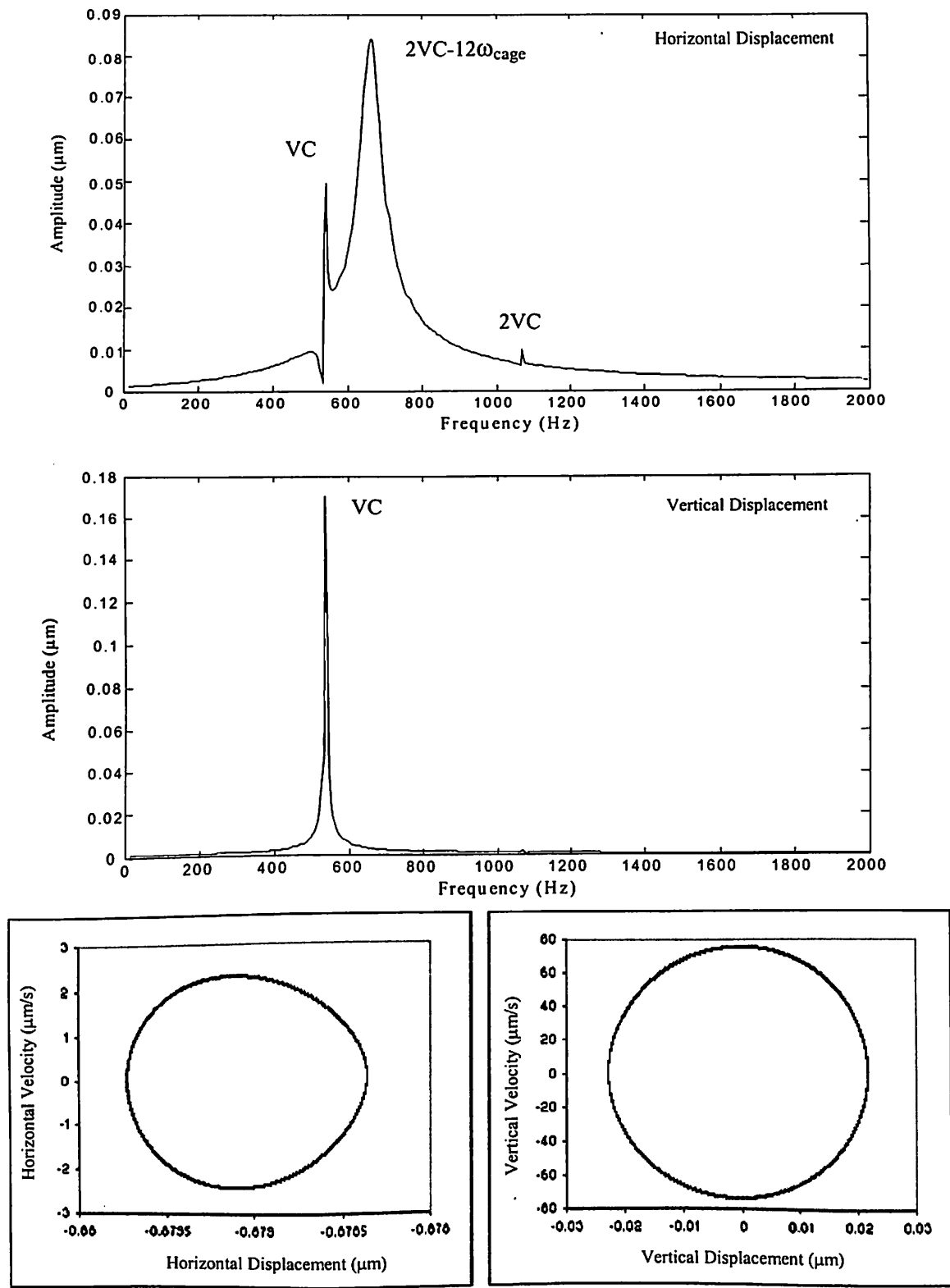
Fig. 5.38 Response plot for ball size variation at  $N_b = 11$



Poincaré Maps

**Fig. 5.39** Response plot for ball size variation at  $N_b = 13$





Poincaré Maps

Fig. 5.40 Response plot for ball size variation at  $N_b = 16$

**Table 5.4** Summary of variation due to number of off-sized balls

<b>Number of Balls</b>	<b>Peak Amplitude at</b>	<b>Harmonic in Vibration Spectrum</b>
3	$VC = 3\omega_{cage}$	$2VC, 3VC, 4VC$
4	$VC = 4\omega_{cage}$	$2VC, 3VC$
5	$VC = 5\omega_{cage}$	$2VC$
6	$VC = 6\omega_{cage}$	$2VC, 3VC$
7	$VC = 7\omega_{cage}$	$2VC, 2VC + \omega_{cage}$
8	$VC = 8\omega_{cage}$	$2VC$
9	$VC = 9\omega_{cage}$	$2VC - \omega_{cage}$
10	$VC = 10\omega_{cage}$	$2VC, VC - 3\omega_{cage}$
11	$VC = 11\omega_{cage}$	$2VC - 4\omega_{cage}$
13	$VC = 13\omega_{cage}$	$2VC - 7\omega_{cage}$
16	$VC = 16\omega_{cage}$	$2VC - 12\omega_{cage}$

## 5.4 CONCLUSIONS

In the present investigation, theoretical model of a rotor bearing system has been developed to obtain the vibration response due to distributed defects in various bearing elements. The model predicts discrete spectrum with specific frequency components for each order of waviness. From the theoretical study of the dynamic response of a rotor bearing system due to distributed defects the following conclusions may be drawn.

### A. Outer race waviness

- a. The frequency of the vibrations due to outer race waviness depends on the waviness order and can be given as

Waviness orders	Frequency of vibration caused by waviness	
$n = qN_b \pm k$	$\omega = qN_b \omega_{cage}$	(5.6)

However, this equation is applicable to major peaks and because of the load deflection relation for the balls is non-linear, hence for some cases this equation is not satisfy.

- b. A clear transformation from  $q = 1$  to  $q = 2$ ,  $q = 2$  to  $q = 3$  and  $q = 3$  to  $q = 4$  can be observed in the vibration spectrum as the number of waves increases and the amplitude of peak decreases with increasing number of waves ( $N_w$ ), which has also been proved by Wardle (1988b) and Aktürk (1999).
- c. For outer race waviness, the spectrum has components at varying compliance frequency ( $VC = N_b \times \omega_{cage}$ ) and its harmonics.
- d. Severe vibrations are observed for an order of waviness  $n = qN_b \pm 1$  and  $n = N_b$ . For some order of waviness, the vibrations produced due to waviness are negligible.

### B. Inner race waviness

- a. The frequency of the vibrations due to inner race waviness depends on the waviness order and can be given as

Waviness order	Frequency of vibration caused by waviness	
$n = qN_b \pm k$	$\omega = qN_b (\omega_{inner} - \omega_{cage}) \pm k\omega_{inner}$	(5.7)

However, this equation is applicable to major peaks only.

- b. For the transformations, the peaks can be at:

$$i\omega_{wp} \pm j\omega_{inner} \quad \text{OR} \quad i(\omega_{inner} - \omega_{cage}) \pm j\omega_{cage}$$

- c. The prediction methods are useful to detect peaks at major frequencies due to inner race waviness while peaks at other frequencies are also present.
- d. The most severe vibrations (chaotic) occur for waviness order  $n = qN_b \pm 1$ .
- e. For the inner race waviness order ( $n$ ), the peaks or its super-harmonics are observed at wave passage frequency (WPF)  $\omega_{wp} = N_b(\omega_{inner} - \omega_{cage})$ .

### C. Ball waviness

- a. A ball with wavy surface in the set will cause vibrations at two frequencies i.e. at the  $\omega_{cage}$  and at the wave passage frequency of the ball ( $N_w\omega_{roll}$ ), which has also been proved experimentally by Wardle (1988b) and theoretically (for low speeds) by Yhland (1992).
- b. Peaks at  $N_w\omega_{roll} \pm k\omega_{cage}$  are also found to appear in the vibration spectrum.
- c. When  $N_w\omega_{roll} \pm k\omega_{cage}$  or  $\omega_{cage}$  coincides with the natural frequency of the system severe (chaotic) vibrations take place.
- d. Relatively higher peaks appear at  $N_w\omega_{roll} \pm \omega_{cage}$ .
- e. For bearing with odd number of waves (1, 3, 5, 7, 11,.....), the deformation of ball is zero because of the inertia of the ball but the rotor is excited. Hence, the rotor vibrations corresponding to odd wave numbers of ball waviness often appear at the cage speed  $\omega_{cage}$ .

### D. Ball size variation

- a. The off-sized balls in the bearing cause vibration peaks at the varying compliance frequency  $N_b\omega_{cage} = VC$  and its harmonics, depending on their arrangement within the bearing.
- b. The other major peaks of the vibrations due to ball size variation are observed at  $VC \pm k\omega_{cage}$ .

# CONCLUSIONS AND SCOPE FOR FUTURE WORK

In the present study, the non-linear dynamic behavior of a horizontal rigid rotor supported by rolling element bearing is analyzed theoretically. The two important effects considered are the non-linear support characteristics and the parametric excitation of the rolling element bearing. The non-linearity in the bearing support is due to the nonlinear load deflection characteristics as given by the elastic Hertzian contact between the rolling element and inner and outer races. The radial internal clearance and distributed defects such as surface waviness of the bearing components and off-size rolling element also makes the load deflection characteristics discontinuous. Clearance in the bearing also determines the contact zone between the races and rolling elements, thereby affecting the stiffness of the bearing. Parametric effect is primarily due to the variation of bearing stiffness as the position of rolling elements changes in the load zone. Analysis shows that the parametric excitation introduces a varying compliance (VC) frequency, which for the rolling bearing is about to 3.2 times the rotational speed.

The effects of parameters such as the radial internal clearance, rotor speed and the unbalanced rotor force for point and line contact with the distributed defects have been studied in detail.

Theoretical analysis for balanced and unbalanced rotor over a wide range of rotor speed reveals several regions of instability as well as deterministic chaotic response. An important finding from the present analysis is the existence of unstable and chaotic response regions at a high speed primarily due to bearing clearance, which has not been reported in previous literature. There is very little work reported in the published literature on non-linear dynamic response of an unbalanced rotor. The results of the present analysis also show the several operating regions through the intermittence mechanism, in which the response characteristics continuously change from periodic to chaotic and vice versa. Spectral analysis of response at various speeds and combination of parameters of study has revealed the presence of sub-synchronous harmonic and super-

synchronous components, varying compliance (VC) and its harmonics and linear combination of synchronous and varying compliance frequencies. Even the periodic orbits acquired a complicated multi-loop character because of the presence of large number of frequency components in the response spectra. When the response is periodic, a perfect line spectrum is obtained. For chaotic response the spectra has a banded structure. Poincarè maps and phase trajectories also verified the chaotic response.

In this study, the vibration response of a rotor bearing system due to distributed defects has been analyzed. The distributed defects considered are the waviness of outer race, inner race and rolling element, and off-size rolling element. The discrete spectrums are obtained with specific frequency components for each order of waviness. The theoretical / experimental studies of other researchers using distributed defects have been confirmed by the simulation model presented in this thesis. For outer race waviness, the severe vibrations occur when varying compliance frequency and its harmonics coincide with the natural frequency. For inner race waviness, the chaotic vibrations occur for waviness of order  $n = qN_b \pm 1$ . For ball waviness, the vibration occurs at the two frequencies i.e. at the cage speed  $\omega_{cage}$  and at the wave passage frequency of the ball ( $N_w \omega_{roll}$ ). For the off-size rolling element, the model predicts discrete spectra having significant components at multiples of varying compliance frequency.

Following important conclusions as regards the effects of various parameters on dynamic response from the present study can be made:

**Effect of Clearance:** Large clearance introduces strong non-linearity and presence of chaotic and unstable region grow wide.

**Effect of Unbalance:** The unbalance results in wide regions of high amplitude and chaotic response, which is by way of period doubling and intermittency.

**Effect of Waviness:** Each order of waviness affects the stability of a rotor bearing system. Available prediction methods are useful to detect peaks at major frequencies due to waviness.

The knowledge base generated from the analysis is expected to help a maintenance engineer in detecting the cause of instability and its preventive measures resulting in improvement of rotor bearing system life.

### **Scope of future work**

The first and foremost is to be able to observe and record the chaotic response experimentally in a rotor bearing system. Once this is made possible, the next obvious step should be to vary various parameters like clearance, pre-load, unbalance level and distributed defects. Also to establish the regions of operating speed and combination of above parameters, in which the response becomes unstable and chaotic.

Since many rotors in practical use are flexible rotors, such laboratory tests need to be conducted on flexible rotors too in order to establish the regimes for unstable and chaotic response. Clearance will be more dominant in vertical rotors, so control tests need to be performed to establish the conditions, which will render the rotor response unstable and chaotic.

## REFERENCES

1. Aktürk, N. and Gohar, R., The Effects of Ball Size Variation on Vibrations Associated with Ball Bearings, Proc. ImechE, Part J: Engineering Tribology, Vol. 212, 1998, pp. 101 – 110.
2. Aktürk, N., The Effect of Waviness on Vibrations Associated With Ball Bearings, ASME Journal of Tribology, Vol. 121, 1999, pp. 667-677.
3. Aktürk, N., Uneeb, M. and Gohar, R., Vibration of a Shaft Supported by Angular Contact Ball Bearings, ASME Paper: PD-Vol. 47, ESDA Joint Conference on Engineering Systems Design and Analysis, June 29 - July 3, Istanbul, Turkey, 1992, pp. 95 – 101.
4. Bal'mount, V. B., Varlamov, E. B. and Gorelik, I. G., Structural Vibrations of Ball Bearings, Soviet Machine Science, Vol. 11, 1987, pp. 82 – 88.
5. Barish, T., Ball Speed Variation in Ball Bearings and Its Effect on Cage Design, Journal of American. Society of Lubrication Engineering, Vol. 8, 1969, pp. 110-116.
6. Bathe, K. and Wilson, E., Numerical Methods in Finite Element Analysis, Englewood Cliffs, Prentice-Hall, New Jersey, 1976.
7. Beatty, R.F. and Hine, M.J., Improved Rotor Response of the Uprated High Pressure Oxygen Turbo pump for the Space Shuttle Main Engine. ASME Journal of Vibrations, Acoustics, Stress and Reliability in Design, Vol. 111, 1989, pp. 163-169.
8. Bently, D., Forced Sub-rotative Speed Dynamic Action of Rotating Machinery, ASME Paper No. 74-PET, Petroleum Mechanical Engineering Conference, Dec. 12-15, Dallas, TX, 1974, pp. 16-20.
9. Cena, K.M. and Hobbs, R.A., The Effects of Ball Quality, Radial Clearance and Grease Specification on the Noise and Vibration of an Electric Motor, Tribology Conventions, ImechE, London, 1972, pp. 93-102.
10. Childs, D.W. and Moyer, D.S., Vibration Characteristics of the HPOTP (High Pressure Oxygen Turbo-pump) of the SSME (Space Shuttle Main Engine), Journal of Engineering for Gas Turbines and Power, Vol. 107, 1985, pp. 152-159.



11. Childs, D.W., Fractional Frequency Rotor Motion due to Non-symmetric Clearance Effects, *Trans. ASME, Journal of Engineering. Power*, Vol. 104, 1982, pp. 533-542.
12. Choi, Y.S. and Noah, S.T., Nonlinear Steady-State Response of a Rotor-Support System, *Trans. ASME, Journal of Vibration, Acoustics, Stress and Reliability in Design*, Vol. 109, 1987, pp. 255 - 264.
13. Choudhury, A. and Tandon, N., A Theoretical Model to Predict the Vibration Response of Rolling Bearings to Distributed Defects Under Radial Load, *ASME Journal of Vibration and Acoustics*, Vol. 120, 1998, pp. 214-220.
14. Chu, F. and Holmes, R., The Effect of Squeeze Film Damper Parameters on the Unbalanced Response and Stability of a Flexible Rotor, *Journal of Engineering for Gas Turbine and Power*, Vol. 120, 1998, pp. 140-148.
15. Datta, J. and Farhang, K., A Nonlinear Model for Structural Vibrations in Rolling Element Bearings: Part I – Derivation of Governing Equations, Part – II Simulation and Results, *ASME Journal of Tribology*, Vol. 119, 1997, pp. 126 – 131.
16. Day, W.B., Asymptotic Expansions in Nonlinear Rotor Dynamics, *Quarterly of Applied Mathematics*, Vol. 44, 1987, pp. 779-792.
17. Eschmann, P., *Ball and Roller Bearings- Theory, Design and Application*. Wiley, New York, 1985.
18. Ehrich, F.F. and O'Connor, J.J., Stator Whirl Rotors in Bearing Clearance, *Trans. ASME, Journal of Engineering for Industry*, Vol. 89, 1967, pp. 381-390.
19. Ehrich, F.F., High Order Subharmonic Response of High Speed Rotors in Bearing Clearance, *Trans. ASME, Journal of Vibration, Acoustic, Stress and Reliability in Design*, Vol. 110, 1988, pp. 9 - 19.
20. Ehrich, F.F., Observation of Subcritical Superharmonic and Chaotic Response in Rotordynamics, *Trans. ASME, Journal of Vibration and Acoustic*, Vol. 114, 1992, pp. 93-100.
21. Ehrich, F.F., Observations of Subcritical Superharmonic and Chaotic Response in Rotordynamics, *Trans. ASME, Journal of Vibration and Acoustic*, Vol. 114, 1991, pp. 93-108.

22. Ehrich, F.F., Subharmonic Vibration of Rotors in Bearing Clearance, ASME-paper, No. 66- MD, Vol. 7, 1966, pp. 221- 230.
23. Ehrich, F.F., Sum and Difference Frequencies in Vibration of High Speed Rotating Machinery, Journal of Engineering for Industry, Vol. 23, 1972, pp. 181-192.
24. Flowers, G.T. and Wu, Fang Sheng, Disk/Shaft Vibration Induced by Bearing Effects: Analysis and Experiments, Journal of Vibration and Acoustic, Vol. 118, 1996, pp. 204-208.
25. Franco, J., Aktürk, N. and Gohar, R., Vibration of a Rigid Shaft Supported by Radial Ball Bearings with Several Defects, ASME Paper no: 92-GT-164, Int. Gas Turbine and Aeroengine Congress and Exposition, June 3-7, Cologne, Germany, 1992, , pp. 1-4.
26. Fukata, S., Tamura, H, Gad, E. H., Kondou, T. and Ayabe, T., On the Radial Vibration of Bearings (Computer Simulation), Bulletin of the JSME, Vol. 28, 1985, pp. 899-904.
27. Gad, E. H., Fukata, S. and Tamura, H., Computer Simulation of Rotor Radial Vibration due to Ball Bearings, Memoirs of the Faculty of Engineering, Kyushu University, Vol. 44, 1984a, pp. 83-111.
28. Gad, E.H., Fukata, S. and Tamura, H., Computer Simulation of Rotor Axial and Radial Vibrations based on Ball Bearings, Memoirs of the Faculty of Engineering, Kyushu University, Vol. 44, 1984b, pp. 169-183.
29. Gargiulo, Jr. E.P., A Simple Way to Estimate Bearing Stiffness, Machine Design, Vol. 24, 1980, pp. 107-110.
30. Goldman, P. and Muszynska, A., Chaotic Behaviour of Rotor/Stator Systems with Rub, Trans. of ASME, Journal of Engineering for Gas Turbines and Power, Vol. 116, 1994a, pp. 692-701.
31. Goldman, P. and Muszynska, A., Dynamic Effects in Mechanical Structures with Gaps and Impacting: Order and Chaos, Trans. of ASME, Journal of Vibration and Acoustics, Vol. 116, 1994, pp. 541-547.
32. Gupta, P.K., Frictional Instabilities in Ball Bearings, Tribology Trans., Vol. 31, 1988, pp. 258-268.

33. Harris, T.A., *Roller Bearing Analysis*, John Wiley and Sons, New York, 1991.
34. Igarashi, T. and Hamada, H., *Studies on the Vibration and Sound of Defective Roller Bearings (First Report: Vibration of Ball Bearings with One Defect)*, *Bulletin of the JSME*, Vol. 25, 1982, pp. 994 – 1001.
35. Igarashi, T. and Kato, J., *Studies on the Vibration and Sound of Defective Roller Bearings (Third Report: Sound of Ball Bearing with Multiple Defects)*, *Bulletin of JSME*, Vol. 28, 1985, pp. 492 – 499.
36. Igarashi, T. and Yabe, S., *Studies on the Vibration and Sound of Defective Roller Bearings (Second Report: Sound of Ball Bearing with One Defect)*, *Bulletin of the JSME*, Vol. 26, 1983, pp. 1791 – 1798.
37. Ishida, Y., *Nonlinear Vibration and Chaos in Rotor Dynamics*, *JSME International Journal Series C*, Vol. 37, 1994, pp. 237-245.
38. Jang, G.H. and Jeong, S.W., *Nonlinear Excitation Model of Ball Bearing Waviness in a Rigid Rotor Supported by Two or More Ball Bearings Considering Five Degrees of Freedom*, *ASME Journal of Tribology*, Vol. 124, 2002, pp.82-90.
39. Kim, Y.B. and Noah, S.T., *Bifurcation Analysis for A Modified Jeffcott Rotor with Bearing Clearances*, *Nonlinear Dynamics*, Vol. 1, 1990, pp. 221-241.
40. Kim, Y.B. and Noah, S.T., *Quasi Periodic Response and Stability Analysis for a Nonlinear Jeffcott Rotor*, *Journal of Sound and Vibration*, Vol. 190, 1996, pp. 239-253.
41. Lalanne, M. and Ferraris, G., *Rotordynamics Prediction in Engineering*, John Wiley and Sons, New York, 1990.
42. Lim, T.C. and Singh, R., *Vibration Transmission through Rolling Element Bearings Part 1: Bearing Stiffness Formulation*, *Journal of Sound and Vibration*, Vol. 139, 1990, pp. 179-199.
43. Marsh, E.R. and Yantek, D.S., *Experimental Measurement of Precision Bearing Dynamic Stiffness*, *Journal of Sound and Vibration*, Vol. 202, 1997, pp. 55-56.
44. Meldau, E., *Die Bewegung der Achse von Walzlagern bei geringen Drehzahlen*, *Werkstadt und Betrieb*, Vol. 7, 1951, pp. 308 - 313.
45. Mevel, B. and Guyader, J.L., *Routes to Chaos in Ball Bearings*, *Journal of Sound and Vibration*, Vol. 162, 1993, pp. 471-487.

46. Meyer, L.D., Ahlgren, F.F. and Weichbrodt, B., An Analytical Model for Ball Bearing Vibrations to Predict Vibration Response to Distributed Defects, ASME Journal of Machine Design, Vol. 102, 1980, pp. 205-210.
47. Mitropoiskii', Yu. A., Problems of Asymptotic Theory of Nonstationary Vibrations, Israel programme for Scientific Transactions, Vol. 11, 1965, pp. 232 – 246.
48. Muszynska, A., Partial Lateral Rotor to Stator Rubs, I.MechE, Part C, Vol. 84, 1984, pp. 281-292.
49. Nayfeh, A.H. and Balachandran, Balkumar, Applied Nonlinear Dynamics Analytical, Computational and Experimental methods, Wiley, New York, 1995.
50. Nayfeh, A.H. and Mook, D.T., Nonlinear Oscillations, Wiley, New York, 1979.
51. Padmanabhan, C. and Singh, R., Analysis of Periodically Excited Nonlinear Systems by a Parametric Continuation Technique, Journal of Sound and Vibration, Vol. 184, 1995, pp. 35 – 58.
52. Parker, T.S., and Chua, L.O., Practical Numerical Algorithms for Chaotic Systems, Springer-Verlag, New York, 1989.
53. Perret, H., Elastische Spielschwingungen Konstant Belaster Walzger, Werkstatt und Betrieb, Vol. 3, 1950, pp. 354-358.
54. Press, W. H., Teukolsky, S. A., Vetterling, W. T. and Flannery, B. P., Numerical Recipes in C: the art of Scientific Computing, Cambridge University Press, Cambridge, 1992.
55. Rahnejat, H. and Gohar, R., The Vibrations of Radial Ball Bearings, Proceedings of the Institution of Mechanical Engineers, Vol. 199(C3), 1985, pp. 181-193.
56. Rao, J.S., Rotor Dynamics, New Age Intl. Publishers, III-Edition, 1996.
57. Sankaravelu, A., Noah, S.T. and Burger, C.P., Bifurcation and Chaos in Ball Bearings, Nonlinear and Stochastic Dynamics, AMD-Vol. 192/DE-Vol. 78, ASME, 1994, pp. 313-325.
58. Satio, S., Calculation of Nonlinear Unbalance Response of Horizontal Jeffcott Rotors Supported by Ball Bearings with Radial Clearances, Trans. of ASME, Journal of Vibration, Acoustics, Stress and Reliability in Design, Vol. 107, 1985, pp. 416-420.

59. Sayles, R.S. and Poon, S.Y., Surface topography and Rolling Element Vibration, Precision Engineering, Vol. 3, 1981, pp. 137-144.
60. SKF, The Measurement of Vibration in Ball Bearings, The Ball Bearing Analysis, 1961, pp. 2-8.
61. Su, Y. T. and Lin, S. J., On Initial Fault Detection of a Tapered Roller Bearing: Frequency Domain Analysis, Journal of Sound and Vibration, Vol. 114, 1992, pp. 342 – 355.
62. Su, Y. T., Lin, M. H. and Lee, M. S., The Effects of Surface Irregularities on Roller Bearing Vibrations, Journal of Sound and Vibration, Vol.165, 1993, pp. 455 – 466.
63. Sunnersjo, C.S., Rolling Bearing Vibrations- The Effects of Geometrical Imperfections and, Journal of Sound and Vibration, Vol. 98, 1985, pp. 455-474.
64. Sunnersjo, C.S., Varying Compliance Vibrations of Rolling Bearings, Journal of Sound and Vibration, Vol. 58, 1978, pp. 363-373.
65. Tallian, T.E. and Gustafson, O.G., Progress in Rolling Bearing Vibration Research and Control, ASLE Trans., Vol. 8, 1965, pp. 195-207.
66. Tallian, T.E., Gustafson, O.G., et al., Research Report on study of the Vibration Characteristics of Bearings, Report: AL 631 023, Reg: 585 14: 4223, SKF Industry Inc., 1963.
67. Tamura, A. and Taniguchi, O., Ball Bearing Vibrations (1<sup>st</sup> report), Trans. of the JSME, Vol. 26, 1960, pp. 19-25.
68. Tamura, A., On the Vibrations Caused by Ball Diameter Differences in a Ball Bearing, Bull. Jap. Soc. Mech. Engrs., Vol. 11, 1968, pp. 229-234.
69. Tamura, H. and Tsuda, Y., On the Spring Characteristics of a Ball Bearings (Fluctuation due to Ball Revolution), Bulletin of the JSME, Vol. 23, 1980, pp. 1905-1912.
70. Tandon, N. and Nakara, B. C., Detection of Defects in Rolling Element Bearings by Vibration Monitoring, Journal of Institution of Engineers (India)- Mechanical Engineering Division, Vol. 73, 1993, pp. 271 – 282.
71. Thomas, T.R., Rough Surfaces, Longman, London, U.K., 1982.

72. Thompson, J.M.T. and Stewart, H.B., *Nonlinear Dynamics and Chaos- Geometrical methods for Engineers and Scientists*, New York, John Wiley and Sons, 1986.
73. Tiwari, R. and Vyas, N.S., Estimation of Nonlinear Stiffness Parameters of Rolling Element Bearing from Random Response of Rotor – Bearing Systems, *Journal of Sound and Vibration*, Vol. 187, 1995, pp. 229-239.
74. Tiwari, R. and Vyas, N.S., Parameter Estimation in Imbalance Non-linear Rotor Bearing Systems from Random Response, *Journal of Sound and Vibration*, Vol. 208, 1997, pp. 1-14.
75. Tongue, B. H., Characteristics of Numerical Simulations of Chaotic Systems, *Journal of Applied Mechanics*, Vol. 54, 1987, pp. 695-699.
76. Wardle, F.P. and Poon, S.Y., Rolling Bearing Noise - Cause and Cure, *Chart. Mechanical Engineering*, July / Aug., 1983, pp. 36-40.
77. Wardle, F.P., Vibration Forces Produced by Waviness of the Rolling Surfaces of Thrust Loaded Ball Bearings, Part-I: Theory, *Proceedings of the Institution of Mechanical Engineers*, Vol. 202, 1988(a), pp. 305-312.
78. Wardle, F.P., Vibration Forces Produced by Waviness of the Rolling Surfaces of Thrust Loaded Ball Bearings, Part-II Experimental Validation, *Proceedings of the Institution of Mechanical Engineers*, 202, 1988(b), pp. 313-319.
79. White, M.F., Rolling Element Bearing Vibration Transfer Characteristics: Effect of Stiffness, *Journal of Applied Mechanics*, Vol. 46, 1979, pp. 677-684.
80. Yamamoto, T., Ishida, Y., Ikeda, T. and Yamada, M., Subharmonic and Summed-and-differential Harmonic Oscillations in an Unsymmetrical Rotor, *Bull. Jap. Soc. Mech. Engrs.*, Vol. 24, 1981, pp. 192-199.
81. Yamamoto, T., On the Vibration of a Rotating Shaft, *Memoirs of Faculty of Engineering, Nagoya University*, Vol.9, 1957, pp. 24.
82. Yamamoto, T., On the Vibration of a Shaft Supported by Bearing Having Radial Clearances, *Trans. JSME*, Vol. 21, 1955, pp. 182-192.
83. Yhland, E., A Linear Theory of Vibrations Caused by Ball Bearings With Form Errors Operating at Moderate Speed, *ASME Journal of Tribology*, Vol. 114, 1992, 348 – 359.

84. Yhland, E.M., Waviness Measurement – An Instrument for Quality Control in Rolling Bearing Industry, Proceedings of Institute of Mechanical Engineers, Vol. 82, Part-K, 1967, pp. 438-445.
85. Zheng, T. and Hasebe, N., Nonlinear Dynamic Behaviours of a Complex Rotor-Bearing System, ASME Journal of Applied Mechanics, Vol. 67, 2000, pp. 485 – 495.

## Appendix A

# PROPERTIES OF ROLLING ELEMENT BEARINGS

From the manufacturers catalogs, a standard ball bearing and a roller bearing are chosen (Fig. A.1). The geometrical and physical properties of the bearing, required for the calculations are listed in Table A.1.

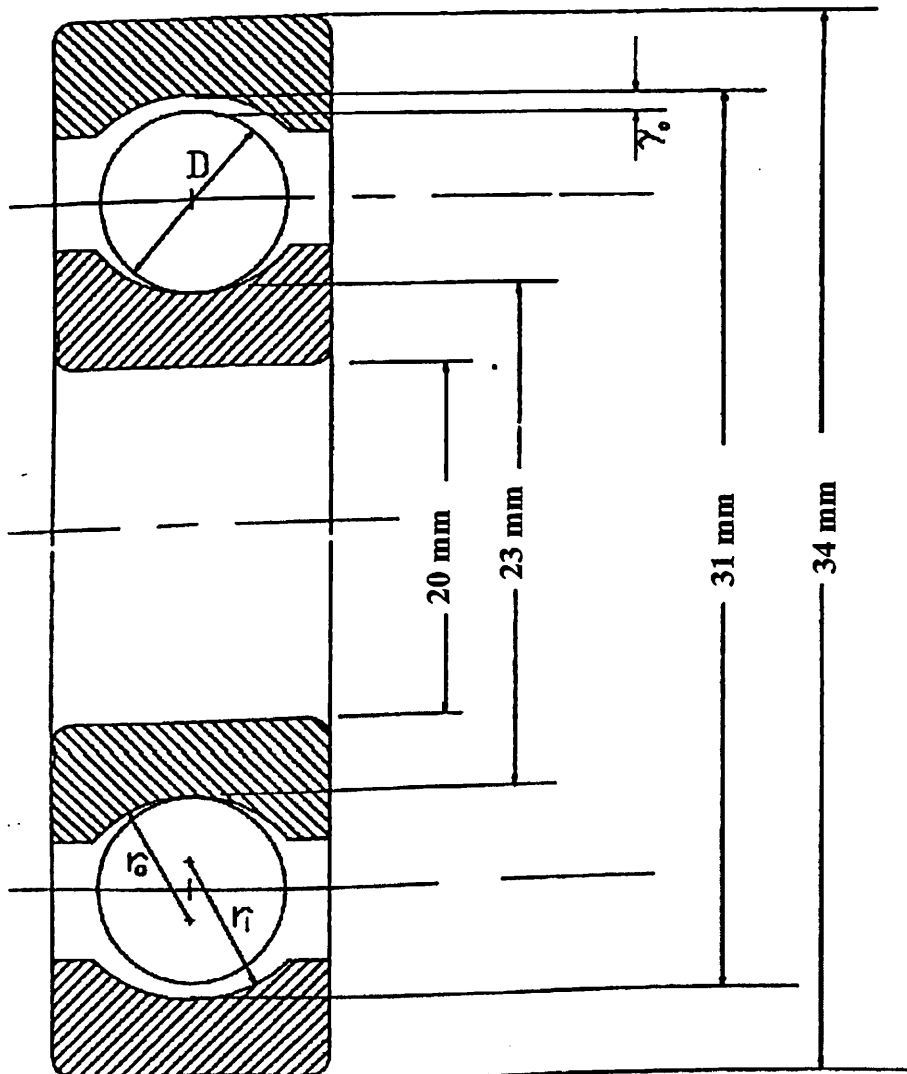


Fig. A.1 Dimensions of rolling element bearing



**Table A.1** Geometric and physical properties used for the ball and roller bearings

Mass of rolling element ( $m_j$ )	0.009 kg
Mass of the inner race ( $m_{in}$ )	0.06 kg
Mass of the outer race ( $m_{out}$ )	0.065 kg
Mass of the rotor ( $m_r$ )	5.5 kg
Radius of inner race with point of contact with the rolling element ( $r$ )	23 mm
Radius of outer race with point of contact with the rolling element ( $R$ )	31 mm
Radius of each rolling element ( $\rho_r$ )	3.98 mm
Radial load ( $W$ )	6 N
Pitch radius of ball set	2.7 mm
Maximum amplitude of waviness ( $I_p$ )	2 $\mu\text{m}$
Initial amplitude of waviness ( $I_0$ )	1 $\mu\text{m}$
Initial radial position of $j^{\text{th}}$ Rolling Element ( $\rho_j$ )	27 mm
Outside diameter	68 mm
Mass of bearing	0.22 kg
Moment of inertia of each rolling element ( $I$ )	$7.2 \times 10^{-8} \text{ kg.m}^2$
Moment of inertia of the inner race ( $I_{inner}$ )	$2.7 \times 10^{-5} \text{ kg.m}^2$
Moment of inertia of the outer race ( $I_{outer}$ )	$6.9 \times 10^{-5} \text{ kg.m}^2$
Moment of inertia of the rotor ( $I_{rotor}$ )	$3.7 \times 10^{-3} \text{ kg.m}^2$
Number of rolling elements ( $N_b$ )	8
Angular separation between elements ( $\beta = 2\pi / N_b$ )	45 deg
Length of roller over which it rolls ( $l_{eff}$ )	11 mm

## Appendix B

# ROLLING ELEMENT BEARING STIFFNESS

### 1. Ball Bearing

Hertz considered the stress and deformation in the perfectly smooth, ellipsoidal, contacting elastic solids. The application of the classical theory of elasticity to the problem forms the basis of stress calculation for machine elements as ball and roller bearings. Therefore, the *point* contact between the race and ball develop into an area contact, which has the shape of an ellipse with  $a$  and  $b$  as the semi major and semi minor axes respectively. The curvature sum and difference are needed in order to obtain the contact force of the ball. The curvature sum  $\sum \rho$  is obtained as from (Harris, 1991) is expressed as:

$$\sum \rho = \rho_{I1} + \rho_{I2} + \rho_{II1} + \rho_{II2} = \frac{1}{r_{I1}} + \frac{1}{r_{I2}} + \frac{1}{r_{II1}} + \frac{1}{r_{II2}} \quad (\text{B.1})$$

The curvature difference  $F(\rho)$  is expressed as:

$$F(\rho) = \frac{(\rho_{I1} - \rho_{I2}) + (\rho_{II1} - \rho_{II2})}{\sum \rho} \quad (\text{B.2})$$

The parameters  $r_{I1}, r_{I2}, r_{II1}, r_{II2}, \rho_{I1}, \rho_{I2}, \rho_{II1}, \rho_{II2}$  are given dependent upon calculations referring to the inner and outer races as shown in Fig.B.1. If the inner race is considered,

$$\begin{aligned} r_{I1} = D/2, r_{I2} = D/2, r_{II1} = d/2, r_{II2} = r \quad \text{and} \\ \rho_{I1} = 2/D, \rho_{I2} = 2/D, \rho_{II1} = 2/d, \rho_{II2} = -1/r \end{aligned} \quad (\text{B.3})$$

If outer race is considered, they are given as:

$$\begin{aligned} r_{I1} = D/2, r_{I2} = D/2, r_{II1} = D/2, r_{II2} = R \quad \text{and} \\ \rho_{I1} = 2/D, \rho_{I2} = 2/D, \rho_{II1} = -2/D, \rho_{II2} = -1/R \end{aligned} \quad (\text{B.4})$$

As per the sign convention followed, negative radius denotes a concave surface. Using Table – B.1 calculation of all the parameters including curvature difference at inner and outer race can be done. For the contacting bodies being made of steel, the relative approach between two contacting and deforming surface is given by:

## Appendix B

# ROLLING ELEMENT BEARING STIFFNESS

### 1. Ball Bearing

Hertz considered the stress and deformation in the perfectly smooth, ellipsoidal, contacting elastic solids. The application of the classical theory of elasticity to the problem forms the basis of stress calculation for machine elements as ball and roller bearings. Therefore, the *point* contact between the race and ball develop into an area contact, which has the shape of an ellipse with  $a$  and  $b$  as the semi major and semi minor axes respectively. The curvature sum and difference are needed in order to obtain the contact force of the ball. The curvature sum  $\sum \rho$  is obtained as from (Harris, 1991) is expressed as:

$$\sum \rho = \rho_{I1} + \rho_{I2} + \rho_{II1} + \rho_{II2} = \frac{1}{r_{I1}} + \frac{1}{r_{I2}} + \frac{1}{r_{II1}} + \frac{1}{r_{II2}} \quad (\text{B.1})$$

The curvature difference  $F(\rho)$  is expressed as:

$$F(\rho) = \frac{(\rho_{I1} - \rho_{I2}) + (\rho_{II1} - \rho_{II2})}{\sum \rho} \quad (\text{B.2})$$

The parameters  $r_{I1}, r_{I2}, r_{II1}, r_{II2}, \rho_{I1}, \rho_{I2}, \rho_{II1}, \rho_{II2}$  are given dependent upon calculations referring to the inner and outer races as shown in Fig.B.1. If the inner race is considered,

$$\begin{aligned} r_{I1} = D/2, r_{I2} = D/2, r_{II1} = d/2, r_{II2} = r \quad \text{and} \\ \rho_{I1} = 2/D, \rho_{I2} = 2/D, \rho_{II1} = 2/d, \rho_{II2} = -1/r \end{aligned} \quad (\text{B.3})$$

If outer race is considered, they are given as:

$$\begin{aligned} r_{I1} = D/2, r_{I2} = D/2, r_{II1} = D/2, r_{II2} = R \quad \text{and} \\ \rho_{I1} = 2/D, \rho_{I2} = 2/D, \rho_{II1} = -2/D, \rho_{II2} = -1/R \end{aligned} \quad (\text{B.4})$$

As per the sign convention followed, negative radius denotes a concave surface. Using Table – B.1 calculation of all the parameters including curvature difference at inner and outer race can be done. For the contacting bodies being made of steel, the relative approach between two contacting and deforming surface is given by:

$$\delta = 2.787 \times 10^{-8} Q^{2/3} (\sum \rho)^{1/3} \delta^* \quad (\text{B.5})$$

Where  $\delta^*$  is a function of  $F(\rho)$ .

Hence, the contact force (Q) is:

$$Q = \left\{ (3.587 \times 10^7)^{3/2} (\sum \rho)^{-1/2} (\delta^*)^{-3/2} \right\} \delta^{3/2} \quad (N) \quad (\text{B.6})$$

The elastic modulus for the contact of a ball with the inner race is:

$$K_i = \frac{Q}{\delta_{in}} = (3.587 \times 10^7)^{3/2} (\sum \rho_i)^{-1/2} (\delta_i^*)^{-3/2} (\delta)^{1/2} \quad \left( \frac{N}{mm} \right) \quad (\text{B.7})$$

And for the contact of a ball with the outer race is:

$$K_o = \frac{Q}{\delta_{out}} = (3.587 \times 10^7)^{3/2} (\sum \rho_o)^{-1/2} (\delta_o^*)^{-3/2} (\delta)^{1/2} \quad \left( \frac{N}{mm} \right) \quad (\text{B.8})$$

Then the effective elastic modulus K for the bearing system is written as:

$$K = \frac{1}{\left( \frac{1}{K_i^{1/n}} + \frac{1}{K_o^{1/n}} \right)^n} \quad (\text{B.9})$$

In the equation (B.7) and (B.8), the parameters  $\delta_i^*$  and  $\delta_o^*$  can be attained from Table A.1, if the values of  $F(\rho)_i$  and  $F(\rho)_o$  are available with using of Table – B.1. The effective elastic modulus (K) for bearing system with using geometrical and physical parameters is written as:

$$K = 7.055 \times 10^5 \sqrt{\delta} \quad \frac{N}{mm} \quad (\text{B.10})$$

The nonlinear stiffness associated with point contact of spring for the inner and outer races is calculated by using Equation (B.10) is:

$$(k_{in}) = 7.055 \times 10^5 \left[ \{r + \rho_r\} - \chi_j \right]^{1/2} \quad (\text{B.11})$$

$$(k_{out}) = 7.055 \times 10^5 \left[ R - \{\rho_j + \rho_r\} \right]^{1/2} \quad (\text{B.12})$$

$$\frac{\partial k_{in}}{\partial \rho_j} = -3.5725 \times 10^5 \left[ \{r + \rho_r\} - \chi_j \right]^{-1/2} \frac{\partial \chi_j}{\partial \rho_j} \quad (\text{B.13})$$

$$\frac{(\partial k_{out})}{\partial \rho_j} = 3.5725 \times 10^5 [R - \{\rho_j + \rho_r\}]^{-1/2} \quad (B.14)$$

## 2. Roller Bearing

Hertz equation for elastic deformation involving line contact between rollers and races is given by (Eschmann et al., 1985):

$$\delta = \frac{4.05}{10^5} \frac{Q^{0.925}}{l_{eff}^{0.85}} \quad (mm) \quad (B.15)$$

Where Q is the contact force (N) and  $l_{eff}$  is the length over which the rollers are actually in contact. From this equation, the contact force is,

$$Q = 56065.703 \times l_{eff}^{0.92} \delta^{1.08} \quad (N) \quad (B.16)$$

Hence the nonlinear stiffness associated with line contact is given by

$$k = 56065.703 \times l_{eff}^{0.92} \delta^{0.08} \quad \left( \frac{N}{mm} \right) \quad (B.17)$$

$$(k_{in}) = 56065.703 \times l_{eff}^{0.92} \delta_{in}^{0.08} \quad \left( \frac{N}{mm} \right) \quad (B.18)$$

$$(k_{out}) = 56065.703 \times l_{eff}^{0.92} \delta_{out}^{0.08} \quad \left( \frac{N}{mm} \right) \quad (B.19)$$

$$\frac{(\partial k_{in})}{\partial \rho_j} = 4485.256 \times [\delta]_{in}^{-0.92} (l_{eff}^{0.92}) \frac{\partial l_{eff}}{\partial \rho_j} \quad (B.20)$$

$$\frac{(\partial k_{out})}{\partial \rho_j} = 4485.256 \times [\delta]_{out}^{-0.92} (l_{eff}^{0.92}) \quad (B.21)$$

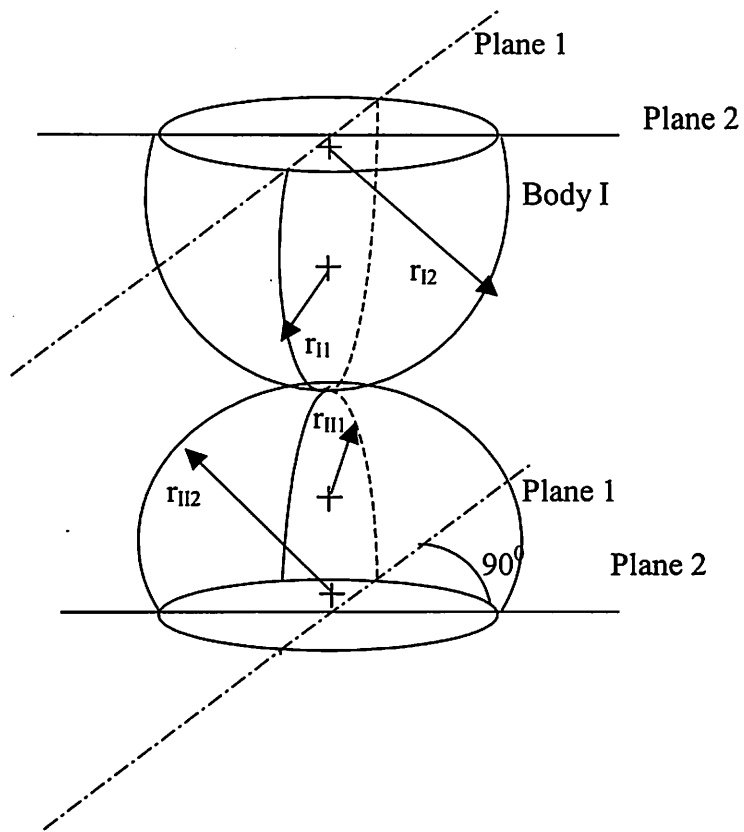


**Fig. B.1** Geometry of Contacting Bodies

## Appendix C

# THE VARIATIONAL EQUATIONS

The vibrational equation is integrated to find out  $D_{x_0}$ ,  $\phi_t(x_0, t_0)$ , the derivative of a trajectory with respect to the initial condition (Parker and Chua, 1993), considering the  $n^{\text{th}}$ - order system

$$\dot{x} = f(x, t), \quad x(t_0) = x_0 \quad (\text{C.1})$$

with solution  $\phi_t(x_0, t_0)$ , that is,

$$\dot{\phi}_t(x_0, t_0) = f[\phi_t(x, t), t], \quad \phi_{t_0}(x_0, t_0) = x_0 \quad (\text{C.2})$$

Differentiating (C.2) with respect to  $x_0$ , we get

$$D_{x_0} \dot{\phi}_t(x_0, t_0) = D_x f[\phi_t(x, t), t] D_{x_0} \phi_t(x_0, t_0) \quad (\text{C.3})$$

$$D_{x_0} \phi_t(x_0, t_0) = I$$

Define  $\phi_t(x_0, t_0) = D_{x_0} \phi_t(x_0, t_0)$ , Eq. (C.3) becomes,

$$\dot{\Phi}_t(x_0, t_0) = D_x f[\phi_t(x, t), t] \Phi_t(x_0, t_0), \quad \Phi_{t_0}(x_0, t_0) = I \quad (\text{C.4})$$

Which is the Variational equation.

Following may be noted

1. The Variational equation is a matrix-valued time varying linear equation. It is the linearization of the vector field along the trajectory  $\phi_t(x_0, t_0)$  and is a function of the trajectory.
2. Since the initial condition is the identity matrix,  $\Phi_t(x_0, t_0)$  is the state transition matrix of the linear system (C.4). It follows that perturbation  $\delta x_0$  of  $x_0$  evolves as,

$$\delta x = \Phi_t(x_0, t_0) \delta x_0 \quad (\text{C.5})$$

The perturbation  $\delta x$  may be interpreted in two ways: as an infinitesimal perturbation of the original system (C.1) or as a (finite) vector-valued solution of the linearized system (C.4). The Variational equation depends on both  $\phi_t$  and  $\Phi_t$ . They are usually calculated at the same time. To perform this simulation integration, the Variational equation is appended to the original system to obtain the combined system,

$$\begin{Bmatrix} \dot{x} \\ \dot{\Phi} \end{Bmatrix} = \begin{Bmatrix} f(x, t) \\ D_x f(x, t)\Phi \end{Bmatrix} \quad (\text{C.6})$$

which is integrated from the initial conditions

$$\begin{Bmatrix} x(t_0) \\ \Phi(t_0) \end{Bmatrix} = \begin{Bmatrix} x_0 \\ I \end{Bmatrix} \quad (\text{C.7})$$



## Appendix D

# MODIFIED NEWMARK- $\beta$ METHOD

Newmark- $\beta$  method is a numerical procedure to calculate dynamic response because it accommodates the calculation of nonlinear response more conveniently. Also it represents an elegant example of effective unconventional thinking in structural analysis. The nonlinear equations of motion are integrated with the Newmark method (see Bathe, 1982). The method is based on a constant-average acceleration scheme and is also referred to as the trapezoid rule. The following assumption are employed:

$$\{\dot{U}\}^{t+\Delta t} = \{\dot{U}\}^t + \left[ (1-\delta)\{\ddot{U}\}^t + \delta\{\ddot{U}\}^{t+\Delta t} \right] \Delta t \quad (D.1)$$

$$\{U\}^{t+\Delta t} = \{U\}^t + \{\dot{U}\}^t \times \Delta t + \left[ \left( \frac{1}{2} - \delta \right) \{\ddot{U}\}^t + \alpha \{\ddot{U}\}^{t+\Delta t} \right] \Delta t^2 \quad (D.2)$$

Where  $\alpha$  and  $\delta$  are parameters that can be determined to obtained integration accuracy and stability. When  $\alpha = 1/6$  and  $\delta = 1/2$ , relations (D.1) and (D.2) correspond to the linear stability. The constant-average acceleration method is unconditionally stable for linear problems. Newmark originally proposed as an unconditionally stable scheme the constant-average acceleration method, in which case  $\alpha = 1/4$  and  $\delta = 1/2$  used (see Fig. D.1). For most nonlinear problems in structural dynamics this also applies. An accuracy analysis shows that the method does not suffer from amplitude decay. With respect to the choice of the time step  $\Delta t$  one must be aware that the method may suffer from period elongation. In addition to (D.1) and (D.2), for solution of the displacements, velocities and accelerations at time  $t + \Delta t$ , the equilibrium equations at this time are also considered:

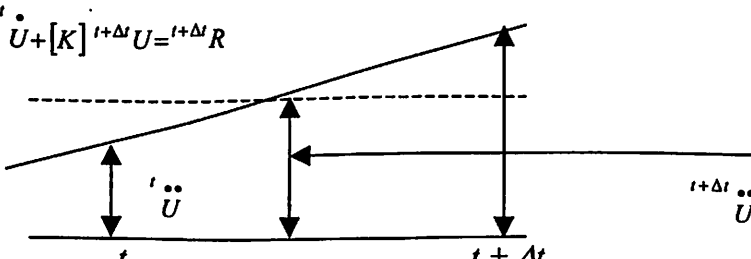
$$[m] \ddot{U}^{t+\Delta t} + [C] \dot{U}^{t+\Delta t} + [K] U^{t+\Delta t} = R^{t+\Delta t} \quad (D.3)$$


Fig. D.1 Newmark constant-average acceleration scheme

Solving from (D.2) for  ${}^{t+\Delta t}\ddot{U}$  in terms of  ${}^{t+\Delta t}U$  and then substituting for  ${}^{t+\Delta t}\ddot{U}$  into (D.1), we obtain equations for  ${}^{t+\Delta t}\ddot{U}$  and  ${}^{t+\Delta t}\dot{U}$  each in terms of the unknown displacements  ${}^{t+\Delta t}U$  only. These two relations for  ${}^{t+\Delta t}\dot{U}$  and  ${}^{t+\Delta t}\ddot{U}$  are substituted into (D.3) to solve for  ${}^{t+\Delta t}U$ , after which, using (D.1) and (D.2),  ${}^{t+\Delta t}\dot{U}$  and  ${}^{t+\Delta t}\ddot{U}$  can be calculated also. The complete algorithm is as follows:

**Initial calculations**

*Step 1:* Select mass (m) and damping (c)

*Step 2:* Initialize  ${}^0U$ ,  ${}^0\dot{U}$  and  ${}^0\ddot{U}$ .

*Step 3:* Select time step ( $\Delta t$ ) and parameters  $\alpha$  and  $\delta$  and calculate the integration constants as:  $\delta \geq 0.50$ ;  $\alpha \geq 0.25(0.5 + \delta)^2$

$$a_0 = \frac{1}{\alpha t^2}, a_1 = \frac{\delta}{\alpha t}, a_2 = \frac{1}{\alpha t}, a_3 = \frac{1}{2\alpha} - 1, a_4 = \frac{\delta}{\alpha} - 1, a_5 = \frac{\Delta t}{2} \left( \frac{\delta}{\alpha} - 1 \right), a_6 = \Delta t(1 - \delta) \text{ and } a_7 = \delta \Delta t$$

**For each time step**

1. Put the values of acceleration and velocity at time (t) in (D.3).

$${}^{t+\Delta t}\ddot{U} = a_0 ({}^{t+\Delta t}U - {}^tU) - a_2 {}^t\dot{U} - a_3 {}^t\ddot{U}$$

$${}^{t+\Delta t}\dot{U} = {}^t\dot{U} + a_6 {}^t\ddot{U} + a_7 {}^{t+\Delta t}\ddot{U}$$

2. Solve the equation for displacement at time  $t + \Delta t$ .
3. Calculate accelerations and velocities at time  $t + \Delta t$ .

Solving the equations of motion by Newmark method, two simultaneous nonlinear equations with two variables x and y.

## List of Publications

### Journals

1. Harsha S. P., K. Sandeep and Prakash R, "Nonlinear Dynamic Behaviors of Rolling Element Bearings Due to Surface Waviness." *Journal of Sound and Vibration*, Vol. 272, No. 3-5, 2004, pp. 557 – 580.
2. Harsha S. P., K. Sandeep and Prakash R, "The Effect of Speed of Balanced Rotor on Nonlinear Vibrations Associated With Ball Bearings." *International Journal of Mechanical Sciences*, Vol.47, No. 4, 2003, pp 725 – 740.
3. Harsha S. P., K. Sandeep and Prakash R, "Effects of Preload and Number of Balls on Nonlinear Dynamic Behavior of Ball Bearing System." *International Journal of Nonlinear Sciences and Numerical Simulation*, Vol. 4, No. 3, 2003, pp. 265 – 279.
4. Harsha S. P., K. Sandeep and Prakash R, "Quasi-periodic, Subharmonic and Chaotic Motions of a Rotor Bearing System." *International Journal of Nonlinear Sciences and Numerical Simulation*, Vol.4, No.4, 2003, pp. 361 – 372.
5. Harsha S. P., K. Sandeep and Prakash R, "Nonlinear Dynamic Behaviors of High Speed Rotor Supported By Rolling Element Bearings." *International Journal of Applied Mechanics and Engineering*, Vol.8, No. 4, 2003, pp. 705 – 720.
6. Harsha S. P., K. Sandeep and Prakash R, "Nonlinear Dynamic Response of a Rotor Bearing System Due to Surface Waviness." *Nonlinear Dynamics, An International Journal of Nonlinear Dynamics and Chaos in Engineering Systems*, Vol. 37, No.2, 2004, pp. 90-123.

### Conferences / Symposiums

1. Harsha S. P., K. Sandeep and Prakash R., "Analysis of Angular Contact Ball Bearings Using Object Oriented Programming." *ISTAM (International Meet)* held at IIT-Kharagpur, 2001, pp. 201 – 209.
2. Harsha S. P., K. Sandeep and Prakash R., "Chaotic Vibrations in High Speed Rolling Element Bearings." *International Conference on Industrial Tribology (ICIT)* held at TATA STEEL- Jamshedpur, 2002, pp. 57 – 63.

3. Harsha S. P., K. Sandeep and Prakash R., "Nonlinear Dynamic Responses in Rolling Element Bearings Due to Surface Waviness Under Radial Load." *International Conference on Vibration Engineering and Technology of Machinery (Vetomac)* held at BARC – Mumbai, 2002, pp. 1- 10.
4. Harsha S. P., K. Sandeep and Prakash R., "Nonlinear Dynamic Behaviors of a Complex Rotor Bearing System Due to Surface Imperfections." *International Symposium on Process on Process Systems Engineering & Control* held at IIT – Bombay, 2003, pp. 241 – 246.
5. Harsha S. P. and Prakash R., "A Model for Structural Vibrations in Rolling Element Bearings." *National Conference on Advanced Trends in Mechanical Engineering Research and Development held at JNTU – Anantapur*, 2001, pp. 31-38.
6. Harsha S. P. and Prakash R., "Dynamic Analysis of High Speed Ball Bearings." *National Conference on Engineering Design* held at MBMEC – Jodhpur, 2001, pp. 87 – 98.

## BIOGRAPHY

Prof Ravi Prakash has 30 years of teaching and research experience. He is currently, Dean, Research and Consultancy Division at BITS, Pilani. Earlier he was the Dean for Faculty Division II. He has been Science Counsellor, Embassy of India, Washington D.C., USA. He has also been the Coordinator, School of Biomedical Engineering, Institute of Technology, Banaras Hindu University. Presently, besides being Dean, he is Coordinator for Centre for Materials Science and Technology, Centre for Robotics and Intelligent Systems and Center for Desert Development Technology. He has published over 100 research papers in various international journals / conferences of repute. He is Fellow of the Institution of Engineers (India) (FIE), Fellow of Ultrasonic Society of India, Fellow of Indian Society for Nondestructive Testing, Member of American Society of Mechanical Engineers (ASME), USA, Member of Indian Society of Mechanical Engineers (ISME) etc.

Suraj Prakash Harsha has 5 years of teaching and research experience. He is currently, faculty of Mechanical Engineering Group at BITS, Pilani. He has published over 12 research papers in various international journals / conferences of repute.